UCGE Reports
Number 20235

Department of Geomatics Engineering

Controlled Indoor GPS Signal Simulation
(URL: http://www.geomatics.ucalgary.ca/research/publications/GradTheses.html)

by

Tao Hu

January 2006

SCHULICH
School of Engineering

UNIVERSITY OF CALGARY

THE UNIVERSITY OF CALGARY

Controlled Indoor GPS Signal Simulation

by

Tao Hu

A THESIS

SUBMITTED TO THE FACULTY OF GRADUATE STUDIES

IN PARTIAL FULFILLMENT OF THE REQUIREMENTS FOR THE

DEGREE OF MASTER OF SCIENCE

DEPARTMENT OF GEOMATICS ENGINEERING

CALGARY, ALBERTA

JANUARY, 2006

Abstract

Laboratory testing is an effective method for GPS receiver manufacturers due to its representative, repeatable and controllable features. However, a fully satisfactory method to simulate signals affected by both indoor type attenuation and large multipath has not yet been developed. In the indoor and urban canyon environments, GPS signals suffer from power attenuation and severe non line-of-sight multipath. In order to understand the characteristics of degraded signals, the code errors and carrier-to-noise density ratios (C/N_0) of these types of signals are analyzed theoretically and empirically herein. Field tests are conducted in a variety of degraded GPS environments to verify the models. The corresponding GPS receiver measurements of signal power fading and estimated pseudorange errors are used to estimate the degraded signal parameters of hardware-in-the-loop simulations using a state-of-the-art GPS signal simulator. The stochastic characteristics of the environment and statistical similarity between field and simulated data are described by probability density functions and correlation coefficients, respectively. The simulated results show a high level of compatibility with the field results, demonstrating clearly the feasibility of the approach and the potential advantages not only to test equipment effectively, but also to meet minimum operational performance standards (MOPS).

Acknowledgements

I would like to express my heartfelt appreciation to my supervisor Dr. Gérard Lachapelle and my co-supervisor Dr. Richard Klukas.   Their valuable guidance and thoughtful advice were essential for the completion of my research and this thesis.   I am extremely thankful to Dr. Gérard Lachapelle for giving me an opportunity to study in a world-class institution, the PLAN group at the University of Calgary.   His excellent supervision, encouragement and support are greatly appreciated.   I firmly believe his guidance and advice will benefit me beyond my study into my future career and life.

I wish to thank my parents Xiangjun Hu and Jinyu Huang, who have supported and inspired me to pursue all of my education.   My father, a professor in the university, taught me to always exert double efforts to achieve my goal.   I am also indebted to my parents-in-law for their untiring support.

My deepest thanks go to my dearest husband, Zhen Liang, for his continuous encouragement and support.   His love gives me the motivation to live and study in a new country here in Canada a few years ago.

Special thanks to my colleagues, Dharshaka Karunanayake and Rob Watson, for their kindness and tireless help.   I can always find sparkles in our professional discussions.

Many thanks to my other colleagues and friends in the PLAN group for their kindly

Table of Contents

List of Tables

List of Figures

xiv

Notation

List of Abbreviations

AGPS	Assisted Global Positioning System
DGPS	Differential Global Positioning System
C/A	Coarse/Acquisition
CC	Correlation Coefficient
C/N_0	Carrier-to-Noise Density Ratio
DC	Direct Current
DLL	Delay Lock Loop
DOP	Dilution of Precision
E-911	Enhanced 911
EIRP	Effective Isotropic Radiated Power
FLL	Frequency Lock Loop
FCC	Federal Communication Commission
GPS	Global Positioning System
HDOP	Horizontal Dilution of Precision
HSGPS	High Sensitivity GPS
LHCP	Left-Hand Circularly Polarized
LHEP	Left-Hand Elliptically Polarized
LOS	Line-of-Sight
LMM	Land Mobile Multipath

LMS	Land Mobile Satellite
MDR	Multipath to Direct Signal Amplitude Ratio
MNED	Maximum Near Echo Delay
MOPS	Minimum Operational Performance Standards
PDF	Probability Density Function
PLL	Phase Lock Loop
PPM	Parts Per Million
PSAP	Public Safety Answering Point
PSD	Power Spectral Density
RF	Radio Frequency
RHCP	Right-Hand Circularly Polarized
TEC	Total Electron Content
TEM	Transverse Electromagnetic
TOA	Time-of-Arrival
TOW	Time-of-week
TTFF	Time-To-First-Fix
UTSFM	Urban Three-State Fade Model

List of Symbols

A	Satellite signal carrier amplitude
b	Parameter of the exponential distribution
c	Speed of light

$c(\ )$	GPS C/A or P code
Cov	Covariance
d	Distance between the transmitting and receiving antennas
d_1	Distance between the cross section and the transmitter
d_2	Distance between the cross section and the receiver
D	Distance from the antenna to the reflector
D_c	Coherent code discriminator
d_{ion}	Ionospheric delay error
$d\rho$	Orbital error
dt	Satellite clock error with respect to GPS time
dT	Receiver clock error with respect to GPS time
d_{trop}	Tropospheric delay error
D_n	Non-coherent code discriminator
D_{nm}	Non-coherent code discriminator in presence of multipath
D_r	Carrier phase discriminator
D_{rm}	Carrier phase discriminator in presence of multipath
E	Estimated pseudorange error
F	Fading
H	Height of the antenna with respect to the ground plane
IE	In-phase early correlation value
IL	In-phase late correlation value
IP	In-phase prompt correlation value
I'_{delay}	Change rate of the multipath delay

n	Number of Fresnel zone and number of variable
n_1	Refractive indices of the first medium
n_2	Refractive indices of the second medium
N	Number of reflected signals
N_0	Noise density
P	Code pseudorange measurement
P'	Modified pseudorange of the rover station
P_{att}	Signal strength loss due to shadowing effect
P_c	Incoming carrier strength
P_e	C/N_0 error due to multipath
$P_h(0)$	Mean power level for echo signals.
PL	Free-space loss
QE	Quadrature-phase early correlation value
QL	Quadrature-phase late correlation value
QP	Quadrature-phase prompt correlation value
r	Radius of the Fresnel zone
$R(\cdot)$	Correlation function
t_0	True code phase offset
T	Cycle of the multipath error undulation
T_c	Chip width
T_d	Spacing between the prompt and early, or prompt and late
α	Azimuth angle of the satellite
α_i	Amplitude ratio of multipath to direct signal

ε	Elevation angle of the satellite
$\varepsilon_{Pmultipath}$	Code range multipath error
ε_{Prx}	Receiver noise
$\hat{\gamma}_c$	Receiver estimate of the incoming signal carrier phase
γ_0	Direct signal phase
γ_e	Multipath phase error
γ_i	the ith reflected signal carrier phase
θ	Incidental angle / Combination of elevation and azimuth
θ_i	Incidental angle
θ_r	Reflected angle
θ_t	Transmitted angle
λ	Wavelength
ρ	Geometric range between satellite and user
ρ_b	Differential correction from the reference station
ρ_{xy}	Correlation coefficient
s_i	Satellite signal
τ_e	Multipath code error
τ	Path delay
$\hat{\tau}_c$	Receiver estimate of the incoming signal code delay
τ_i	the ith reflected signal code delay
ω_0	Satellite signal carrier frequency
σ^2	Variance

Chapter 1

Introduction

1.1 Background

The Global Positioning System (GPS) was originally designed as a military system and has been playing an ever-increasing role in today's society. Conventional GPS receivers were initially designed to operate in open sky and the received satellite signals usually conform to the minimum strength requirement specified by the ICD-GPS-200C (2000). Along with the growing demand for personal safety and location-based services, GPS is utilized in increasingly difficult operational environments. High Sensitivity GPS (HSGPS) and Assisted GPS (AGPS) techniques have been developed to enhance conventional GPS receivers for tracking (High Sensitivity) and acquisition (AGPS). HSGPS/AGPS receivers, referred to as HSGPS receivers in the rest of this thesis utilize longer signal integration time and external navigation data aiding to acquire and track weak signals much lower than conventional GPS, which makes GPS useable in signal degraded environments, such as indoors. Additionally, by providing assistance from external means, signal acquisition performance improves and results in better Time-To-First-Fix (TTFF) (e.g. Karunanayake 2005b). These new techniques have made possible the use of GPS receivers in various signal degraded environments.

Due to the fact that police and emergency rescue teams may not be able to quickly

and precisely locate people who need emergency assistance, location service is very important to all 911 calls. The Enhanced 911 (E-911) mandate from the Federal Communication Commission (FCC) requires that all wireless carriers must provide the location information of a wireless emergency 911 call to the Public Safety Answering Point (PSAP).   This mandate requires an accuracy of 50 m for 67 percent of calls and 150 m for 95 percent for cell phone handset-based solutions (FCC 2000).   In order to meet the FCC criteria, many wireless carriers are looking at AGPS as the solution (Karunanayake *et al* 2004).   AGPS standards and specifications have been defined by some of the leading cell-phone vendors (3GPP 2003).

The E-911 mandate is a primary driver of the development of high sensitivity GPS-enabled mobile telephones. The performance of GPS receivers designed for mobile phones needs to be evaluated in various environments. The signal degraded environment challenges GPS performance because GPS signals may suffer from severe signal power attenuation and strong multipath.   These two factors can cause difficulty in signal acquisition, tracking and introduce large errors in positioning.   The power attenuation and multipath effects on degraded GPS signals are especially related to the nature of the surroundings.

The traditional GPS receiver performance evaluation method is conducted through field-testing, which is costly, time consuming and introduces possible uncertainties due to the uncontrolled testing environments.   An alternative method is simulator testing in a laboratory.   Through such tests, GPS signals are replicated under

strictly controlled conditions and verification of the receiver performance can be conducted. GPS hardware simulators are designed to accomplish this task. They are effective and cost-efficient tools for verifying new GPS product designs because of their capabilities to reproduce the radio frequency (RF) signals of GPS satellites. If the GPS signal replication can be made representative of actual field data in various GPS degraded environments, laboratory testing of GPS enabled devices will cost less and be less time intensive than field testing, but will still provide representative results.

A series of Spirent Communications Inc. hardware GPS signal simulation systems is now available to generate L1, L2 and L5 carriers with Coarse Acquisition (C/A) code, P code and navigation data. The GSS6560 simulator has 12 independent channels with GPS L1 C/A code. It has the capability to generate scenarios and provides full user control of the GPS constellation, errors and atmospheric effects using Spirent's SimGEN software. The simulator configuration used herein supports two RF outputs and 24-channel option for differential or dual antenna applications. A land mobile multipath (LMM) model is employed to simulate the multipath environments (Boulton 2002b). However, previous research indicated that such a LMM model did not produce GPS signals that matched the field signal in a satisfactory manner according to its design requirements, and therefore requires further investigation (Lachapelle *et al* 2003b).

1.2 Literature Review

1.2.1 HSGPS/AGPS Techniques and Receiver Testing

Peterson *et al* (1997) reported the results of early experiments to increase the integration time in order to obtain a higher signal-to-noise ratio. This is the principle of high sensitivity which makes signal reception under indoor environments possible. The use of externally generated assistance information provides high sensitivity receivers with improved acquisition times, sensitivity, and accuracy (Moeglein & Krasner 1998, Garin *et al* 1999).

The performance of HSGPS receivers under various degraded GPS environments were also studied by MacGougan *et al* (2002, 2003), Cannon *et al* (2003) and Lachapelle (2003c). HSGPS receivers showed an ability to track signals at least 9 to 10 dB lower than the standard GPS receiver. MacGougan (2003) also showed how to use a hardware simulator to test the tracking threshold of an HSGPS receiver. The results showed that the SiRF HSGPS receiver could track a signal as low as -185 dBW, which is 13 to 15 dB lower than SiRF's standard GPS receiver and the NovAtel OEM4 GPS receiver, and over 25 dB lower than the power of an undegraded signal.

In terms of AGPS, Karunanayake (2005b) conducted research to evaluate the acquisition and tracking capability of an AGPS receiver and the effect of different assistance data on performance. Tests were also conducted to investigate the effects of kinematics and RF interference (Karunanayake *et al* 2005a). All of the above tests were conducted using the same hardware simulator herein. Singh *et*

al (2005) and Carver (2005) conducted field tests in different environments to compare the performance of AGPS and HSGPS. The results show that an AGPS receiver had a better performance for TTFF and acquisition sensitivity than an HSGPS receiver.

MacGougan (2003) presented a method of using differential C/N_0 measurements and position-constrained pseudorange residuals to indicate the levels of signal fading and pseudorange error estimate for an HSGPS receiver. These two measurements are crucial in this thesis and will be discussed in Chapter 5.

1.2.2 Multipath Effects and Signal Degradation Modelling

Multipath effects on GPS code measurements under indoor conditions were studied by Lachapelle *et al* (2004). The result showed that, under attenuated signal conditions, multipath is large and, in indoor situations, the direct signals are not available which can lead to large reflected signals. The classical multipath rejection techniques developed for line-of-sight signals (e.g. Van Dierendonck *et al* 1992) no longer apply in this case.

Jahn (2001) presented a wideband Land Mobile Satellite (LMS) channel model using discrete tap delay lines with an exponential decay $P_h(\tau)$ versus delay time τ. Adopting this idea, Boulton *et al* (2002a) proposed a multipath model for the Spirent simulator. To study the characteristics of the LMS navigation multipath channel in urban, suburban and rural environments, Steingass and Lehner (2003) simulated satellite signals using an airship. By analysing the delay characteristics of the directed and reflected signals transmitted from the airship, it was found that

the channel had a "strong elevation dependency." Pérez-Fontán *et al* (2004) analysed the experimental data for the satellite-to-indoor channel using a helicopter to simulate the satellite. The details of the environments, such as internal walls, external walls, doors and windows were considered as the factors to produce the reflected and diffracted signals.

Ma *et al* (2001) and Klukas *et al* (2003) utilized an Urban Three-State Fade Model (UTSFM) to describe the GPS signal fading distribution according to satellite elevation angles, based on the analysis of signal power fading measurements gathered over a few hours in several different environments. UTSFM is composed of three types of probability density functions: Rician, Rayleigh and Loo, which respectively describe three types of signals: line-of-sight (LOS) signal and multipath signals, multipath signals only, and attenuated LOS signal and multipath signals. The empirical and UTSFM fading matched well in urban canyon, suburban, road side and open sky environments. The fitting parameters of UTSFM were also provided and were adopted by Boulton *et al* (2002a).

Watson (2005) presented an overall introduction of GPS L1 signal propagation mechanisms for indoor channel modelling. He utilized high-sensitivity techniques to characterize fading and multipath characteristics in two indoor environments. By analyzing the signal characteristics of signal power, positioning performance, Doppler error and phase change, he summarized GPS-indoor channel properties. Based on these GPS-indoor channel properties, a novel GPS-indoor channel model was introduced for specific indoor environments.

1.2.3 Hardware Simulator

Boulton *et al* (2002a) proposed an approach to model the static multipath environment in a hardware simulator for mobile telephone verification testing. The Rician model and a modified Rayleigh model were used to describe the fading on LOS and echo signals, respectively. The delay on the echo channel was random but fixed during the test. However, the results showed a poor agreement in power fading and position-constrained pseudorange residuals between the field and the simulated results. An enhancement to the above research was proposed by Lachapelle *et al* (2003b). They extended the delay model to include a variable delay component and modified the antenna pattern, which resulted in a better fading match between field and simulated data. Nevertheless, comparison of pseudorange residuals between field and simulated data still did not correlate well. Hay (2004) proposed an automotive application for downtown Chicago by using a hardware simulator. Although the simulations did not show a perfect match with the field test data, the receiver's behaviour was similar to that encountered during the field test.

1.3 Research Objectives

The primary objective of this research is to use a hardware simulator to reproduce GPS signals in various degraded signal environments, including indoors and an urban canyon, where conventional GPS receivers fail to track GPS signals and/or experience loss of signal tracking. An HSGPS receiver, capable of acquiring and tracking weaker signals than conventional GPS receivers, developed by SiRF

Technologies Inc., is used to make measurements in such environments for field and simulation testing. The research focuses on the study of the impact of multipath and power attenuation on GPS signal degradation.   Multipath effects on code and C/N_0 errors will be theoretically analysed to derive the statistical characteristics of the errors.   The statistics of the stochastic multipath effects on the SiRF HSGPS receiver are studied to help estimate the multipath parameters in the simulation.

The major objectives of the research are as follows:

- Characterize the theoretical multipath errors and empirical multipath errors with an HSGPS receiver with respect to the multipath signal strength and delay,

- Study the characteristics of measured degraded GPS signals from selected environments and estimate the GPS signal parameters for simulator testing,

- Reproduce the degraded signal environments using a hardware simulation system, and

- Provide an efficient method to compare field and simulated results to assess the statistical level of agreement.

1.4 Thesis Outline

This thesis is composed of eight chapters.   This chapter discusses the necessary

background information, the previous relevant research and results, and the major objectives of this thesis. Chapter 2 presents the electromagnetic propagation properties of GPS signals and major effects experienced in degraded environments. Chapter 3 discusses various error sources in GPS measurements and briefly introduces single differential GPS technology. Chapter 4 introduces the degraded GPS environments and the theory behind multipath, which includes effects on code and C/N_0 measurements as well as the multipath effects on an HSGPS receiver. Chapter 5 describes the test measures and methodology used to assess measurement availability, signal power degradation, pseudorange measurement errors, positioning accuracy, and solution availability. The statistical characteristics of the measurements and the comparison method are also presented in this chapter. Chapter 6 and Chapter 7 describe the indoor and campus outdoor testing environments and the simulated results with comparisons to the field data. Finally, conclusions drawn from this work, and recommendations for future research, are presented in Chapter 8.

Chapter 2

GPS Propagation Properties

A GPS signal is a type of electromagnetic radio wave, which is transmitted at two carrier frequencies, namely 1575.42 MHz (L1) and 1227.60 MHz (L2). To understand the performance of GPS signals in degraded environments, it is important to understand the properties of electromagnetic waves when they propagate and encounter obstacles. This chapter gives a brief description of electromagnetic wave propagation and changes due to diffraction, reflection and refraction.

2.1 Properties of Electromagnetic Waves

When electromagnetic waves propagate through space, the electromagnetic waves are always formed with two perpendicular fields, namely the electric field and the magnetic field. A changing electric field induces a magnetic field and vice-versa. The electromagnetic wave propagates at the speed of light in a vacuum, whereas the speed changes slightly when the wave is traveling through some medium. Figure 2.1 shows the propagation of a linearly polarized electromagnetic wave. The time-varying electric field (E) and magnetic field (H) are perpendicular to the direction of propagation of the wave, which is called a Transverse Electromagnetic (TEM) wave.

Propagation of an Electromagnetic Wave
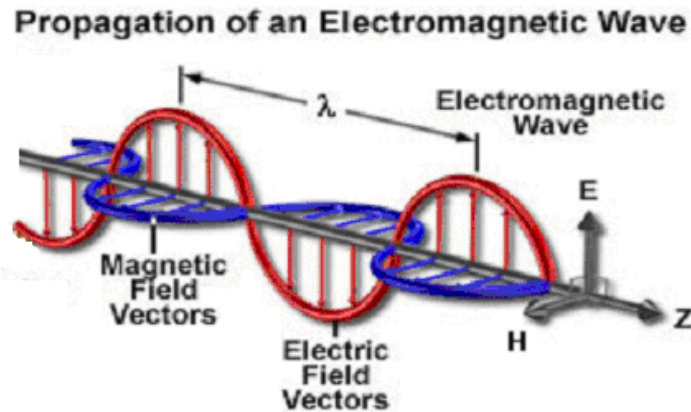
Figure 2.1: Electromagnetic wave propagation

(From:http://www.microscopy.fsu.edu/primer/java/polarizedlight/emwave/)

Polarization is a way to give transmitted signals a specific direction. The orientation of the electric field vector defines the polarization of an electromagnetic wave. The electric field vector may be resolved into two orthogonal components: E_x and E_y, both in a sinusoidal manner of equal frequency. The states of E_x and E_y during wave propagation determines the signal polarization. Consider a stationary plane perpendicular to the direction of the electromagnetic wave propagation, as shown in Figure 2.2. The traces left by the wave over time on the stationary plane indicate the type of polarization. If E_x and E_y remain in the same propagation plane in which they were originally transmitted as they travel through space, the trace in the perpendicular plane is a single line, as shown in Figure 2.2.a. This is called linear polarization. If E_x and E_y rotate in a circular motion as they travel through space, the trace on the perpendicular plane is a circle, as shown in Figure 2.2.b. This is called circular polarization. If the rotation is counter clockwise as the wave traves toward the viewer, it is called right hand

polarization; it is left hand polarized if the rotation is clockwise. Elliptical polarization is a more general situation (Kraus & Carver 1973); the trace left on the perpendicular plane is an ellipse, as shown in Figure 2.2.c.
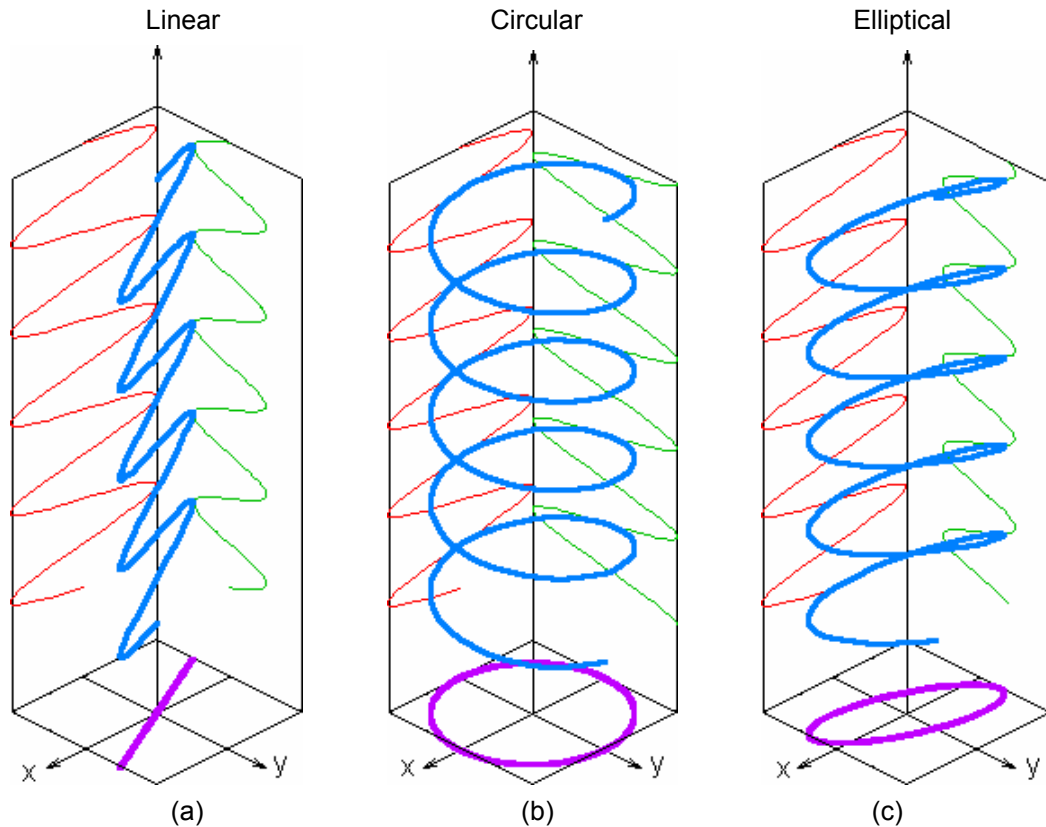
Figure 2.2a-c: Linear, circular and elliptical polarization

(http://en.wikipedia.org/wiki/Polarization)

The signal energy of a linear polarized radio wave only exists in a plane. To receive a linearly polarized signal, the receiver antenna must be correctly lined up with the plane of polarization to allow for the reception of the highest possible power. However, a linearly polarized radio wave may be rotated as the signal travels through the atmosphere. In addition, the geometry of the receiver antenna on Earth with respect to the transmitter satellite antenna may vary due to satellite

motion. It is difficult to keep the antenna aligned with the incoming linearly polarized signals from a satellite. To overcome this disadvantage, circular polarization is most often employed in satellite communication. Since circular polarized antennas transmit and receive radio waves in all directions, circularly polarized radio waves can be received regardless of the direction of the antenna. GPS transmitted signals are a right-hand circularly polarized (RHCP) TEM wave (ICD 2000).

2.2 Properties of Propagation

2.2.1 Free-space Propagation

Signals propagate radially in the vacuum space. Assuming the atmosphere is idealized free-space, the energy loss from the transmitted to the received signal is directly proportional to the square of the distance from the source. If the antenna is isotropic, the path loss or free-space loss PL is expressed as (Rappaport 1996)

$$PL(dB) = 10\log\left(\frac{4\pi d}{\lambda}\right)^2 \qquad\qquad 2.1$$

where d is the distance between the transmitting and receiving antennas, and λ is the wavelength of the propagating signal. The received signal power is predictable in this idealized propagation. Assuming the effective isotropic radiated power (EIRP) of the GPS satellite antenna is 24.5 dBW, after travelling 20,000 km (the approximate distance between a GPS satellite and the Earth), the signal power will lose approximately 182.5 dB due to free-space loss. Assuming

the atmospheric loss is 2 dB, the effective received power is 24.5 – 182.5 – 2 = -160 (dBW).   This example shows that the satellite antenna to receiver antenna link budget satisfies the minimum received GPS signal strength near ground (ICD 2000).

2.2.2 Diffraction and Fresnel Zones

When an electromagnetic wave meets an obstruction in the propagation path, the wave may not be totally blocked.   Instead, some of the energy in the wave is bent and spread into the shadowed area behind the obstacle.   This phenomenon is called diffraction, which can be explained by Huygens' principle (Parsons 2000). Each point on a wavefront can be considered as a new point source of radiation, and the superposition of all elementary waves result in a new plane wave in the direction of propagation.   Diffraction often occurs due to object edges or corners.

Because of the diffraction effect, obstructions found in a Fresnel zone may cause signal attenuation even though the path has clear line of sight.   The concept of Fresnel zones is illustrated in Figure 2.3.   These zones are concentric ellipsoids centred on the line-of-sight path between transmitting and receiving antennas. The transmitting and receiving antennas are at the foci.   The total path length (T-P-R) via each ellipsoid is $n\lambda/2$ longer than the direct distance of T-R, where n is an integer and λ is the signal wavelength.   The space enclosed by the ellipsoid with n =1 is called the first Fresnel zone.   Signal losses can be avoided if about 56% of the first Fresnel zone is clear of obstructions (Parsons 2000).   The losses become severe when over half of the Fresnel zone is blocked.
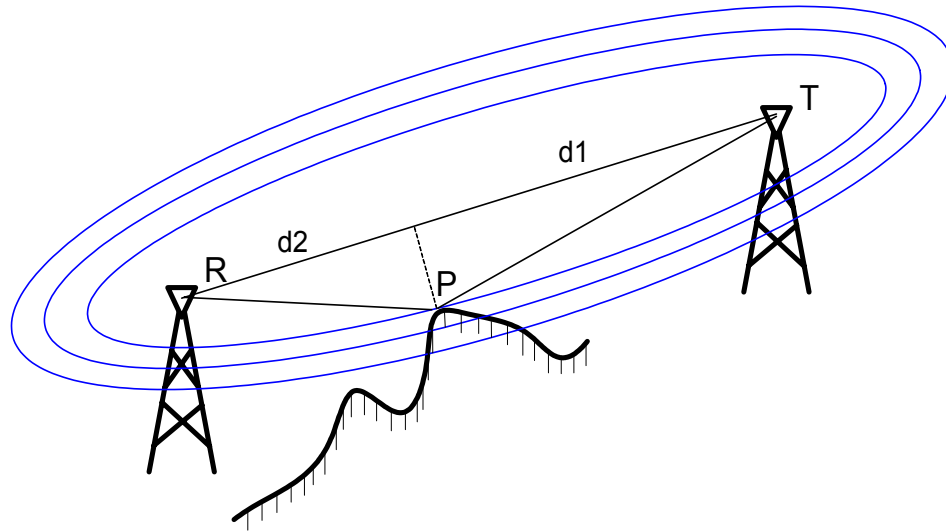
Figure 2.3: Fresnel zone

The cross sections of the Fresnel zones are circular. The radius of the nth zone is given by (Parsons 2000):

$$r = \sqrt{n\lambda \frac{d_1 d_2}{d_1 + d_2}}$$ 2.2

where d_1 is the distance between the cross section and the transmitter (m) and d_2 is the distance between the cross section and the receiver (m). In the case of GPS, d_1 is much larger than d_2 and the first Fresnel zone radius simplifies to:

$$r = \sqrt{\lambda d_2}$$ 2.3

Since the GPS L1 wavelength is approximately 0.19 m, the radius is about $0.44\sqrt{d_2}$ m. The radius of obstruction 100 m away is only 4.4 m. Therefore, diffraction loss occurs if an obstacle is located within approximately 2.5 m radius of the LOS path (4.4 m × 0.56 ≈ 2.5 m). The characteristics of diffracted signals differ greatly from one situation to another and are therefore difficult to model.

2.2.3   Reflection

Reflection occurs when a propagating radio wave encounters an object with another medium having different electrical properties.   Figure 2.4 shows an electromagnetic wave incident upon the boundary between two mediums at an angle θ_i.   The wave is partially reflected back to the first medium at an angle θ_r, and partially transmitted into the second medium at an angle θ_t.   The reflected angle θ_r equals the incident angle θ_i (Rappaport 1996).   The plane of incidence contains the incident, reflected and transmitted rays.   If the second medium is a perfect conductor, then all the incident energy is reflected without energy loss. However, a perfect conductor is not common in daily life.   The energy of the reflected signal is usually weaker than that of the incident signal.   Compared to the energy of the incident signal, this energy loss after reflection is called reflection loss and is discussed in Section 2.2.6.3.
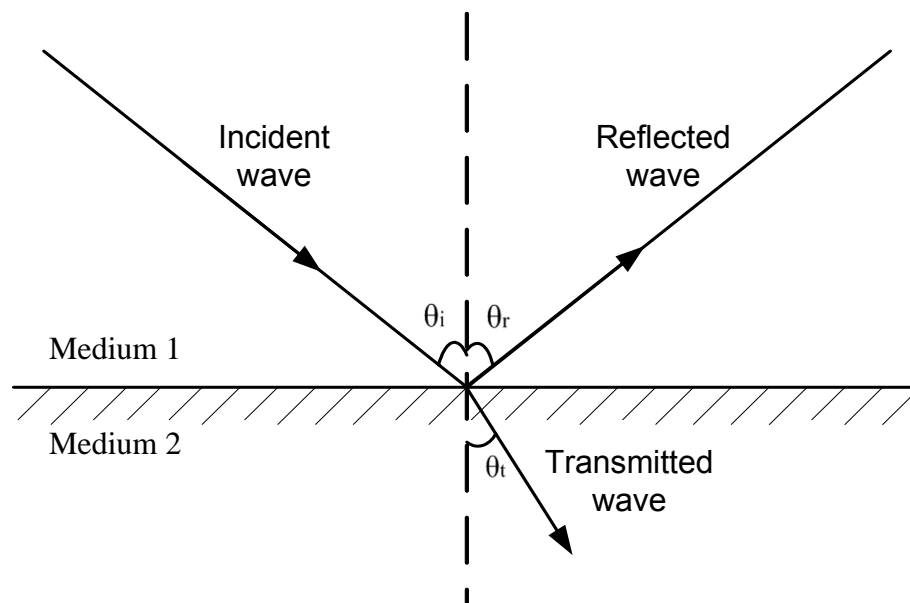
Figure 2.4: Reflection of an incident wave between two mediums

There are two kinds of reflection: specular and diffuse reflections, shown in Figure 2.5.   Specular reflection occurs when the surface of a reflector is smooth, for example, glass surface and metal surface.   The angle of reflection then equals the angle of incidence.   It is easy to predict the direction of a reflected signal if the angle of incidence is known.   Diffuse reflection is the reflection from an uneven or rough surface, e.g. rough stone textured wall and wooden surface.   The reflected signals may exist in all directions because the angle of incidence varies over the surface due to its roughness.   Compared to specular reflection, the signals due to diffuse reflection carry less energy in a certain direction.
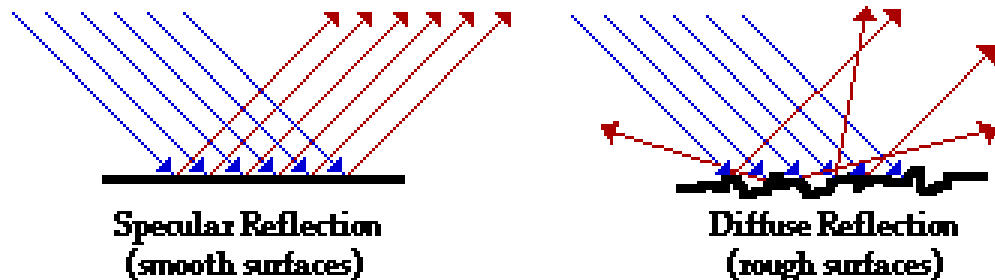
Figure 2.5: Specular reflection and diffuse reflection

(http://www.glenbrook.k12.il.us/gbssci/phys/Class/refln/u13l1d.html**)**

The reflected signal is also called multipath, the term describing the different propagation paths taken by the reflected signals.   After reflection, the GPS signal will change its properties.   When it arrives at the antenna, compared to the LOS signal, the signal's amplitude, phase, polarization, angle of arrival and propagation path length have been changed.

2.2.4 Refraction

When a radio wave travels from one medium to another in which it has a different propagation velocity, refraction occurs. The transmitted wave is refracted and its speed and direction change at the boundary between the media. As shown in Figure 2.4, the angle of refraction θ_t is not equal to the angle of incidence θ_i. The angles of incidence and refraction satisfy Snell's law (Sadiku 2001),

$$n_1 \sin\theta_i = n_2 \sin\theta_t \qquad\qquad 2.4$$

where n_1 and n_2 are the refractive indices of the two media. The refractive index of a medium is a factor that measures how much slower a wave travels in this medium than in a vacuum (Diament 2002).

If one medium is inserted in a second medium, the final angle of refraction of a wave passing through the media is equal to the angle of incidence. If the incident wave is a plane wave, as shown in Figure 2.6, the propagation direction is not changed. Considering that some of the incident energy is reflected, the transmitted wave only carries a part of the incident energy. Moreover, assuming that medium 2 is a lossy medium, which usually exists in reality, the transmitted wave loses additional power as it propagates through it (Sadiku 2001).

Incident wave

Medium 1

θ_i

Medium 2

θ_{t1}

Medium 1

θ_{t2}

$\theta_{t2} = \theta_i$

Transmitted wave
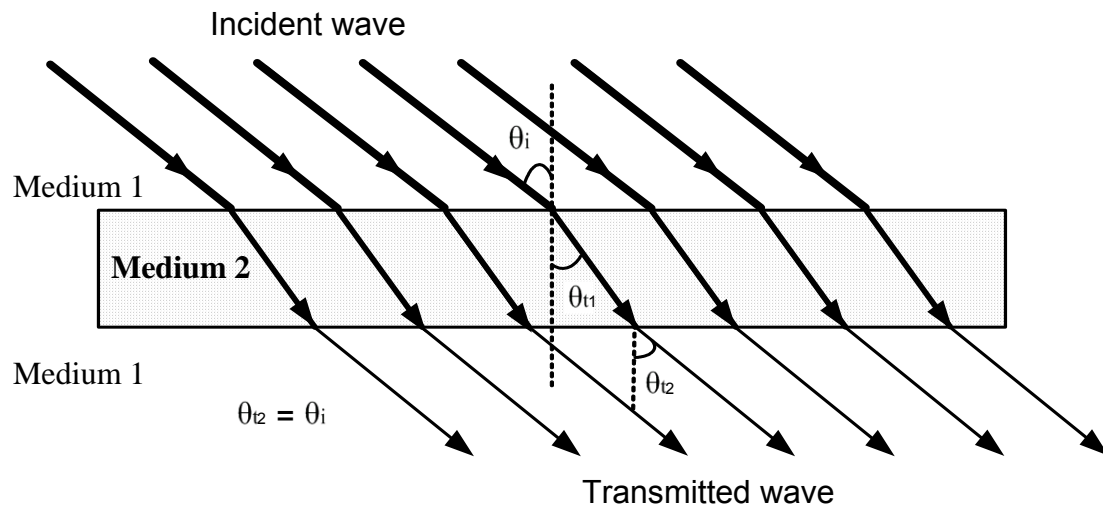
Figure 2.6: Refraction of a plane wave

Refraction of GPS signals occurs in the atmosphere due to the non-homogeneity of the latter and, more importantly, indoors when the signals propagate through walls. Actual refraction effects in this case depend on the materials used and their geometric arrangement.

2.2.5 Polarization Change

Depending on the nature of the reflector, the signal polarization will change and the wave may also change phase by 180° (Schoenbeck 1998). Ray (2000) discussed plane wave polarization change after oblique incidence on a smooth surface. After reflection, depending on the reflector material and the incidence angle, a RHCP GPS signal may reverse to a left-hand circularly polarized (LHCP) or a left-hand elliptically polarized (LHEP) wave (Hoffman- Wellenhof *et al* 2001).

2.2.6 Power Attenuation

2.2.6.1 Atmospheric loss

Atmospheric loss pertains to the energy loss due to effects of atmospheric gases, primarily oxygen and water vapour, when GPS signals propagate through the atmosphere. In the GPS signal link budget, atmospheric loss is 2 dB (Spilker 1996) although it is usually less in practice under a quiet atmosphere, namely around 0.5 dB.

2.2.6.2 Penetration Loss

The direct signal will be attenuated if it penetrates a building, foliage or other obstacles en-route to the receiver. Especially in indoor environments, after travelling through roofs, walls, windows, etc., part of the signal energy is lost due to refraction and energy absorption by construction materials. In the worst conditions, the direct signal may be blocked totally. Stavrou & Saunders (2003) presented the factors influencing radio wave propagation from outdoor to indoor; they included signal frequency, position and nature of nearby buildings, internal construction and size of the penetration side, and construction materials.

Aguirre *et al* (1994) conducted radio propagation experiments from street to buildings and reported that the median penetration losses for paths at 912, 1920, and 5990 MHz were 7.7, 11.6, and 16.1 dB, respectively. Schwengler & Gilbert (2000) performed field tests at 5.8 GHz in a residential area and summarized the mean penetration loss by a residential building was 3.3, 13.2 and 16.2 dB for locations at a closed window, front and rear of the house, respectively. Klukas *et*

al (2004) conducted experiments to study the penetration effects of building materials at GPS L1 frequency and reported attenuations of 0.5 dB, 2.4 dB and 23 dB for gyprock, plywood and cinder block, respectively.

2.2.6.3 Reflection Loss

Signal strength attenuation also occurs when propagating signals meet a barrier. Only some of the signal energy is reflected, and the rest is absorbed by the reflectors. The residual strength of the reflected signal depends on the incident angle, material properties of the reflector and area of the reflecting surface (Ray 2000). The reflection coefficient, indicating the reflection loss, is defined as the ratio of the amplitude of the reflected wave to the amplitude of the incident wave (Kraus & Carver 1973). It generally depends upon the material properties, frequency of the propagating wave, wave polarization, and the angle of incidence (Rappaport 1996). Landron *et al* (1996) presented reflection coefficient measurements for 1.9 GHz and 4.0 GHz linearly polarized signals for rough limestone, smooth metallized glass, and brick building surfaces. In most normal situations, the reflected signal loses much of the transmitted power. Therefore, the reflected signal strength is often smaller than the direct signal.

2.2.6.4 Polarization Mismatch Loss

In order to receive maximum power of a radio wave, the receiver antenna must have the same polarization sense as the received signal. If they are unmatched, the antenna only absorbs part of the received signal power. The energy loss is called polarization mismatch loss. Polarization mismatch loss for various

polarizations is shown in Table 2.1.   Theoretically, a RHCP antenna should reject LHCP signals.   However, this is impossible to achieve in practice.   This will be discussed in the following section.

Table 2.1: Polarization mismatches loss (Raquet 2004)

(unit: dB)	Vertical	Horizontal	RHCP	LHCP
Vertical	0	Inf	3.0	3.0
Horizontal	Inf	0	3.0	3.0
RHCP	3.0	3.0	0	Inf
LHCP	3.0	3.0	Inf	0

2.3 GPS Antennas

Typical GPS antennas are designed to receive RHCP signals only, which not only matches the GPS RHCP signals, but also rejects reflected signals (Salkhi & Shewfelt 2001) due to signal properties of polarization loss and polarization change by reflection.   Hence, the use of antennas with a good rejection of LHCP signals can potentially eliminate multipath effects.   However, in practice, RHCP antennas cannot totally reject LHCP signals; in general, most GPS antennas have a 5-10 dB attenuation for an opposite polarized wave (Ray 2000).

Although the GPS signal is LHCP after the primary reflection, it can be RHCP again after a secondary reflection.   Generally, GPS signals with an odd number of reflections would be LHCP and after an even number of reflections would be RHCP.

Effects due to secondary reflection are possible, but these are normally much weaker than the direct reflections (Boccia *et al* 2003). Therefore, they can be neglected when modelling the multipath signals.

The signal power reaching the digital sampling section of a GPS receiver also depends on the gain pattern of the receiving antenna. The antenna gain pattern is used to describe the relative increase in power of an antenna in the form of a polar plot for an elevation angular pattern in one-sweep planes. Usually, a GPS antenna is an omnidirectional antenna in the horizontal plane. The vertical antenna gain patterns vary with antenna types and models. Normally, the GPS antenna gain pattern has a maximum gain at the zenith and a minimum gain at low elevation angles and below. This is designed to attenuate multipath signals that come from low elevation satellites. The antenna gain pattern used in the simulation is discussed in Chapter 5.

Chapter 3

GPS Error Sources and Differential GPS

3.1 GPS Error

The GPS system utilizes time-of-arrival (TOA) measurements made on signals transmitted from satellites to the user to determine the user's position. By combining the TOAs with the time of transmissions, ranges from multiple satellites to the user are obtained and allow a receiver to determine its position. The calculation of TOA is based on the phase of the C/A code which is modulated on the L1 carrier. This process introduces inevitable errors into the range measurement and a bias to the receiver clock; therefore, the measurement is called the pseudorange. The major pseudorange errors include an orbit error, a clock error, ionospheric and tropospheric delays, receiver noise and multipath. The equation for pseudorange is given by (Lachapelle 2003a)

$$P = \rho + d\rho + c(dt - dT) + d_{ion} + d_{trop} + \varepsilon_{Pr\,x} + \varepsilon_{Pmultipath}$$ 3.1

where, P is code pseudorange measurement (m), ρ is the geometric range between the satellite and receiver antennas (m), $d\rho$ is the orbital error (m), c is the speed of light (m/s), dt is the satellite clock error with respect to GPS time (m), dT is the receiver clock error with respect to GPS time (m), d_{ion} is the ionospheric delay error (m), d_{trop} is the tropospheric delay error (m), $\varepsilon_{Pr\,x}$ is the

receiver noise (m), and $\varepsilon_{Pmultipath}$ is the code range multipath error (m).

3.1.1 Orbital Error

The ephemerides describe the GPS satellite orbits and are used to compute the position of GPS satellites for any time. They are predicted from previous measurements of satellite motion, Kepler's laws and knowledge of the Earth's gravity field and other effects (Lachapelle 2003a). However, the predicted satellite position may differ from the actual position. This difference, called the orbital error, is manifested as an effective pseudorange error. The difference between broadcast and precise orbits is typically of the order of 5 m (1σ) (Lachapelle 2003a). This error can be reduced in differential mode. The differential orbital error is a function of orbital error components, satellite azimuth and elevation, and baseline length (Lachapelle 2003a). Differential orbital errors are typically less than 0.5 ppm (Cannon 2005).

3.1.2 Satellite Clock Error

The synchronization of the satellite clocks is the basis of GPS positioning. Even a small error of 1 ns in the onboard clock results in a 30 cm range error. Although the satellite's atomic clocks are fairly stable, they do drift over time. To resolve the clock drifts, the ground stations continuously monitor and compare them with a master control time base. A prediction model is used to generate clock drift parameters, and the parameters are uploaded to the satellites and broadcast in the navigation message (Lachapelle 2003a, Misra & Enge 2001). GPS receivers subtract the satellite clock errors from the transmit time to yield the true signal

travel time. However, even if the satellite clocks are monitored well, usually the satellite clock errors cannot be precisely determined. The typical accuracy of a satellite clock is within 10 ns. Single differencing between receivers can remove this error (Cannon 2005).

3.1.3 Receiver Clock Error

Similar to satellite clock errors, any error in the receiver clock causes an error in range measurements. However, it is not practical to equip receivers with accurate atomic clocks because of the high cost and extensive maintenance. The receiver clock errors in pseudorange measurements for all satellites are equal at a given instant in time. Therefore, the receiver clock error is taken as one of the unknowns in addition to latitude, longitude and height.

3.1.4 Ionospheric Error

The ionosphere is a region of free electrons, located about 50 km to 1000 km above the Earth's surface. When electromagnetic waves propagate through the ionosphere, their speeds vary due to the free electrons, expressed in terms of the total electron content (TEC). TEC is a function of receiver location, time of day, satellite elevation angle, sunspot cycle and scintillation (Leva *et al* 1996). The impact of the ionosphere on electromagnetic signals depends on the frequency of the signal; the higher the frequency, the smaller the impact. The major ionospheric effects on GPS are code delay, carrier phase advance, signal power absorption, Faraday rotation, Doppler shift, dispersion, refraction and scintillation (Lachapelle 2003a). The state of the ionosphere is affected primarily by solar

radiation and its complex interaction with the Earth's geomagnetic field; hence, the magnitude of the ionosphere effect is usually greater during the day than during the night.   The ionospheric delays of satellites at the zenith are usually three times more than those of satellites near the horizon (Leva *et al* 1996).

The typical code delay at low elevations due to the ionospheric effect is about 10 m when the ionosphere is considered quiet, but can increase to tens of metres under an active ionosphere (Lachapelle 2003a).   Fortunately, the ionospheric error is temporally and spatially correlated.   It can be reduced by single differencing between receivers.

3.1.5 Tropospheric Error

The troposphere is the lower level of the atmosphere, extending up to 9 km over the poles to 16 km over the equator and containing most of the water vapor in the atmosphere (Lachapelle 2003a).   When GPS signals propagate through the troposphere, they are refracted by the dry gases and water vapour, which results in both code and carrier delays.   The effect of the delay is dependent upon the local temperature, pressure and relative humidity (Parkinson 1996).   The range equivalent of the delay typically varies from about 2.4 m at the zenith to about 9.3 m at a 15° elevation angle (Lachapelle 2003a).

The tropospheric delay consists of dry and wet components.   The dry component due to the dry air contributes about 90% of the tropospheric delay and can be predicted accurately.   The wet component due to the water vapor in the atmosphere is more difficult to model because of uncertainty of the atmospheric

distribution (Leva *et al* 1996). Tropospheric delays are correlated spatially and temporally and can be significantly reduced by single differencing. Typical differential errors are less than 1 ppm (Cannon 2005).

3.1.6 Multipath

The principle of GPS positioning is based on measuring the "straight" distances between the receiver and satellites. We assume that the satellite signals travel directly to the receiver. But in reality, the received signals contain not only the direct signals, but also reflected signals from objects nearby and reach the GPS antenna through an indirect path, known as multipath.

Multipath signals always arrive after the direct signals and usually with less power. The direct and multipath signals combine to produce a resultant received signal. The resultant signal causes a distortion of the correlation properties of the C/A code and results in a code measurement error, which leads to errors in the position solution. Besides the code error, the composite signal also introduces errors in the carrier phase and C/N_0 measurements.

Multipath is one of the largest error sources in both single point and differential positioning. It is highly localized and hence cannot be removed through differential techniques. Multipath delay is determined by satellite position and the geometry of objects existing in the surroundings. If the outdoor surroundings are constant over time, multipath errors are correlated from day-to-day for a given location (e.g. Ray 2000). The multipath power level is determined by the incident angle, the reflector material and antenna gain pattern.

In indoor and urban canyon environments, multipath results in large position errors. This is because multipath signals are often the only ones available, the direct signals being blocked by obstructions. In this case, the classical GPS multipath assumptions and reduction methods valid for the outdoors where LOS is available no longer apply and errors are no longer bounded. The layout of the building, the construction materials, the building type, and the objects inside the building influence the features of the multipath signals. The qualities of the received GPS signals are degraded by multipath signals to various extents. More detailed multipath effects will be discussed in Chapter 4.

3.1.7 Receiver Noise

Thermal noise is the major receiver noise and is produced by the movement of the electrons in any material that has a temperature above 0 degree Kelvin. Almost all devices, including the amplifier, cable, and connectors that the signal travels through, introduce thermal noise. This affects an important measure of the received signal strength – C/N_0. The value of C/N_0 determines the quality of the code and carrier phase observations. The inter-channel bias is another error and results from the fact that channels inside the receivers have slightly different delays depending on the frequency of the incoming signals. These delays are usually very stable over time and thus can be calibrated (Lachapelle 2003a). In addition, Johnson and Zaugg (2001) reported that the inter-channel biases were correlated with the receiver type and their magnitude was in the decimeter level. Empirically, receiver noise introduces sub-metre errors in the pseudorange measurement (Lachapelle 2003a).

The signal power level also affects the noise level of pseudorange measurements. A signal with lower C/N_0 introduces higher noise. Figure 3.1 shows the functional relationship of a HSGPS receiver C/N_0 with respect to the measured pseudorange standard deviation (Lachapelle *et al* 2003c). The data exhibits both a linear and an exponential trend. The measurement noise level increases with a drop in C/N_0, especially when the latter is below 17 dB-Hz, in which case this trend accelerates.
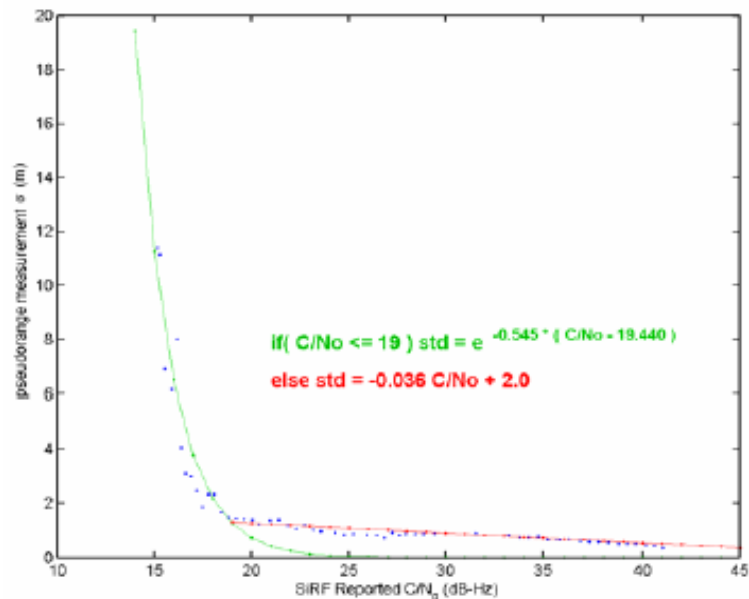
Figure 3.1: A HSGPS receiver output C/N_0 versus pseudorange measurement noise standard deviation (Lachapelle *et al* 2003c)

3.2 Differential GPS (DGPS)

Differential GPS is used to reduce as much of the correlated errors as possible from the range measurements when tracking a satellite at the same time from two receivers. One of the receivers, whose precise position is well surveyed, is called the reference station while the other receivers are denoted 'rovers' or 'remote'

stations (Lachapelle 2003a). Since the reference station position is known, the

'bias' of its pseudorange can be calculated by differencing the pseudorange

measurement and the satellite-to-reference station geometric distance. The bias

includes the errors discussed in Section 3.1.
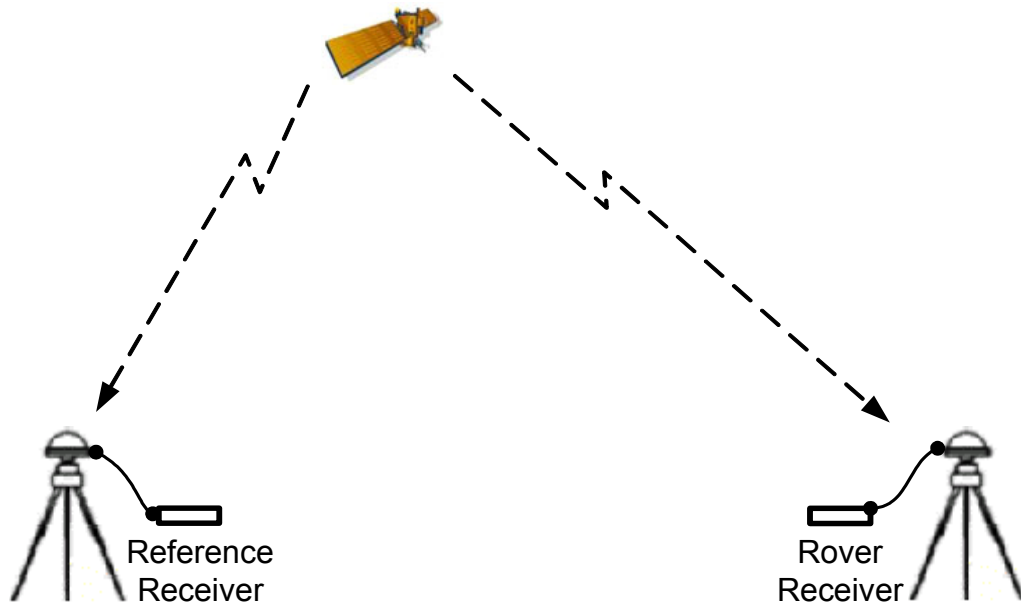
Figure 3.2: Single differencing between receivers

Subtracting the pseudorange at the reference station from the true range of the

satellite-to-reference station, using Equation 3.1, the bias ρ_b becomes

$$\rho_b = d\rho + c(dt - dT) + d_{ion} + d_{trop} + \varepsilon_{Pr\,x} + \varepsilon_{Pmultipath}.$$ 3.2

The bias ρ_b can be used to correct the pseudorange measurements in the rover

stations. Subtracting the bias ρ_b from the pseudorange at the rover station, the

modified pseudorange *P'* of the rover station is

$$P' = \rho + \Delta d\rho - c\Delta dT + \Delta d_{ion} + \Delta d_{trop} + \Delta \varepsilon_{\text{Pr}\,x} + \Delta \varepsilon_{Pmultipath}\,. \qquad 3.3$$

In Equation 3.3, not only is the satellite clock error totally removed, but the orbital error and atmospheric errors are reduced. Assuming the rover station and reference station are very close, the orbital error and atmospheric errors can be negligible after correcting by bias ρ_b. Then Equation 3.3 is simplified to

$$P' = \rho - c\Delta dT + \Delta \varepsilon_{\text{Pr}\,x} + \Delta \varepsilon_{Pmultipath}\,. \qquad 3.4$$

Hence, the pseudorange of the rover station is improved by applying the differential correction, bias ρ_b.

In this thesis, DGPS is used during the field tests to remove the orbital and atmospheric errors affecting the measurements. This process, described in more detail in Chapter 5, results in measured pseudorange errors that better represent the noise and multipath effects present in the test environments.

Chapter 4

Degraded GPS Environments and Multipath Errors

Indoors and urban canyons are two typical degraded GPS signal environments that are more likely to be encountered by cell phone users. When GPS signals penetrate buildings, some of the signal power is lost. The total signal loss is determined by the thickness and material of the obstructions. The obstructions and construction inside the building inevitably cause many multipath signals indoors. In an urban canyon environment, the large buildings may not only totally block satellite signals, but also act as specular reflectors introducing strong multipath. Multipath is a very important factor under these conditions. A good understanding of multipath effects assists in determining the multipath parameters for a simulation. This chapter derives the code and C/N_0 multipath errors resulting from a single multipath signal entering a stationary receiver, and the statistics of both errors as well. Observations are made regarding the statistical characteristics of multipath for later use in the construction of simulation scenarios.

4.1 Multipath Environment

The term multipath describes the phenomenon whereby signals travel over multiple reflective paths. Figure 4.1 shows an indoor environment with multipath signals. The powers of all satellite signals are attenuated after penetration. The reflected signals lose additional power due to reflection loss. In contrast, if the antenna is located outdoors and is unobstructed, direct signals only suffer

free-space loss while reflected signals suffer reflection losses as well.
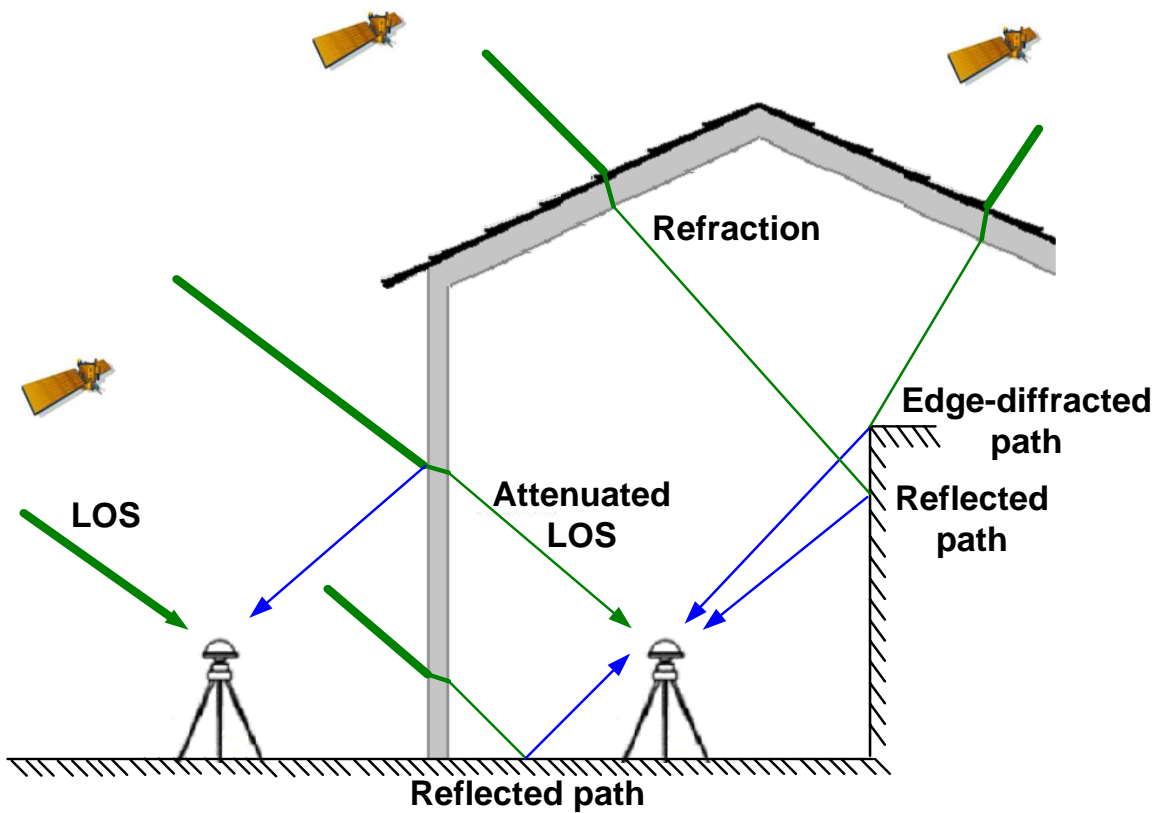
Figure 4.1: GPS signals in multipath environment

Unlike direct signals, a reflected signal always arrives after the direct signal and usually with less power. The longer time to reach the receiver antenna relative to the direct signal causes a pseudorange error, which leads to errors in the position solution. When multipath propagation occurs, the incoming signal may contain both LOS and one or more reflected signals. The resulting C/N_0, code and carrier phase measurements are for the combined signal made up of the various received signals. Multipath not only degrades the accuracy of code and carrier-phase measurements, but also varies the strength of the composite signal. The in-phase and out-of-phase multipath signals produce constructive and destructive

interference, called multipath fading.   In the worst situations, the reduced overall signal strength can cause loss of lock in the tracking loops.

4.2 Multipath Delay

Compared to LOS signals, the reflected and diffracted signals travel a longer distance to arrive at the antenna.   The extra length, called the multipath delay or path delay, depends on the geometry of the objects near the antenna. Investigation of a multipath delay model is necessary for successful simulations. Diffraction usually occurs at the edge of an object and is difficult to model (Ray 2000).   Reflection may occur at any surface.   In reality, vertical walls and horizontal ground are the most common surfaces.   In order to simplify the multipath model, the multipath delay due to the vertical plane and ground plane are discussed in this section.

4.2.1 Vertical Reflection

The reflector is usually a wall near the GPS antenna.   Figure 4.2 shows the situation where a satellite signal is reflected by a vertical reflecting plane and received at an antenna in front of the reflector.   The reflected surface is assumed to be smooth in this example.
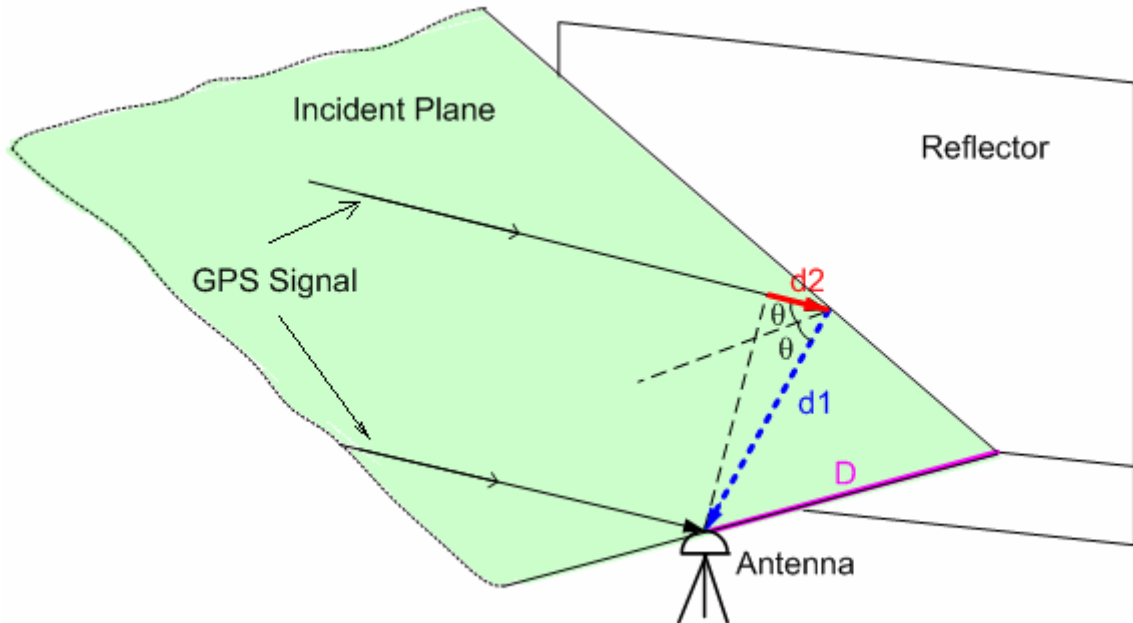
Figure 4.2: Vertical reflection

Because the satellites are far away from the ground user, the signals coming from them can be considered as plane waves. Therefore, the signals arriving at the reflecting point could be considered parallel to the signals arriving at the antenna. The plane of incidence contains the LOS and reflected signals and is shown as the green plane in Figure 4.2. This plane is perpendicular to the reflector plane. The total signal delay due to the additional path is

$$
\begin{aligned}
l_{delay} &= d1 + d2 \\
&= d1 \cdot (\cos 2\theta + 1) \\
&= \frac{D}{\cos\theta} \cdot (\cos 2\theta + 1) \\
&= 2D\cos\theta
\end{aligned}
$$

4.1

where D is the distance from the antenna to the reflector within the incident normal plane. θ is the incident angle of reflection, which is determined by the elevation

angle of the satellite and the orientation of the reflector.

If the incident plane is normal to the ground as well, the incident angle θ is equal to the elevation angle of the satellite.

4.2.2 Ground Reflection

The ground is a good reflector of all satellite signals.   Ground reflection occurs almost everywhere.   The reflected signal usually reaches the antenna from below. Therefore, an antenna usually has a low gain for low elevation angles.   This is designed to reduce the multipath effect from low elevation angel signals.   Figure 4.3 displays an example of ground reflection.
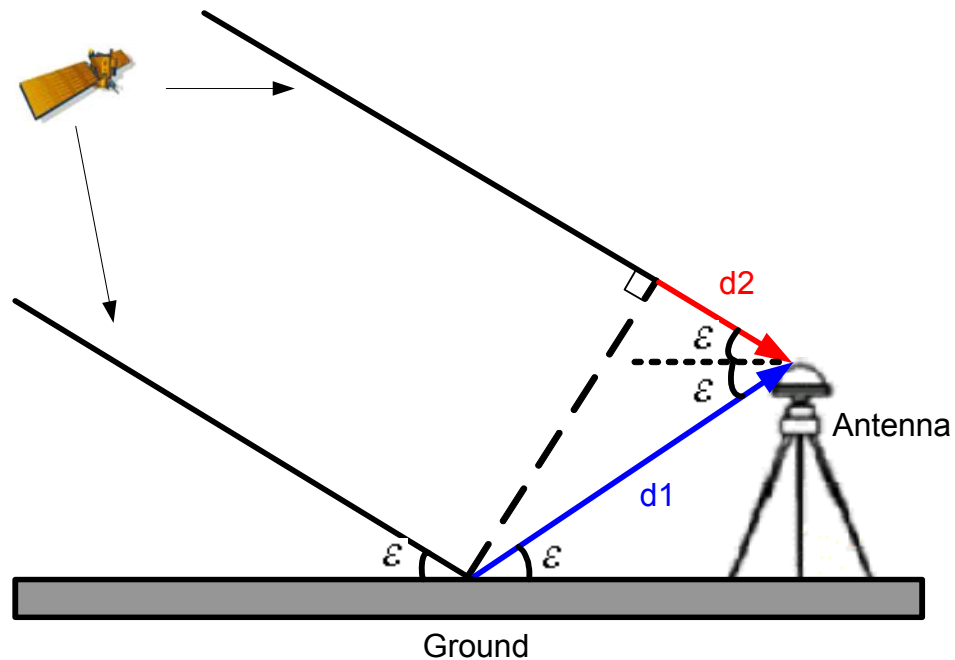
Figure 4.3: Ground Reflection

The path delay is calculated by

$$l_{delay} = d1 - d2$$
$$= d1 \cdot (1 - \cos 2\varepsilon)$$
$$= \frac{H}{\sin \varepsilon} \cdot (1 - \cos 2\varepsilon) \qquad 4.2$$
$$= 2H \sin \varepsilon$$

where H is the height of the antenna with respect to the reflecting ground plane and ε is the elevation angle of the satellite.

Since the angles θ and ε change with the satellite's motion, the multipath delay is usually not constant. In the static case, multipath delay will only change according to the moving satellites, whereas, it is determined by satellite, antenna, and reflector motion in kinematic conditions. In this thesis, we only discuss the static case. The change rate of multipath delay can be obtained by deriving the equations for the multipath delay. Equation 4.1 indicates that the multipath delay may change faster for a longer distance D and Equation 4.2 indicates that the multipath delay may change faster for a larger antenna height H.

4.3 Multipath Errors

The combined signals cause distortion of the receiver correlation function and discriminator function and hence errors appear. Assuming that the multipath signal frequency is the same as the direct signal frequency, the composite input signal $S_I(t)$ can be expressed as follows (Ray 2000):

$$S_i(t) = A \sum_{i=0}^{N} \alpha_i c(t - \tau_i) \cos(\omega_0 t + \gamma_i) \qquad\qquad 4.3$$

where A is the satellite signal carrier amplitude (V), N is the number of reflected signals and i = 0 corresponds to the direct signal, α_i is the amplitude ratio of multipath to direct signal (MDR), α_o is the direct signal and is equal to 1, $c( )$ is the GPS C/A or P code, τ_i is the satellite signal code delay (s), ω_0 is the satellite signal carrier frequency (rad/s), and γ_i is the satellite signal carrier phase (rad) where γ_0 corresponds to the direct signal phase.

In order to acquire a GPS satellite signal, the receiver must replicate the PRN code of that satellite and shift the phase of the replica code until it correlates with the satellite PRN code. When the phases of the replica code and the received satellite PRN code match, the correlation reaches a maximum value (Ward 1996). The input signal is beaten with the local in-phase and quadrature-phase replicas of the carrier. The prompt (P), early (E) and late (L) versions of the locally generated code signal are correlated with the input signal. When the prompt replica code matches the incoming signal, the correlation reaches the maximum, while the early and late replica codes produce a smaller correlation value than that of the prompt. The exact correlation values of the early and late replica codes depend on the spacing between the prompt and early codes or the prompt and late codes. The prompt, early and late correlation values in the in-phase and quadrature-phase arms (IP, QP, IE, IL, QE, QL) are generally used by the discriminator functions in the loop filters for code tracking and carrier tracking (Ward 1996, Ray 2000).

$$IP = \sum_{i=0}^{N} \alpha_i \frac{A}{2} R(\hat{\tau}_c - \tau_i) \cos(\gamma_i - \hat{\gamma}_c)$$ 4.4.a

$$QP = \sum_{i=0}^{N} \alpha_i \frac{A}{2} R(\hat{\tau}_c - \tau_i) \sin(\gamma_i - \hat{\gamma}_c)$$ 4.4.b

$$IE = \sum_{i=0}^{N} \alpha_i \frac{A}{2} R(\hat{\tau}_c - \tau_i + T_d) \cos(\gamma_i - \hat{\gamma}_c)$$ 4.4.c

$$QE = \sum_{i=0}^{N} \alpha_i \frac{A}{2} R(\hat{\tau}_c - \tau_i + T_d) \sin(\gamma_i - \hat{\gamma}_c)$$ 4.4.d

$$IL = \sum_{i=0}^{N} \alpha_i \frac{A}{2} R(\hat{\tau}_c - \tau_i - T_d) \cos(\gamma_i - \hat{\gamma}_c)$$ 4.4.e

$$QL = \sum_{i=0}^{N} \alpha_i \frac{A}{2} R(\hat{\tau}_c - \tau_i - T_d) \sin(\gamma_i - \hat{\gamma}_c)$$ 4.4.f

where T_d is the spacing between the prompt and early, or the prompt and late correlators, $R(\cdot)$ is the correlation function, $\hat{\tau}_c$ is the receiver estimate of the incoming signal code delay (m), and $\hat{\gamma}_c$ is the receiver estimate of the incoming signal carrier phase (rad). To simplify the analysis, we assume that A=2 and neglect the signal amplitude A/2 for all IP, QP, IE, QE, IL and QL later in this research.

4.3.1 Carrier Tracking Loops

Phase lock loop (PLL) and frequency lock loop (FLL) are used to recover the incoming signal carrier and perform the carrier wipe off function. The PLL discriminators produce phase errors and the FLL discriminator produces frequency errors. Generally, the PLL is more accurate than the FLL, whereas the

FLL is less sensitive to dynamic stress. The PLL is more often used when the dynamics can be predicted.

The Costas loop is one of the PLL discriminators. It is insensitive to 180° carrier phase changes that occur due to the 50 Hz navigation data bit transition. Table 4.1 shows several common Costas loop discriminator functions.

Table 4.1: Common Types of PLL Costas Discriminators (Ray 2000)

Discriminator Description	Comments
Dr = sign(IP)·QP	Least computational burden. Output proportional to sin (phase error)
Dr = IP·QP	Moderate computational burden. Output proportional to sin (2×phase error)
Dr = arctan (QP/IP)	High computational burden. Output proportional to the phase error

Assuming the signal includes the LOS and one reflected signal, the arctan discriminator function can be expressed as:

$$
\begin{aligned}
D_{rm} &= \arctan\left(\frac{QP}{IP}\right) \\
&= \arctan\left(\frac{R(\hat{\tau}_c - \tau_0)\sin(\gamma_0 - \hat{\gamma}_c) + \alpha_1 R(\hat{\tau}_c - \tau_i)\sin(\gamma_1 - \hat{\gamma}_c)}{R(\hat{\tau}_c - \tau_0)\cos(\gamma_0 - \hat{\gamma}_c) + \alpha_1 R(\hat{\tau}_c - \tau_i)\cos(\gamma_1 - \hat{\gamma}_c)}\right)
\end{aligned}
$$

4.5

where γ_0 is the direct signal phase, $\hat{\gamma}_c$ is the receiver's estimated carrier phase, γ_e is the carrier phase error due to the multipath signal. Assuming τ_0

and γ_0 to be zero, by setting $D_{rm} = 0$, the carrier phase multipath error

$\gamma_e = \hat{\gamma}_c - \gamma_0$ is obtained by

$$\gamma_e = \arctan\left(\frac{\alpha_1 R(\hat{\tau}_c - \tau_1)\sin\gamma_1}{R(\hat{\tau}_c) + \alpha_1 R(\hat{\tau}_c - \tau_1)\cos\gamma_1}\right).$$

4.6

4.3.2 Code Tracking Loops

The code tracking loop, called the delay lock loop (DLL), is used to implement the code synchronization to achieve and maintain the alignment of the locally generated code with the received signal code. Table 4.2 shows several GPS coherent and non-coherent DLL discriminator functions.

Table 4.2: Common Types of Delay Lock Loop Discriminators (Ray 2000)

Discriminator Types	Description	Comments
Coherent	$D_C = IE - IL$	Simplest of all. Does not require correlation values in the quadrature arm correlators
Non-coherent	$D_n = (IE2 + QE2) -$ $(IL2 + QL2)$	Early minus late power.
	$D_n = \sqrt{IE^2 + QE^2} - \sqrt{IL^2 + QL^2}$	Early minus late envelope.
	$Dn = IP \cdot (IE - IL) +$ $QP \cdot (QE - QL)$	Dot-product type of discriminator. It uses all three correlators.

The coherent DLL discriminator is the simplest of all. It does not require correlation values in the quadrature arm correlators, but requires the carrier phase

to be locked. Although non-coherent DLL discriminators are generally more popular than coherent code discriminators, the latter is used here to simplify the analysis. Assuming that there is only one multipath signal with a direct signal, the coherent discriminator is expressed as

$$
\begin{aligned}
D_c &= IE - IL \\
&= [R(\hat{\tau}_c - \tau_0 + T_d) - R(\hat{\tau}_c - \tau_0 - T_d)]\cos(\gamma_0 - \hat{\gamma}_c) \\
&\quad + \alpha_1[R(\hat{\tau}_c - \tau_1 + T_d) - R(\hat{\tau}_c - \tau_1 - T_d)]\cos(\gamma_1 - \hat{\gamma}_c)
\end{aligned}
\qquad . \qquad 4.7
$$

The code phase error $\tau_c = \hat{\tau}_c - \tau_0$ is the code error due to the multipath. Figure 4.4 shows the coherent DLL discriminator's ideal response to a single multipath signal. The multipath signal is in-phase with the direct signal. The spacing of the early-late correlator is one chip, and hence is called the standard correlator or wide correlator. Curves A, B and C correspond to the discriminator functions due to the direct signal, multipath signal and composite signal respectively. The multipath has a τ_1 delay and half amplitude with respect to the direct signal. Curve A illustrates the standard coherent DLL discriminator function curve with only the direct signal. The zero-crossing at t_0 of the discriminator function means the true code phase offset is t_0. Curve C illustrates the distortion of the discriminator curve because of the presence of the multipath signal. The zero-crossing of the curve C occurs at $t_0 + \tau_e$. Thus, the difference τ_e between curve A and curve C is the code error due to curve B of the multipath signal (Ray 2000). When the amplitude of curve B increases, its slope increases. This results in the zero-crossing of curve A being farther away from t_0 and the code error τ_e increases accordingly.
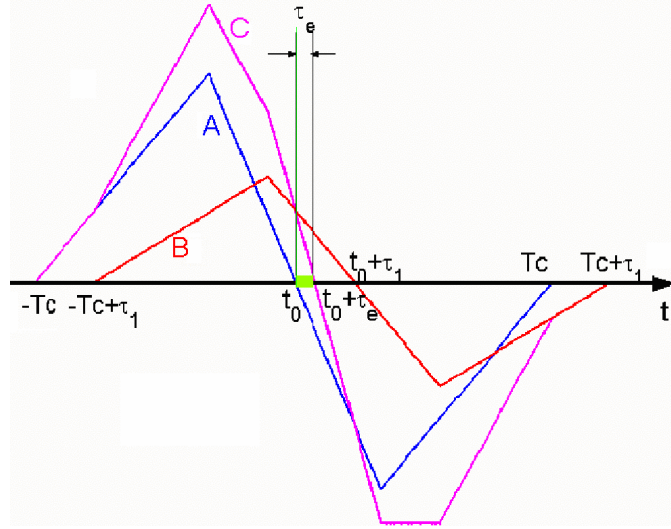
Figure 4.4: DLL discriminator response for in-phase multipath

Figure 4.5 shows the discriminator response due to the same single multipath as in Figure 4.4, except that the multipath signal has a 180° phase offset with respect to the direct signal. The sign of the code error τ_e is opposite that of the code error of in-phase multipath and the absolute amplitude of the code error is different than that of the code error of in-phase multipath.
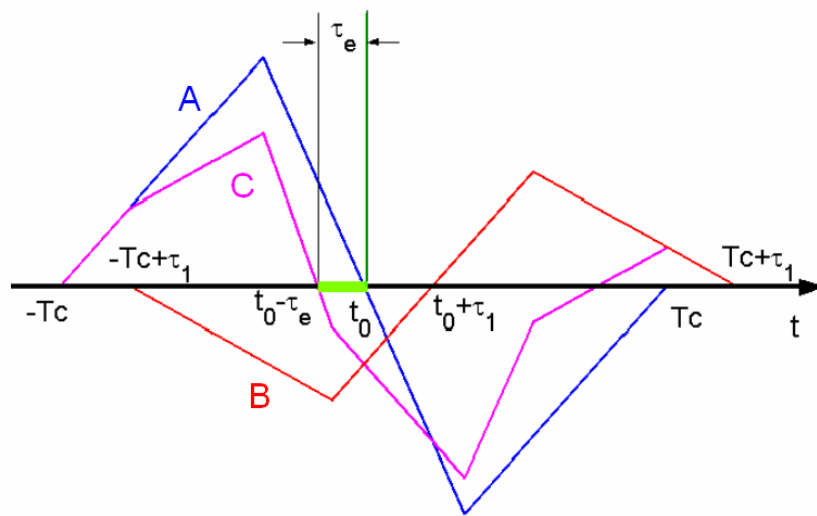
Figure 4.5: DLL discriminator response for 180° out-of-phase multipath

Since the coherent discriminator is linear, curve C is the sum of curve A and curve B. Here, infinite bandwidth is assumed for the signal, which results in a sharp peak for the correlation triangle.   However, the bandwidth of the signal is finite in practice and the peak of the correlation triangle is rounded-off (van Nee 1993, Ray 2000).

The multipath code error envelope is a function of relative multipath amplitude α_1 and delay τ_1, given in Figure 4.6 (Ray 2000).   The upper curve represents the error due to the multipath signal that is in-phase with the direct signal, and the bottom curve represents the out-of-phase case.   This figure indicates that the magnitude of the error initially increases with the multipath delay, and becomes constant after a particular multipath delay (no constant curve for a standard correlator, i.e. T_d = 0.5 chip).   Exceeding another particular multipath delay, the multipath code error magnitude decrease until it drops to zero at the delay of (T_c+T_d) chips.   In the following sections, all multipath errors are discussed for the condition of T_d = 0.5 chip, i.e. early-late correlator spacing is one chip.   Then, the maximum multipath delay producing error is 1.5 chip or 450 m, provided the direct signal is available to start with.   For a reflected only signal, the multipath delay can in principle be infinite.
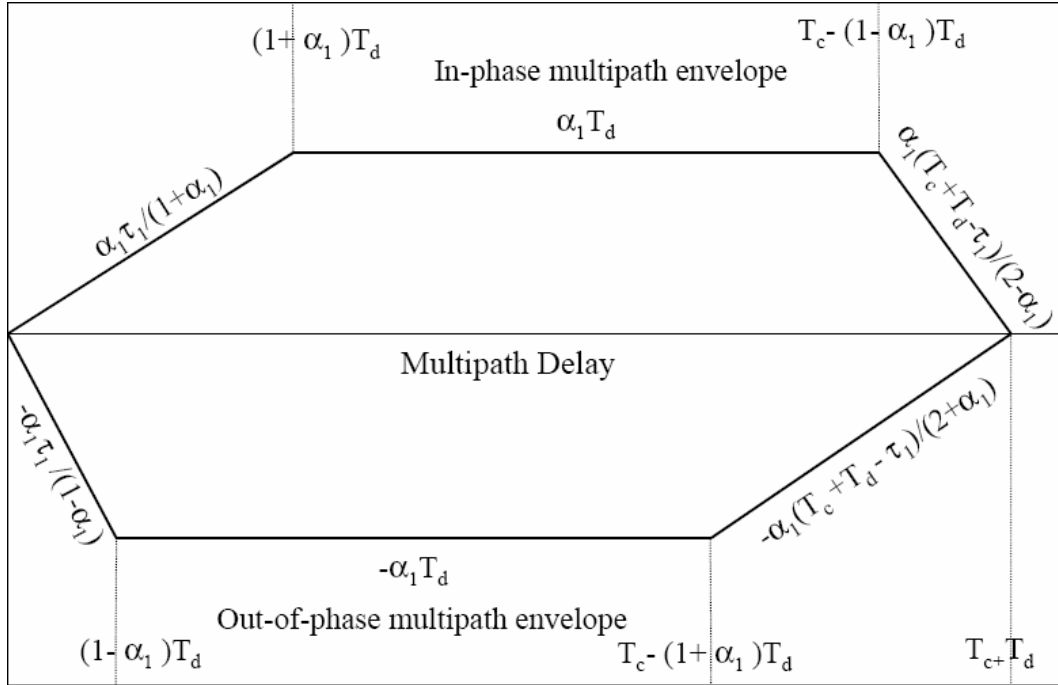
Figure 4.6: Multipath code error envelope with respect to multipath delay (Ray 2000)

Assuming that the same processing technique is used in a DLL, then, if one of the multipath signal parameters (amplitude, delay and phase) is changed, the code error will change accordingly. Code error represents the range error of GPS measurements. Therefore, different multipath signals introduce different ranges of errors.

4.3.3 Signal Strength

The C/N_0 is considered a primary parameter describing GPS receiver performance and is commonly used to describe signal strength. The C/N_0 is a measure of total received carrier strength relative to the receiver noise power density regardless of the signal bandwidth. If the incoming carrier strength is P_c and the noise density is N_0, the C/N_0, in units of dB-Hz, is given by

$$C/N_0 = 10\log_{10}(\frac{P_c}{N_0}).$$

4.8

The true average signal power with direct signal only is expressed as

$$P_t = IP^2 + QP^2 = R^2(\hat{\tau}_c - \tau_0).$$

4.9

Assuming there is one reflected signal and one direct signal, the average signal power is expressed as

$$P_m = IP^2 + QP^2$$
$$= R^2(\hat{\tau}_c - \tau_0) + \alpha_1^2 R^2(\hat{\tau}_c - \tau_1) + 2\alpha_1 R(\hat{\tau}_c - \tau_0)R(\hat{\tau}_c - \tau_1)\cos(\gamma_0 - \gamma_1)$$

.4.10

The C/N_0 error due to the multipath is obtained by

$$P_e = 10\log_{10}(\frac{P_m}{N_0}) - 10\log_{10}(\frac{P_t}{N_0})$$
$$= 10\log_{10}(\frac{P_m}{P_t})$$

4.11

where P_e is also affected by the multipath delay, τ_1 and MDR, α.

4.4 Multipath Effects on Code and C/N_0

4.4.1 Theoretical Analysis

The effect of multipath on the code and the C/N_0 is a function of its delay, phase and MDR.   The multipath phase is determined by the delay and the phase change due to reflection.   However, the phase change due to reflection is very difficult to predict in practice.   Thus, we only consider the multipath phase due to the delay in

this research.   Although most multipath scenarios involve multiple echo signals, much insight is achieved from the analysis of a single multipath case (Braasch 1996).

Figure 4.7 shows code error and C/N_0 error due to a single, weaker than direct, multipath signal.   The magenta part is the code error while the green part is the C/N_0 error.   The multipath delay is up to 450 m.   The early-late correlator spacing is one chip-width and the bandwidth is 10 MHz.   The DLL discriminator is coherent. There are positive and negative values of code and C/N_0 errors as a function of multipath delay.
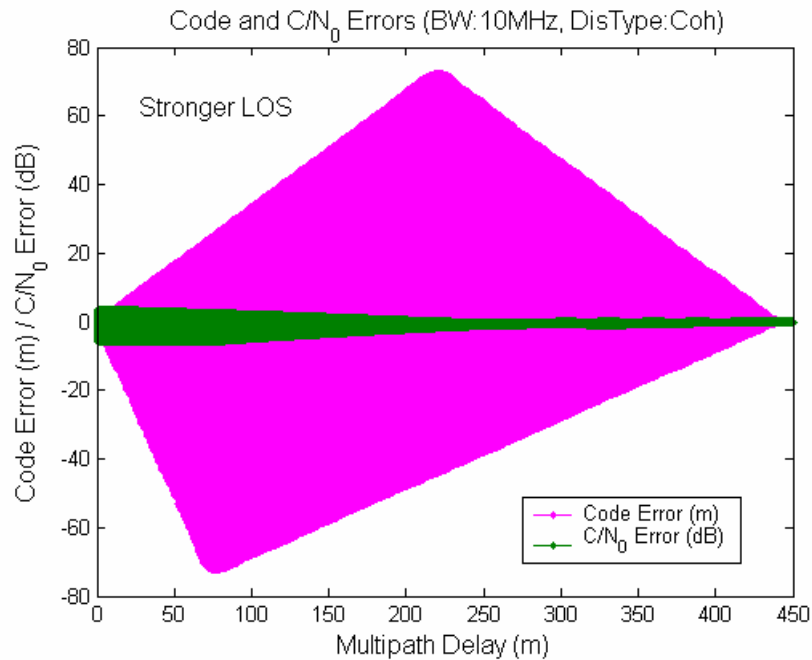
Figure 4.7: Code and C/N_0 errors of stronger direct signal with multipath delay range up to 450 m

To better understand the behaviour of the error curves in Figure 4.7, a more

detailed view of the code error and C/N_0 error with the multipath delay up to 1.5 m
is shown in Figure 4.8.   The code error and C/N_0 error are both undulating with a
sinusoid-like trend about zero.   They have an in-phase relation and undulate
within the same cycle.   The amplitude of code error increases as the multipath
delay increases, while the amplitude of the C/N_0 errors seems to stay relatively
constant.   Although the code error undulates about zero, it does not have a mean
value of zero (van Nee 1993, Braasch 1996).
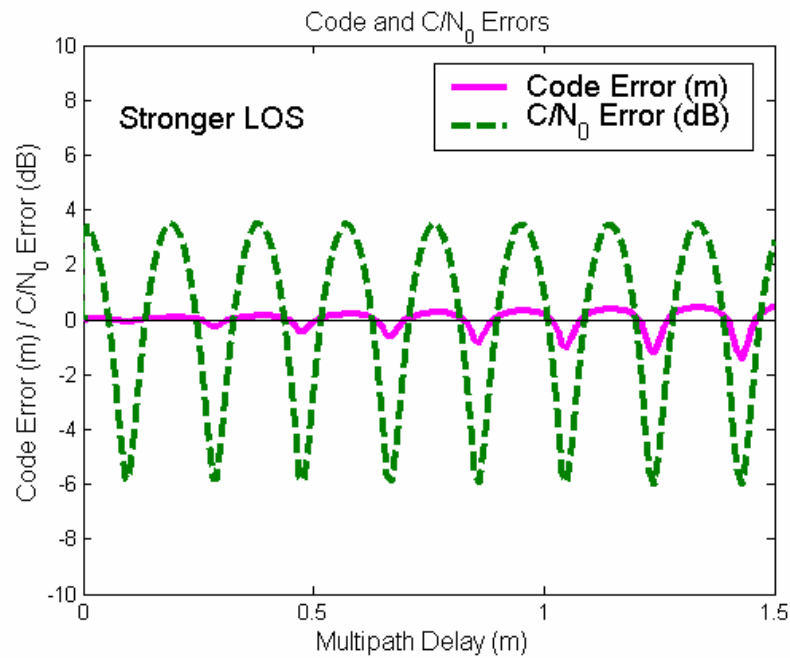
**Figure 4.8: Code and C/N_0 errors of stronger direct signal with multipath
delay range up to 1.5 m**

Figure 4.9 shows the code and C/N_0 errors due to a single, stronger than direct,
multipath signal.   Different from the code error due to weak multipath signal, code
error due to strong multipath signal only has positive values.   The code error
increases significantly as the multipath delay increases.   The C/N_0 error has a

similar trend to the C/N$_0$ error due to a weak multipath signal, shown in Figure 4.7.

The C/N$_0$ error undulates about zero within the envelope and the amplitude of the

error decreases when the multipath delay increases.
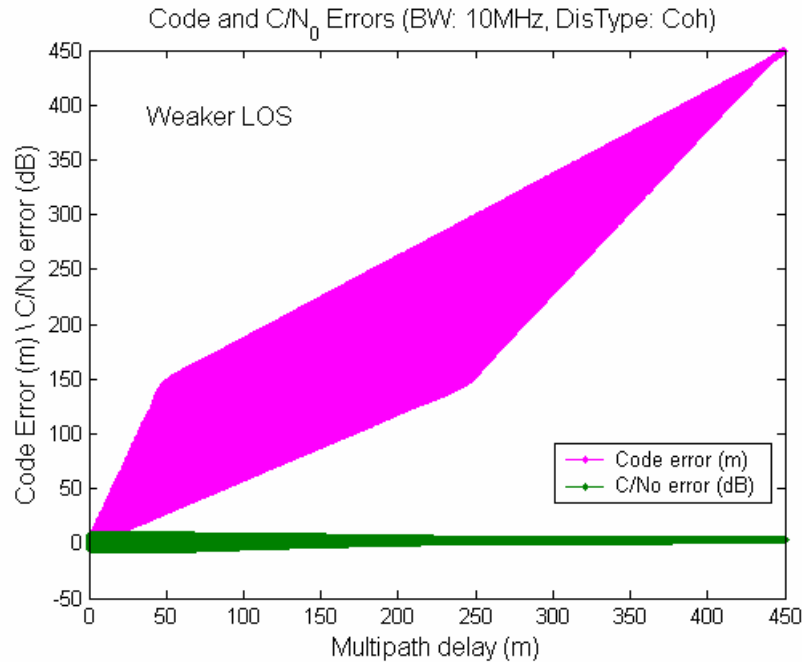
Figure 4.9: Code and C/N$_0$ errors of weaker direct signal with multipath delay range up to 450 m

More detailed errors in a small range of multipath delays are shown in Figure 4.10.

Different from the in-phase relation between the code and C/N$_0$ errors for the weak

multipath signal case shown in Figure 4.8, they are 180° out-of-phase for a strong

multipath signal.   Regardless of whether the multipath signal is stronger or

weaker than the direct signal, all the errors undulate with the same L1 wavelength

of 19 cm.   The undulation of the code and C/N$_0$ errors will be discussed in Section

4.4.3.
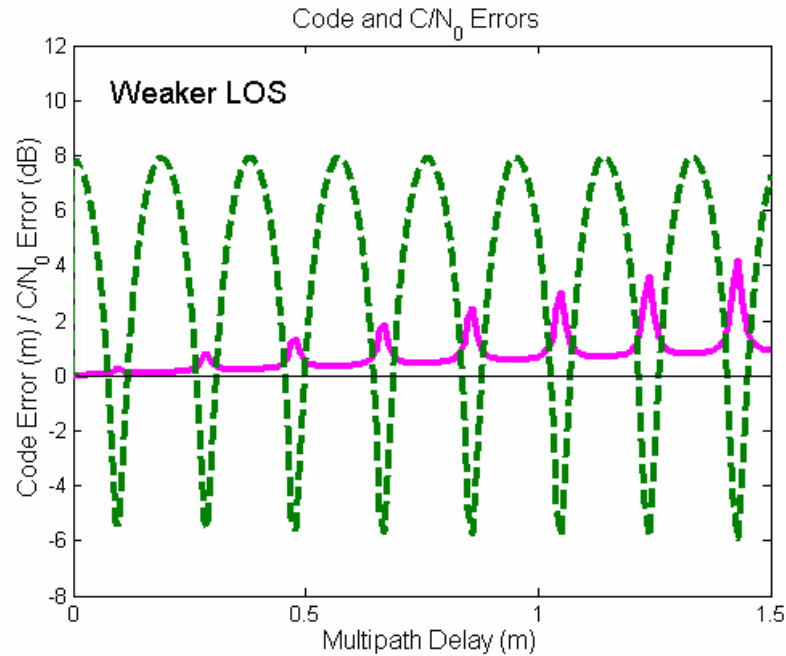
Figure 4.10: Code and C/N$_0$ errors of weaker direct signal with multipath delay range up to 1.5 m

The code and C/N$_0$ errors are determined by the MDR, multipath delay and carrier phase change. Since the carrier phase change is based on the multipath delay, the MDR and multipath delay are the main factors that affect multipath errors.

There are two methods to calculate the mean and standard deviation of the multipath errors with respect to the multipath delays for different multipath strengths. One method is to vary the multipath phase in discrete steps of the complete cycle and computing the multipath error at each step, and then taking their statistics (Ray 2000). Another method is to use samples from a single cycle of 19 cm to calculate the statistics of the errors; this can be done since the amplitude changes gradually. The above methods assume that the same processing technique is used, e.g. a standard correlator. Both methods yield

similar results. Although indoor multipath can in principle be infinite when only a reflected signal is available, it rarely exceeds 100 m in practice and the following discussion focuses on multipath delays less than 100 m.

Figure 4.11 shows the code error mean with respect to the multipath delay and its amplitude ratio to the direct signal. They are calculated by the first method introduced previously. The error is calculated by using a 1 chip-width of early-late correlator spacing, a 10-MHz bandwidth and a coherent discriminator. The parameter α is the MDR, with values from 0 to 2, indicating the multipath signal strength. The value of α < 1 means that the direct signal is stronger than the multipath one, while α > 1 means the multipath signal is stronger than the direct one.

When the direct signal is stronger than the multipath signal (α < 1), the code error mean is less than 20 m. Above a certain value of the multipath power level, when multipath is stronger than the direct signal (α > 1), the mean code error increases significantly as the multipath delay increases. This is because the stronger multipath signal becomes the dominant component of the composite signal and the code error becomes close to the total multipath delay. If there is no direct signal, the code error exactly equals the multipath delay. Figure 4.12 illustrates the code error mean in more detail for the area α < 1 in Figure 4.11. The increasing multipath delay introduces an increasing error.
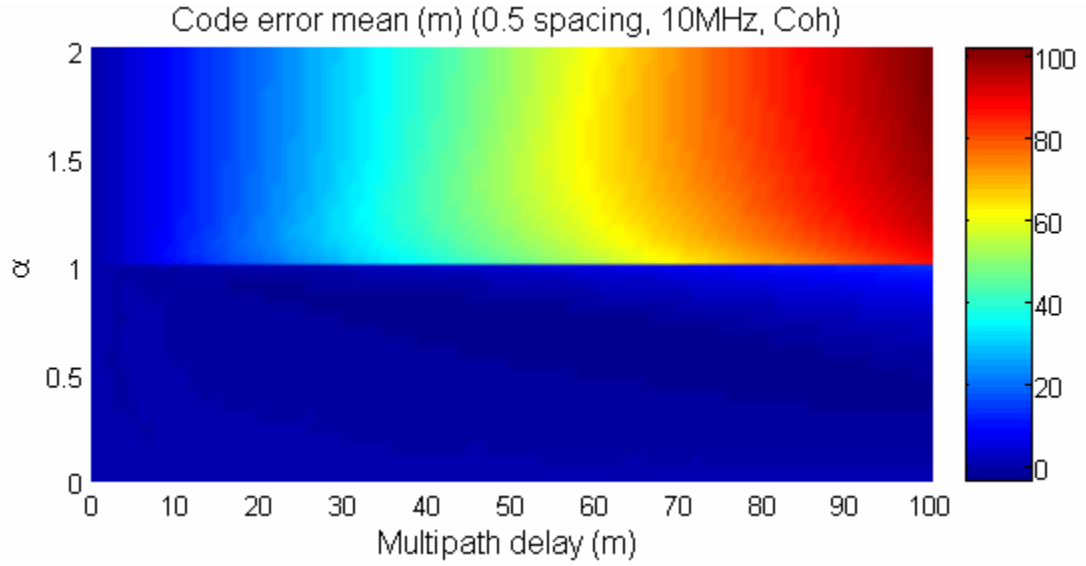
Figure 4.11: Code error mean with respect to multipath delay and MDR
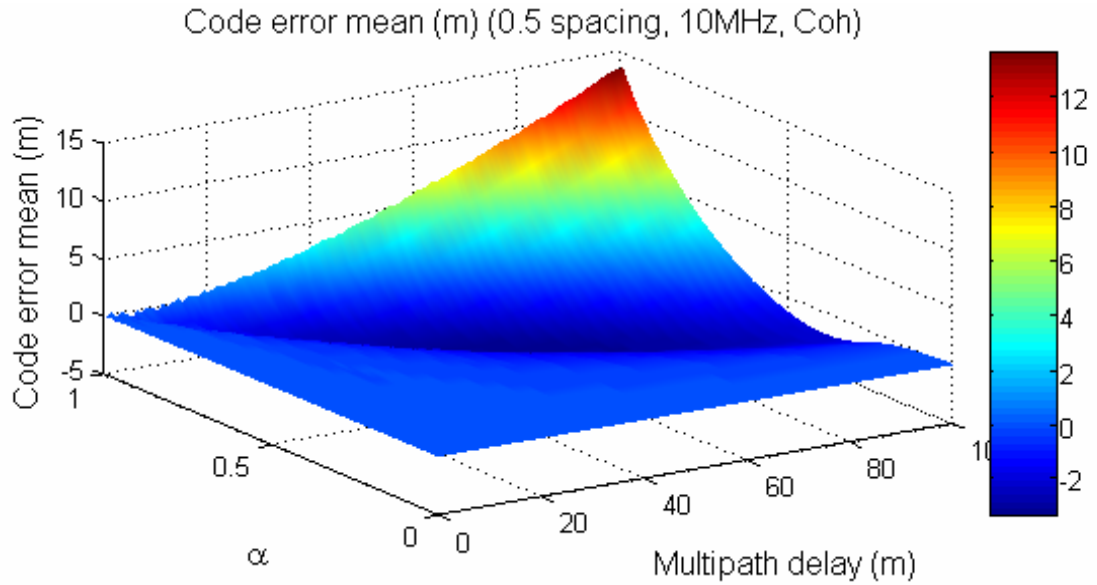
Figure 4.12: Code error mean with respect to multipath delay and MDR   (α

< 1)

Figure 4.13 shows the code error standard deviation. For a certain value of

multipath delay, when α approaches one from either side, the code error standard

deviation increases. This indicates that when the multipath signal strength is

closer to the direct signal strength, it has a stronger impact on the composite signal and results in larger variations in the amplitude of the code error.
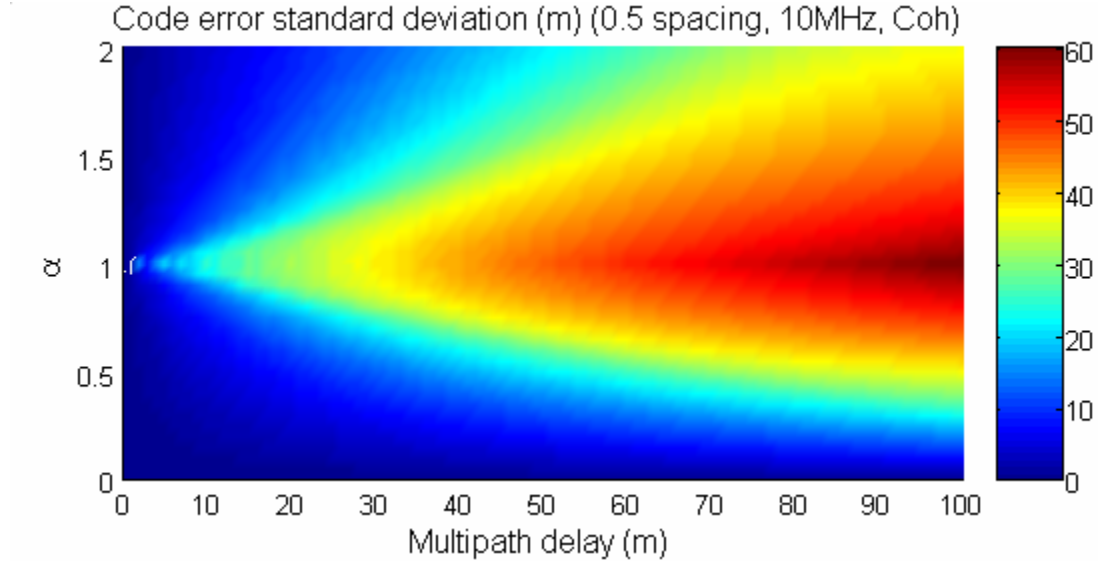
Figure 4.13: Code error standard deviation with respect to multipath delay and MDR

Figure 4.14 shows the mean C/N_0 errors. For a given value of multipath delay, when $\alpha > 1$, the C/N_0 error mean value increases as α increases, whereas, when $\alpha < 1$, the mean value is small and close to zero.

Figure 4.15 shows the C/N_0 error standard deviation. For a certain value of the multipath delay, this standard deviation increases as α approaches one from either direction. This indicates that when the multipath signal strength is closer to the direct signal strength, the multipath signal has a stronger impact on the composite signal and results in larger variations in the amplitude of the C/N_0 error. The amplitude of the C/N_0 error decreases with increasing multipath delay.
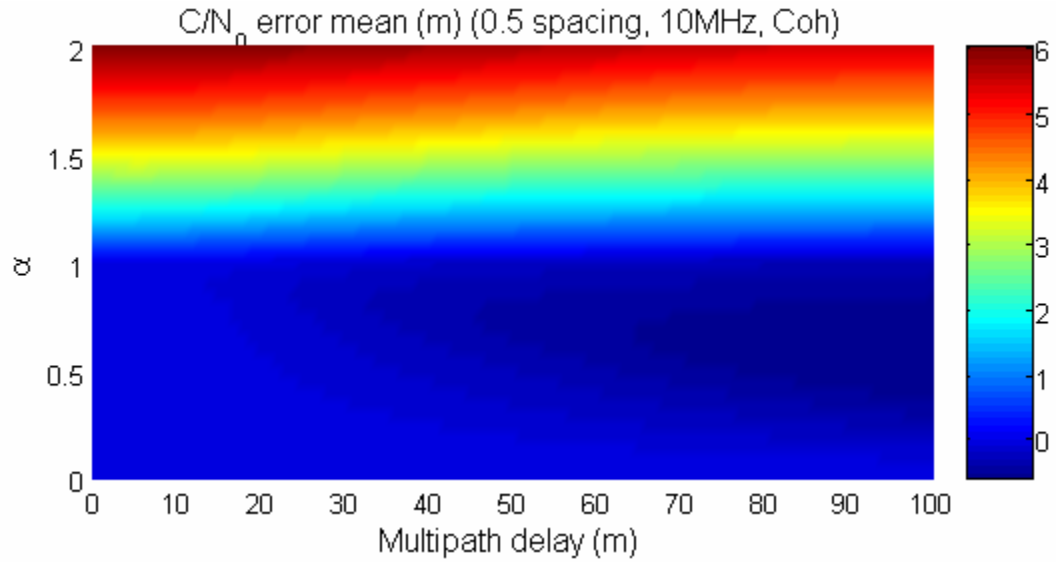
Figure 4.14: C/N$_0$ error mean with respect to multipath delay and MDR
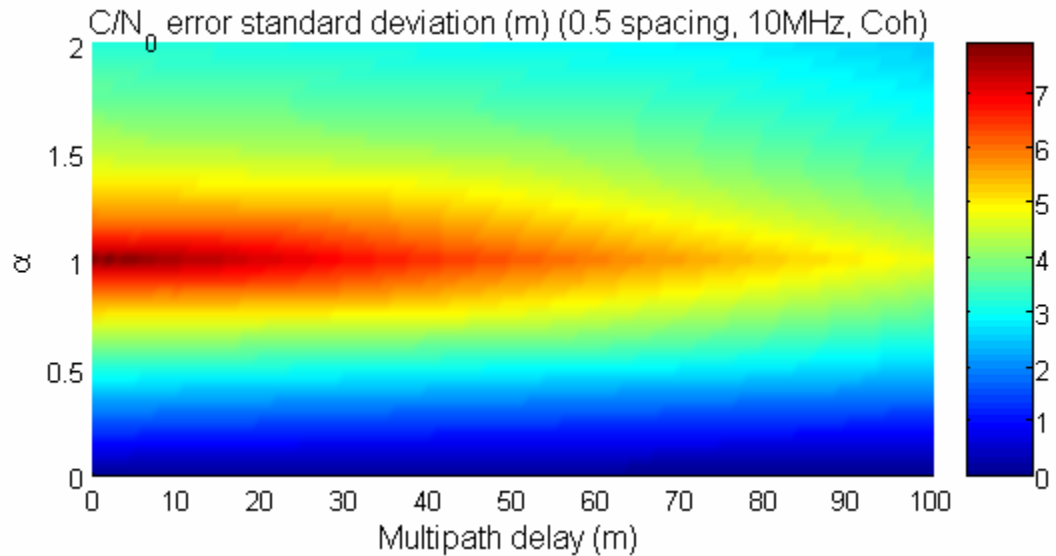
Figure 4.15: C/N$_0$ errors standard deviation with respect to multipath delay and MDR

4.4.2 Empirical Analysis

Besides the parameters of the multipath signals, the processing techniques applied by different receivers will also affect the multipath errors. The various

models of receivers have different multipath effects. To achieve a reasonable assumption of the multipath parameters in the real world from the measurements made by a receiver, the performance of that type of receiver due to multipath must be analyzed.

The simulated signals, consisting of one direct signal and one multipath signal, were produced by a hardware GPS simulator. A SiRF HSGPS receiver was used to receive the simulated signals and make the measurements to calculate the errors. Figure 4.16 and Figure 4.17 display the code and C/N_0 errors measured by the receiver due to weaker and stronger multipath signals than the direct signal, respectively. They have trends similar to those seen in Figure 4.7 and Figure 4.9.
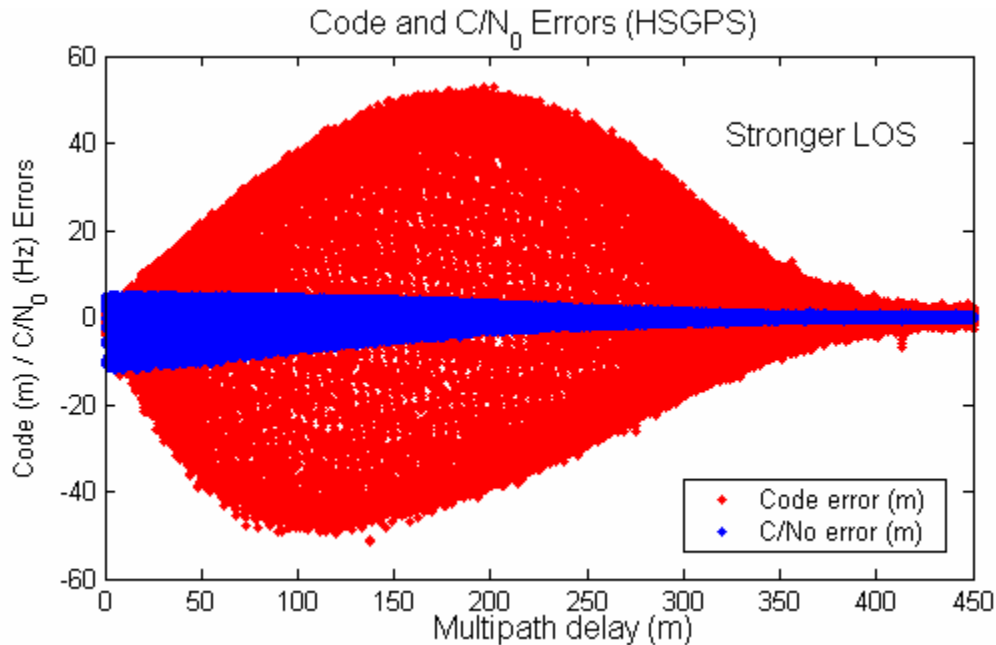
Figure 4.16: Code and C/N_0 errors of stronger direct signal measured by SiRF HSGPS receiver
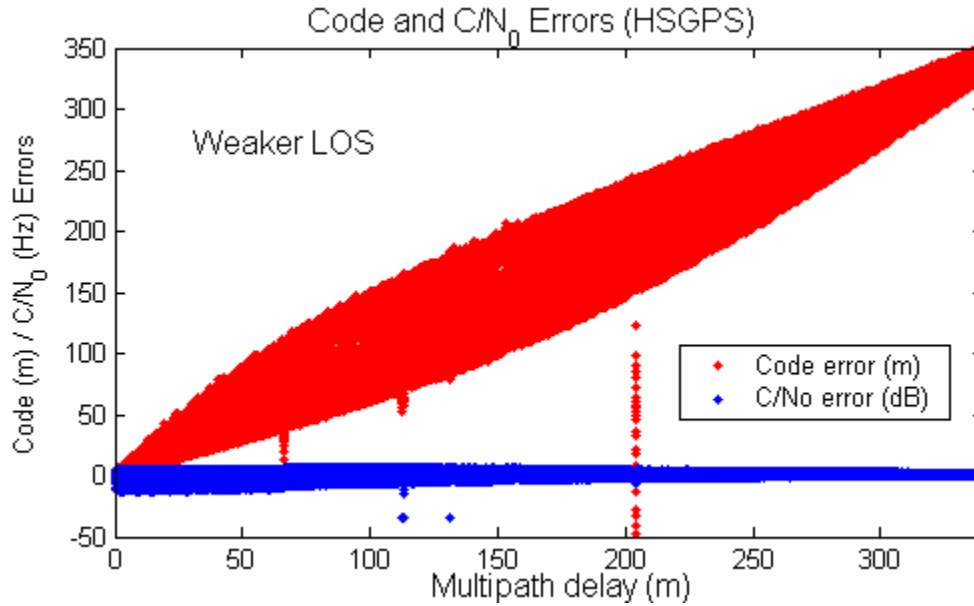
Figure 4.17: Code and C/N₀ errors of weaker direct signal measured by SiRF HSGPS receiver

In order to study multipath effects as a function of multipath signal power, six tests were conducted. The multipath MDRs were chosen as 0.2, 0.5, 0.8, 1.2, 1.5 and 1.8. The multipath delay was up to 100 m with steps of 0.01 m. As a result, each whole cycle is a continuous 19 samples of data. Every continuous cycle of data is taken in consideration to compute the multipath error statistics. Figure 4.18 to Figure 4.21 illustrate the statistics of multipath code and C/N₀ errors of the receiver due to a single multipath signal. They also show different performances for $\alpha < 1$ and $\alpha > 1$.
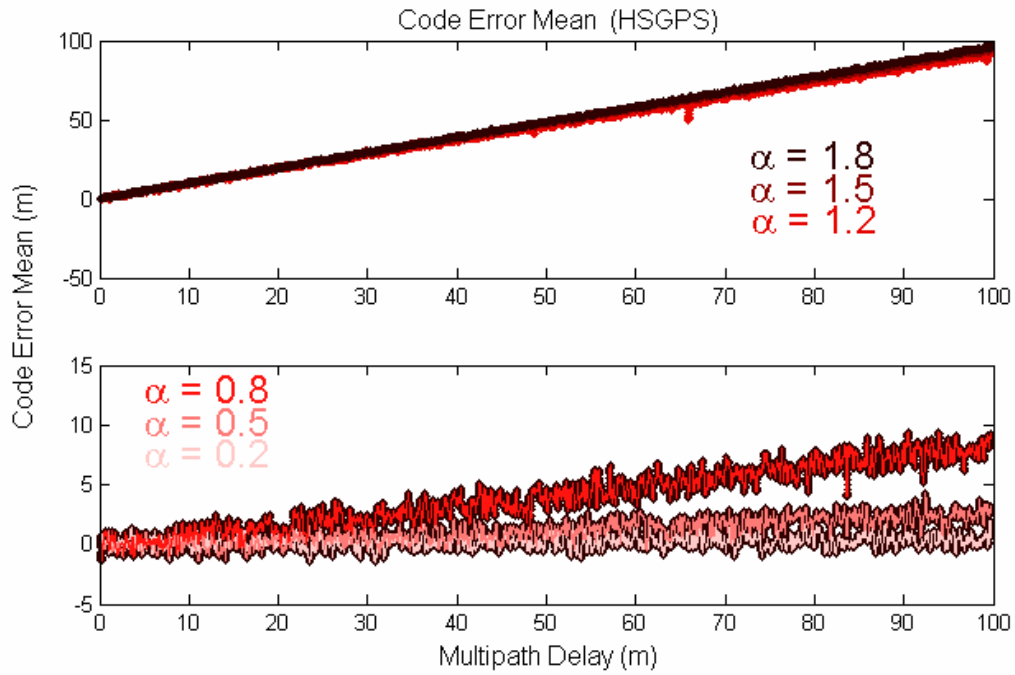
Figure 4.18: Code error mean due to a single multipath with respect to the multipath delay of a HSGPS receiver
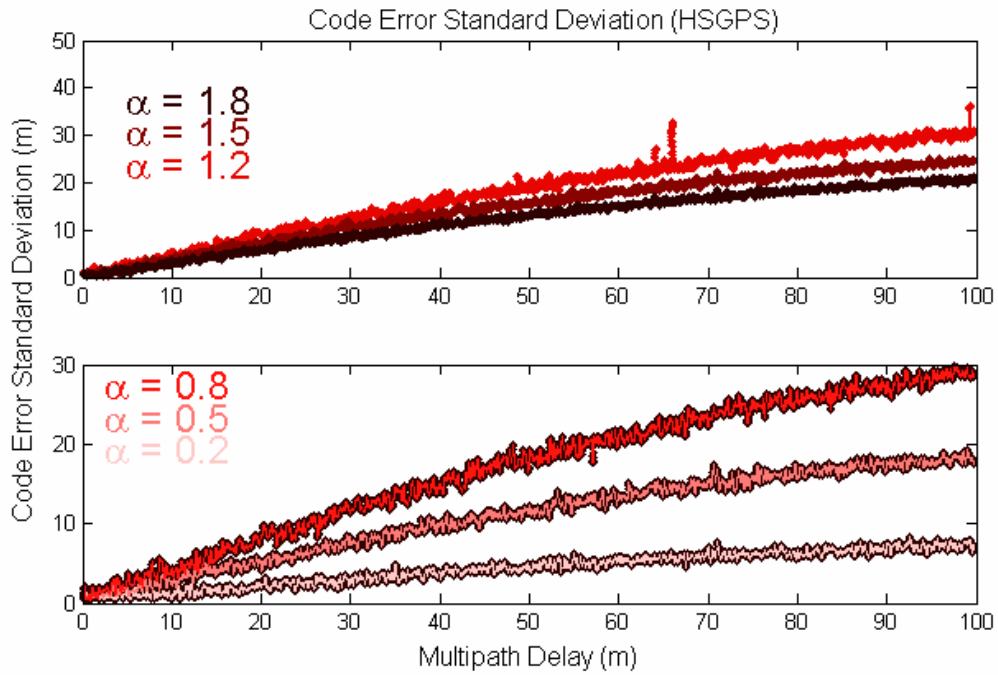
Figure 4.19: Code error standard deviation due to a single multipath with respect to the multipath delay of a HSGPS receiver
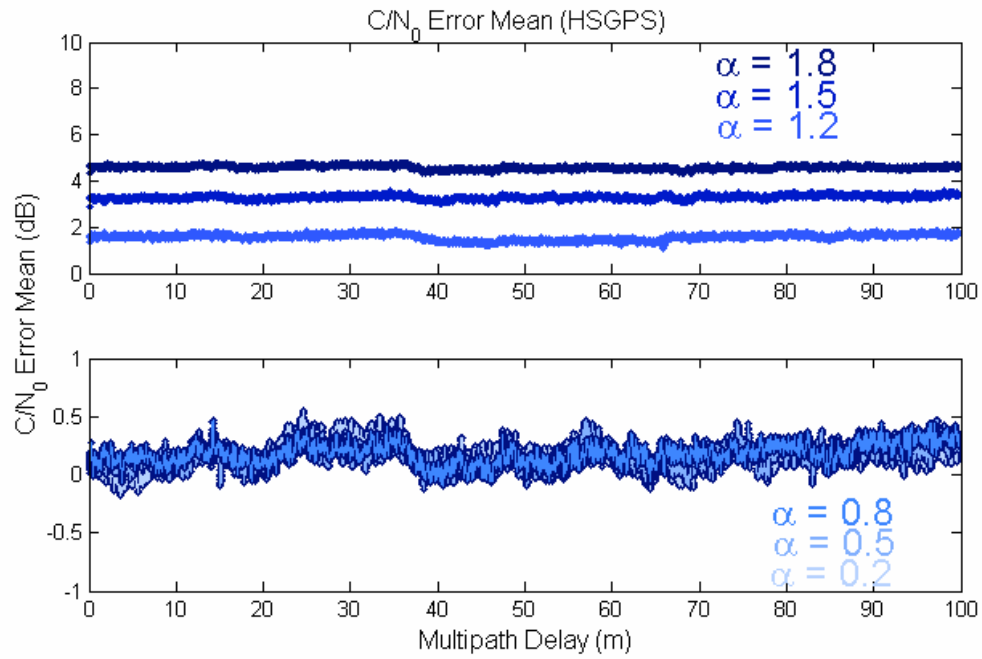
Figure 4.20: C/N$_0$ error mean due to a single multipath with respect to the multipath delay of a HSGPS receiver
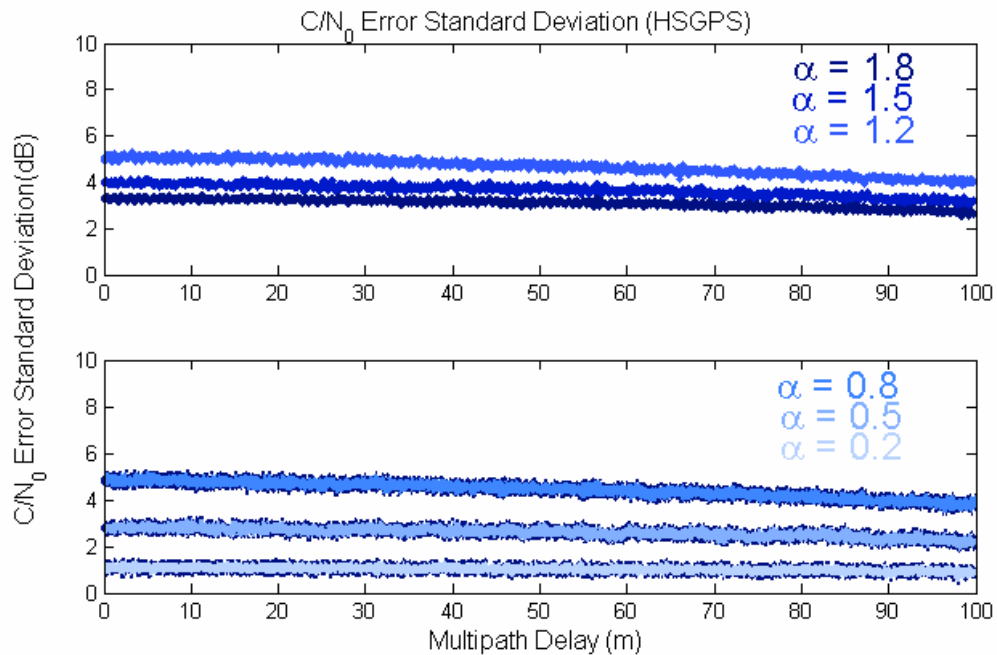
Figure 4.21: C/N$_0$ error standard deviation due to a single multipath with respect to the multipath delay of a HSGPS receiver

Some observations regarding the code and C/N_0 errors with respect to the multipath delay (0 to 100 m) and MDR (0 to 2) can be made from Figure 4.18 to Figure 4.21. They are

a) Both the mean and standard deviation of the code errors increase with the lengthening of multipath delay;

b) If the multipath signal is stronger than the direct signal, the code error mean increases significantly and approximately equals the multipath delay;

c) The C/N_0 error mean is close to zero when the direct signal is stronger;

d) The code and C/N_0 error standard deviations increase when the multipath strength approaches the direct signal strength;

e) Increasing the multipath delay causes small changes (< 6 dB) in C/N_0 error mean and standard deviation;

f) For the case when the multipath signal is stronger than the LOS signal, the C/N_0 error mean increases as the multipath strength increases, given that the multipath delay is constant.

If multipath errors can be observed in the field data, the statistical characteristics of multipath errors discussed above can be used to roughly estimate the multipath simulation parameters.

4.4.3 Undulation of the Multipath Error

The code and C/N_0 errors due to multipath vary as the multipath delay changes. If the multipath delay is constant with respect to time, the multipath errors are also fixed with respect to time. In reality, however, even if the antenna is static, the multipath delay changes as a function of time due to satellite motion. Figure 4.8 illustrates the sinusoidal-like pattern of multipath errors as a function of multipath delay. The higher the multipath signal strength, the less likely the errors follow a sinusoidal pattern (Ray 2000). Equations 4.7 and 4.10 indicate that the undulation of the sinusoidal pattern results from the sinusoidal function of the carrier phase change due to multipath delay. The cycle of the undulation equals the wavelength of the carrier, which is approximately 19 cm for the L1 signal.

If the rate of change of the multipath delay is known, the period of the multipath error undulation can be obtained by

$$T = \frac{0.19}{l'_{delay}} \qquad\qquad 4.12$$

where T is the cycle of the multipath error undulation (s), and l'_{delay} is the change rate of the multipath delay (m/s).

One can estimate the rate of change for the multipath delay if the cycle of the error is observed. For example, if T is 2 minutes, l'_{delay} is about 1.6 mm/s. Also, the faster the delay change rate, the larger the undulation frequency. Therefore, similar undulation frequencies can possibly be reproduced in simulation.

Chapter 5

Test Measures and Methodology

The main objective of this thesis is to replicate GPS signals in indoor environments using a hardware simulator. In order to study the characteristics of measured degraded GPS signals from selected environments, the following specific test metrics are proposed: the satellite availability, fading, the estimated pseudorange errors, the positioning accuracy, and the solution availability. To validate the simulation, the correlation coefficient is proposed as the measure of the statistical comparison between simulated and field results. The Spirent GSS6560 is introduced to show the operations to perform the simulations. The procedures to implement the field testing, data analysis, simulation and comparison are also introduced in this chapter.

5.1 Test Measures

The test measures of interest include: satellite availability, fading, estimated pseudorange errors, position accuracy, dilution of precision, and solution availability.

5.1.1 Satellite Availability

Satellite availability represents the number of available measurements obtained by the GPS receiver at each epoch. It is affected by the signal strength of every satellite and reflects the signal's degraded level in the particular environment.

The availability of measurements influences the dilution of precision and positioning accuracy.

5.1.2 Fading

According to the guaranteed minimum signal level requirement, the typically received GPS L1 C/A code signal power is specified to be at least -160 dBW for elevation angles between 5º and 90º (ICD 2000). However, the signal power may not satisfy this minimum level in signal-degraded environments such as indoor and urban canyon settings.

Signal power degradation is known to be caused by two effects: shadowing and fading. The shadowing effect mainly includes the attenuation of signal strength due to penetration loss, reflection loss and polarization loss. This signal shadowing causes direct losses in signal strength. The fading effect results from the constructive and destructive interference that occur when the GPS signal experiences multipath (Lachapelle *et al* 2003c) and the interference causes changes in signal amplitude (Watson 2005). The fading effect indicates the portion of the C/N_0 error due to multipath. Nevertheless, in this thesis, the term fading will be used to refer to both the shadowing effect and the interference fading effect. Therefore, the relationship between fading and multipath C/N_0 error is described as

$$F = P_{att} - P_e$$
5.1

where F is the level of signal fading, P_{att} is the signal strength loss due to the

shadowing effect, and P_e is the portion of the C/N$_0$ error due to multipath interference. For outdoor signals, P_{att} is usually zero.

Signal fading in a degraded GPS signal environment is the signal strength degradation compared to the undegraded signal measured at the same site but under open sky. However, in reality, it is impractical to switch the type of the environments for the same test site. Therefore, a reference station near the test site under open sky is established to provide the reference C/N$_0$ measurements. If the C/N$_0$ has a linear relationship with the actual signal power variation with a slope of 1.0, it can be measured by differencing the C/N$_0$ from the rover receiver with that from a reference receiver. The formula is given as (MacGougan 2003)

$$F = C/N_0^{reference} - C/N_0^{rover}$$

5.2

where F is the level of signal fading, $C/N_0^{reference}$ is the C/N$_0$ measurements made at the reference station, and C/N_0^{rover} is the C/N$_0$ measurements made at rover stations. However, the SiRF HSGPS receiver used for this research is not characterized by a linear relationship with a slope of 1.0. Thus, the following formulas presented by MacGougan (2003) are used to estimate a reasonable fading test measure from the C/N$_0$ difference measured by the SiRF HSGPS receiver.

$$F = \frac{C/N_0^{reference} - C/N_0^{rover}}{0.83}, \qquad \text{for } C/N_0^{rover} \geq 21\,\text{dB-Hz} \qquad 5.3$$

$$F = \frac{C/N_0^{reference} - 21}{0.83} + \frac{21 - C/N_0^{rover}}{0.35}, \qquad \text{for } C/N_0^{rover} < 21\,\text{dB-Hz} \qquad 5.4$$

This method of computing fading assumes that there is no signal degradation at the reference due to its local environment. Because C/N_0 is a measurement dependent upon the processing technique of the receiver, it is necessary that the receivers used at the reference and rover stations be of the same type. In addition, selection of like-type antennas (i.e. similar gain pattern) and similar cable losses are necessary to ensure similar signal conditions.

In general, signal fading is expected to be positive because the signal strength observed under open sky conditions should be no less than signals in degraded environments. However, this is not always true. Although the reference station is located in an open sky environment, multipath interference is possible, especially for low elevation satellites. If the signal of one satellite has destructive multipath interference at the reference receiver, whereas the signal of the same satellite has constructive multipath interference and little shadowing effect at the rover station, the C/N_0 at the rover station may be larger than that observed at the reference station. As a result, negative fading occurs.

5.1.3 Estimated Pseudorange Error (EPE)

The pseudorange measurement contains primarily the geometric satellite-to-user range and the clock offset. However, it is also affected by many other factors

such as multipath, spatial propagation delay, noise, etc. In indoor or urban canyon environments, multipath is the major error source and introduces more significant errors in pseudorange measurements than other error sources. To determine the extent to which these errors degrade the pseudorange measurements in the test environment, the receiver's raw data can be post-processed using the single differential technique. The relative 3D position between the two receivers is established through other means. The difference between the measured and calculated pseudoranges is the pseudorange error at the rover. The estimated pseudorange error (EPE) is referred to as the code error due to multipath and is analysed further, as follows.

5.1.3.1 Computation of EPE

The least-squares method is one of the common techniques used to estimate the user's position in GPS navigation. Since the test position is known, if the user's position is fixed to this known position, the pseudorange error can be calculated. This calculation was accomplished herein by the use of $C^3NavG^{2™}$, an epoch-by-epoch least-squares software package developed by the PLAN Group. $C^3NavG^{2™}$ is a C program that is capable of processing GPS pseudorange and Doppler data in either static or kinematic modes to determine position and velocity in either single point or differential mode (Petovello *et al* 2000). Since the position is held fixed, the least-squares portion is used only to estimate the receiver clock correction.

5.1.3.2 Relativity of EPE

The receiver clock bias is equal for all pseudorange observables at a given time. The clock bias can be estimated by least-squares if the true position is well known, as described in the previous section. However, the clock bias estimation is not entirely precise because the bias absorbs some unmodelled errors, such as multipath. The unmodelled errors in the measurements can be observed in the residuals of a position-constrained least-squares solution.

Figure 5.1 shows an example of the EPE measurements. Two sets of EPEs for the same satellite were computed from an identical dataset. The difference is that one set of EPEs was computed using the satellite above an elevation angle of 5° and another was computed using the satellite above an elevation angle of 45°. Although the trends of the two sets are similar, a mutual offset exists. The EPE set with an elevation angle above 45° is smoother than the other. This can be explained by the fact that the signals on the higher satellite experience less multipath interference than those on the lower satellite. If the satellites that experience less multipath interference could be determined and used in a least-squares estimation process, the resulting clock bias would be closer to its true value. The EPE solutions of other satellites even with severe multipath interference based on this clock bias would be more accurate and the relativity effect described above could be mostly avoided. However, it is difficult to determine which satellites experience less severe multipath in an indoor environment. In such a case, all available satellites have to be used for computing the EPEs and their relativity is inevitable.
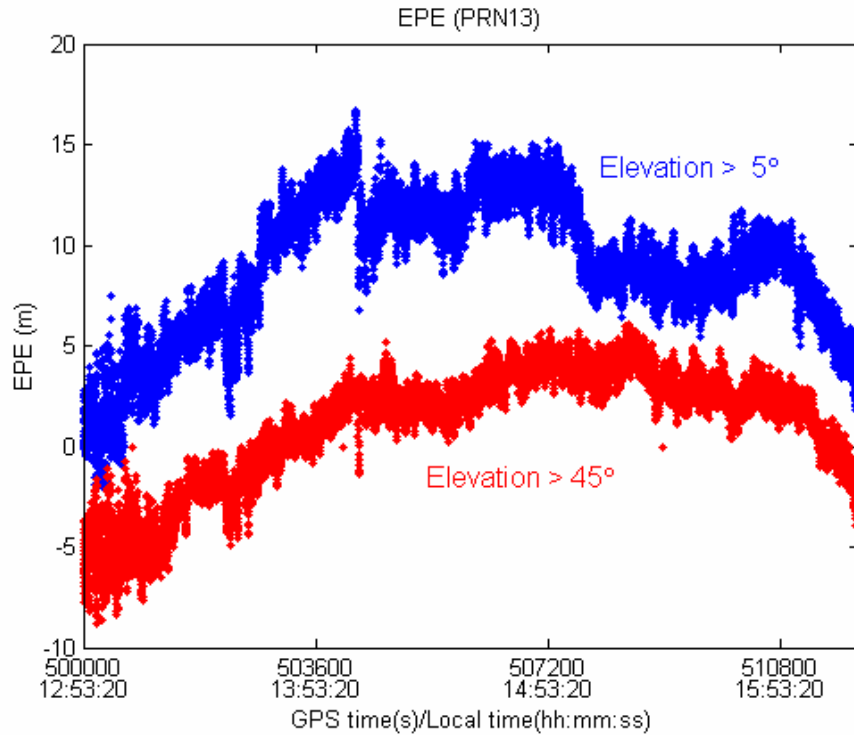
Figure 5.1: EPEs with 5° and 45° elevation cut-off

5.1.3.3 EPE and Multipath Code Error

The GPS errors that affect the pseudorange measurements have been discussed in Chapter 3. The satellite clock error, orbital errors and atmospheric delay can be eliminated or reduced using the single differential technique between the two receivers for the present application. The errors remaining in the pseudorange measurements include mainly multipath and noise. In the degraded GPS signal environments studied in this thesis, multipath is the major remaining error source. The error induced by noise is one to two orders of magnitude smaller. Hence, we can take the EPEs to represent multipath code errors. Because EPEs are the residuals of pseudorange measurements, they have a negative signal in comparison to the multipath code errors:

$$E = -\tau_e \qquad\qquad 5.5$$

where E is the EPE and τ_e is the code error due to multipath.

The values of the code errors due to stronger multipath signal or multipath-only signal are positive as discussed in Section 4.4. The corresponding EPE values should be negative. However, according to the relativity of EPE, it is possible that the EPEs of a multipath-only signal could be positive if there was another multipath-only signal having a larger multipath delay.

5.1.4 Position Accuracy and HDOP

The errors in the pseudorange measurements influence the quality of the ultimate position solution. In order to assess the impact of the pseudorange errors induced in each test, it is necessary to examine the position accuracy, which is deduced from the available measurements. The dilution of precision (DOP) provides a simple characterization of the user-satellite geometry. The lower the DOP, the better the quality of the position estimation. HDOP denotes the corresponding DOP value for the horizontal component. Position solutions were computed on an epoch-by-epoch least-squares basis using C^3NavG^{2TM} in differential mode with a 5° elevation cut-off. Solutions with a HDOP larger than 5.0 were excluded.

5.2 Statistical Analysis

To accurately represent the statistical characteristics of the signal, a probability density function and power spectral density are used to describe the signal

distributions. A correlation coefficient is used to compare and identify the statistical matching level between field and simulation results.

5.2.1 Probability Density Function (PDF)

Due to the complexity of the environments encountered in practical conditions, it is meaningless and impossible to completely replicate all signals in the time domain for a given environment. Therefore, an attempt is made to produce simulated measurements that have statistical characteristics similar to those of the field measurements. Probability density functions are used to describe the statistical characteristics of the test measurements in the time domain.

5.2.2 Power Spectral Density (PSD)

A probability density function describes the distribution of the data only in time. Of interest in this regard, the multipath delay change rate would affect the frequency of the multipath error undulation. The frequency characteristics of the signal can be obtained by signal spectral analysis. Power spectral density is one of the spectral analysis methods that can be used to describe the distribution of signal power in the frequency domain. If there is an obvious frequency component within a signal, a peak will appear at the corresponding frequency in its power spectral density function. Power spectral density is mathematically defined as the Fourier Transform of the autocorrelation sequence of the time series.

5.2.3 Correlation Coefficient (CC)

A correlation coefficient is a normalized measure employed to indicate how well

trends match between two variables. Assuming that there are two random variables *x* and *y*, the covariance of their standardized forms is known as their correlation coefficient, given by (Williams 2003)

$$\rho_{xy} = \frac{Cov(x,y)}{\sigma_x \sigma_y}$$
 5.6

where $Cov(x,y)$ is the covariance of x and y, and σ_x^2 and σ_y^2 are the variances of x and y. Another convenient equation to compute the correlation coefficient is

$$\rho_{xy} = \frac{n\sum xy - \sum x \sum y}{\sqrt{n\sum x^2 - (\sum x)^2}\sqrt{n\sum y^2 - (\sum y)^2}}$$
 5.7

where n is the length of the variables. If the correlation coefficient is equal to 0, one may say that x and y are uncorrelated. When x and y are nearly positively related, the correlation coefficient is near 1.

The correlation coefficient will be used herein to verify if the simulation data statistically matches the field data. The comparison items include the PDFs of the fading, the EPEs and their associated first and second order derivatives, the PDF of satellite availability, the PDF of horizontal positions, the PDF of the HDOP, and the PDFs of the fading and EPE PSDs.

5.3 Spirent GSS6560 Hardware Simulation System

This simulator consists of two major sub-systems: a hardware RF signal generator

and software, named SimGEN.   This combination provides flexibility to the researcher in generating scenarios in an intuitive Windows-based environment (Boulton 2002b).   The RF signal generator is capable of producing twelve independent channels of GPS L1 C/A code signals (channels) under the control of the SimGEN software.   The signal associated with a channel is described by the mathematics of the model applied.   Each channel is an independent signal, which can simulate a LOS signal or multipath signal at a controlled power level, Doppler, timing and message content corresponding to a satellite in-view.   The signals in these channels are combined, constituting an RF output that simulates a real world GPS signal under a designed scenario.   With the aid of SimGEN, the simulator can reproduce GPS signals consistent with the required time and location. SimGEN supports the combination of two RF signals as a 24-channel simulator, thus making available up to 24 channels that can be individually controlled to each reproduce one LOS or one multipath signal.

In default static conditions, the signals produced are LOS and simulated for open sky conditions.   In order to reproduce GPS signals for a degraded situation, such as indoors, the LMM model and/or UserActions function are employed to create multipath signals and adjust the LOS signal strength.   LMM and UserActions are introduced in Section 5.3.1.4.   An antenna gain pattern is used in SimGEN to adjust the signal power attenuation for certain types of antennas.   The version of SimGEN used for research purposes in this thesis is v4.21.

5.3.1 Simulation Configuration

To implement a complete simulation in this research, five fundamental steps need to be performed in SimGEN with the data being saved in the individual source files.

5.3.1.1 Date / Time

The start time and duration time must be specified. Based on this input time, SimGEN will calculate the week number and Time-of-week (TOW) as time passes, as shown in Figure 5.2.
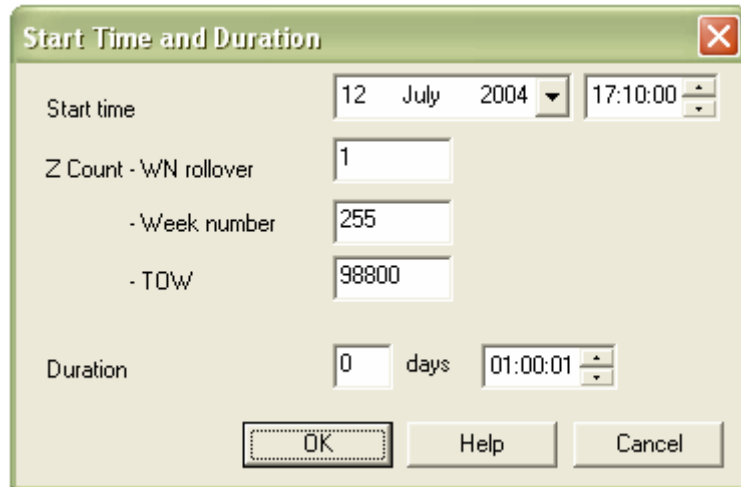

Figure 5.2: Data/Time setup in SimGEN

5.3.1.2 GPS constellation

SimGEN uses the U.S. Coast Guard Almanac information to generate the GPS constellation for the time and location of the simulation (Boulton *et al* 2002a). The user is allowed to change these orbit parameters in a comprehensive file editor. SimGEN calculates the orbit trajectory and Almanac and Ephemeris data for the GPS navigation data. Both current and previous GPS almanacs in YUMA format, a widely used ASCII format for recording and disseminating almanac sets, are

available from the U.S. Coast Guard website (Boulton 2002b). Figure 5.3 shows an example of the sky plot of the satellites used in a simulation.
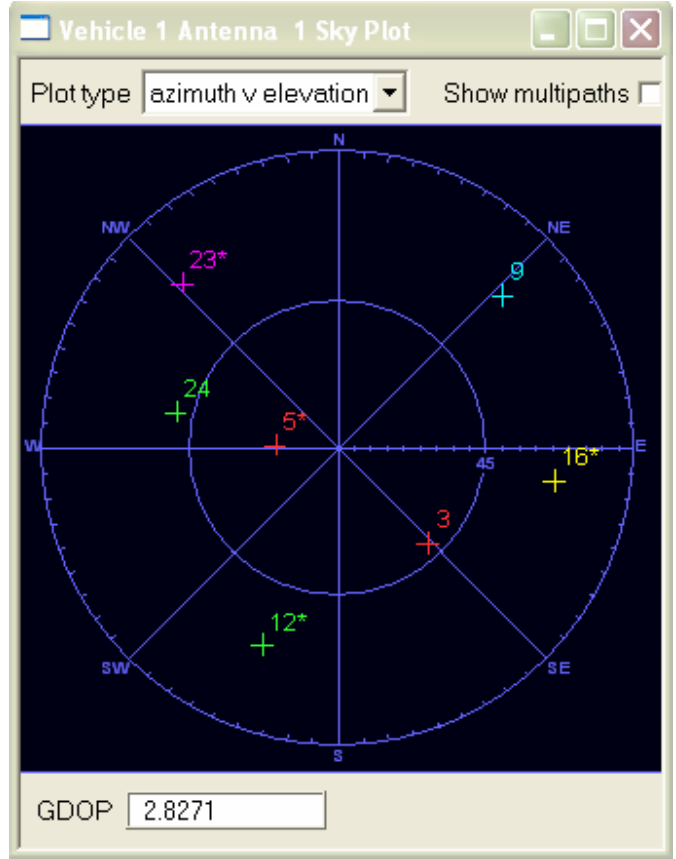

Figure 5.3: Sky plot of simulated satellites in SimGEN

5.3.1.3 Initial reference coordinates

The initial reference of longitude, latitude and height are the coordinates of the test point, as shown in Figure 5.4.
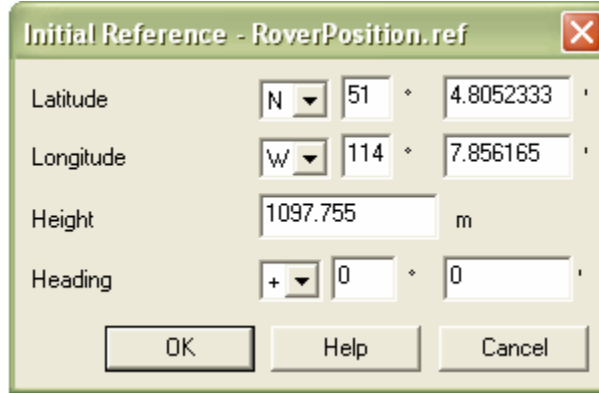
Figure 5.4: Initial reference setup in SimGEN

5.3.1.4 Environment setup

SimGEN provides two methods, referred to as the LMM and UserActions methods, to complete the setup for the multipath signal parameters. In the first method, SimGEN takes charge of creating all of the multipath signals based on the LMM model parameters set by the user. In the second method, all of the multipath signals are created by the user. The requisite signal parameters, such as the channel number, signal power level, multipath number, and etc., are written in an ASCII file to command the simulator to create the required signals.

LMM method

In the LMM model, the LOS and multipath signals are created depending upon an angle pair (elevation and azimuth) defining an arrival-related, user-defined, category mask. In this regard, there are four potential categories:

- Category A: obscured signal (satellites are not simulated)

- Category B: LOS only (no obscuration)

- Category C: LOS + reflections (echoes)

- Category D: reflected signals (echoes only)

A hemispherical category mask (see Figure 5.5) is mapped with these four categories based on the immediate environment. A particular satellite located in a certain category area will be treated as generically defined by that particular category. For example, if one satellite is located in Category A, it will not be simulated; if located in Category D, only the multipath signal will be simulated. The signal power fading follows Rician's model on the LOS channels and a modified Rayleigh's model on the echo channels. The delay of the echo channels is defined by a variable delay multipath model, which is discussed in Section 5.3.2.
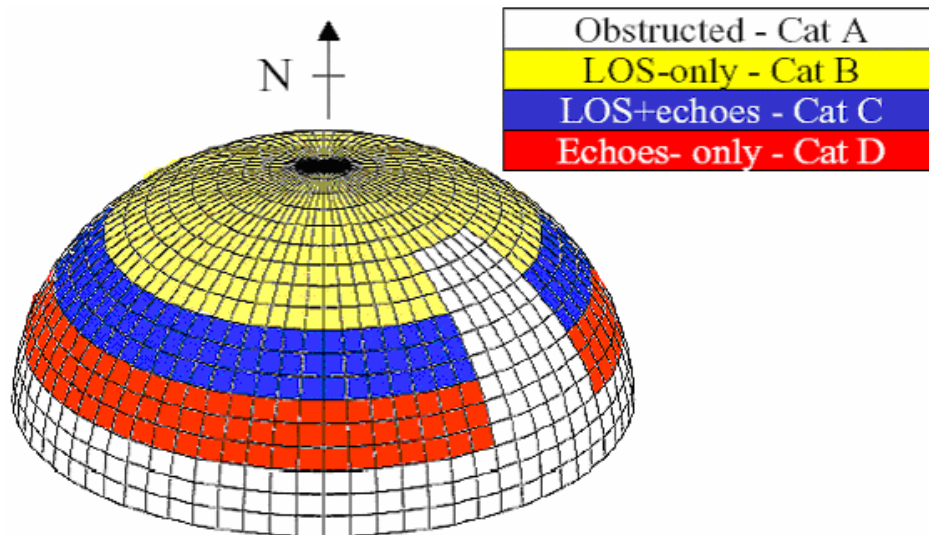

Figure 5.5: Category mask (Boulton *et al* 2002a)

The Rician distribution and a modified Rayleigh distribution were used to model the power fading of the LOS and multipath signals in the LMM model because they had a good match with the empirical data according to studies by Ma *et al* (2001)

and Klukas *et al* (2003). However, this approach does not imply that the power levels of the individual LOS and multipath signals have the same distributions as the composite signals. In theory, the designer of SimGEN may intend to use Rician and Rayleigh distributions to adjust the power level of each single channel and, based on this assumption, may expect similar distributions to appear in the fading of the simulated results. However, this result is not borne out in practice, since having individual LOS and multipath signals with power levels consistent with Rician and Rayleigh distributions does not necessarily imply that the composite signals will produce the same distributions. Hence, the intent in this research is to reduce the effects of the two distributions.

The following is a summary of the most important parameters used in the LMM model (Boulton 2002).

- **$K_{Riciean}$ and $K_{Rayleigh}$**: These parameters are used to change the variation of the power level of the LOS and multipath signals. The fluctuations of the LOS and multipath signal power are inversely proportional to $K_{Riciean}$ and $K_{Rayleigh}$. In order to reduce the influence of the two distributions on the power level of the LOS and multipath signals, $K_{Riciean}$ and $K_{Rayleigh}$ were set as large values for the simulations carried out herein.

- **$P_h(0)$**: It is the mean power level for echo signals.

- **b**: The initial path delay τ on the echo channel is calculated at random with an exponential distribution. b is the parameter of the exponential distribution shown as

$$f_{exp}(\tau) = \frac{1}{b}\exp[\frac{-\tau}{b}].$$ 5.8

- **Maximum near echo delay (MNED)**: MNED is an upper limit parameter imposed on determining the echo path delay τ.

Two constellation-related options associated with the LMM method are as follows:

- **Satellite selection never changes**: This option is selected to prevent the re-allocation of the simulated satellite set established at the start of the test, and does not deal with the rising/setting of satellites during the simulation. Otherwise, a new simulated set of LOS and echo signals is determined during the simulation process.   This option was chosen in this research.

- **Satellite position modeling**: This option allows the multipath signal delay to be modified geometrically according to the change in satellite position.

The LMM model adopts a variable delay multipath model to define the multipath delay.   This multipath delay model is shown in Section 5.3.3.

In the LMM method, SimGEN creates all LOS and multipath signals and automatically assigns the channels of the simulator to the simulated signals.

UserActions

UserActions is an alternative user-modified method.   It can be used to set up many useful scenario modifications in a time-ordered queue.   The modifications include (Boulton 2000b):

- Modify power level

- Change power mode

- Turn power on/off

- Apply pseudo-range ramps

- Switch LMM masks and environments

- Force/ban/include or apply multipath to selected channels/SVIDs

Users can establish the modifications as commands in an ASCII file to direct SimGEN to complete the required operations. The ASCII file is referred to as the user actions file.

The first and last commands in the above list were used in this research. The first command was used to adjust the power levels for the LOS and multipath signals. The last command was used to create multipath signals of a LOS signal and define their delay and power offset to the LOS.

The UserActions method allows for flexibility when creating scenarios. However, if LMM has not been used, the option to maintain satellite selection ("satellite selection never changes") is not permitted. Because the satellites in-view may change during the simulation, the satellite trajectory must be known in advance to allow the creation of multipath signals for the proper satellites in-view. In addition, UserActions supports only a 1-Hz data update rate in SimGEN v4.21. The input signal data can be updated only every second using the UserActions method,

whereas the LMM method can support a hardware update interval as short as 4 ms. Depending upon the UserActions to create multipath signals, the user actions file will have at least 21600 lines of commands for the condition of a 1 Hz data update, six satellites simulated, and 1 hour testing time.

5.3.1.5 Antenna gain pattern

The antenna gain pattern quantifies the attenuation of the receiver antenna at discrete angular intervals of elevation and azimuth.   An attenuation mask defined in SimGEN is used to represent the receiving antenna gain pattern (Boulton 2002b).   The pattern is based on the manufacturer's specification of the antenna used in the test.   It has a 5.0° increment in azimuth and elevation over the range -87.5° to 87.5° in elevation, and -177.5° to 177.5° in azimuth.

The NovAtel 702 antenna was used herein.   Its L1 gain pattern is as shown in Figure 5.6.   The maximum gain occurs at the zenith, with progressively lower gain levels observed as elevation angle decreases.   Consequently, the attenuation increases with decreasing elevation angles.   Signals coming from elevation angles below the horizontal plane of the antenna will be attenuated by at least 12.5 dB.   This antenna gain pattern also shows that signals with left-hand polarization have at least 15 dB of power attenuation more than signals with right-hand polarization.   This feature mitigates reflected signals that have left-hand polarization.
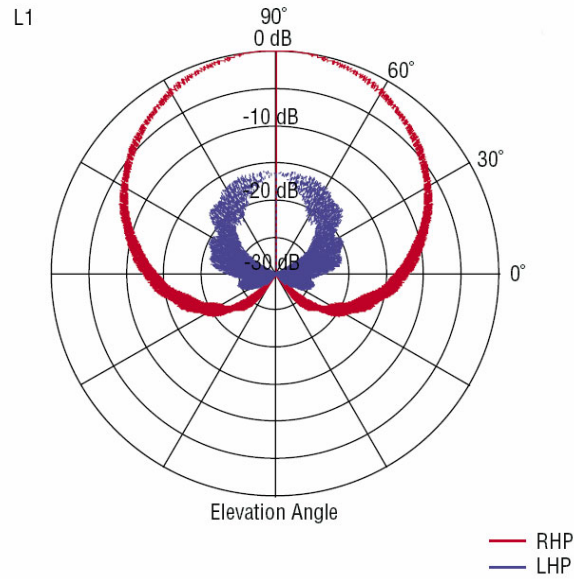
Figure 5.6: Gain pattern for L1 NovAtel 702 Antenna

In practice, however, the simulated result did not coincide with the actual field result if only based on direct application of the antenna gain pattern provided by the manufacturer in the simulations. Therefore, based on the empirical data, the antenna gain pattern was modified to compensate for the difference between the field and simulated results.

Figure 5.7 shows field C/N_0 measurements with respect to the elevation angles at a 1˚ increment. The data represented by green circles was measured using a HSGPS receiver and the NovAtel 702 antenna. The data was collected on the roof of the CCIT Building, University of Calgary. Every C/N_0 value with respect to a particular elevation angle was averaged from all C/N_0 measurements of the satellites with that elevation angle. The total testing time was more than thirty hours. The observed C/N_0 values indicate that the signal power experiences greater attenuation when signals originate at lower elevation angles. This result

is consistent with the antenna gain pattern shown in Figure 5.6. The fluctuation in the C/N$_0$ curve with low elevation angles may be the result of multipath interference or variation in antenna gain. The curve with red dots shows the smoothed C/N$_0$. The curve with blue Xs depicts the C/N$_0$ measurements produced by the same HSGPS receiver connected to the simulator without applying antenna gain pattern and multipath.
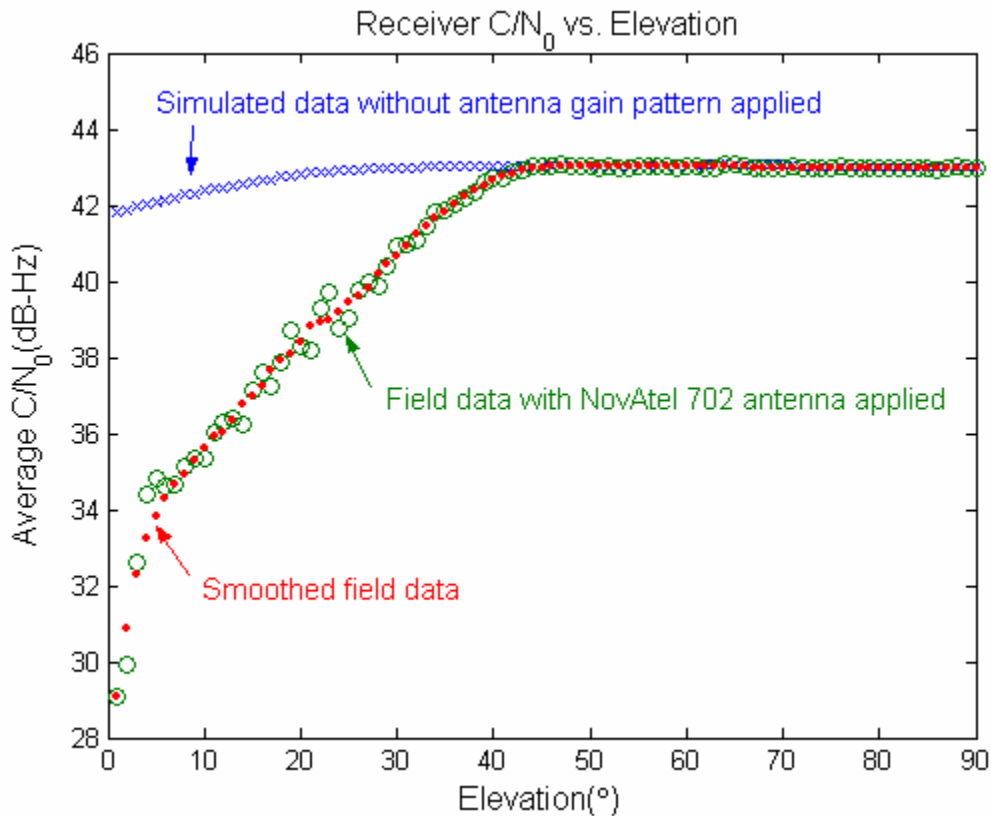

Figure 5.7: An HSGPS receiver C/N$_0$ output vs. signal elevation angles

The C/N$_0$ differences could not be directly taken as a measure of the antenna gain pattern, since the C/N$_0$ measurements of the HSGPS receiver do not have a linear relationship with respect to the simulator relative channel power as discussed in

Section 5.1.2.   In order to convert the C/N_0 to a level compatible with the simulator input signal power, the relation between input signal power and output C/N_0 from the receiver was derived.   The result of the variation of C/N_0 measured by the HSGPS receiver due to the variation of the simulator power is shown in Figure 5.8. The signal power of the simulator is depicted, relative to a reference value of -160 dBW.
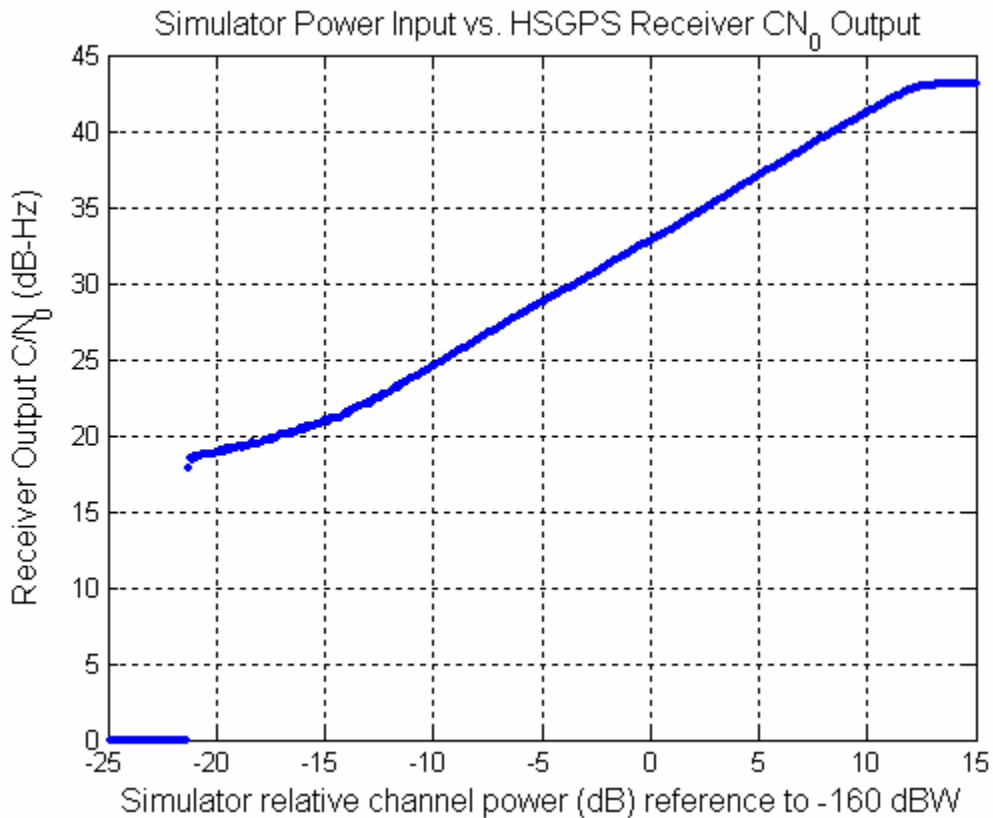

Figure 5.8: An HSGPS receiver C/N_0 output vs. simulator input power

Based on the results shown in Figure 5.8, the C/N_0 values were converted to the input signal power level.   The differences in input power between the field and simulated C/N_0 measurements, as shown in Figure 5.7, are known as the antenna

gain pattern shown in Figure 5.9. SimGEN only supports the antenna gain pattern file with a 5° increment. Therefore, the simulated antenna gain data with respect to a given elevation angle was an average value of data within 5° ranges. In addition, this antenna gain pattern is tailored to receive data only from this range of elevation angles because only signals originating at elevation angles above 0° were considered in the simulation.
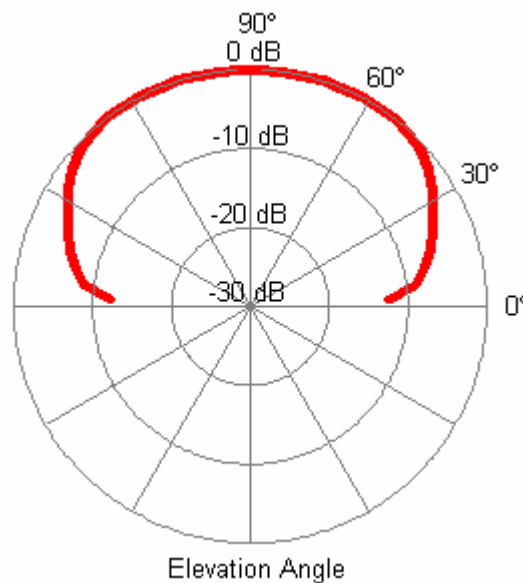

Figure 5.9: Simulated antenna gain pattern

5.3.2 Signal Power Level

The original simulated power level of a satellite signal is based on the minimum signal level of -160 dBW, specified in ICD-GPS-200 (2000). Due to the fact that the satellite transmitters broadcast more power and the atmospheric loss is smaller, a typical received power is up to 8 dB higher than the minimum signal level (Misra & Enge 2001). A base level is used to set a constant power level offset. Moreover, the additional variations of the power level simulate the losses from the

antenna pattern and free-space propagation.   The variation due to the free-space loss is based on a reference range from a receiver on the ground to a GPS satellite at 0° elevation.   The original power level can then be adjusted by the LMM model or by the user actions file.   This empirical procedure is a crucial operation of the simulations in this research.

5.3.3 Variable Delay Multipath Model

Multipath delay is satellite-receiver-reflector geometry-related.   A variable delay multipath model was presented by Lachapelle *et al* (2003b) and employed by SimGEN with the following assumptions:

- Multipath signals are reflected from a vertical plane;

- The reflection surface is considered a smooth and regular plane and signal reflection is uniform in all directions;

- The signal source is considered remote such that incident angles are effectively the same at all points in the immediate vicinity.

Figure 5.10 shows a single vertical reflector.   The total additional path delay is given by (Lachapelle *et al* 2003b)

$$\delta = 2D \cos\theta \qquad\qquad\qquad 5.9$$

where D is the distance from the receiving antenna to the vertical reflector, and θ is a combination of elevation ε and azimuth α components.   The relationship among the three angles is given by (Lachapelle *et al* 2003b)

$$\cos(\theta) = \cos(\varepsilon) \times \cos(\alpha). \qquad\qquad 5.10$$

The delay δ lengthens as the distance D increases. If signals have the same azimuth angles, the signals with low elevation angles have larger delays than those with high elevation angles. For a given θ, the larger the D, the larger the delay and delay change rate.
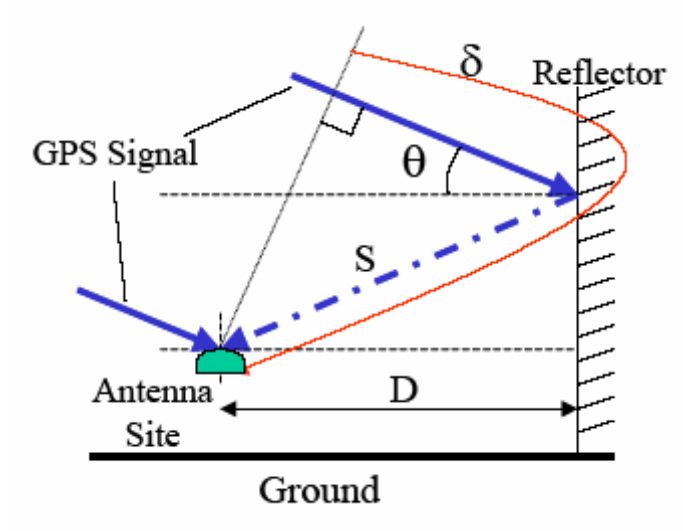

Figure 5.10: Multipath vertical reflection (Lachapelle *et al* 2003b)

5.3.4 Channel Assignment

The maximum available number of channels in the simulator system is 24, and it is necessary to choose a realistic number of satellites for the simulations. If assigning an equal number of channels to each satellite, four or six channels per satellite is a reasonable assignment. However, a set of four satellites is the minimum required to achieve a position solution for the general case. If, a single satellite is lost during the test, no position solution is available. Six satellites were chosen and each was assigned four channels. Depending on the actual situation, four channels can be associated with one LOS channel with three multipath

channels or, alternatively, four multipath channels without LOS signal.

In reality, various forms of signal reflection can occur and three channels of multipath may not accurately represent the actual conditions. In order to study the impact due to the number of multipath channels, five simulation tests were performed with multipath channel numbers of 1, 3, 5, 9, and 19 respectively. Figure 5.11 displays the multipath effects on fading and EPEs depending on the number of multipath signals. The fading and EPEs with more multipath channels exhibit more nonperiodic variations. Because a greater number of multipath signals lead to more combinations of the LOS and multipath signals, this results in more possibilities for the non-periodic variations. In general, fading and EPEs tend to vary in a non-periodic fashion. If more channels were available, this non-periodicity could be simulated with greater fidelity. If two multipath signals have nearly identical delays, they actually act like one stronger multipath signal. Therefore, the larger the delay difference between the multipath signals, the greater the extent of non-periodicity observed in fading and EPEs.

The non-periodicity in fading and EPEs also affects their distributions. Figure 5.12 shows the probability density function of the fading and EPE values depicted in Figure 5.11. With an increase in the number of multipath signals, the distributions of the fading and EPEs become more dispersed. Accordingly, the peaks of the curves become flatter.
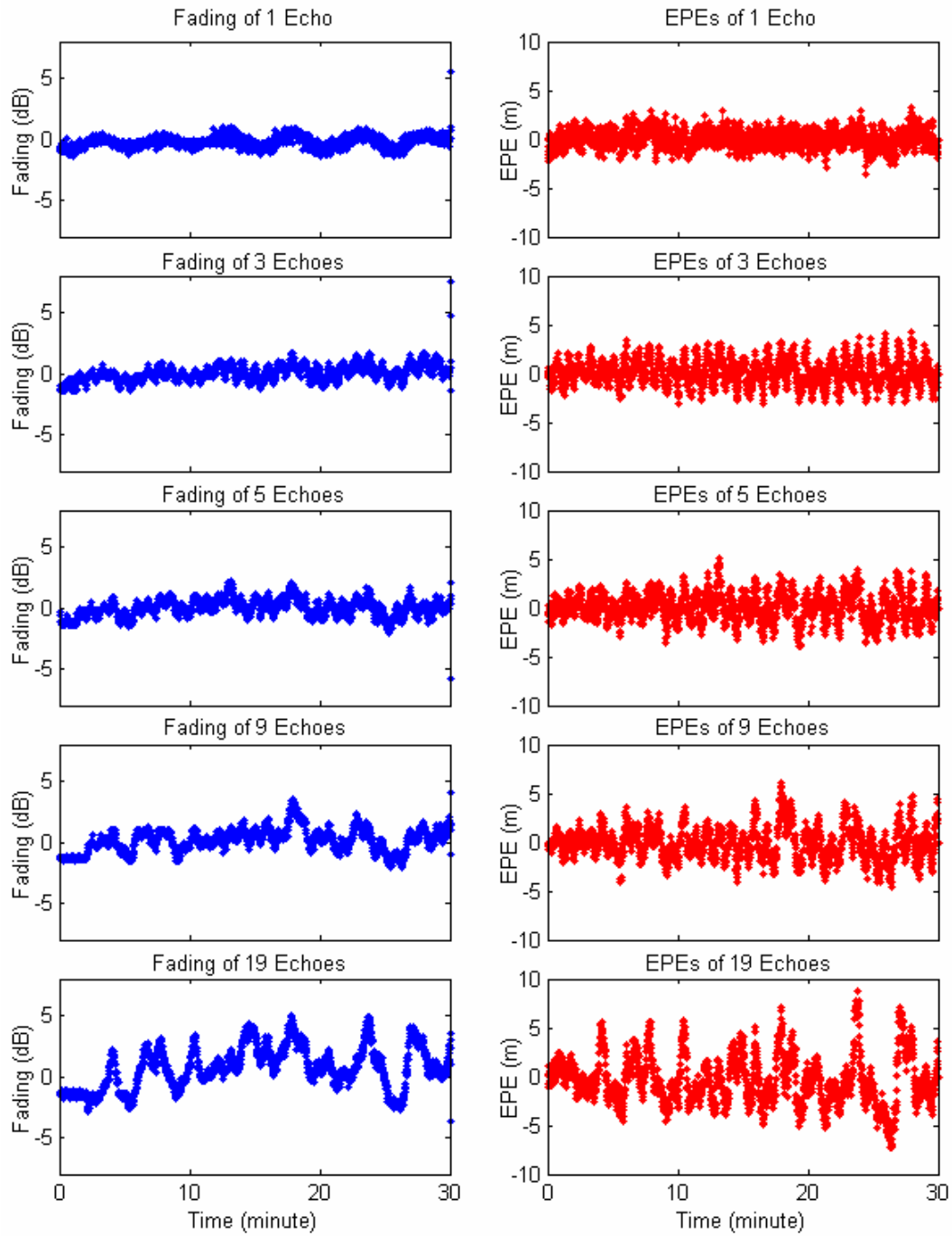
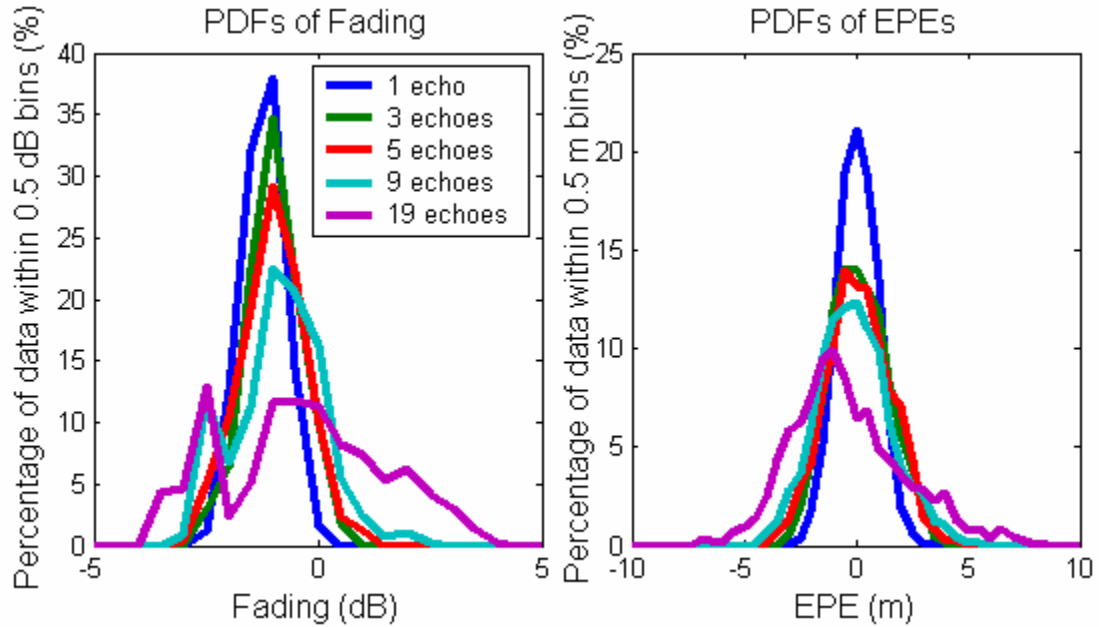**Figure 5.11: Fading and EPEs with various numbers of multipath signals**

Figure 5.12: PDF of Fading and EPEs with various numbers of multipath signals

5.4 Testing Methodology

The receivers deployed as reference and rover stations are of the same type, for the reasons discussed previously. Using antennas of the same type and cables of equal loss is necessary to facilitate the computation of fading. Four distinct environments of GPS signal degradation were identified for field-testing and simulation. Each test began with a warm-up period of twenty minutes operating under LOS conditions. This is required to allow the SiRF HSGPS receiver to obtain all information needed to utilize the high sensitivity technique. The nearby reference station was located on the roof of the CCIT building, with clear LOS, as shown in Figure 5.13. The positions of the antenna at the reference and rover stations had been previously surveyed and are well known in WGS84.

Figure 5.13: Reference station on CCIT Building Roof

All of the simulations are based on measurements of the fading and EPEs made in selected representative field environments. The mean and standard deviation of the fading and EPEs with respect to the azimuth and elevation in the test environment, referred to as the pierce-point, will be presented. This analysis allows an insight into the statistical characteristics of the fading and EPEs and the spatial characteristics of the test environment (Lachapelle *et al* 2003c). Thus, according to the observations introduced in Section 4.4, the approximate values of the parameters of signal attenuation, multipath strength and multipath delay of a satellite signal coming from a specific direction can be estimated.

In the simulation for each environment, 40 minutes of data was selected. After conducting each simulation test, fading and EPEs were computed from the measurements made by the HSGPS receiver. The statistical characteristics of the fading and EPEs were compared with the field results to evaluate the validity of the simulation using correlation coefficients. A trial and error method, beginning with parameters based on field data characteristics, was used to adjust the

simulated signal parameters to improve the correlation between the simulated data and field data. The entire trial-and-error process flow chart is shown in Figure 5.14.
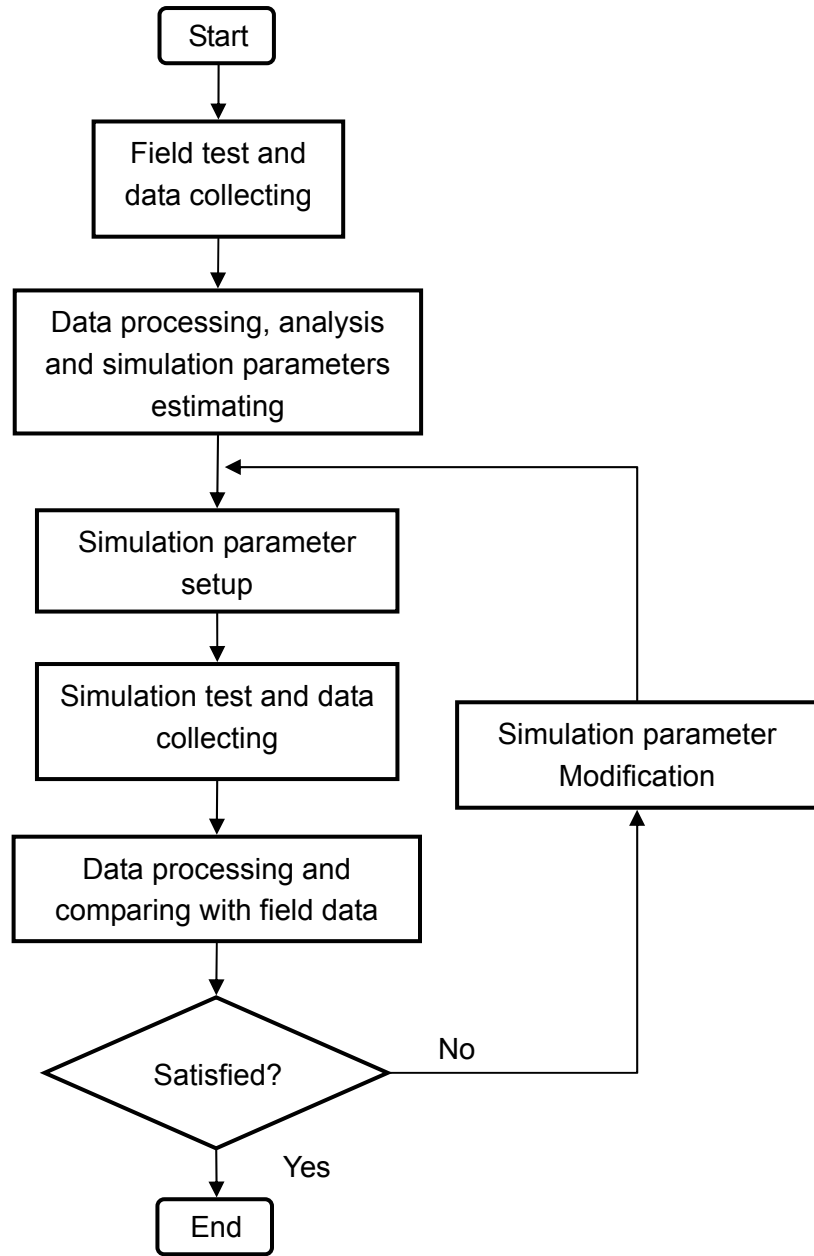

Figure 5.14: Process flow chart

Chapter 6

Simulations of Indoor Environments

For simulation purposes, three indoor environments were selected. Field tests were performed in a residential garage, a concrete underground pit and a covered sport arena. The relative dimensions of these three environments increase from the garage to the underground pit, and to the covered sport arena.

6.1 Residential Garage

6.1.1 Field Testing Description

The testing environment is a typical attached residential car garage in North America. The exterior and interior of the house and garage are shown in Figure 6.1. The garage has a wooden door, gypsum wallboards, a partially concrete wall structure, a living room above, and a concrete-tiled roof. The dimensions of the garage are 9 m × 5.6 m × 2.5 m. The GPS coordinates of the test point inside the garage, which is 4.3 km away from the reference station, were surveyed independently. The wooden garage door was closed during the test, which lasted for four hours.

Figure 6.1: Exterior and interior residential garage environment

6.1.2 Satellite Availability

The satellite availability during the test is shown in Figure 6.2 over time. A PDF of the number of available satellites is shown for the entire test in Figure 6.3. At least four satellites were available approximately 95% of the time. Thus, a position solution was probably available 95% of the time.
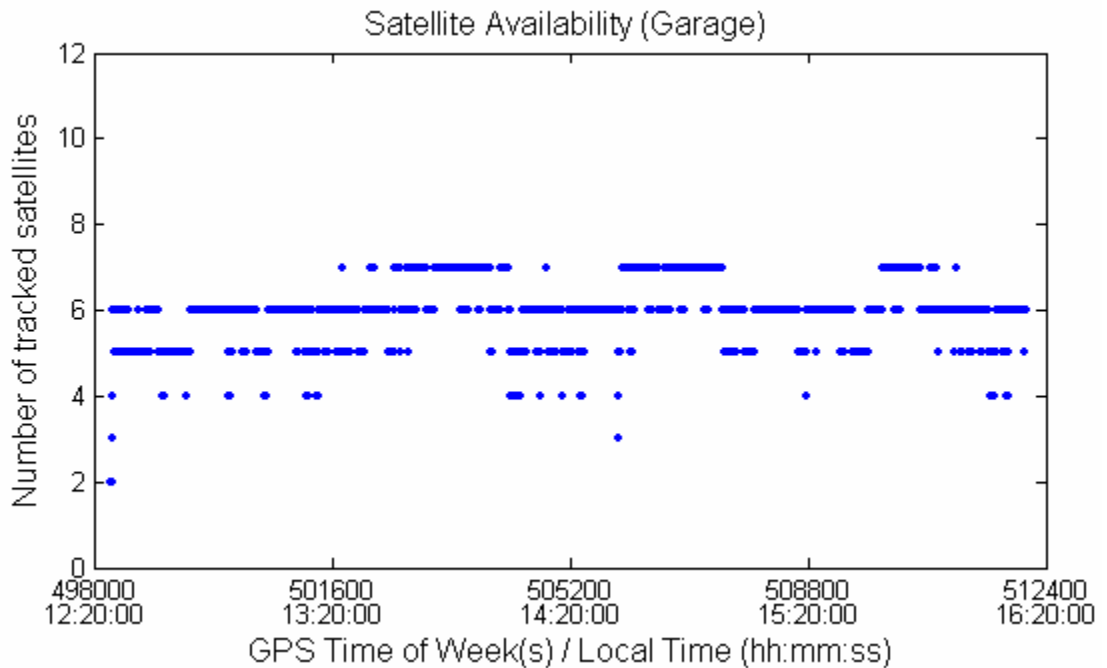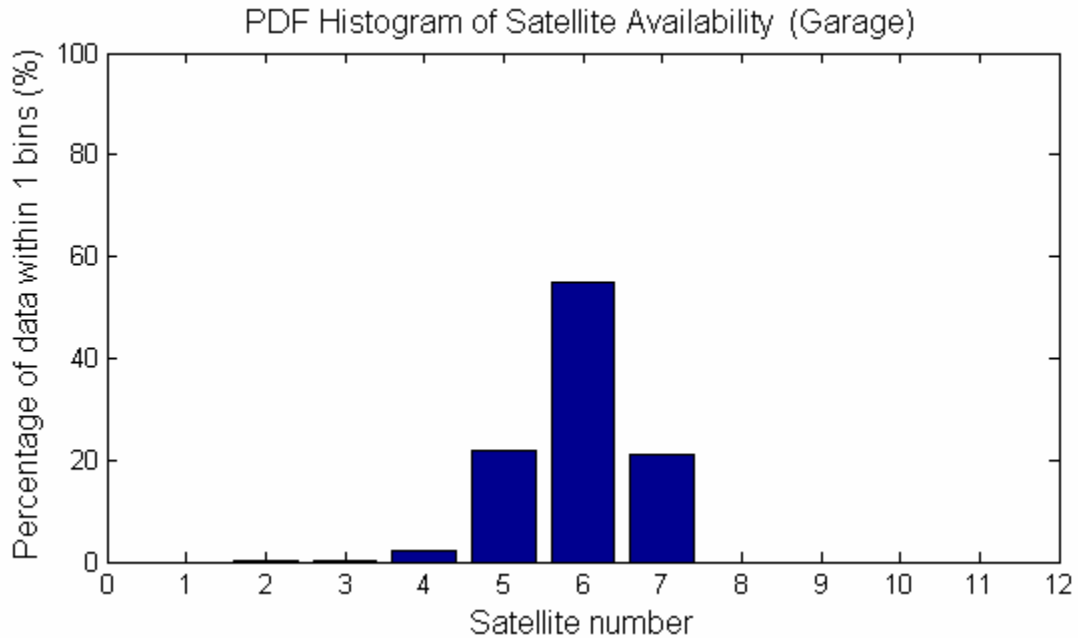

Figure 6.2: Satellite availability — garage test

Figure 6.3: PDF of satellite availability — garage test

6.1.3 Fading

The signal fading measurements for all satellites during the indoor test are shown in Figure 6.4. The fading values were between -5 dB and 45 dB. Negative fading did occur when satellites were at elevations lower than 20°. The low elevation satellites were more likely to experience multipath interference. As discussed in Section 5.1.2, the C/N_0 at the rover station may be larger than that at the reference station, resulting in negative fading.
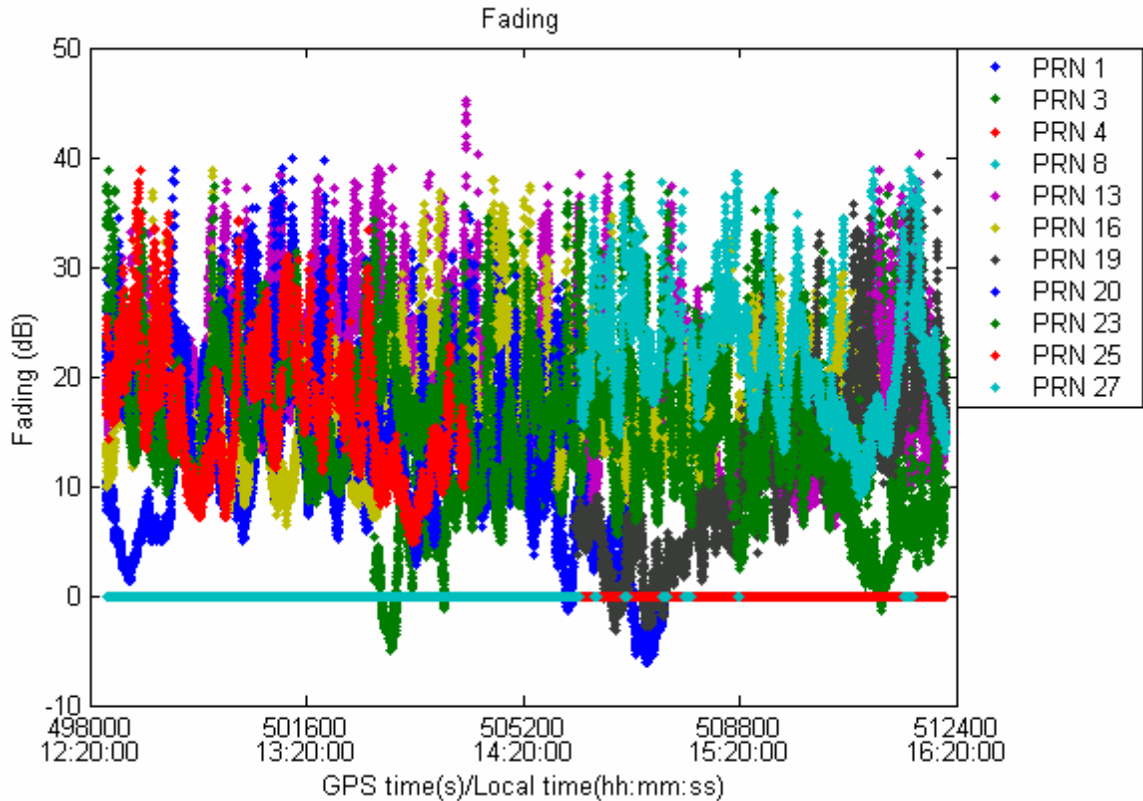
Figure 6.4: Signal fading for all satellites — garage test

Figure 6.5 and Figure 6.6 present the results of the satellite pierce-point analysis. This analysis provides insight into the spatial characteristics of the test environment. It shows the signal's statistical fading profile having a strong correlation with the test environment. The signal fading was grouped into bins of 3° azimuth by 3° elevation, with statistical data derived for every group. The grey background track lines indicate the overall satellite positions in-view during the test, and the thin lines describe the inside outline of the garage. The mean fading values of each 3° × 3° bin are shown. Almost all the signals passing through the walls and roof and captured by the receiver were attenuated except for some passing through the wooden garage door, which attenuated the signals to a lesser

extent than the walls and roof. Moreover, all negative values of mean fading occurred for the garage door. Assuming that multipath signals were weaker than the LOS signals, the mean C/N_0 error due to multipath should be close to zero (see observation (c) in Section 4.4.2). Then, the fading mean could be taken as representing the magnitude of signal attenuation. Figure 6.6 shows the fading standard deviations. Observation (d) in Section 4.4.2 indicated that the signals with fading values characterized by large standard deviations were possibly affected by stronger multipath signals than those with smaller standard deviations.
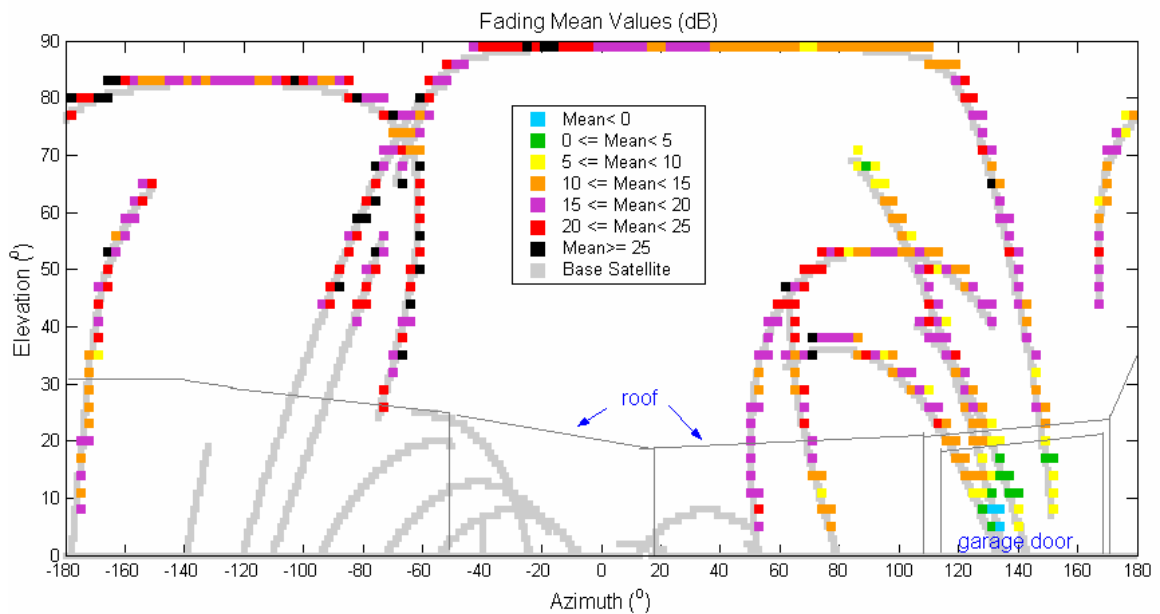
Figure 6.5: Fading Mean of 3˚x3˚ bin — garage test
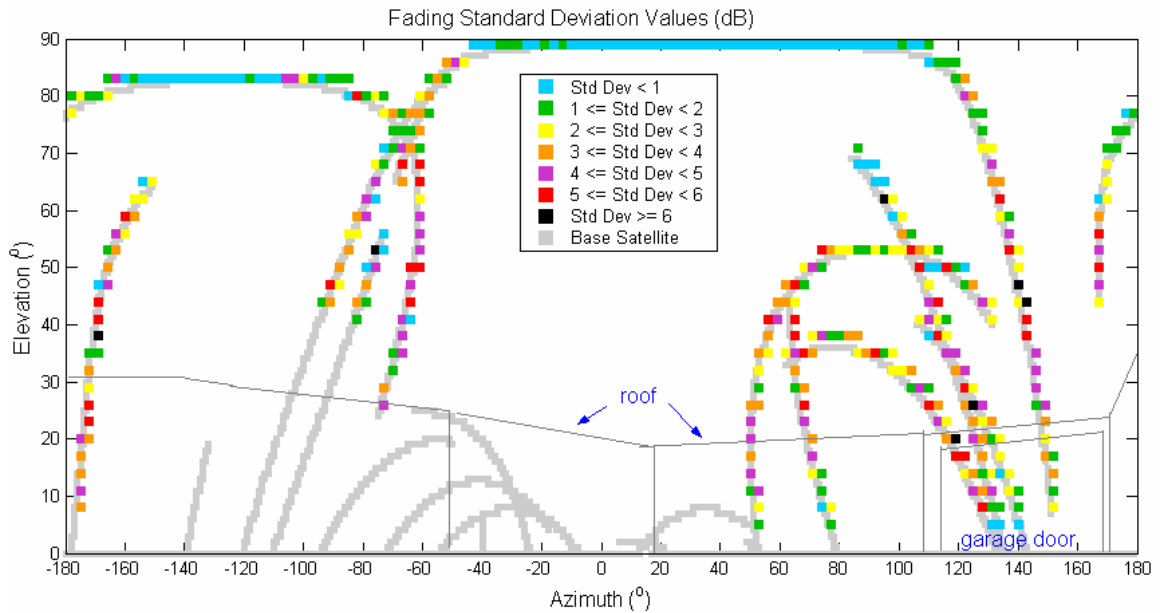
Figure 6.6: Fading standard deviations of 3˚x3˚ bin — garage test

The overall fading distributions are presented in Figure 6.7. The fading and its first and second order derivative PDFs are shown in solid blue, green dash and magenta dotted lines, respectively. N_0, N_1 and N_2 indicate their numbers of samples. The data range and bin size used to calculate the PDFs are shown as well. Sixty one percent of the fading was located in a range stretching from 10 dB to 20 dB, centred approximately at 15 dB. This indicated the attenuation levels after signals passed through the building. The first and second order derivatives constitute a measure of the magnitude of the data variations. Therefore, the analysis of the derivatives can assess the simulation more completely. They were centred and symmetrical about 0, which implies that the increased and decreased extents of the fading were almost equivalent. The sharp peaks indicate that the variations of the fading were in a narrow range, from -5 dB to +5 dB.
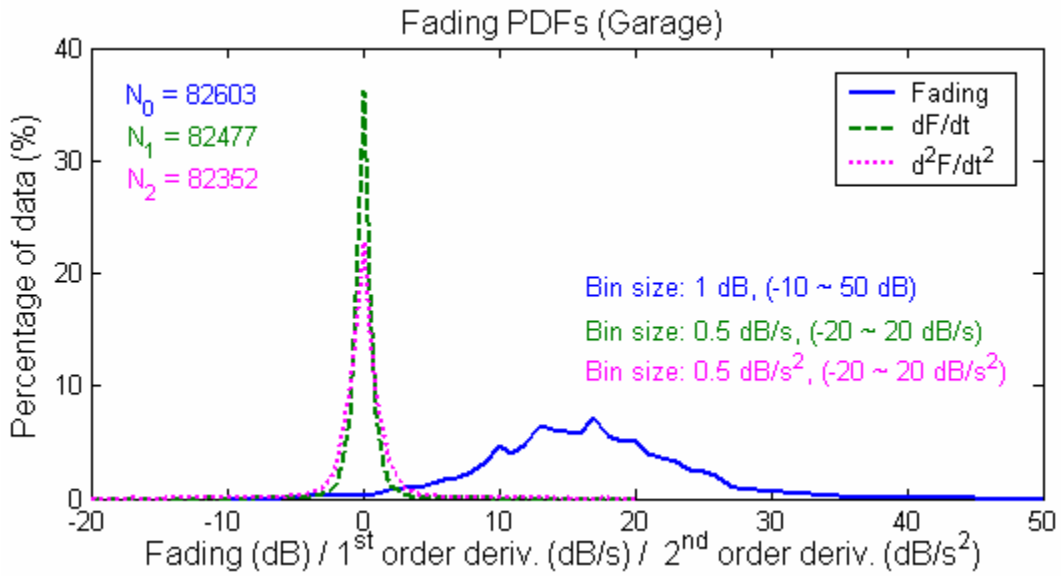
Figure 6.7: PDFs of fading and associated 1st & 2nd order derivatives — garage test

In order to further analyse the signal fading in more detail, Figure 6.8 displays the fading profile and elevation of PRN 23, which was available for the longest time in the test. The negative values appeared when the satellite elevation was below 20° (GPS time between 510600 s and 511500 s). The smallest fluctuation cycle T_f, that can be clearly observed was 200 s, corresponding to a frequency of 0.005Hz. This implies that most of the frequency components were less than 0.005 Hz.
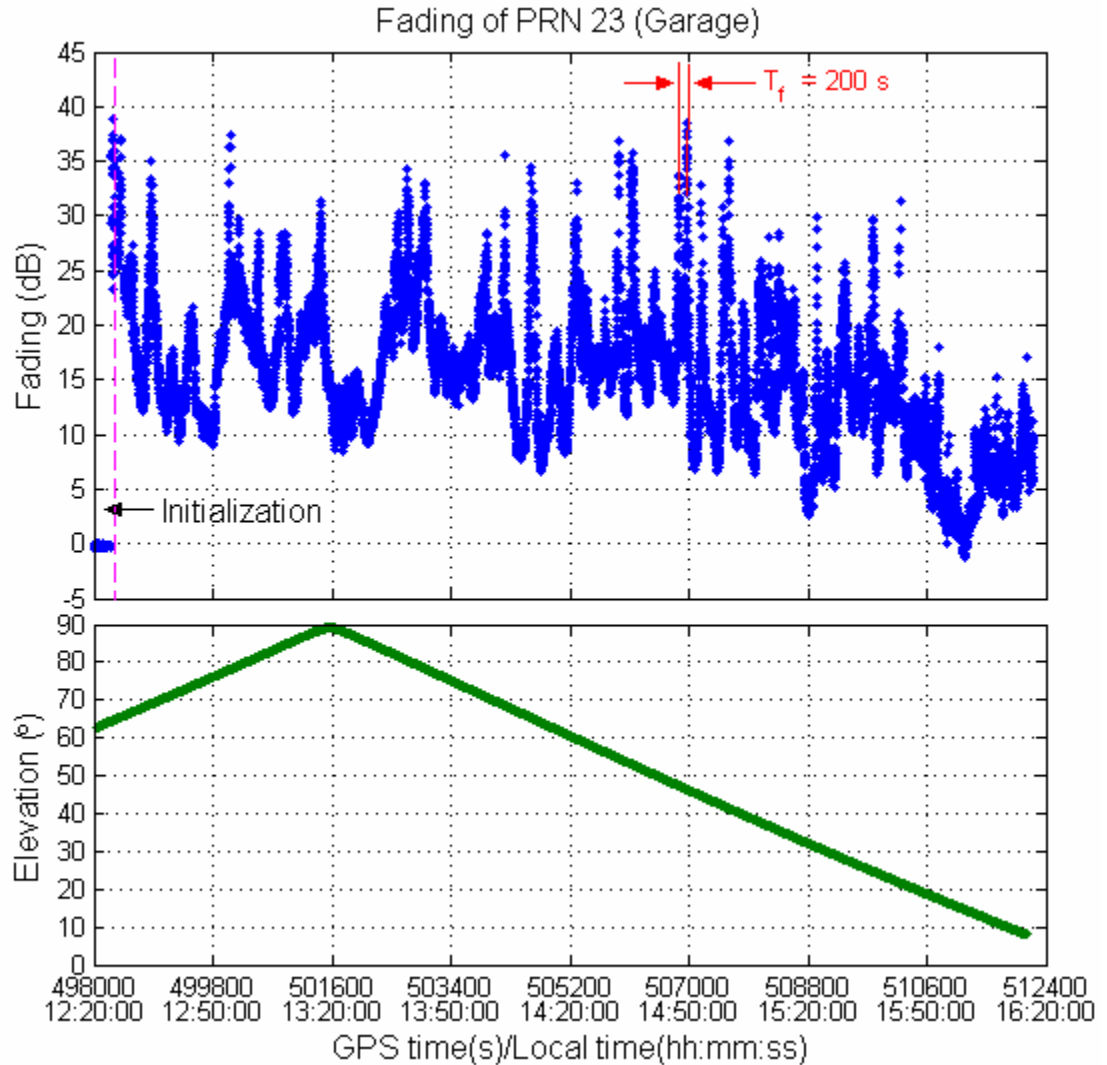
Figure 6.8: Fading of PRN 23 and elevation in garage test

The analysis of the fading variations depends on the PSD distribution. The variation frequency is only of concern. However, the power attenuations in the fading act as a DC (direct current) component in the fading's frequency domain. In order to eliminate its impact, the mean of the fading needs to be removed in the PSD analysis. The fading PSD distribution of PRN 23 is displayed in Figure 6.9. More than 90% of the fading frequency components are smaller than or equal to

0.005 Hz, coinciding with the previous analysis.
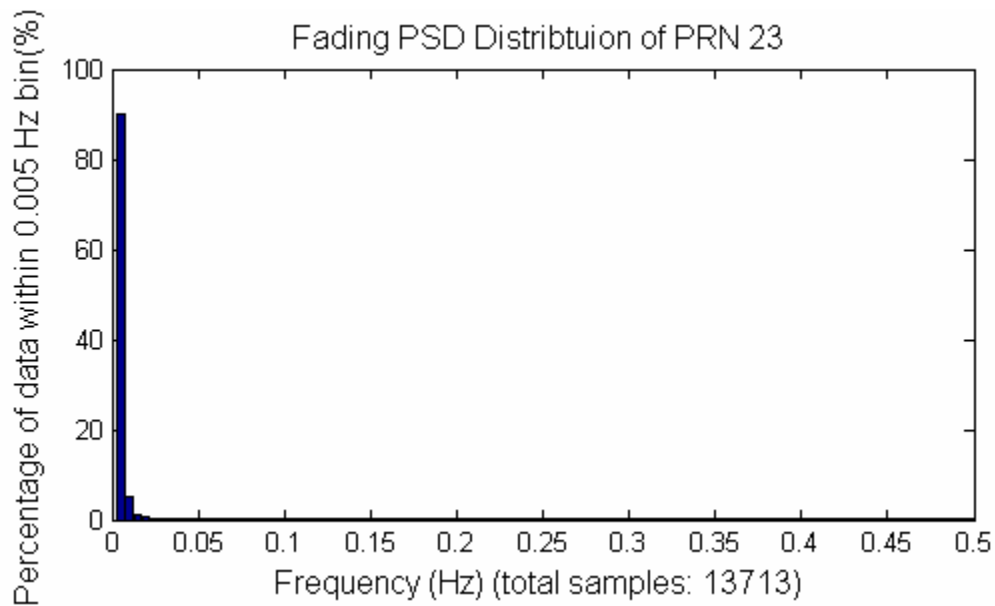
Figure 6.9: Fading PSD distribution of PRN 23 in garage test

6.1.4 Estimated Pseudorange Errors

Figure 6.10 and Figure 6.11 present the means and standard deviations of the EPE measurements binned into 3° × 3° elevation and azimuth groups.   Most of the EPE mean values are between -5 m and +5 m, while most of the EPE standard deviation values are less than six metres.   Although the fading mean for the garage door area exhibited obvious differences compared to the other areas (see Figure 6.5), the EPE means in the door area did not show a significant difference in characteristics compared to the other areas.   The reason is that the error is a function of the multipath to LOS amplitude ratio, as opposed to the signal power level.   Assuming all of the multipath signals originated from indoor reflections of the LOS signals propagating through the garage door, even if the garage door was open, the multipath code error could be the same as those for the closed door case.

If the multipath signals were weaker than the LOS signals, according to observations (a) and (d) in Section 4.4.2, the signals characterized by large standard deviations contain the multipath signals with longer delay or stronger power levels than the signals with small standard deviation values. Based on this assumption, the signals coming from the zenith presumably include shorter multipath delay than those coming from the low elevation angles.
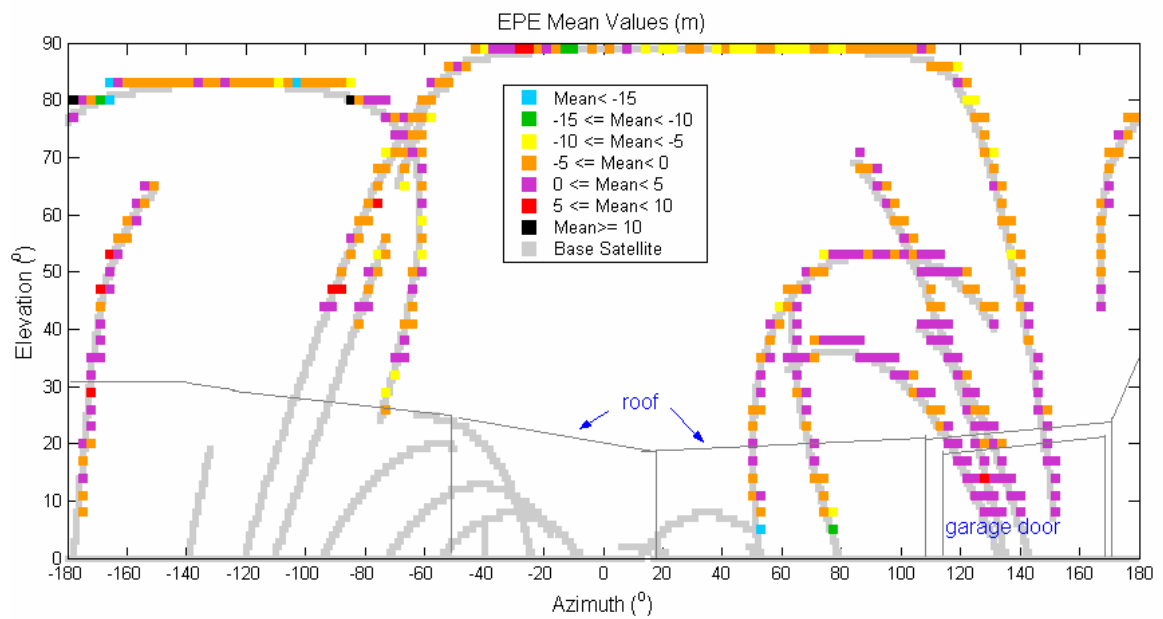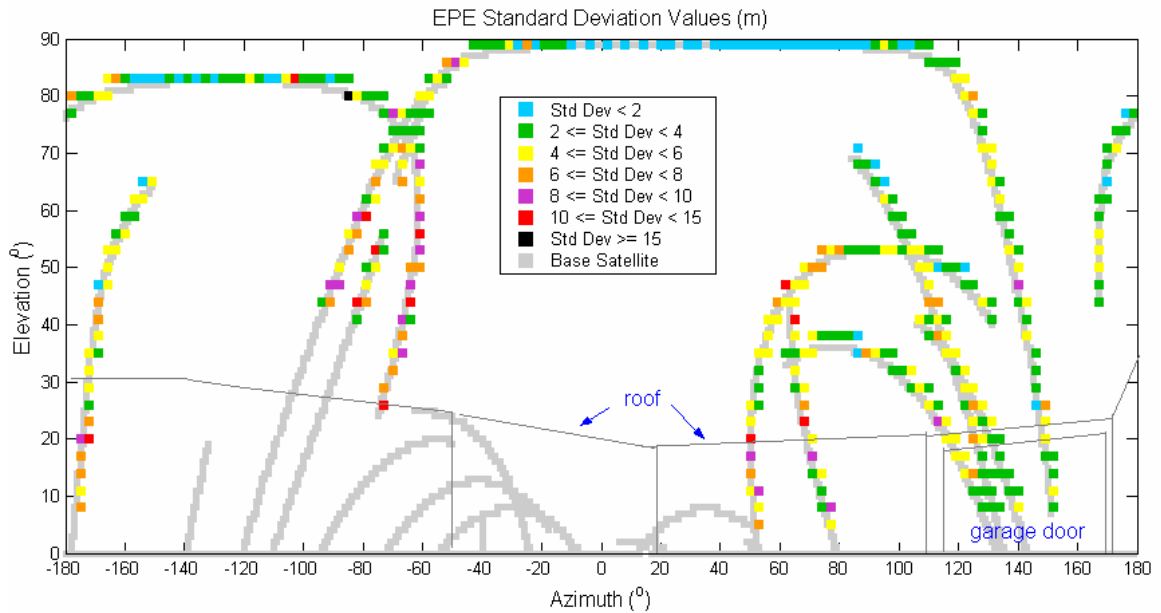
Figure 6.10: EPE Means of 3˚x3˚ bin — garage test

Figure 6.11: EPE standard deviations of 3˚x3˚ bin — garage test

Figure 6.12 displays the distributions of the EPE measurements and the associated first and second order derivatives.   They are all centred on zero, and have symmetrical characteristics.   More than 90% of the EPEs were between -10 m and +10 m.   Ninety seven percent of the first order derivatives fluctuated within a range of ±5 m/s.   The PDF of the horizontal position errors is shown in Figure 6.13.   More than 90% of the position errors were smaller than 20 m, a level congruent with the EPEs.
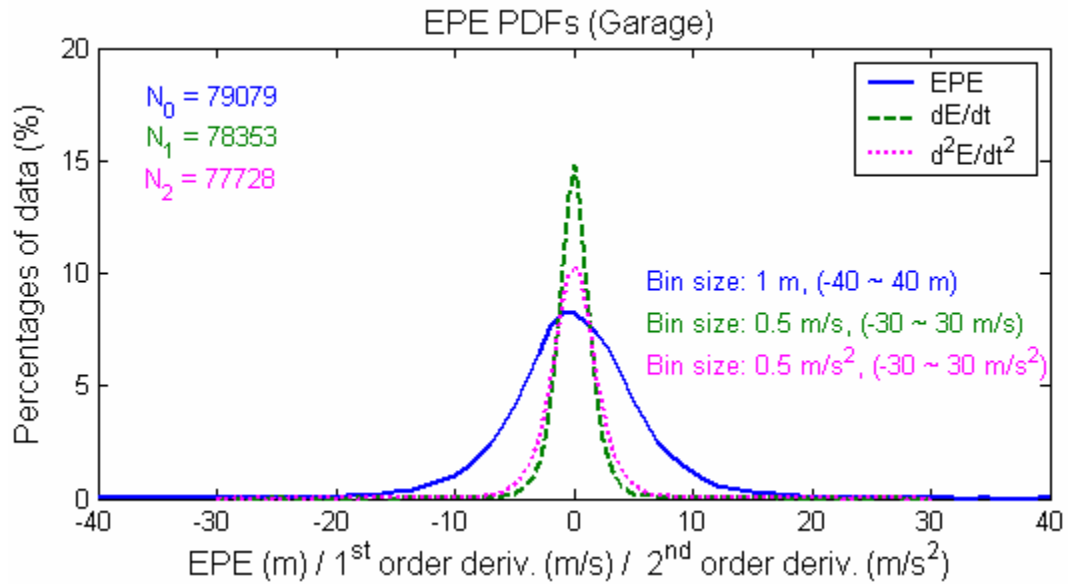
Figure 6.12: PDFs of EPE and associated 1st & 2nd order derivatives — garage test
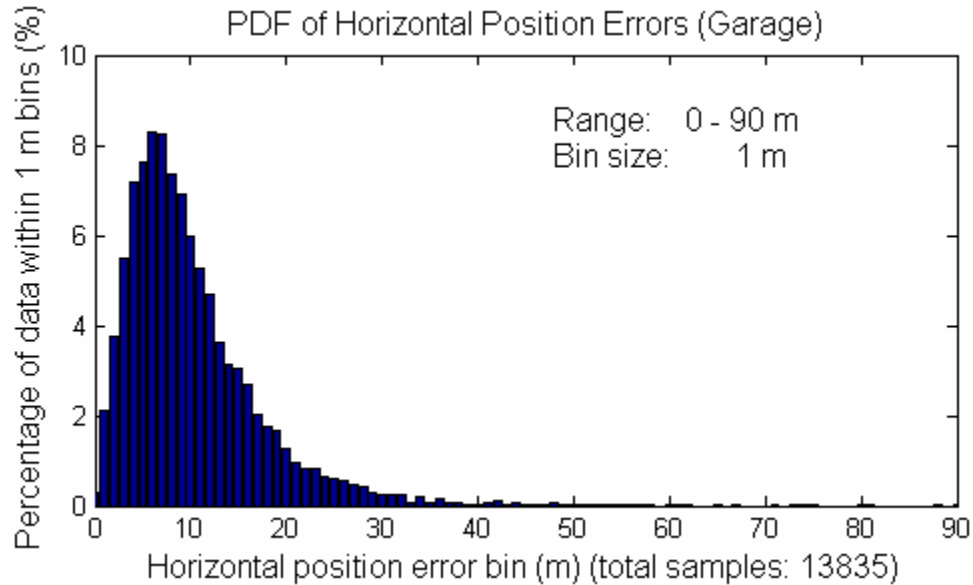

Figure 6.13: PDF of horizontal position errors — garage test

Figure 6.14 displays the EPEs of PRN 23. These EPEs fluctuate about the zero level. Compared to the fading of PRN 23 (see Figure 6.8), the EPEs are noisier

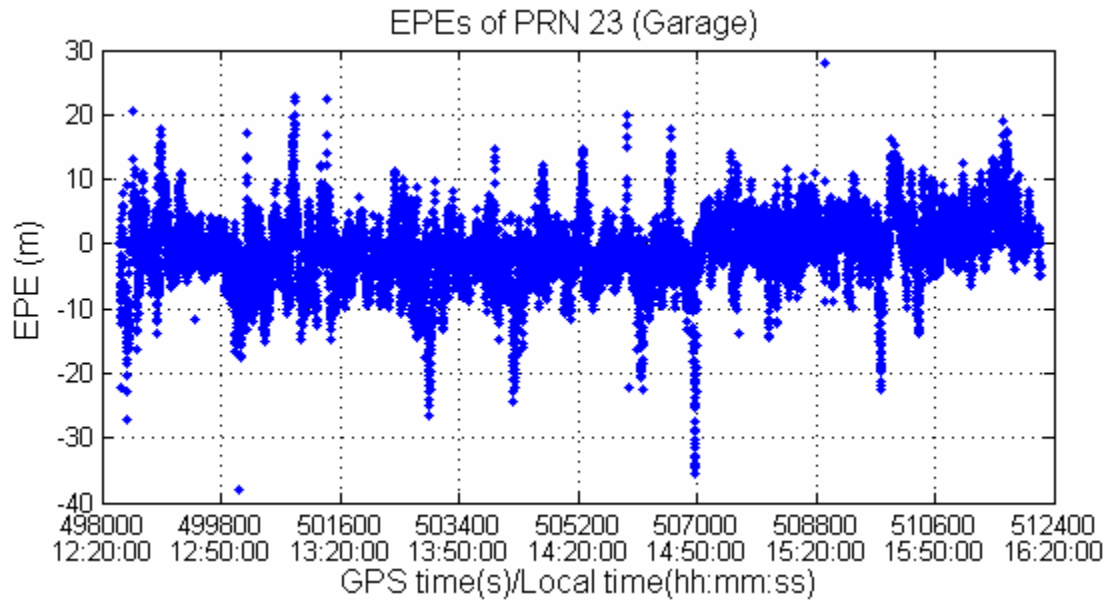and contain higher frequency components.

Figure 6.14: EPEs of PRN 23 in garage test

In the EPE PSD analysis, the mean of EPEs is also removed.   As shown in Figure

6.15, the distribution of the EPE PSD for PRN 23 contains higher frequency

components (up to 0.10 Hz) than does the fading.   About 50% of the frequency

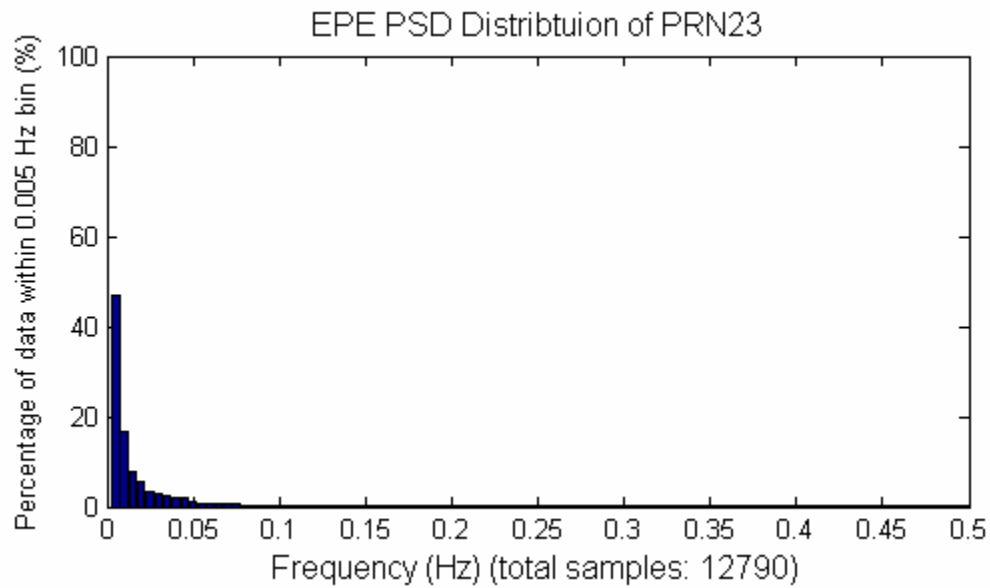components are also smaller than or equal to 0.005 Hz.

Figure 6.15: EPE PSD distribution of PRN 23 in garage test

6.1.5 Simulation Results

6.1.5.1 Simulation Setup

A 40-minute period was chosen for simulation. The six satellites chosen are shown in Figure 6.16, with circles indicating the starting points of their trajectories. The parameters discussed in the following are the final best parameter set after several trial-and-error experiments. During the test period, the attenuation of each satellite signal was at the same level. All LOS signals were attenuated by 15 dB. The multipath mean power levels were set to around -10 dB with respect to the LOS strength. The MNED was set to 50 ns, corresponding to a 15 m maximum delay.
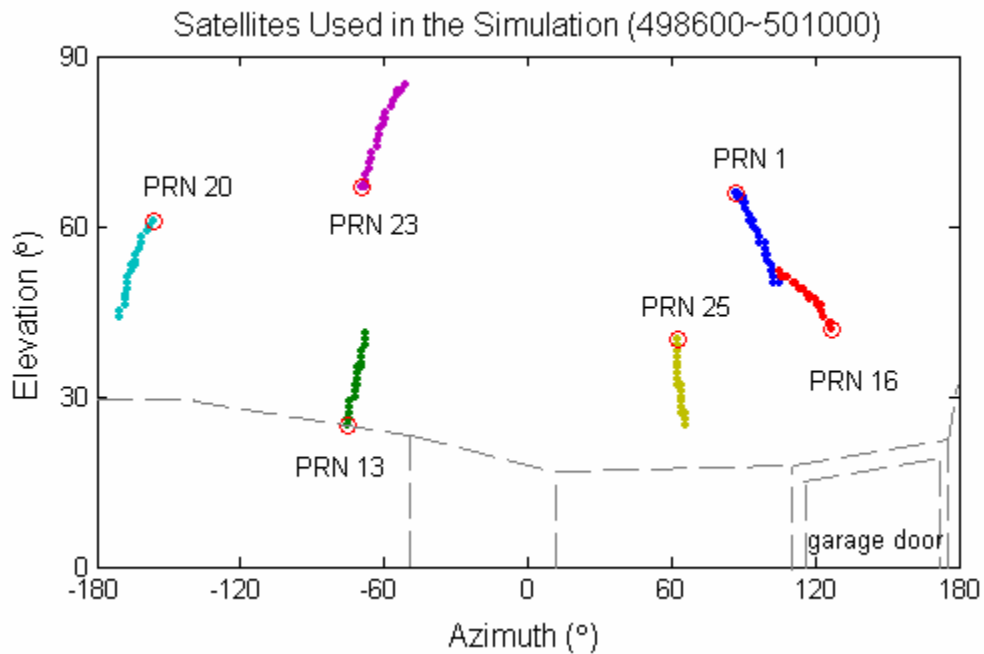
Figure 6.16: Satellites chosen for simulation — garage test

6.1.5.2 Satellite Availability

The satellite availability over the simulation time is shown in Figure 6.17 for both field and simulated data. Figure 6.18 displays the probability distribution of number of satellites tracked. Under the test conditions, the chosen receivers were capable of tracking five or six satellites in both the field test and the simulation. The simulated signals show a slightly better performance.   This may be due to the stronger destructive multipath interference or attenuation in the field test. Nevertheless, the value of the correlation coefficient, 0.936, indicates a relatively compatible level between field and simulation results.
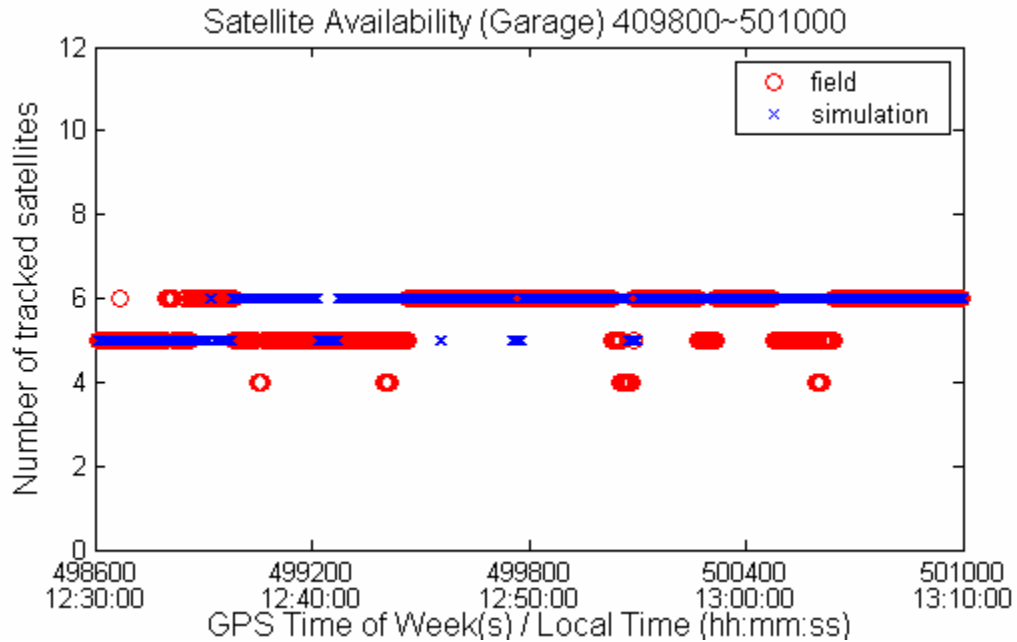
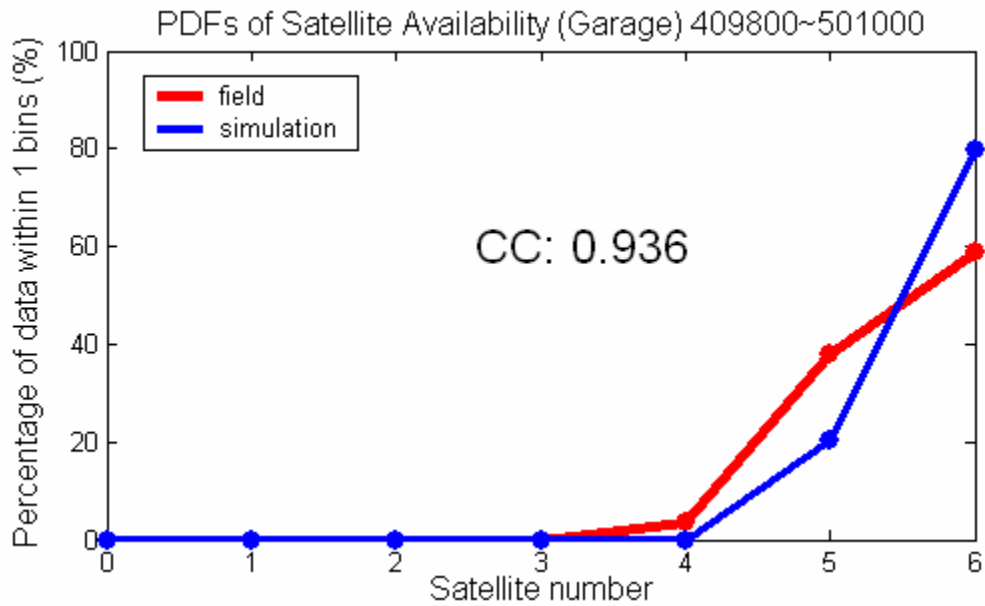**Figure 6.17: Field and simulator satellite availability — garage test**

Figure 6.18: Field and simulator PDFs of satellite availability — garage test

6.1.5.3 Fading and EPEs

The garage field test and simulation fading values are shown in Figure 6.19.

Owing to their attenuation after traveling through the garage, the field fading of each satellite displayed a fluctuation around a mean level of 15 to 20 dB, which was the original estimation of the signal attenuation for the LOS signals. The amplitude of the fluctuation was determined by the relative strength of the multipath to the LOS, whereas the frequency of the fluctuation was determined by the multipath delay change rate. The simulated fading exhibits similar characteristics to the fading measured during the test. Figure 6.20 shows the EPEs obtained in the field test and simulation. The simulated EPEs also display similar characteristics to the measured EPEs during the test.
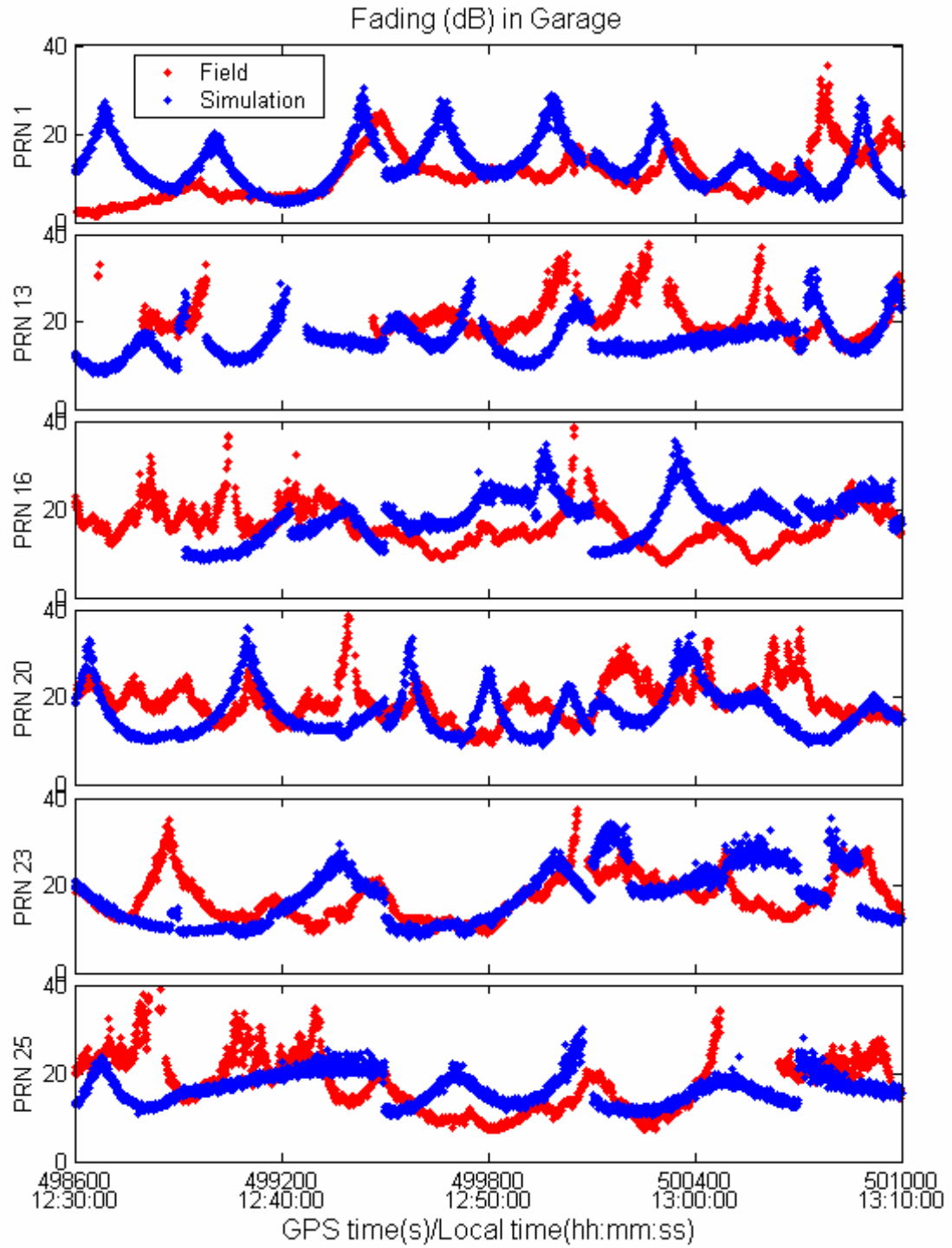
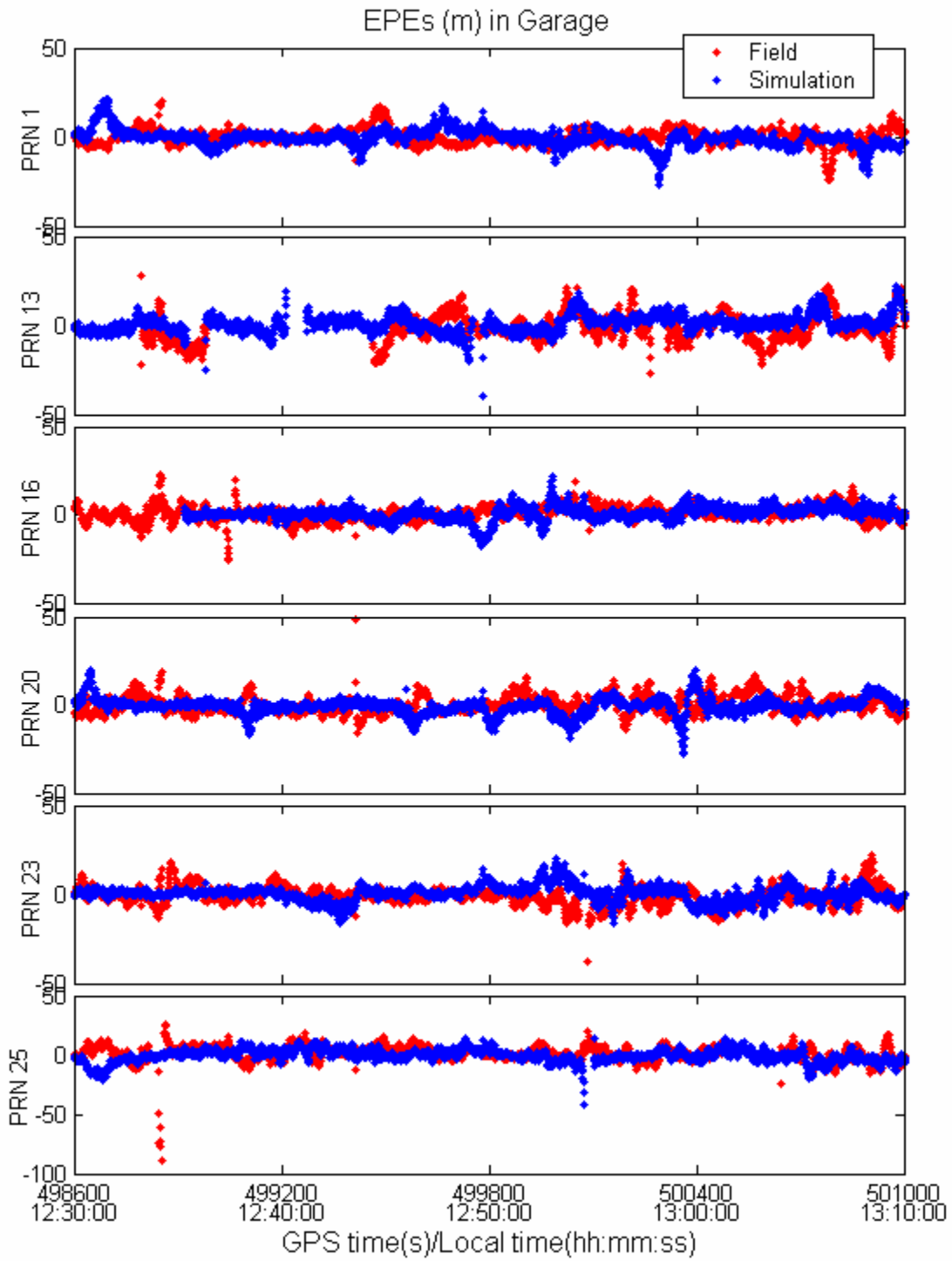**Figure 6.19: Field and simulator fading measurements — garage test**

Figure 6.20: Field and simulator EPE measurements — garage test

Figure 6.21 and Figure 6.22 provide a more detailed look at the fading and EPEs of

PRN 23. The measured and simulated fading and EPEs displayed some correlation. In-phase and 180° out-of-phase relations between the fading and EPEs could be found in both the field test and simulation. The fading fluctuated more smoothly than the EPEs, in which case EPEs had a greater proportion of high frequency components than the fading did.
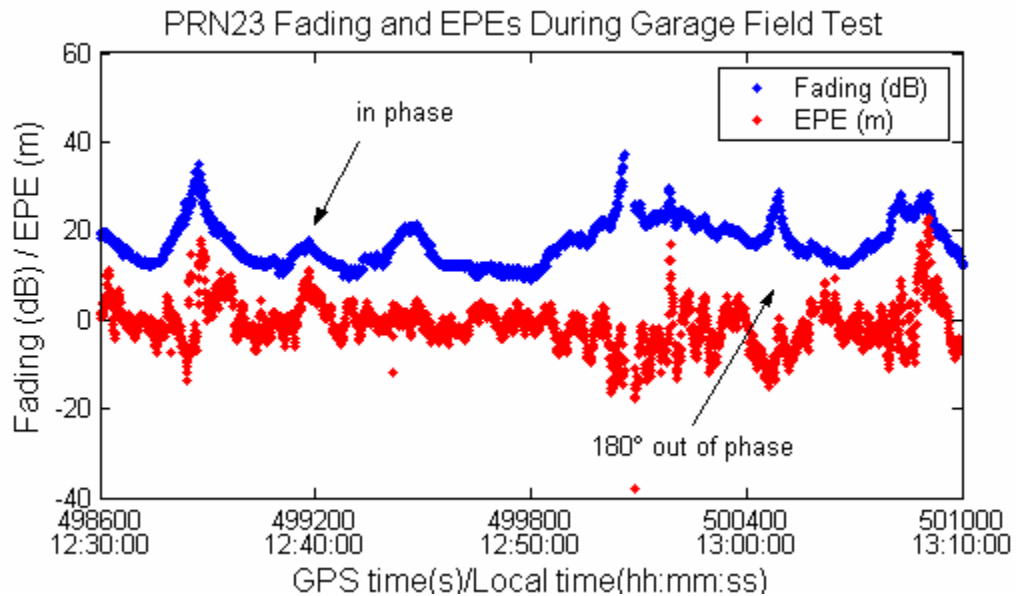

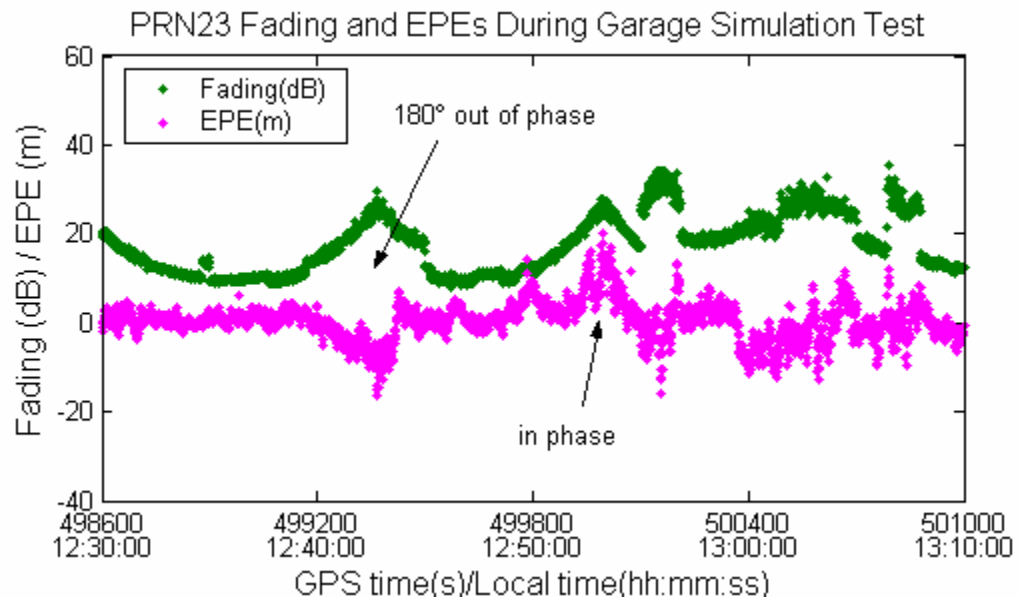**Figure 6.21: Field fading and EPE measurements of PRN 23 — garage test**

Figure 6.22: Simulator fading and EPE measurements of PRN 23 — garage test

Figure 6.23 shows the PDF of PSDs for the fading and EPE measurements. Coinciding with the discussion about the frequency of fluctuations above, the EPEs contain more high frequency components than the fading does. The simulation replicated this characteristic very well.
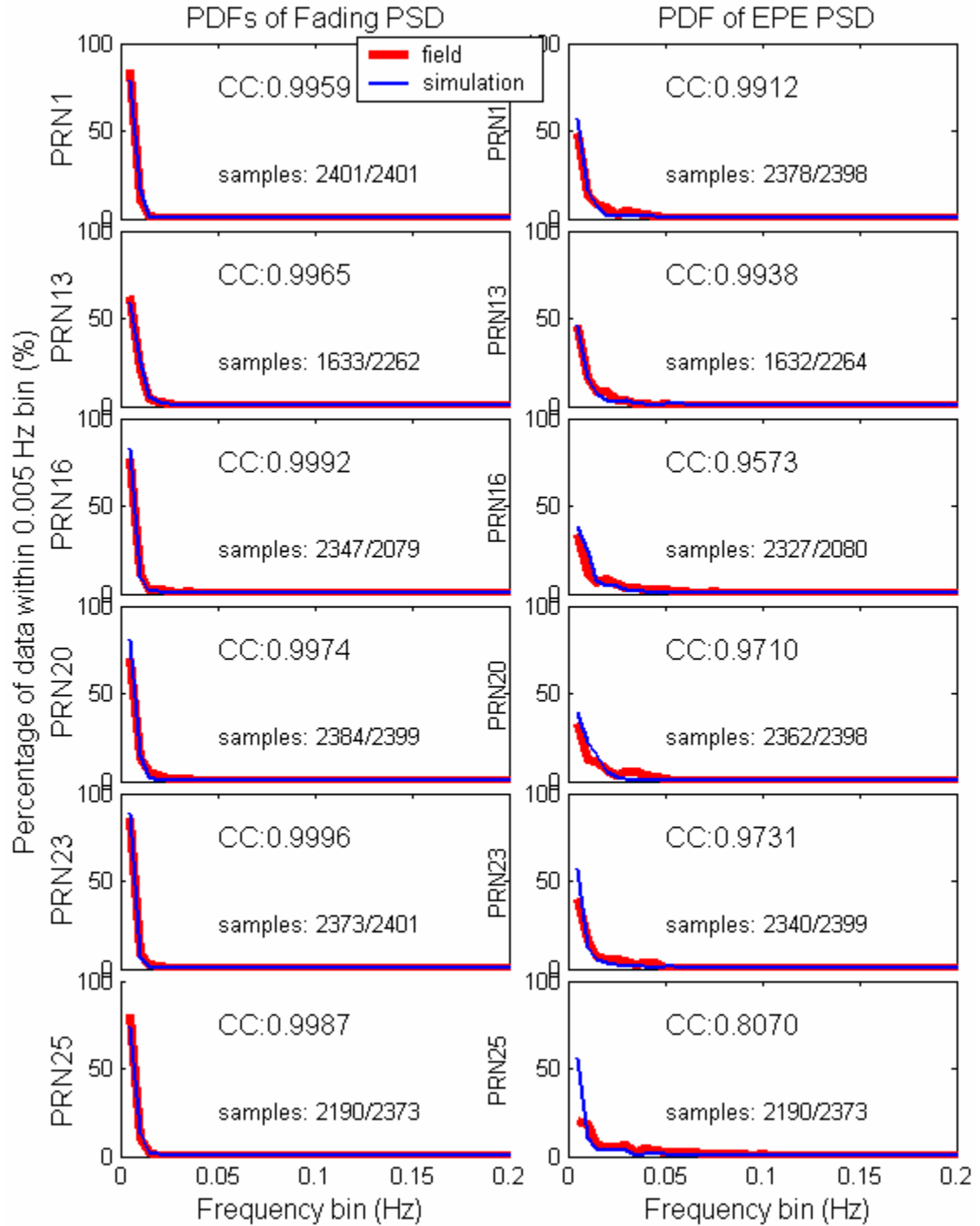
Figure 6.23: Field and simulator PDFs of fading and EPE PSDs — garage test

Figure 6.24 shows the fading and its first and second order derivative PDFs in the

field test and simulation.   The simulated fading results displayed a high correlation with field results.   The high correlation could also be found for EPEs, as shown in Figure 6.25.   However, the PDF curve of the field EPEs exhibits more dispersed spread than that of the simulated EPEs.   This may be the result of the limited number of simulated multipath signals, as discussed in Section 5.3.4.   More dispersed EPEs would be expected to produce a great number of dispersed position errors.
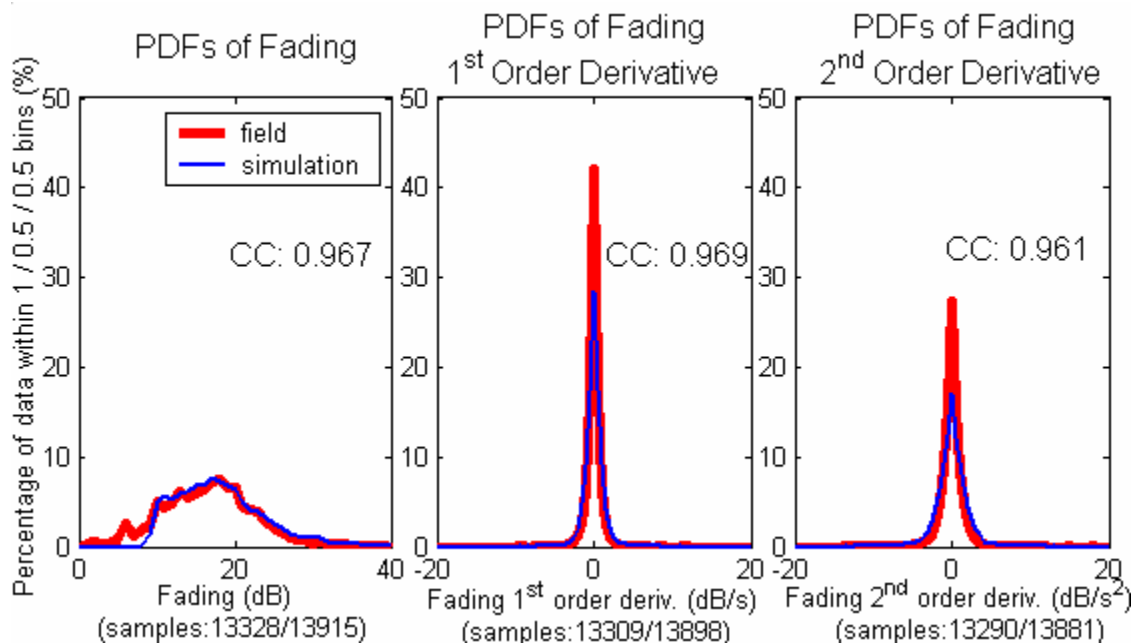

Figure 6.24: PDFs of fading and associated 1st & 2nd order derivatives in the field test and simulation — garage test
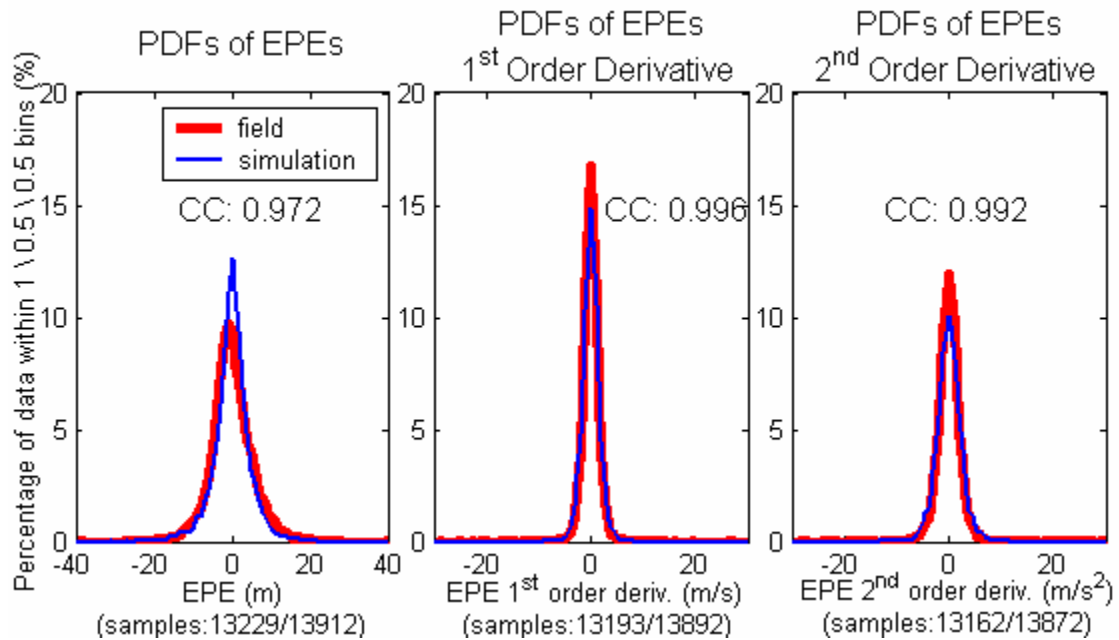
Figure 6.25: PDFs of EPE and associated 1st & 2nd order derivatives in field test and simulation — garage test

6.1.5.4 Positioning Accuracy and HDOP

The horizontal position errors for the garage test and its simulation are shown in Figure 6.26.   The position errors obtained in the field test are larger than those in the simulation.   The position error PDF, as shown in Figure 6.27, also shows the same situation, which coincides with the presence of larger EPEs in the field data set.   Figure 6.28 and Figure 6.29 show the HDOPs and HDOP PDF, respectively. Although there is a good degree of consistency between the field and simulation results, there are a few larger HDOPs in the field test.   This is also a reason for the larger position errors in the field test.
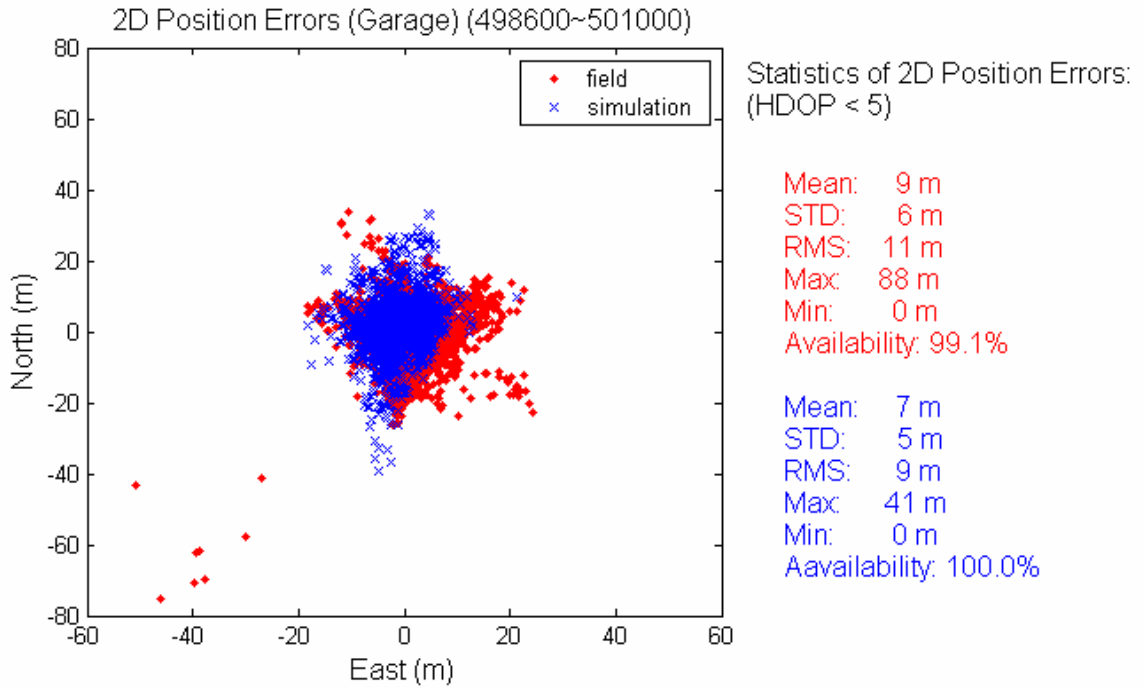
Figure 6.26: Field and simulator horizontal position errors — garage test
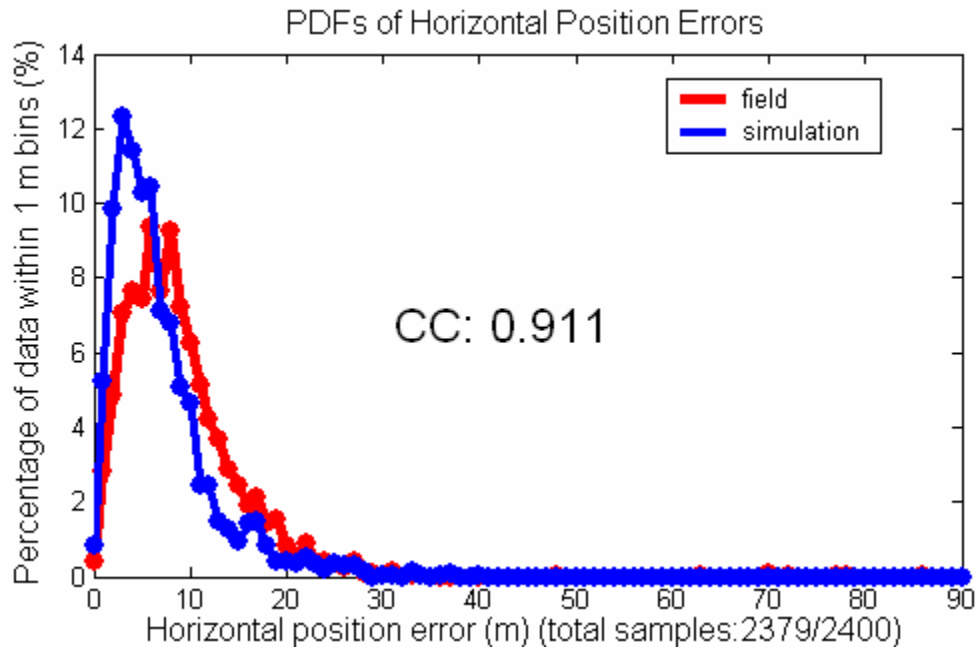

Figure 6.27: Field and simulator PDFs of horizontal position errors — garage test
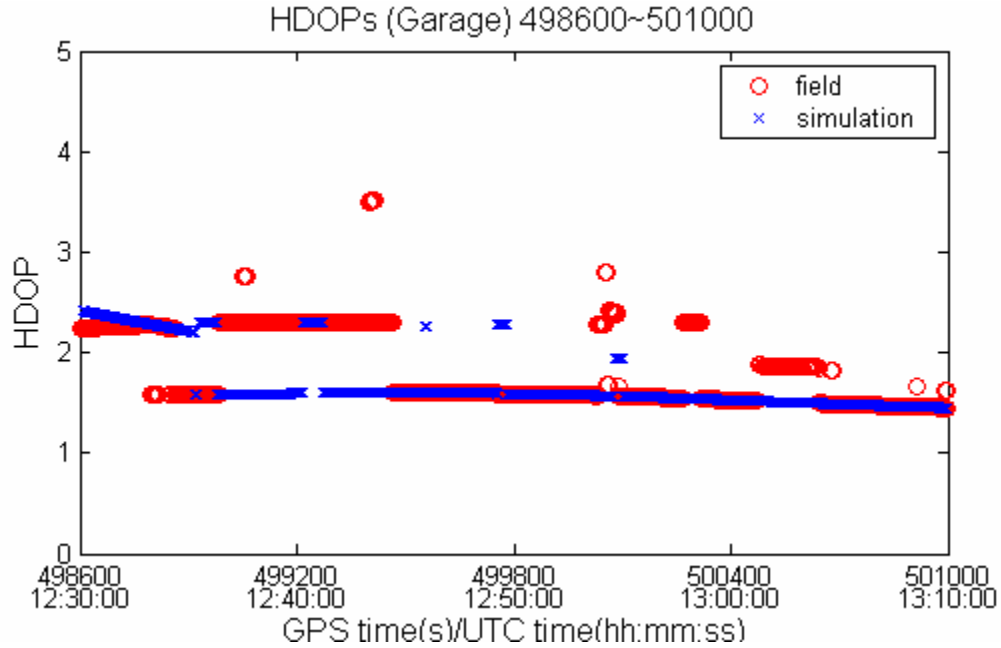
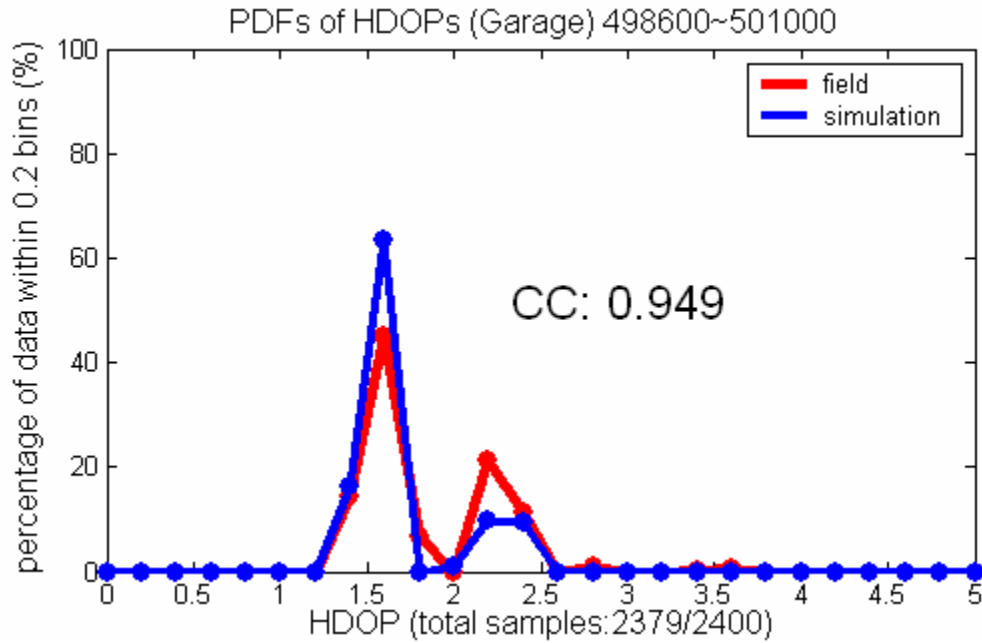**Figure 6.28: Field and simulator HDOPs — garage test**

Figure 6.29: Field and simulator PDFs of HDOPs — garage test

Table 6.1 gives the overall correlation coefficients for the field and simulation data.

All but one of the correlation coefficients are more than 0.9, indicating a relatively

strong match between the field and simulated data.

Table 6.1: Garage field test and simulation correlation coefficients

Items		Correlation Coefficients	
		Fading	**EPE**
(.) (bin size: 1 dB, 1 m)		0.967	0.972
d(.)/dt (bin size: 0.5 dB, 0.5 m)		0.969	0.996
d^2(.)/dt^2 (bin size: 0.5 dB, 0.5 m)		0.961	0.992
Power Spectral Density (bin size: 0.005 Hz)	PRN 1	0.9959	0.9912
	PRN 13	0.9965	0.9938
	PRN 16	0.9992	0.9573
	PRN 20	0.9974	0.9710
	PRN 23	0.9996	0.9731
	PRN 25	0.9987	0.8070
	Average	**0.9979**	**0.9489**
Satellite Availability (bin size: 1)		0.936	
Position error (bin size: 1 m)		0.911	
HDOP (bin size: 0.2)		0.949	

6.2 High Bay

6.2.1 Field Testing Description

The "High Bay" is part of the CCIT Building located on the campus of the University

of Calgary. It is a one-floor concrete chamber with an underground pit inside.

The roof consists of a metal deck and steel structure.   The dimensions of the pit and the whole High Bay are 7 m × 13 m × 4.5 m and 16 m × 14 m × 16 m, respectively.   The GPS antenna was mounted in the underground pit.   Figure 6.30 shows the exterior and interior of the High Bay.   The field test lasted 24 hours and all doors were closed during the test.

Figure 6.30: Exterior and interior of CCIT High Bay

6.2.2 Satellite Availability

The satellite availability and its PDF are shown in Figure 6.31 and Figure 6.32.   At some epochs during testing, the receiver could only track up to three or satellites. However, at least four satellites were available 90% of the time.
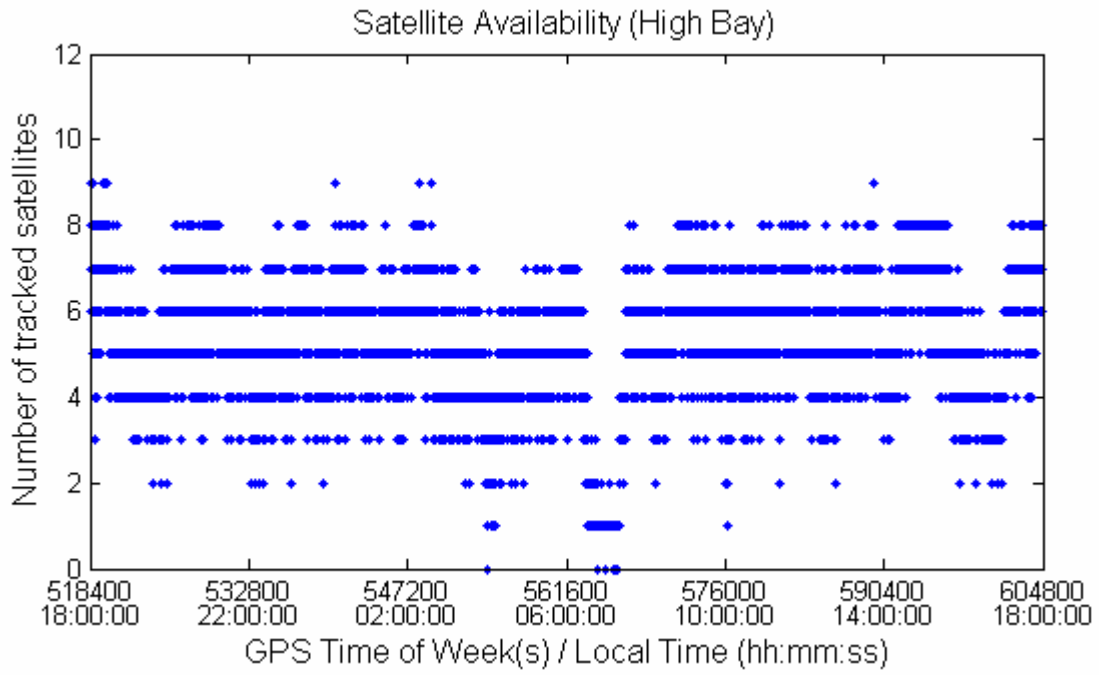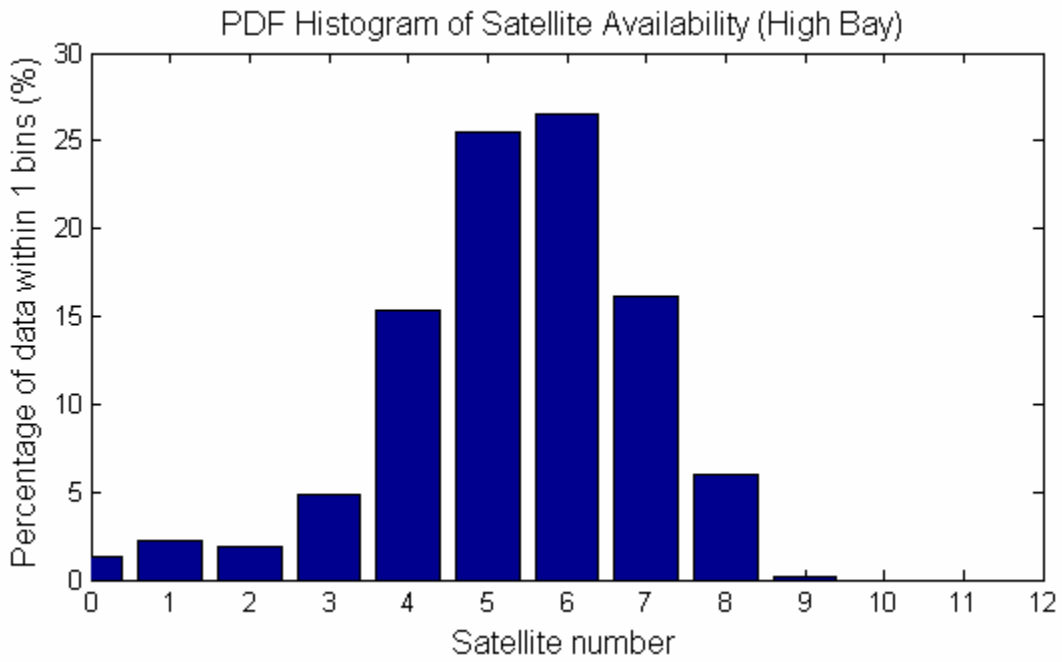
Figure 6.31: Satellite availability — High Bay test

Figure 6.32: PDF of satellite availability — High Bay test

6.2.3 Fading

Figure 6.33 and Figure 6.34 show the pierce-point analysis of the fading means and standard deviations, respectively.   The metal deck and steel structure of the roof are expected to severely attenuate the signals.   This results in signals arriving through the roof suffering heavier power attenuation than those arriving via the walls.   The relatively small standard deviations of the signals arriving from the roof indicate that the multipath signals associated with this route were relatively weak.   The small fading values (5 dB to 15 dB) appeared in areas below ground level, and the signals are not expected to contain LOS signals.
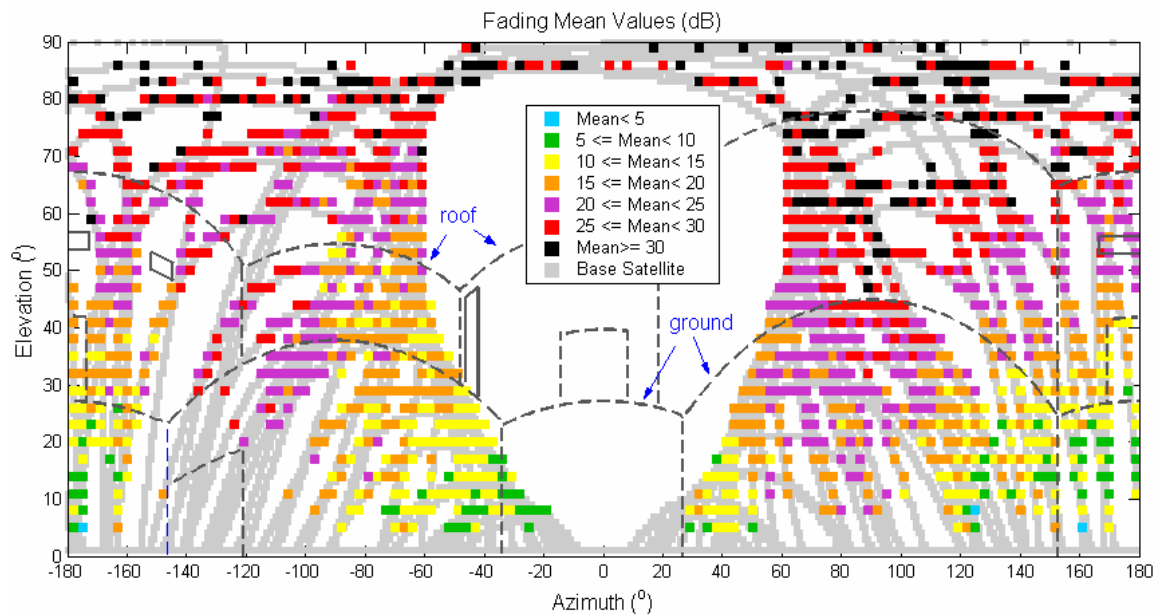

Figure 6.33: Fading means of 3˚x3˚ bin — High Bay test
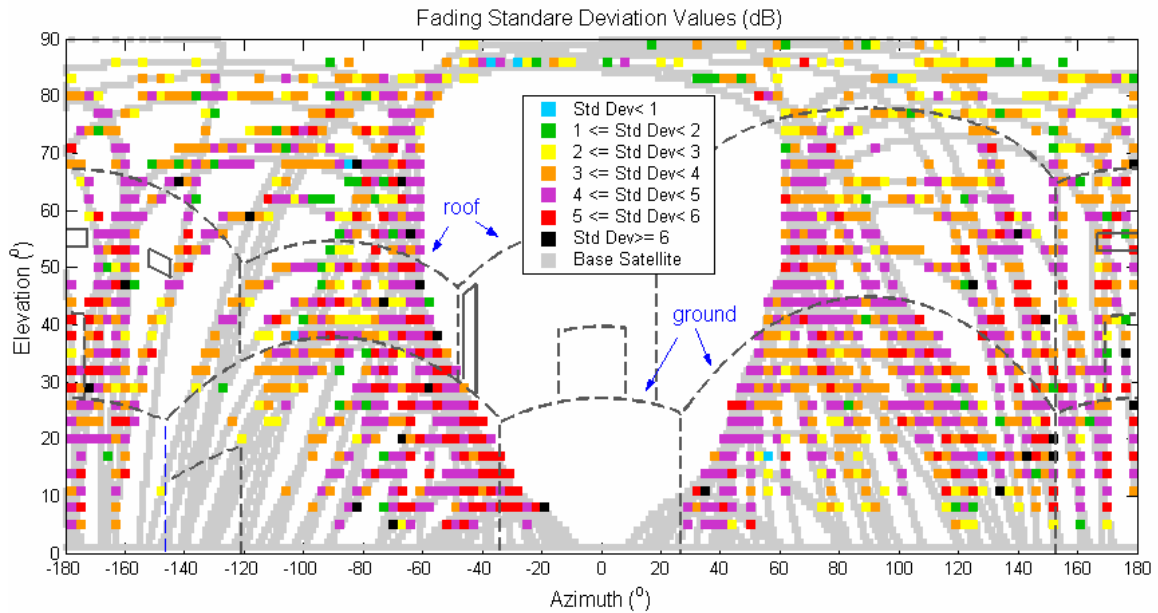
Figure 6.34: Fading standard deviations of 3˚x3˚ bin — High Bay test

Figure 6.35 depicts the overall fading PDFs, showing that the PDF of fading is centred at approximately 18 dB and 58% of the fading was in the range of 13 dB to 23 dB. There appears to be a higher degree of the fading associated with large values in the High Bay than in the garage. This indicates that the signals in the High Bay were attenuated more acutely than those received in the garage. More than 95% of the first and second order derivatives were in the range of ±5 dB/s and ±5 dB/s^2, respectively.

Figure 6.35: PDFs of fading and associated 1st & 2nd order derivatives — High Bay test

6.2.4 Estimated Pseudorange Errors

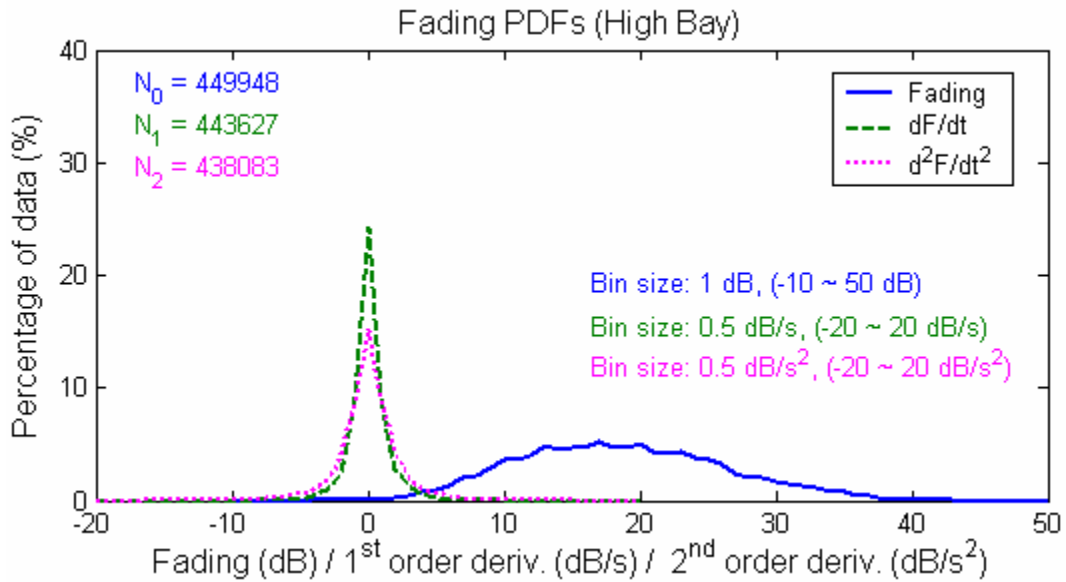Given that the dimensions of the High Bay are larger than those of the garage, it is plausible that larger code errors may result as a consequence of longer delays experienced in the High Bay. Additionally, the signal strength in the High Bay was lower than in the garage, producing an increased noise level in the pseudorange measurements and the EPEs.

Figure 6.36 and Figure 6.37 display the pierce-point analysis of the EPE means and standard deviations. Since the GPS antenna was located below ground, some of the signals originating from satellites with low elevation angles were not able to reach the antenna directly. Therefore, the signals arriving from the satellites in these areas were multipath-only signals. In the absence of LOS signals, multipath signals are capable of producing only positive code errors. The

larger blue areas (azimuths of 60° to 100° and elevations of 0° to 30°) with negative values appearing in Figure 6.36 indicate that the signals were likely restricted to multipath-only. This coincides with the assumption that the ground blocks the LOS signals arriving at low elevation angles. However, as the area is also underground, some EPE mean values in the area between azimuths of -60° to -100° and elevations of 0° to 30° are not negative. The values are closer to zero and even positive. The potential reason is that other multipath-only signals with longer multipath delay existed at the same time. Therefore, the relativity of EPE could explain this phenomenon.
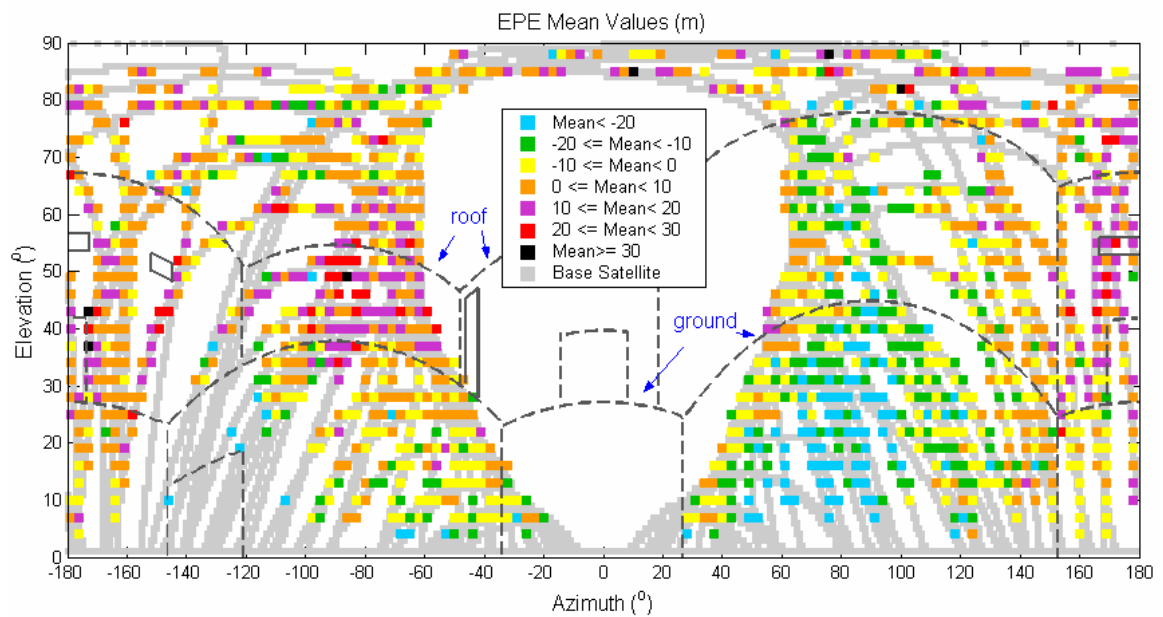
Figure 6.36: EPE means of 3˚x3˚ bin — High Bay test
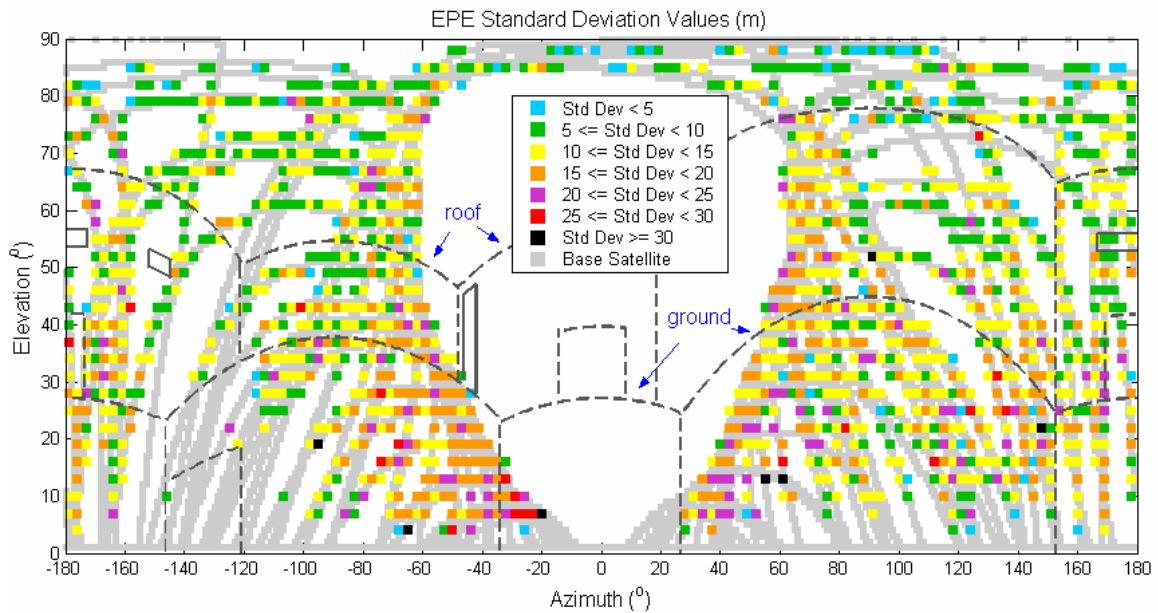
Figure 6.37: EPE standard deviations of 3°x3° bin — High Bay test

Figure 6.38 shows the overall PDFs of the EPEs and the associated first and second order derivatives.   Ninety eight percent of the EPEs are in the range of -50 m to 50 m, which obviously is larger than observed in the garage.   Consequently, the position errors will be larger in the High Bay than those observed in the garage. The position errors, which are shown in Figure 6.39, reached up to 350 m with 89% of the errors lying between 0 and 50 m.
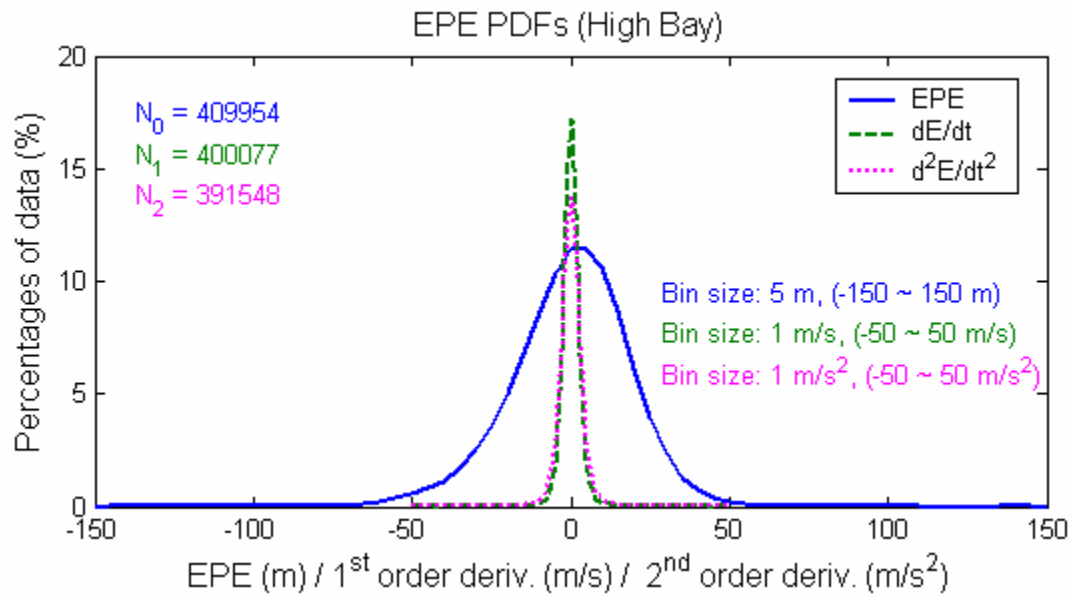
Figure 6.38: PDFs of EPE and associated 1st & 2nd order derivatives — High Bay test
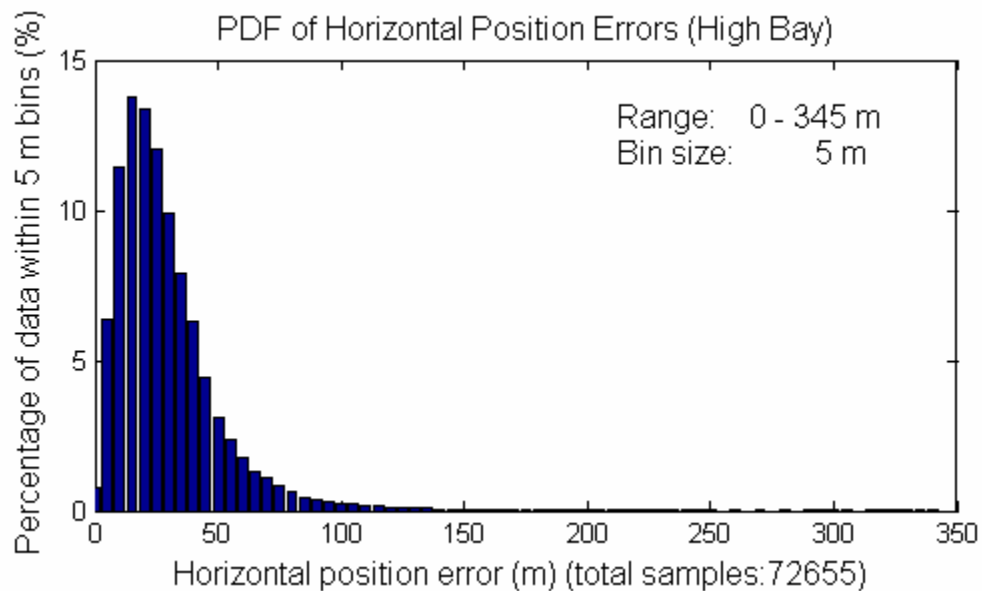
Figure 6.39: PDF of horizontal position errors — High Bay test

6.2.5 Simulation Results

6.2.5.1 Simulation Setup

A 40-minute period was chosen for the simulation.   The configuration of the six satellites chosen for the simulation is as shown in Figure 6.40.   PRN 11 was established as a multipath-only signal with all four channels set as multipath signals.   The remaining satellites were simulated as compound signals, composed of one LOS and three multipath signals.   The LOS signals were attenuated by 20.5 dB.   The multipath mean power was set to around -6.5 dB with respect to the LOS signal power strength.   The MNED was set to 200 ns, corresponding to a 60 m maximum delay.   The LMM method was used to create multipath signals for this simulation.
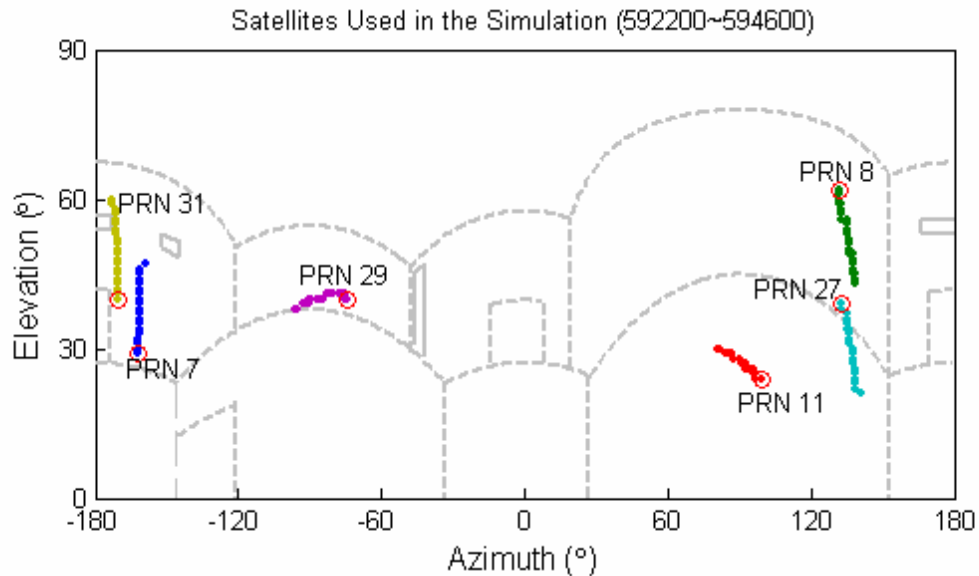
Figure 6.40: Satellites chosen for simulation — High Bay test

6.2.5.2 Satellite Availability

The availability of satellites and the PDF of the number of available satellites are shown in Figure 6.41 and Figure 6.42. At least four satellites could be tracked 100% of the time during the simulation, whereas the same number was available only 97% of the time in the field test. Although the result of the simulation displayed a slightly better tracking performance than that of the field test, the value of the correlation coefficient is 0.911, showing a compatible level of tracking performance.

Figure 6.41: Field and simulator satellite availability — High Bay test
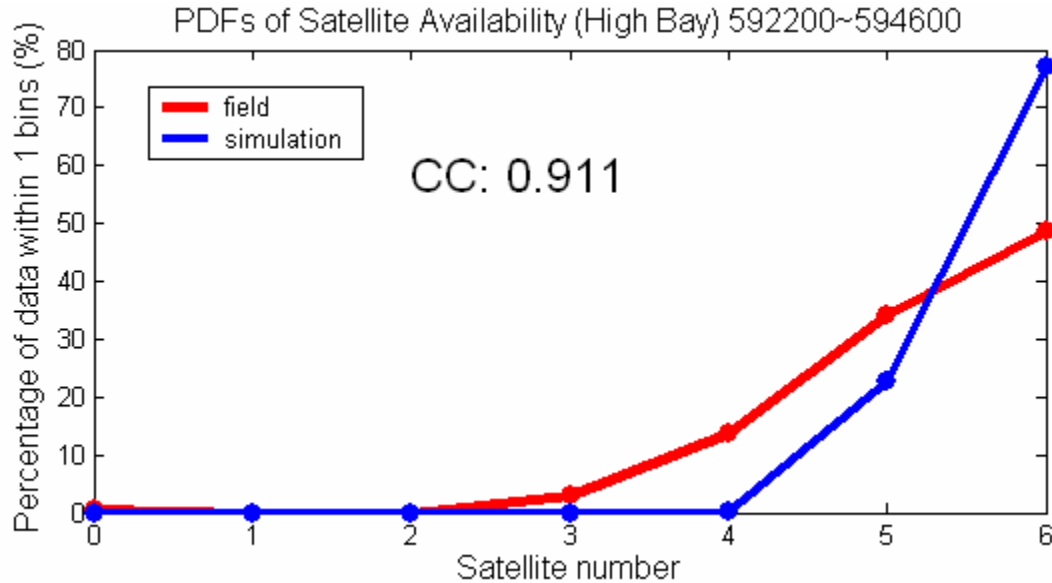
Figure 6.42: Field and simulator satellite availability PDFs — High Bay test

6.2.5.3 Fading and EPEs

The fading for both the field test and the simulation is shown in Figure 6.43, where it can be observed that simulation fading is characterized by a higher frequency change rate than that of the corresponding garage case. In addition, the signal attenuation is obviously higher than that observed during the garage test. The fading of each satellite fluctuates around a level centred between 20 dB and 25 dB, which was taken as the original estimate of the LOS attenuation in the simulation. The fluctuation of PRN 31 is obviously faster in the simulated data than in the field data. This would result in a low correlation value in the PSD distribution. Due to the fact that the multipath delay is randomly created by the simulator, the multipath delay change rate of the simulated data may be somewhat different from the field data. A larger MNED would introduce a larger range of the distance between the receiver antenna and the reflector. For a given satellite, the larger the distance

between the antenna and the reflector, the larger the delay and delay change rate (see Equation 5.9).   Therefore, a larger MNED introduces more chances that the randomly created delay and delay change rate are different from the field data.

The EPEs for each satellite are shown in Figure 6.44.   The EPE values are also significantly larger than those observed in the garage test.   The field EPEs of PRN 11 fluctuate around a negative value of -10 m, which was taken as the basic delay for this satellite in the simulation.   Since PRN 11 was set to a multipath-only signal, its EPEs fluctuate about -10 m.   The simulated data displays similar characteristics to the field data in terms of amplitude and fluctuation frequency.
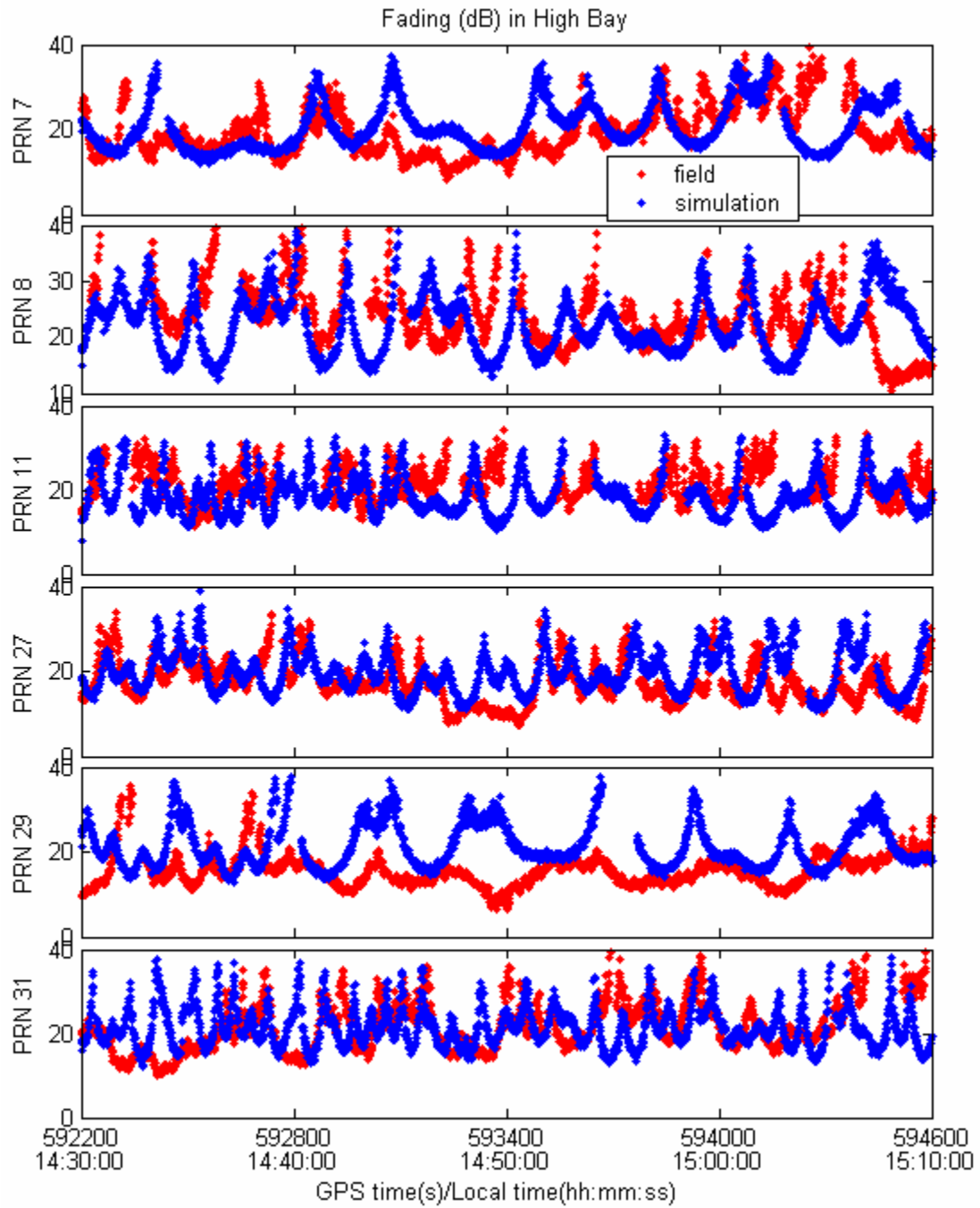
Figure 6.43: Field and simulator Fading measurements — High Bay test
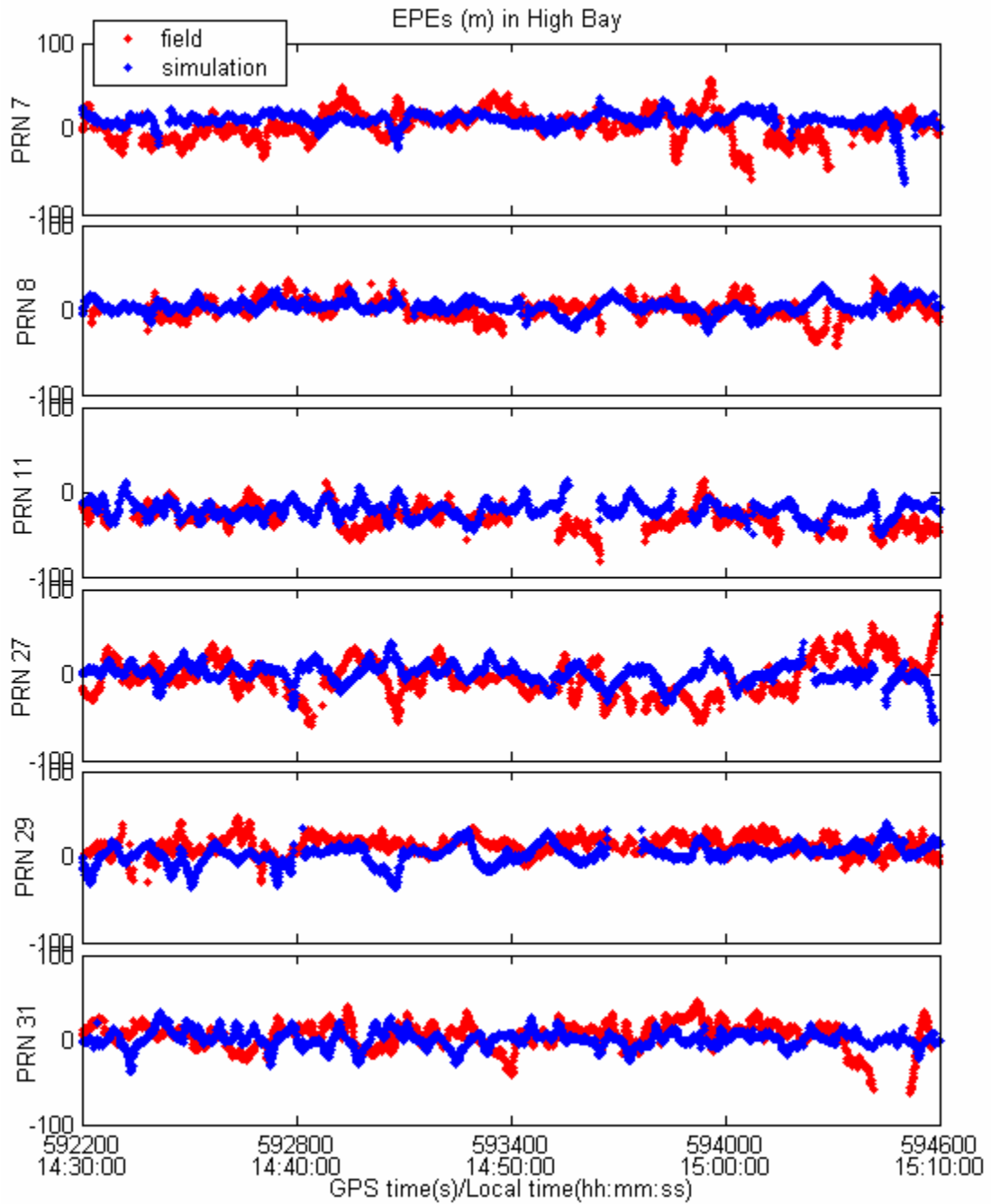
Figure 6.44: Field and simulator EPE measurements — High Bay test

Figure 6.45 shows the fading and its first and second order derivative PDFs for the

field test and simulation.   The correlation between the two sets of results is high.

A high correlation can also be found for the EPEs, as shown in Figure 6.46. However, in the case of the field test, the PDFs are somewhat more dispersed than those observed during the simulation. A greater numbers of the EPEs exist around 0 m during the simulation.
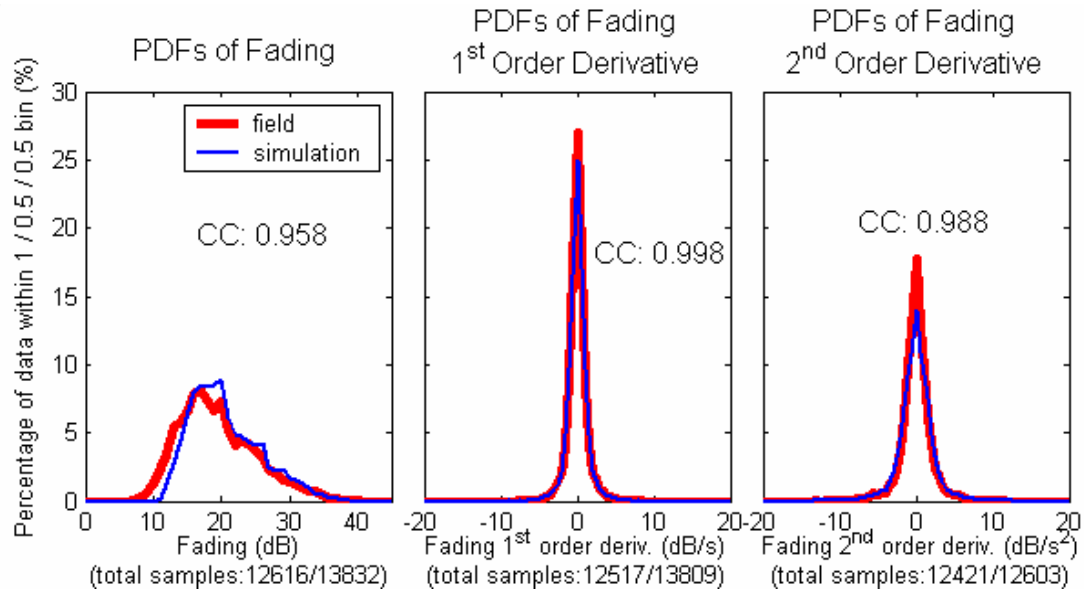

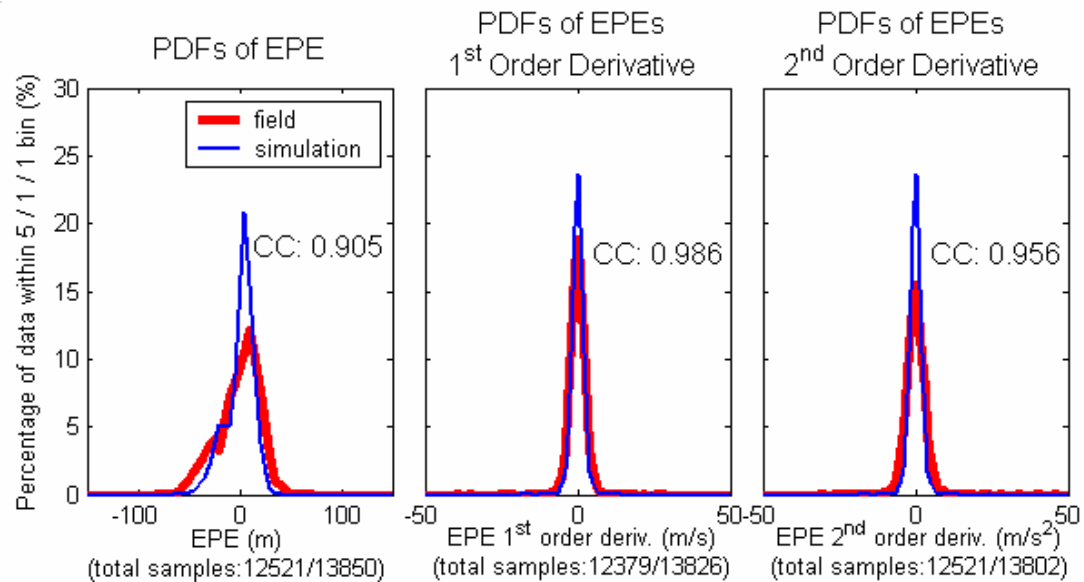**Figure 6.45: PDFs of fading and associated 1st & 2nd order derivatives — High Bay test**

Figure 6.46: PDFs of EPE and associated 1st & 2nd order derivatives — High Bay test

6.2.5.4 Positioning Accuracy and HDOP

The horizontal position errors are shown in Figure 6.47. Similar to the garage case, errors are characterized by greater dispersion in the field test. Ninety six percent of the errors were less than 50 m in the simulated results, whereas only 84% of field test results were as accurate. The horizontal position error PDF is shown in Figure 6.48.   There are a greater number of large errors during the field test. Figure 6.49 and Figure 6.50 show HDOPs and the associated PDF. A greater number of large HDOPs (>3) were observed during the field test. These larger values result in a greater number of large position errors.
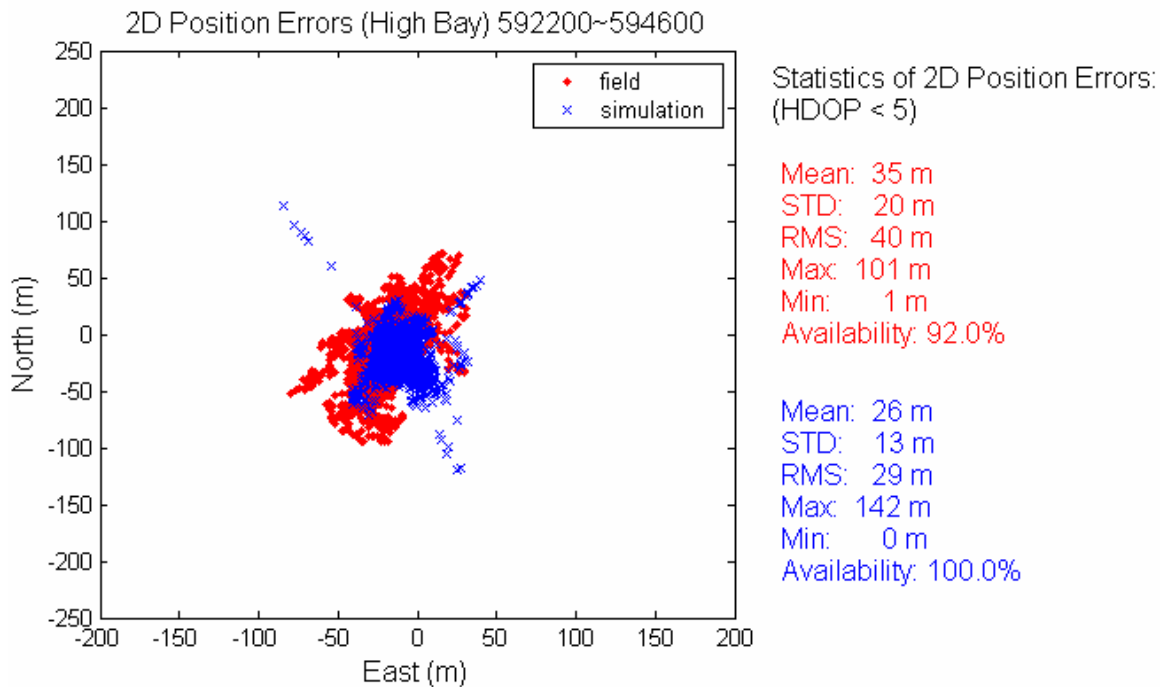
Figure 6.47: Field and simulator horizontal position errors — High Bay test
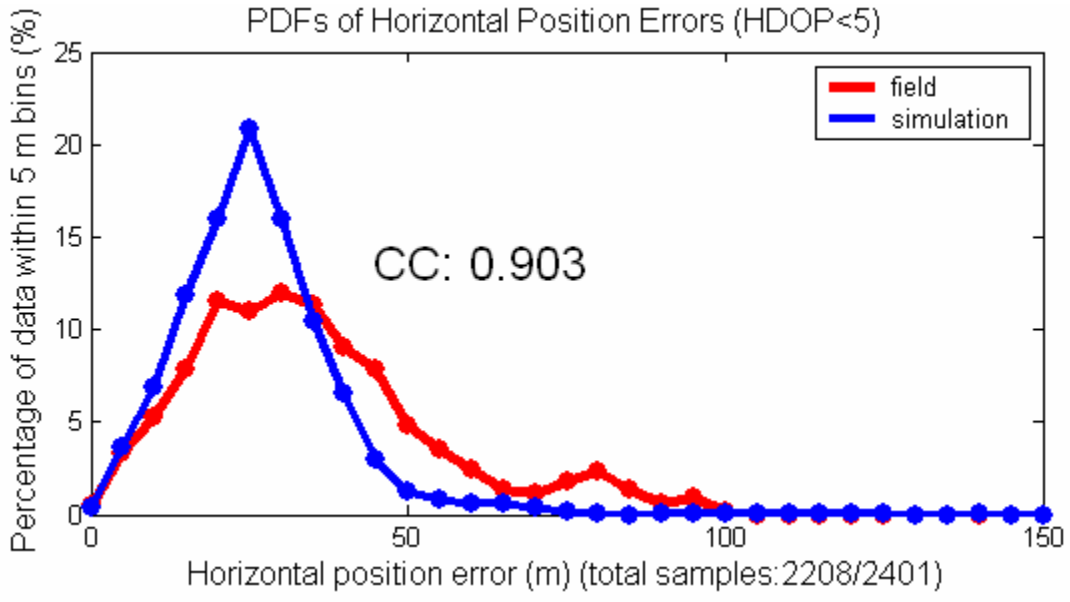
Figure 6.48: Field and simulator horizontal position error PDFs — High Bay test

Figure 6.49: Field and simulator HDOPs — High Bay test

Figure 6.50: Field and simulator HDOP PDFs — High Bay test

Table 6.2 gives the overall correlation coefficients of the field test and simulation. The statistical level of compatibility is relatively high. Compared to the results obtained for the garage, the EPE correlation coefficients are smaller, resulting in smaller position error correlation coefficients.

Table 6.2: High Bay field test and simulation correlation coefficients

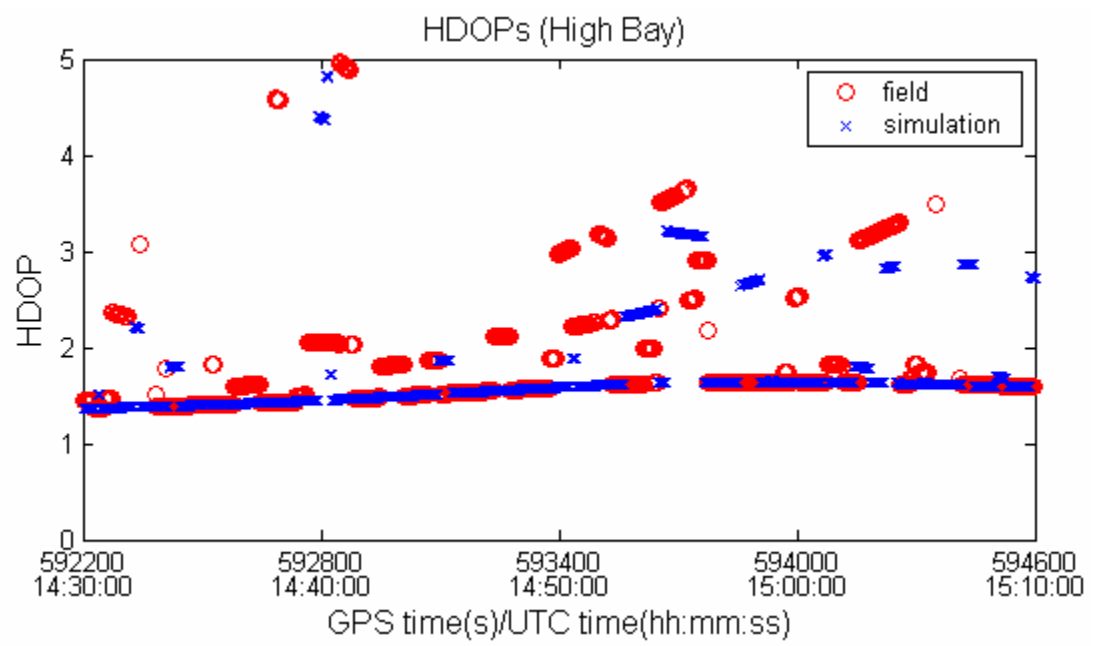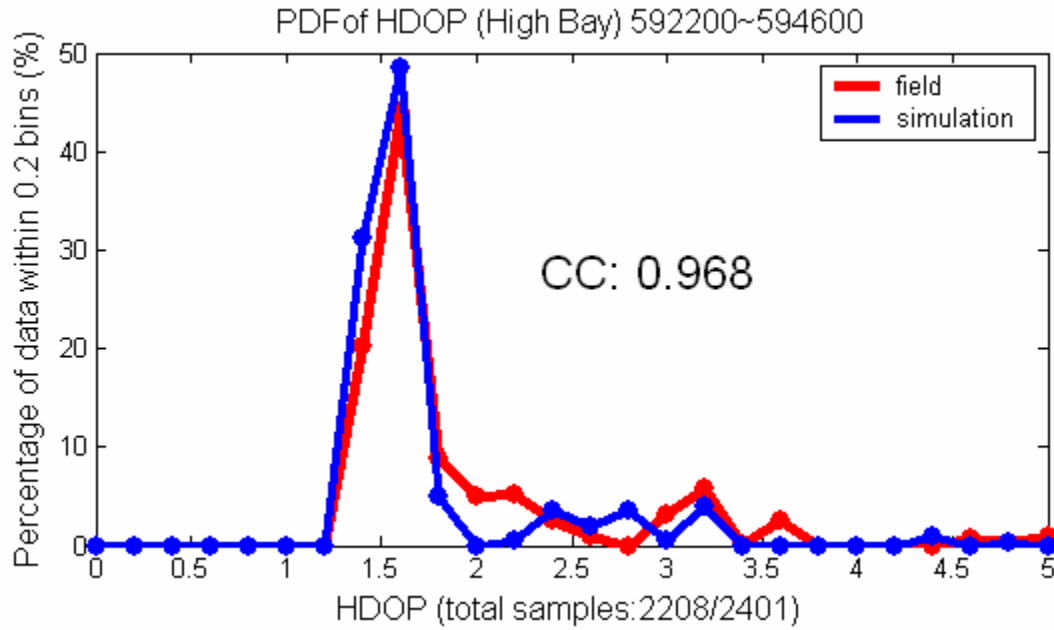| Items		Correlation Coefficients	
		Fading	**EPE**
(.) (bin size: 1 dB, 5 m)		0.958	0.905
d(.)/dt (bin size: 0.5 dB, 1 m)		0.998	0.986
d^2(.)/dt^2 (bin size: 0.5 dB, 1 m)		0.988	0.956
Power Spectral Density (bin size: 0.005 Hz)	PRN 7	0.9844	0.9185
	PRN 8	0.9357	0.9959
	PRN 11	0.8829	0.6610
	PRN 27	0.6983	0.7303
	PRN 29	0.9671	0.9852
	PRN 31	0.3347	0.8919
	Average	**0.8005**	**0.8638**
Satellite Availability (bin size: 1)		0.911	
Position Error (bin size: 1 m)		0.903	
HDOP (bin size: 0.2)		0.968	

6.3 Olympic Oval

6.3.1 Field Testing Description

The Olympic Oval, a covered speed skating arena on the University of Calgary campus, is one of the largest sport concrete frame structures in the world.   The dimensions of the structure are approximately 200 m × 80 m × 20 m.   The arch

roof structure of the Olympic Oval (Oval), with an unsupported span, is composed of three layers: metal cladding, insulation, and a waterproof membrane, all of which are covered by porcelain panels.   Figure 6.51 shows its exterior and interior. The antenna was located on the ground of the running track.   Ten hours of data were collected inside the Oval.

Figure 6.51: Exterior[*] and interior Oval environment

(*: from http://www.groupsci.com/images/Oval%20areal%20complete.jpg)

6.3.2 Satellite Availability

The satellite availability and the associated PDF are shown in Figure 6.52 and Figure 6.53.   In terms of satellite availability, the interior space exhibits poor performance as a receiving environment.   Strong signal attenuation was produced by the metal clad roof.   During 30% of the test duration, the receiver could track only three or fewer satellites at any given epoch.   This will result in a poor availability in position solutions.
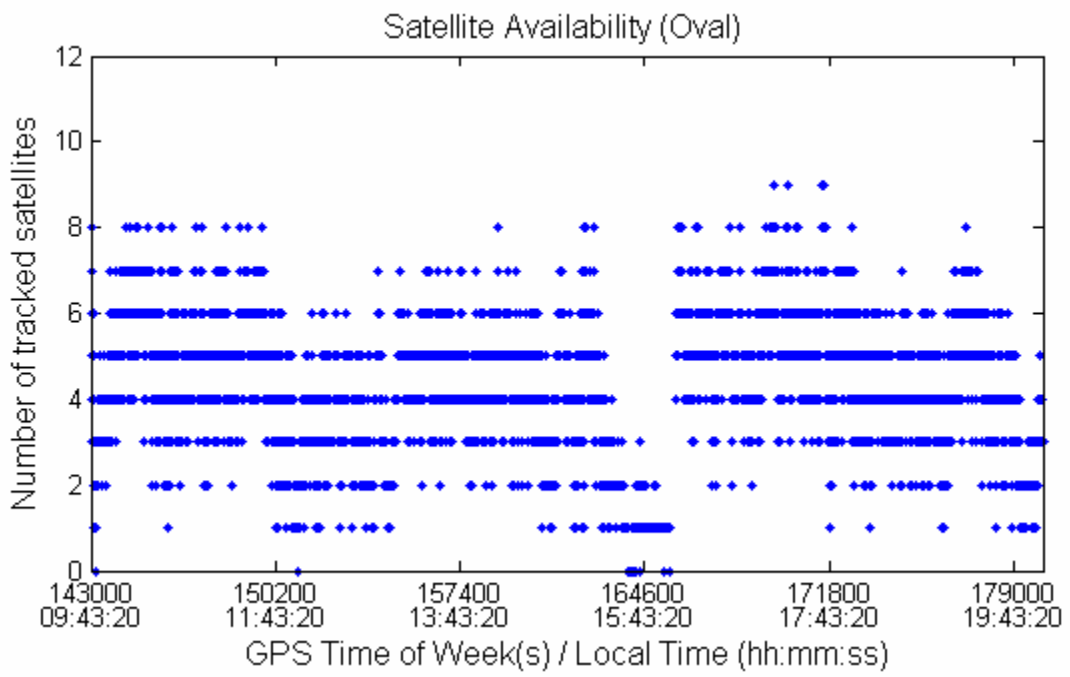
Figure 6.52: Satellite availability — Oval test
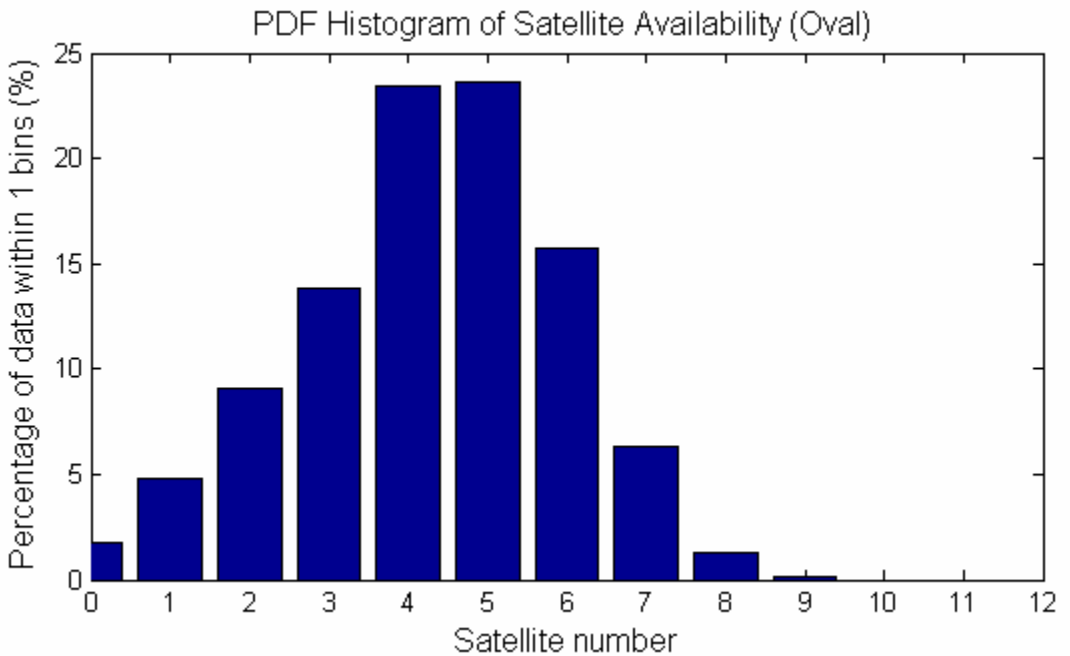
Figure 6.53: PDF of satellite availability — Oval test

6.3.3 Fading

Figure 6.54 and Figure 6.55 show the pierce-point analysis of the fading means and standard deviations. These figures support the hypothesis that the metal clad roof heavily attenuated the satellite signals and obstructed most of the signals from the zenith. Some small fading mean values could be observed to the west (azimuths of -120° to -100°; elevations of 0° to 10°), where there is a large overhead door used by vehicles to access the inside of the Oval. The door of the entrance was sometimes opened during the test, and LOS signals were able to reach the GPS antenna.
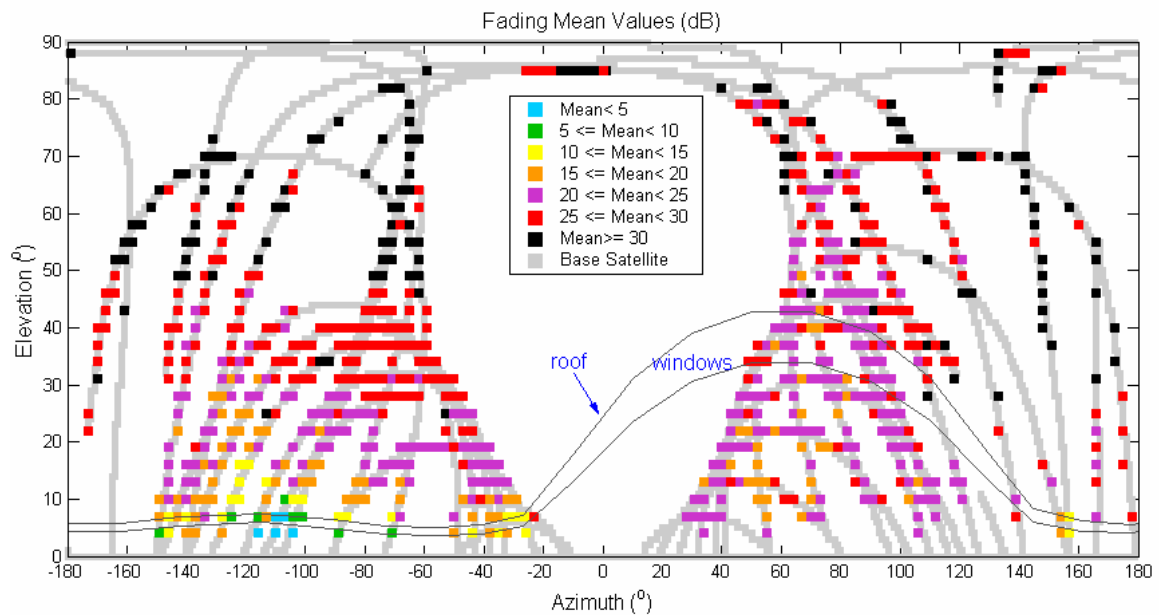
Figure 6.54: Fading means of 3˚x3˚ bin — Oval test
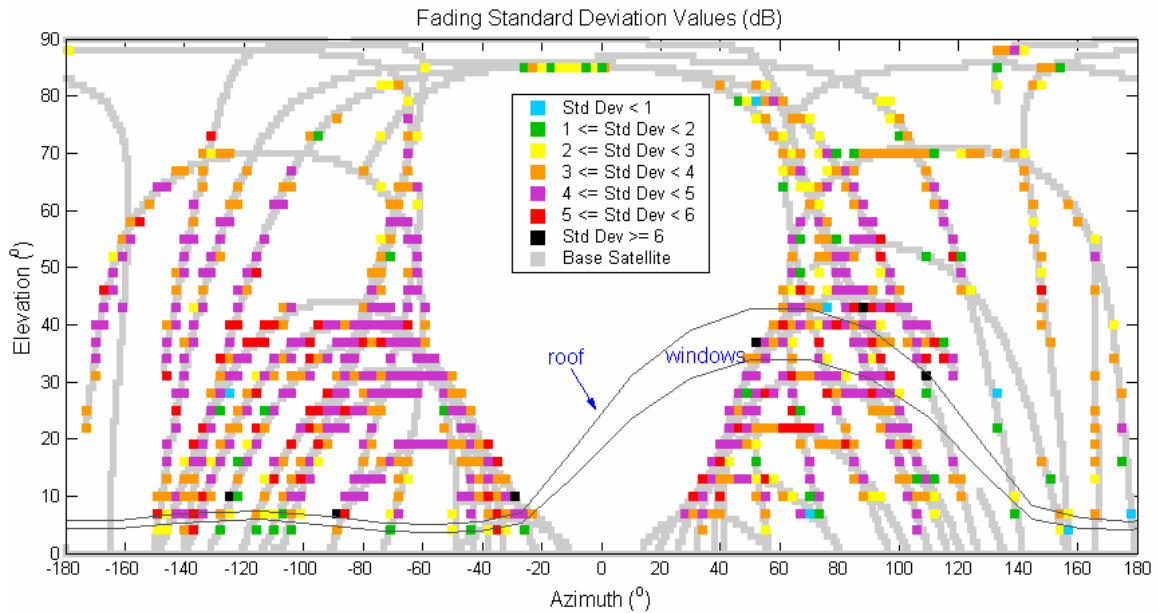
Figure 6.55: Fading standard deviations of 3˚x3˚ bin — Oval test

The fading PDF, shown in Figure 6.56, is characterized by an approximately symmetrical centre at 23 dB, which is higher than that observed during the garage and High Bay tests. Sixty two percent of the fading is located in a range stretching from 18 dB to 28 dB. There appears to be a higher degree of fading associated with large values in the Oval than in the garage and High Bay. The lowest signal strengths among the three environments would introduce the highest noise levels in the pseudorange measurements and the EPEs.
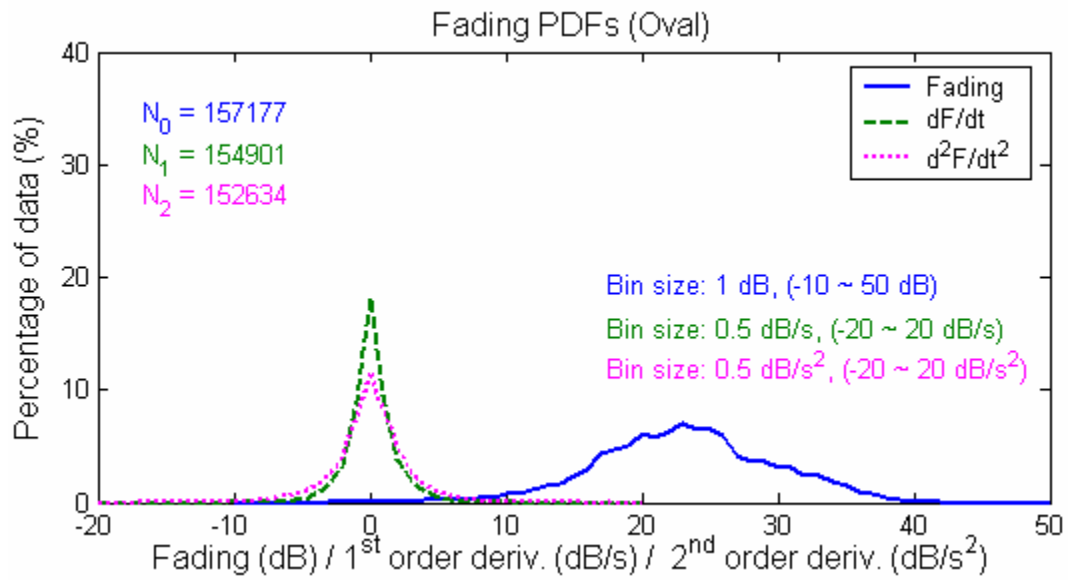
Figure 6.56: PDFs of fading and associated 1st & 2nd order derivatives — Oval test

6.3.4 Estimated Pseudorange Errors

Figure 6.57 and Figure 6.58 show the pierce-point analysis of the EPE means and standard deviations, respectively. The large dimensions of the building resulted in longer multipath delays and produced larger EPEs.
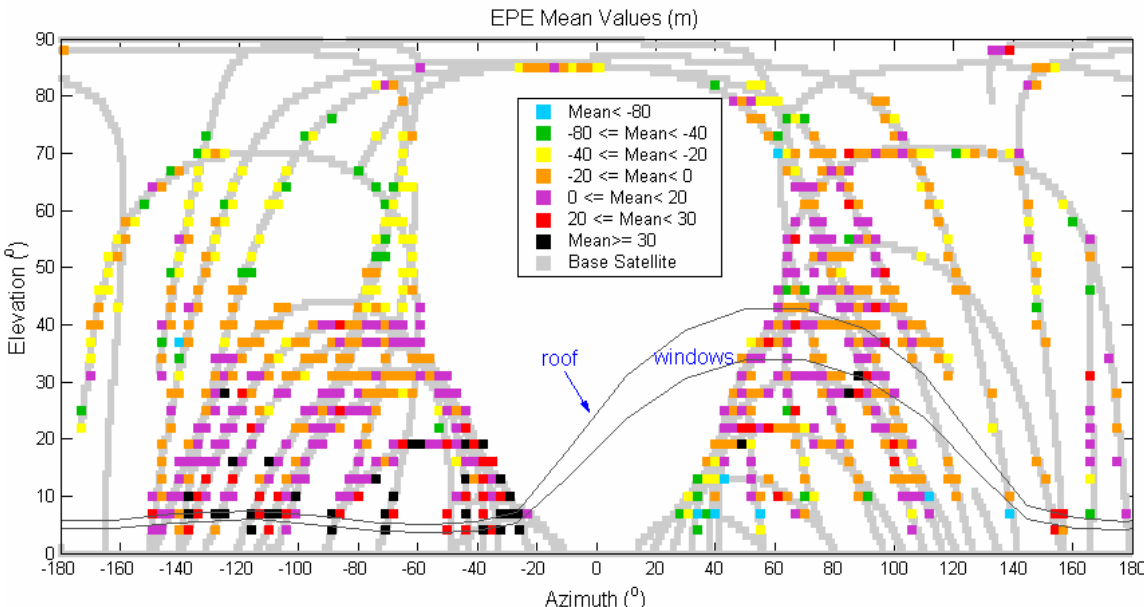
Figure 6.57: EPE means of 3˚x3˚ bin — Oval test
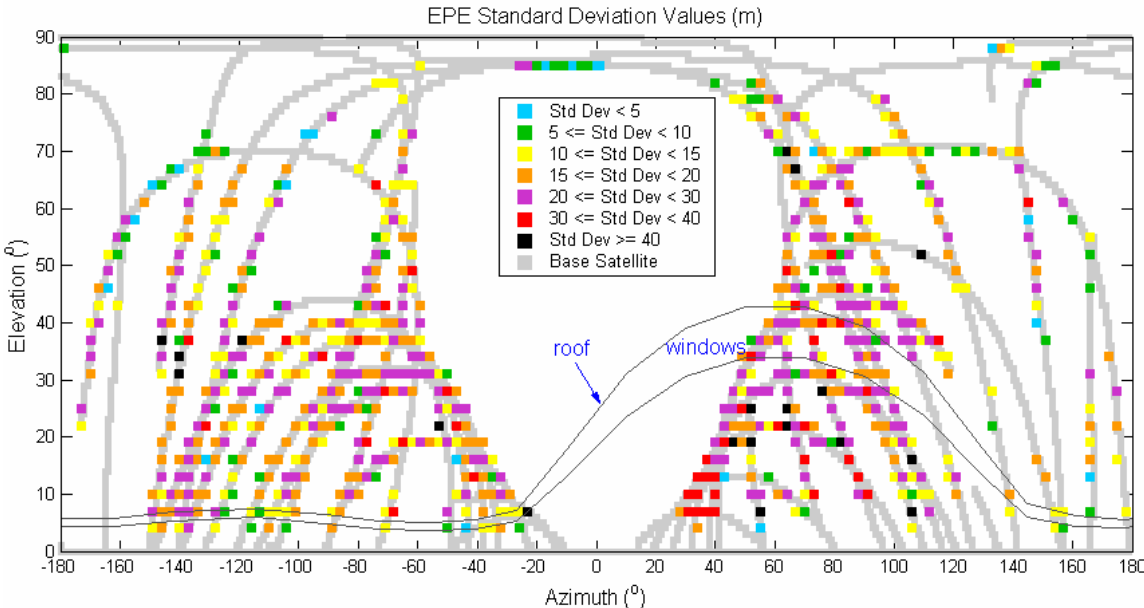
Figure 6.58: EPE standard deviations of 3˚x3˚ bin — Oval test

The EPE and its first and second order derivative PDFs, shown in Figure 6.59, indicate that there are larger EPE values in the Oval than in the garage and High

Bay environments.   Ninety three percent of the EPEs are within the range of -50 m

to 50 m, whereas 98% of the EPEs fell within that range in the High Bay test.

There are 5% more EPEs beyond the range of ±50 m in the Oval test.   The larger

EPE values in the Oval would consequently produce larger position errors than in

the garage and High Bay tests.   The horizontal position error PDF is shown in

Figure 6.60.   Only 67% of the position errors are within 50 m, while this value is

89% in the case of the High Bay test.
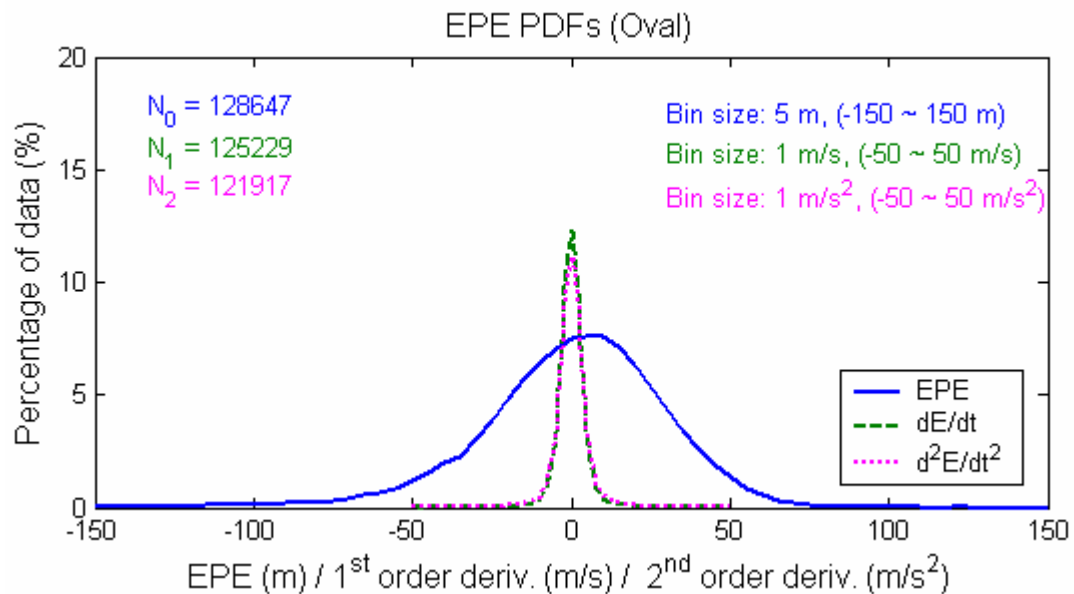
Figure 6.59: PDFs of EPE and associated 1st & 2nd order derivatives — Oval test
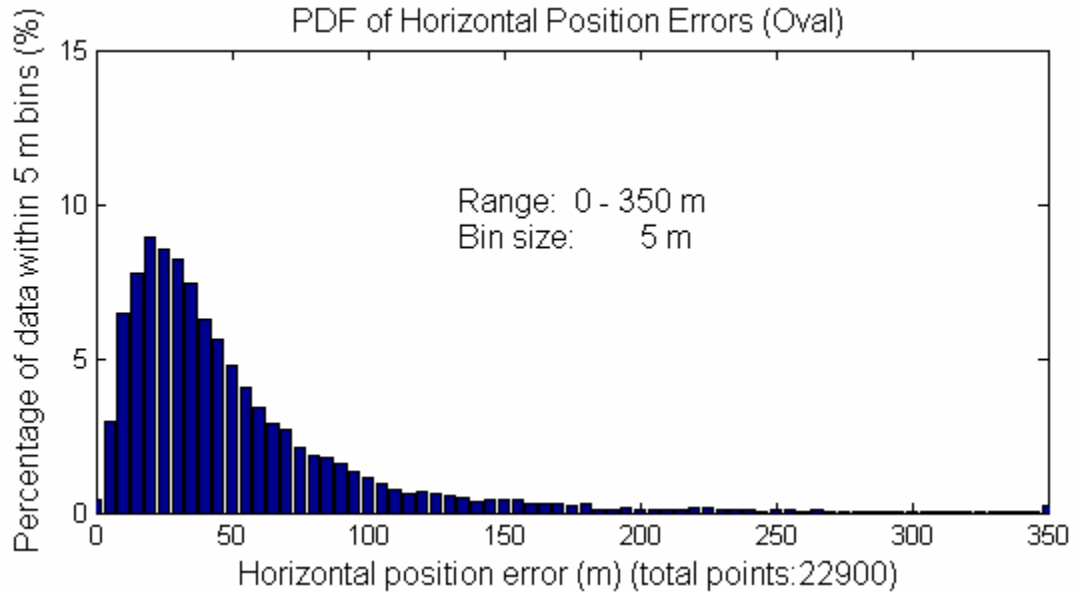
Figure 6.60: Horizontal position error PDF — Oval test

6.3.5 Simulation Results

6.3.5.1 Simulation Setup

Six satellites were chosen for this simulation, as shown in Figure 6.61, over a 40-minute period. The attenuation levels of each satellite signal were different during the simulation. LOS signals were attenuated between 22 dB and 32 dB. The multipath power levels were set to -6 dB to 0 dB, relative to the LOS. The maximum multipath delay was set to 220 m. The UserActions method was used to create multipath signals, including their numbers, delays and power levels, for this simulation.
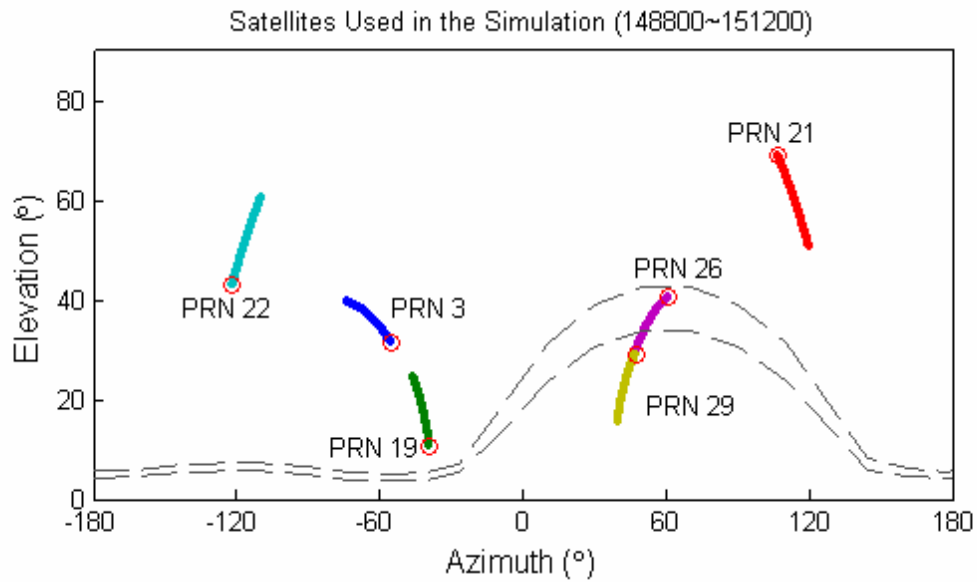
Figure 6.61: Satellites chosen for simulation — Oval test

6.3.5.2 Satellite Availability

The satellite availability over the simulation time is shown in Figure 6.62 for both field and simulated data.   The number of tracked satellites varies from 0 to 6. However, this number is usually in a narrower range of 4 to 6 in the garage and High Bay tests.   Figure 6.63 displays the PDF of the tracked satellite number.   As compared to the other two environments, satellite availability is fairly poor.   The availability of four and more satellites in the field test and simulation are 62% and 76% respectively.   The number of tracked satellites for the longest period over the time span of the field test is four, but five in the simulation. This results in a low correlation coefficient of 0.781, worse than in the other two environments.
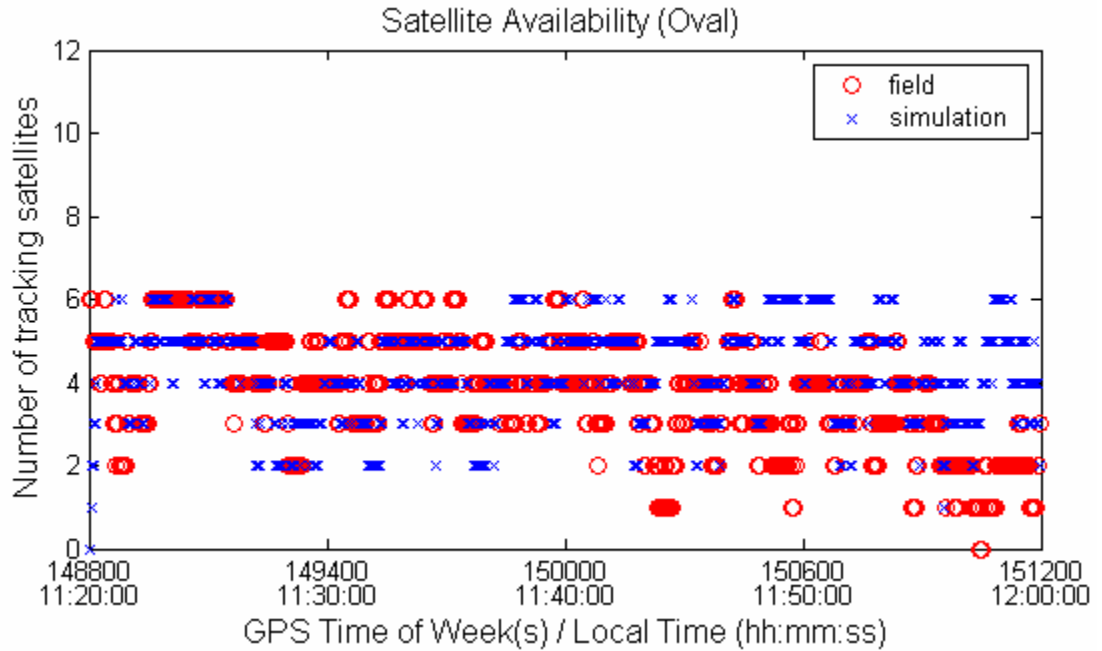
Figure 6.62: Field and simulator satellite availability — Oval test
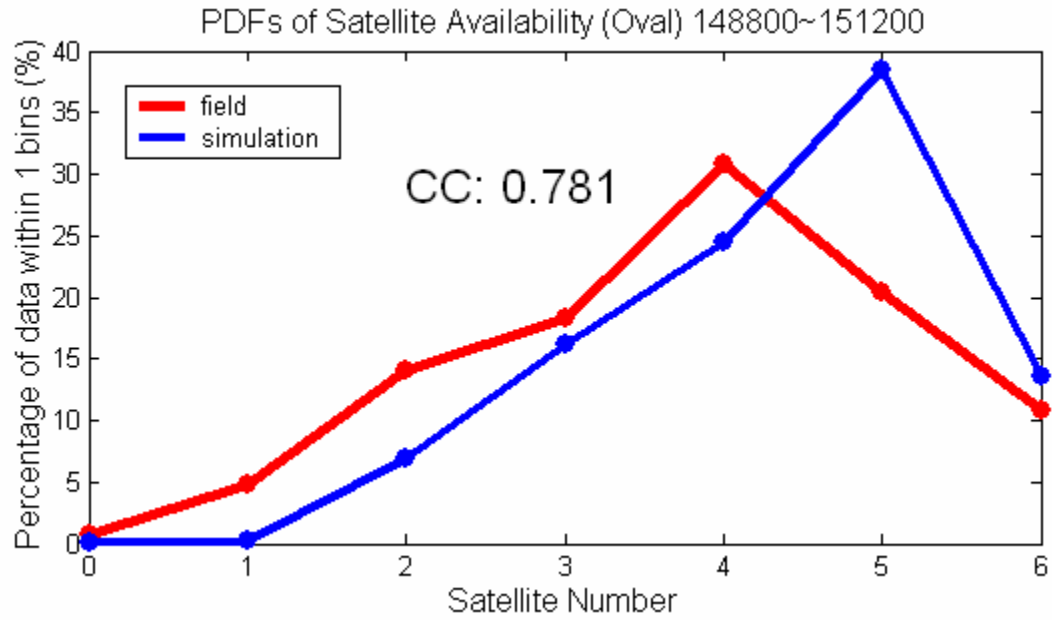
Figure 6.63: Field and simulator satellite availability PDFs — Oval test

6.3.5.3 Fading and EPEs

The fading observed in the simulation and the field tests is shown in Figure 6.64.

The fading exhibited a higher frequency of change rate than in the High Bay case. The fading of PRN 19 and PRN 29 fluctuated around a mean of about 22 dB, smaller than that of the other satellites, which had mean fading levels of about 32 dB. The overall attenuation levels were higher than in the garage and High Bay cases. More incidents of signal tracking loss result in fewer numbers of sample data.

The EPEs for both the field test and simulation are shown in Figure 6.65. Due to the poor satellite availability, the number of the EPEs is significantly lower than that in the garage and High Bay cases. The amplitudes of the fluctuations are larger than those observed in the garage and High Bay cases.
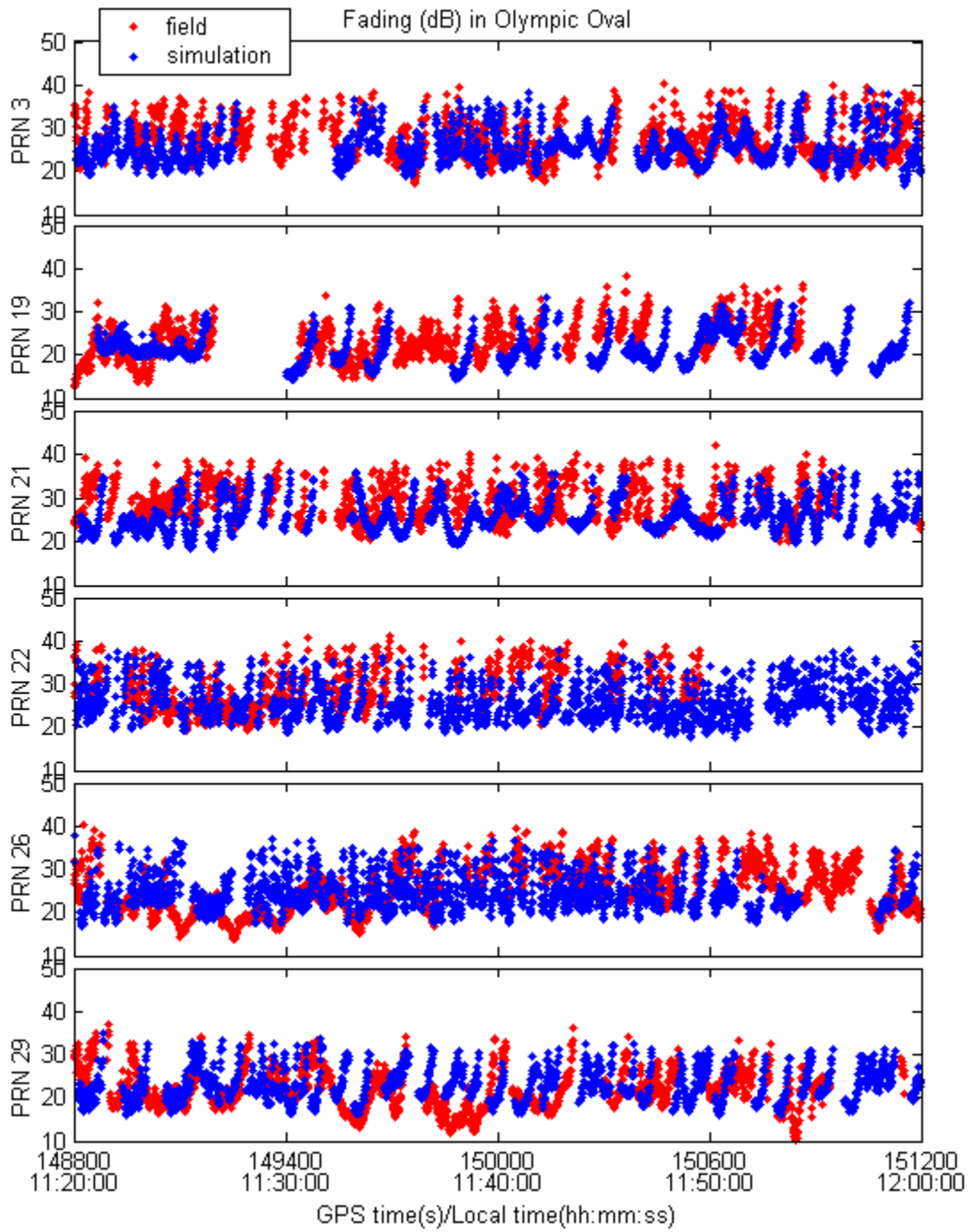
Figure 6.64: Field and simulator Fading measurements — Oval test
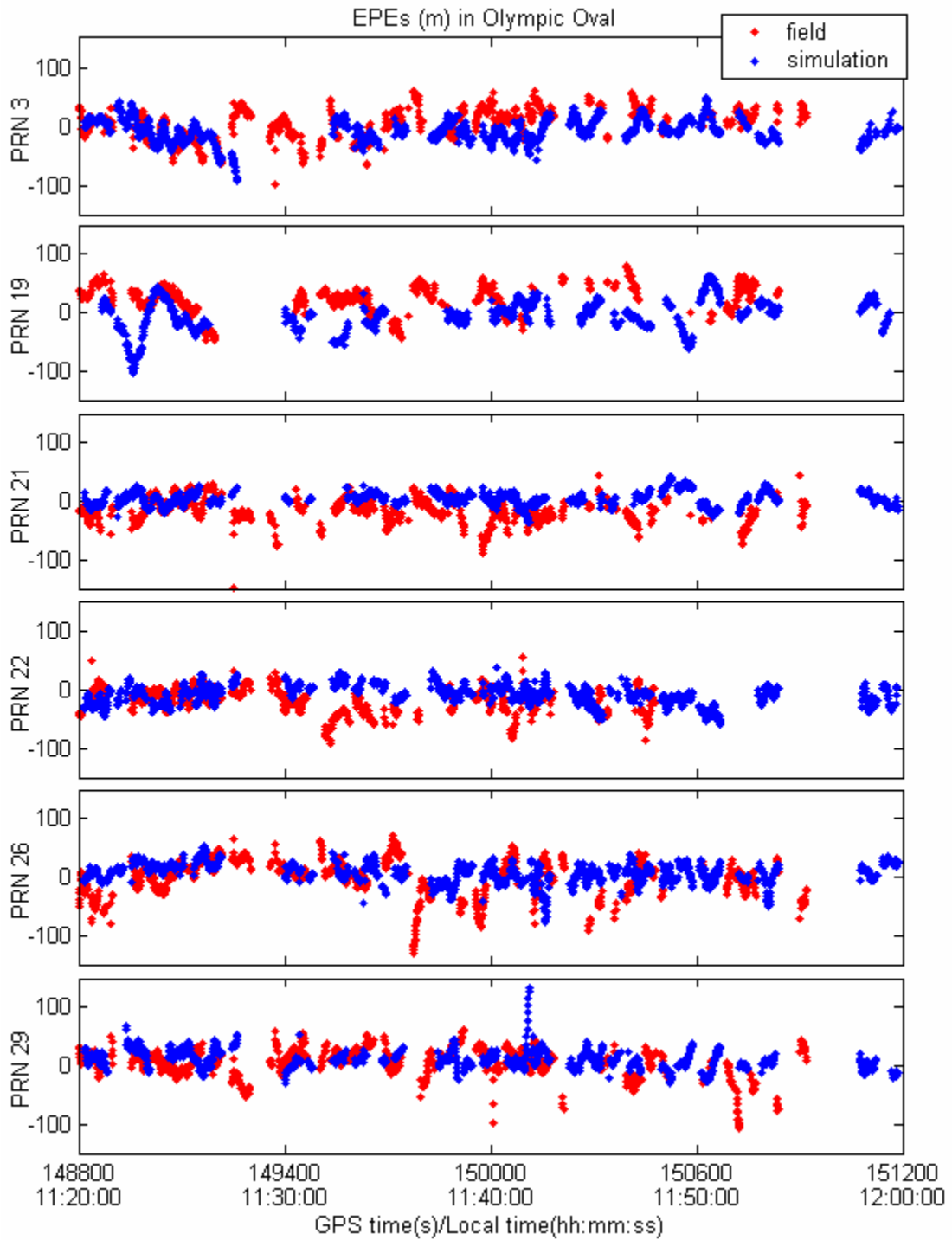
Figure 6.65: Field and simulator EPE measurements — Oval test

Figure 6.66 shows the fading and its first and second order derivative PDFs.   The

level of correlation between the field and simulation results is relatively high.

Figure 6.67 shows the EPE and its first and second order derivative PDFs. The EPE PDF has a sharp peak centred near 0 m in the simulation while, it is rather more dispersed in the field test.
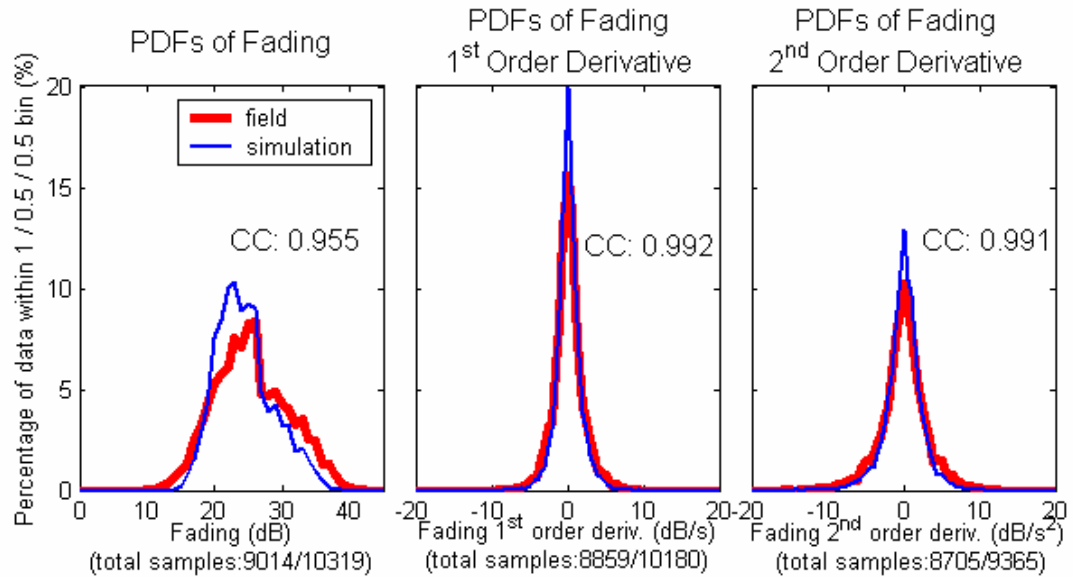
Figure 6.66: PDFs of fading and associated 1st & 2nd order derivatives — Oval test
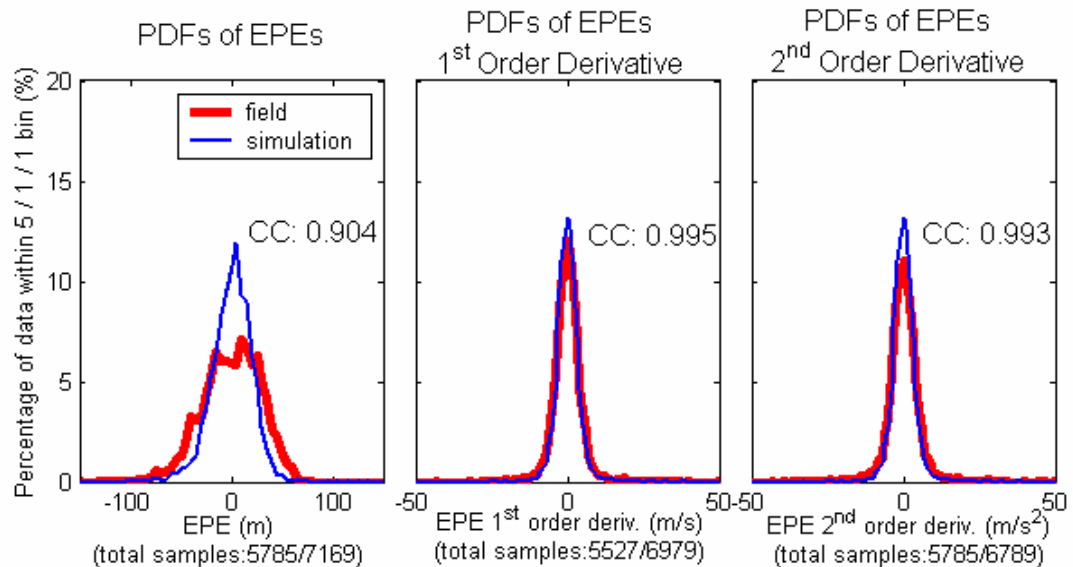
Figure 6.67: PDFs of EPE and associated 1st & 2nd order derivatives — Oval test

6.3.5.4 Positioning Accuracy and HDOP

The horizontal position errors are shown in Figure 6.68.   The poor satellite availability resulted in degraded position accuracy.   In addition, the HDOP threshold (≤ 5) also reduced the number of position solutions available.   The horizontal position error PDFs are shown in Figure 6.69.   The position errors are significantly larger than in the garage and High Bay tests, whereas the sample number is significantly smaller than in the other two tests.   The saw-shaped curves of the PDFs are likely the result of the limited number of samples.
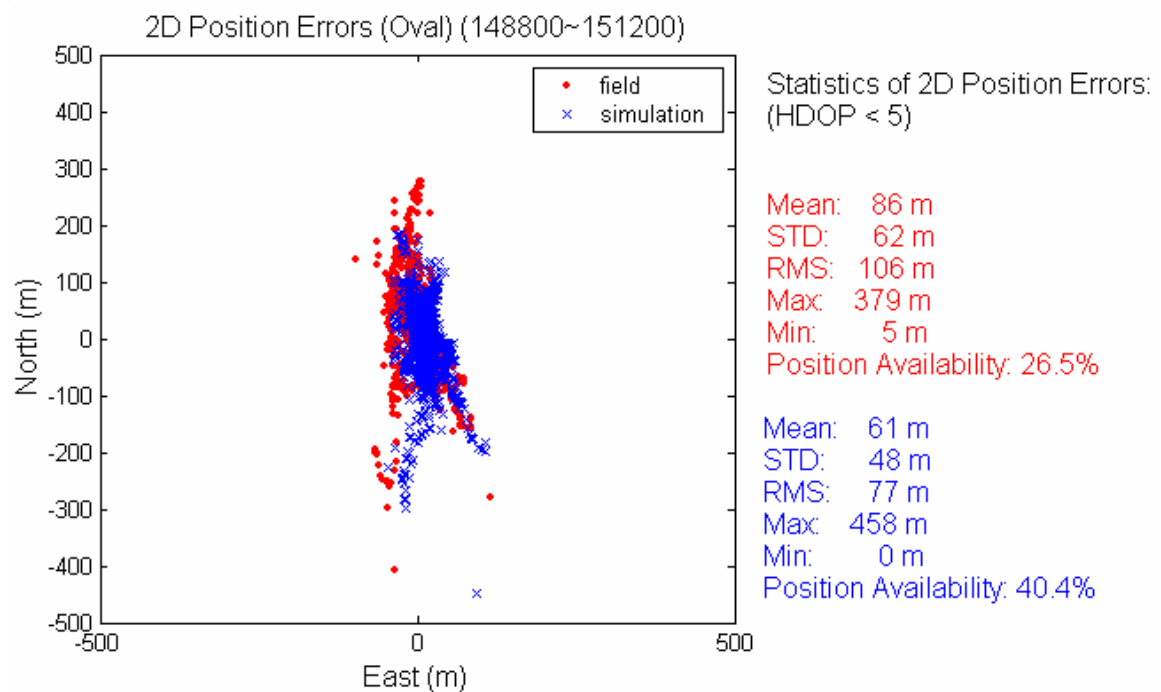
Figure 6.68: Field and simulator horizontal position errors — Oval test
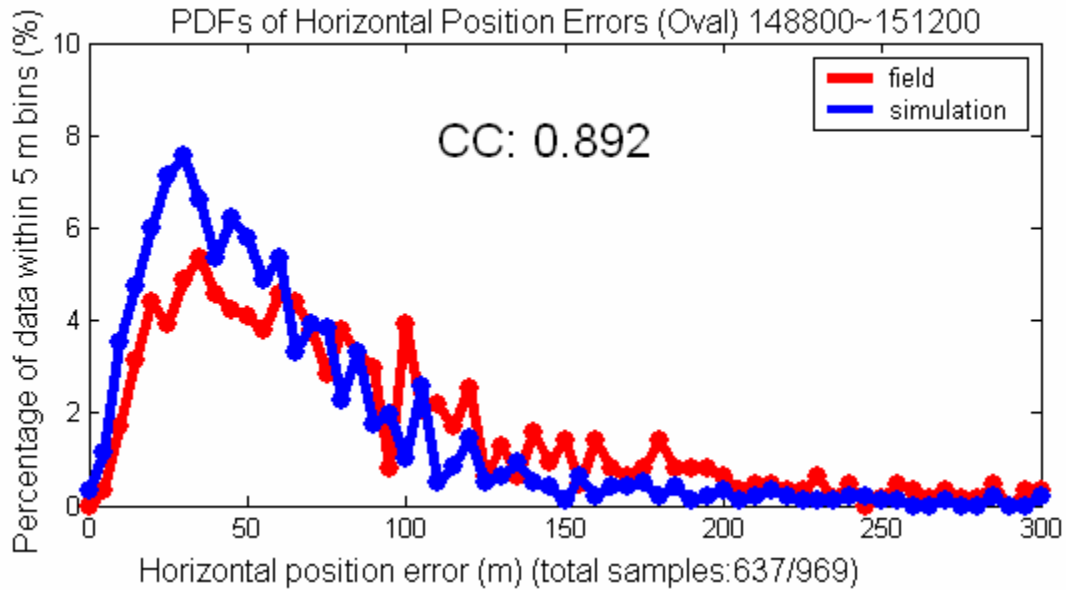
Figure 6.69: Field and simulator horizontal position error — Oval test

Figure 6.70 shows the HDOP values. They were obviously larger than those in the garage and High Bay cases and close to the HDOP threshold of 5. The relatively high values of HDOP introduced larger position errors. The relatively high values of HDOP introduced larger position errors, although the HDOP trend in the simulation looks similar to that in the field data. However, as shown in Figure 6.71, the correlation coefficient of their PDFs is only 0.772.
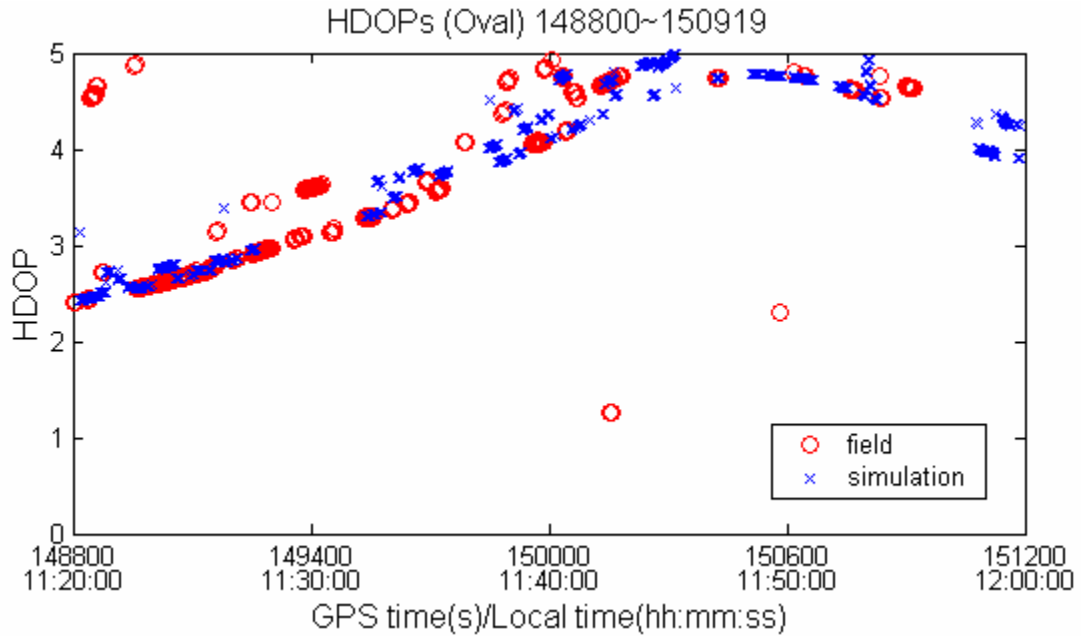
Figure 6.70: Field and simulator HDOPs — Oval test
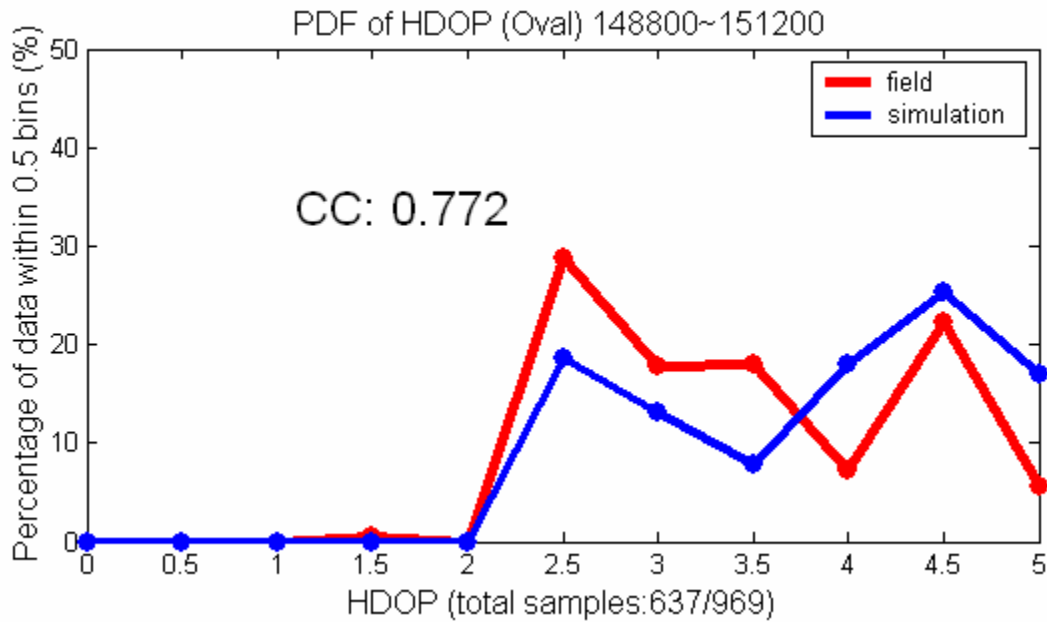
Figure 6.71: Field and simulator HDOP PDFs — Oval test

Table 6.3 gives overall correlation coefficients for the field test and the simulation.

The correlation coefficients of the distributions of the satellite availability and

HDOPs display are lower for the Oval than for the garage and High Bay tests. The Oval is the worst for GPS positioning among these three indoor environments. The highest power attenuation, the longest multipath delay and the worst satellite availability indicate that the Oval is the most complex environment among the three indoor environments. This results in the poorest correlation between the field test and the simulation.

Table 6.3: Oval field test and simulation correlation coefficients

Items		Correlation Coefficients	
		Fading	**EPE**
(.) (bin size: 1 dB, 5m)		0.955	0.904
d(.)/dt (bin size: 0.5 dB, 1 m)		0.992	0.995
$d^2(.)/dt^2$ (bin size: 0.5 dB, 1 m)		0.991	0.998
Power Spectral Density (Bin size: 0.005 Hz)	PRN 3	0.8307	0.9901
	PRN 19	0.7199	0.8048
	PRN 21	0.9100	0.9216
	PRN 22	0.7060	0.9789
	PRN 26	0.3595	0.9222
	PRN 29	0.7271	0.8602
	Average	**0.7089**	**0.9130**
Satellite Availability (bin size: 1)		0.781	
Position Error (bin size: 1 m)		0.892	
HDOP (bin size: 0.5)		0.772	

Chapter 7

Simulation for the Urban Canyon Environment

The urban canyon is another type of GPS signal degraded environment that has many people concerned. Large buildings and short distances between buildings result in severe signal blocking and multipath interference in urban canyon environments. The smooth surfaces of large buildings act as strong specular reflectors and induce large multipath effects. Line-of-sight signals with low elevation angles are easily blocked and only echo signals can be tracked. The signals would be expected to exhibit different characteristics compared to indoor signals.

7.1 Field Testing Description

The field test was performed at a well surveyed location at the University of Calgary campus and will also be referred to as the campus outdoor test in the sequel. This data set was also used by Boulton *et al* (2002a) to test the initial GSS6560 simulator model. Lachapelle *et al* (2003b) used the same data set to demonstrate the improved model as well.

The known point is surrounded by nearby buildings, providing an urban canyon-like environment. Figure 7.1 shows the environment. A seven-floor building called the ICT Building, with glass and metallic exterior walls is located on the east of side of the test site. A two-floor corridor with the same exterior material

as the building lies immediately to the north. These surfaces are probable sources of strong specular signal reflection. The building with three floors on the west side of the test site has small windows and a rough stone-textured exterior, and is a probable source of diffuse signal reflection or obscuration. Six hours of data were collected at this site.

Figure 7.1: Campus outdoor testing environment (MacGougan 2003)

7.2 Satellite Availability

The satellite availability and the associated PDF are shown in Figure 7.2 and Figure 7.3. At any given moment during the test, at least four satellites were available. For 4% of the time, the HSGPS receiver was capable of tracking the maximum number of ten satellites. Satellite availability was better than in indoor environments.
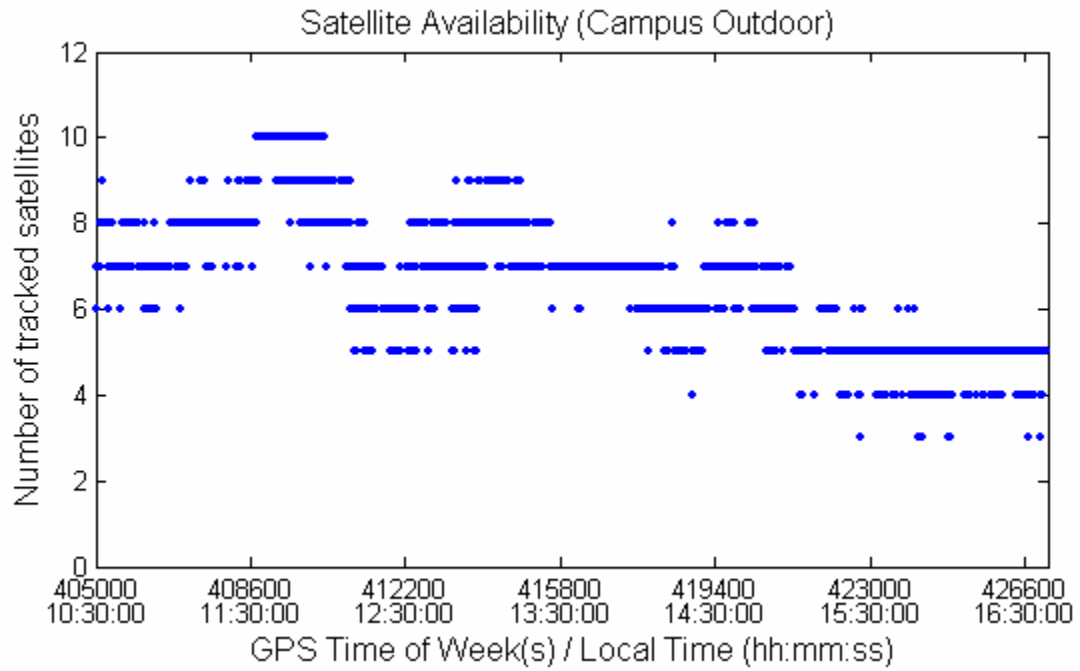
Figure 7.2: Satellite availability — campus outdoor test
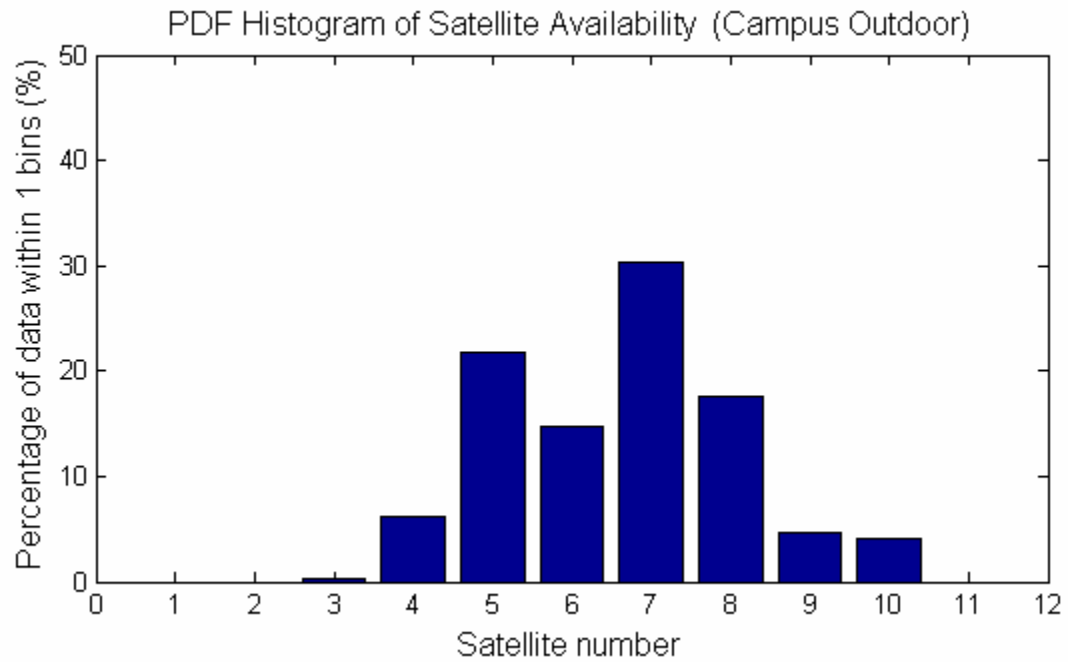
Figure 7.3: PDF of satellite availability — campus outdoor test

7.3 Fading

Figure 7.4 and Figure 7.5 show the results of the fading by using satellite pierce-point analysis. The thin grey lines describe the outline of the buildings near the test site. The signals from satellites behind the buildings had characteristics of significant power degradation and amplitude variation. The glass and metallic exterior walls to the east of the test site most likely acted as strong specular reflectors and provided strong multipath for signals coming from the west. By comparison, a rough exterior wall to the west of the test site acted as a poor reflector for the signals coming from the east. Therefore, signals coming from satellites behind the building to the west of the test site were relatively strong, with a signal power loss of 5 to 10 dB, whereas signals coming from satellites behind the building to the east of the test site were highly degraded, characterized by a signal power loss of 15 to 25 dB. In this case, a negative fading mean was observed in areas where LOS signals existed. Constructive multipath interference provides a reasonable explanation. The small values (1 to 3 dB) of the fading standard deviations indicate that weak multipath signals possibly existed in those areas, where the signals had not been obstructed by the buildings. Signals coming from the south side of the test site were hindered by tall trees on the southern aspect of the site. Therefore, signals coming from that area also exhibit signal power attenuation and obvious variations, as can be seen in Figure 7.4 and Figure 7.5.
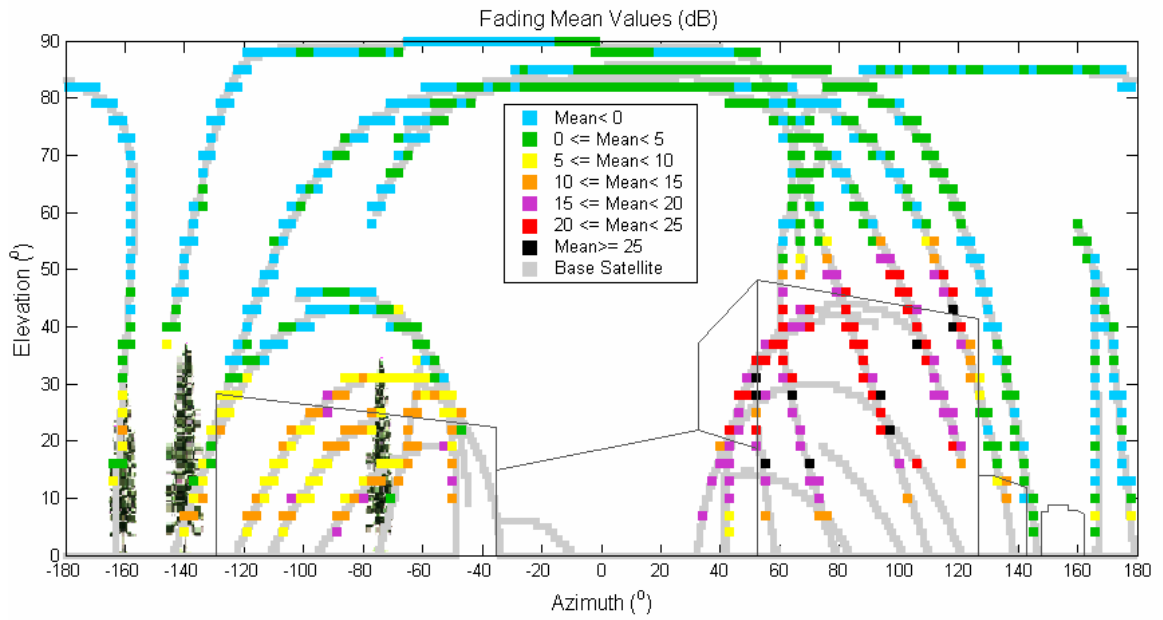
Figure 7.4: Fading means of 3˚x3˚ bin — campus outdoor test
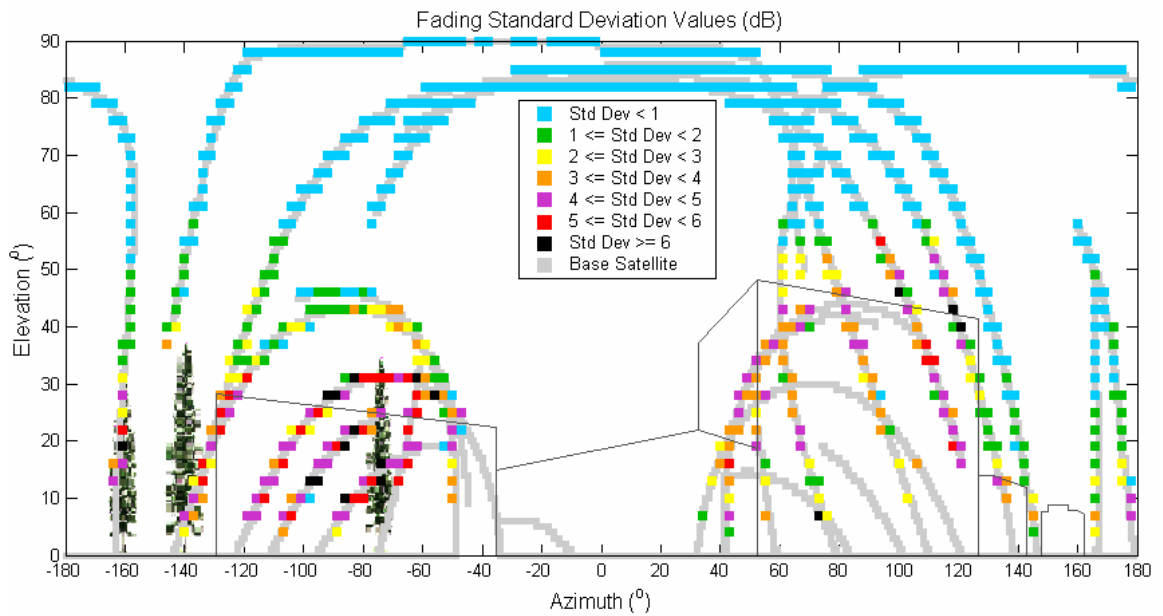
Figure 7.5: Fading standard deviations of 3˚x3˚ bin — campus outdoor test

The overall PDFs of the fading are shown in Figure 7.6. Because many

unattenuated LOS signals are observed at the test site, the PDF of the fading is characterized by a peak at 0 dB. A low, flat slope extending up to 30 dB is the result of the blockage of certain LOS signals. The peak shown at zero in the curve of the fading PDF differs from the indoor fading because the indoor fading PDF has a non-zero peak. The first and second order derivatives are centred and symmetrical about zero, which implies that the increased and decreased extents of the fading are almost equivalent. This is the same case as observed with respect to indoor signals.
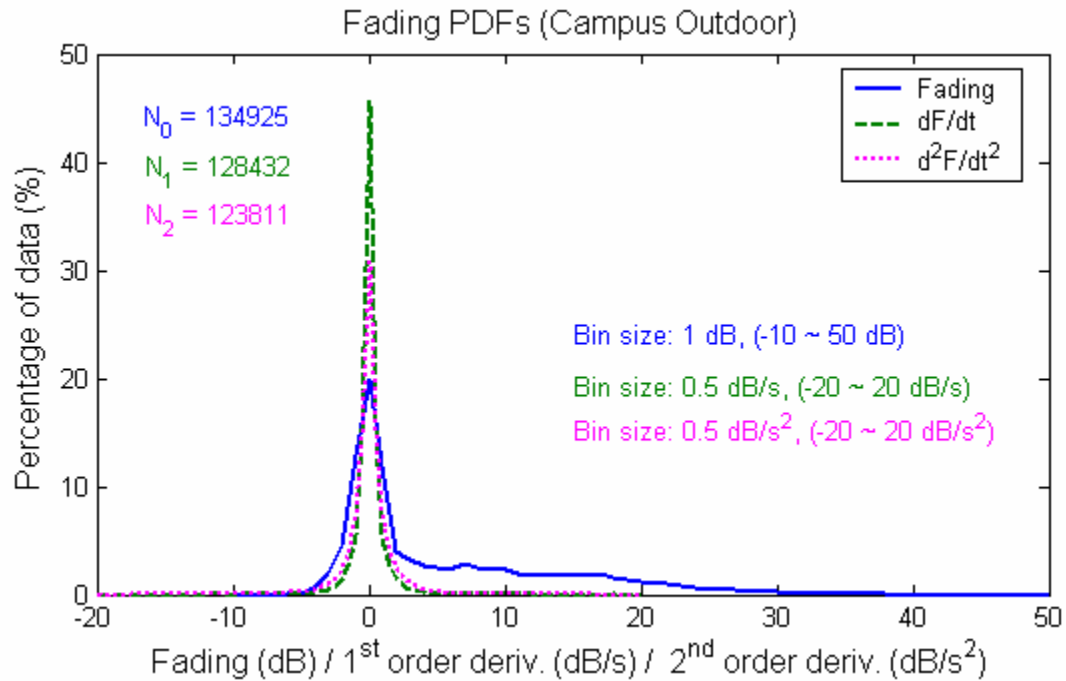
Figure 7.6: PDFs of fading and associated 1st & 2nd order derivatives — campus outdoor test

7.4 Estimated Pseudorange Errors

As opposed to the case of indoor signals, there were unattenuated LOS signals

from high observed during satellites existing in the campus outdoor test. In order to reduce the relativity of the EPEs, signals from the satellites with elevation angles above 40° were used to compute the EPEs in this test. The pierce-point analysis of the EPE means is shown in Figure 7.7. The signals coming from the satellites behind the building to the west of the test site had larger EPEs than the signals originating from satellites behind the building to the east of the test site. Multipath-only signals would introduce negative EPEs. This indicates that the signals coming from satellites behind the building with negative EPE values were multipath-only. The EPE standard deviations are shown in Figure 7.8. The signals coming from the satellites behind the building to the west of the test site had larger EPE standard deviations than the signals coming from the satellites behind the building to the east of the test site. This is similar to the fading standard deviations shown in Figure 7.5.
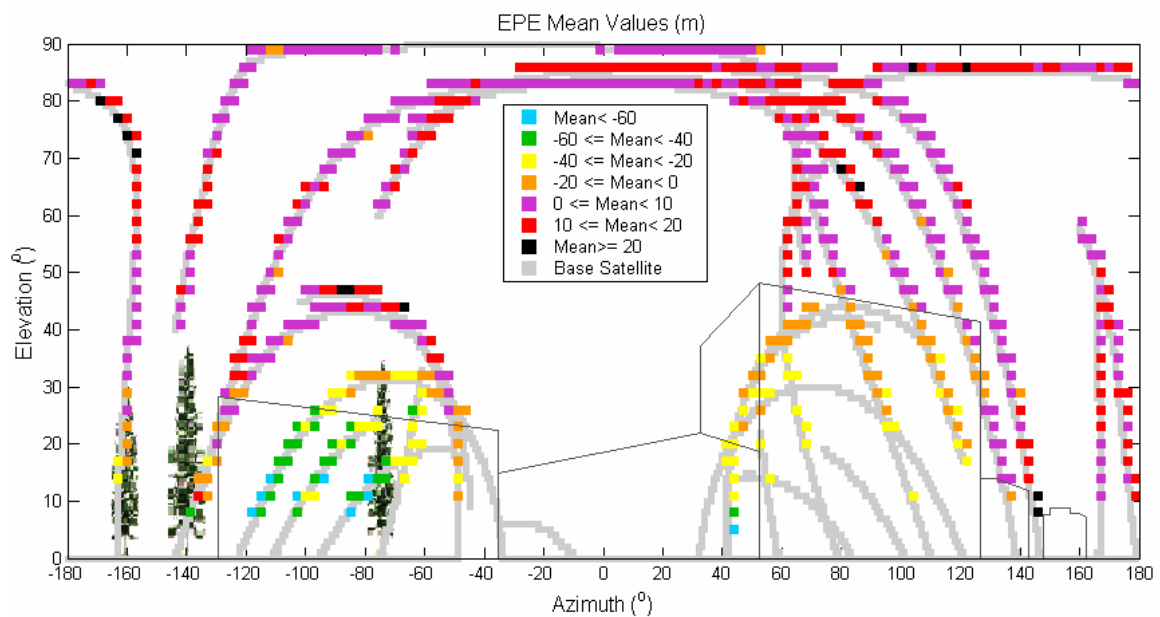
Figure 7.7: EPE Means of 3˚x3˚ bin — campus outdoor test
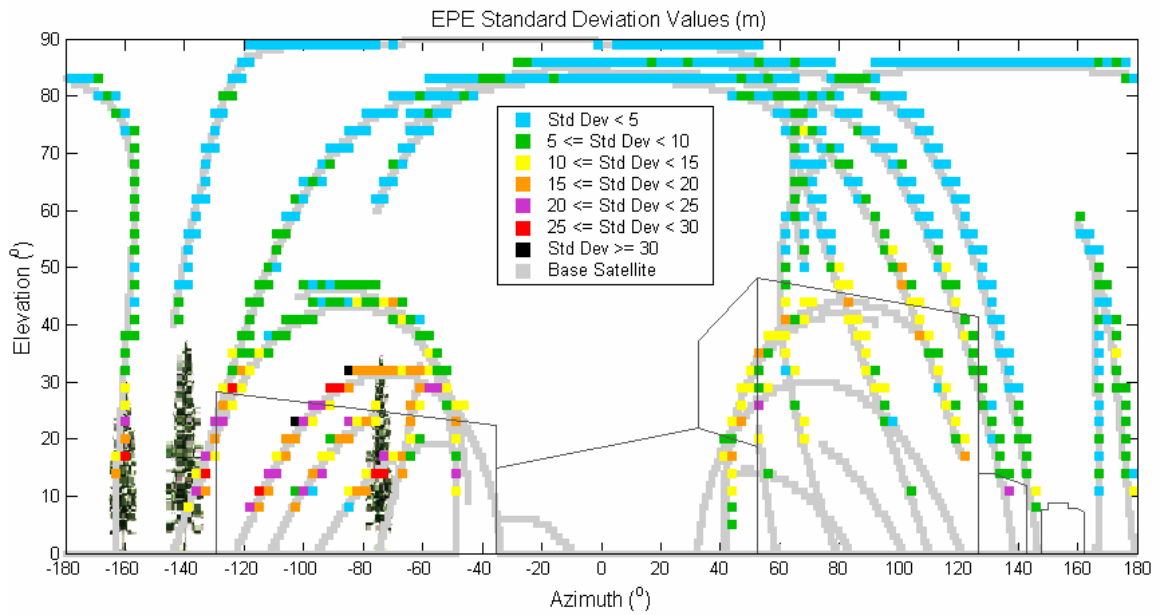
Figure 7.8: EPE standard deviations of 3˚x3˚ bin — campus outdoor test

Figure 7.9 displays the EPE PDF and the associated first and second order derivative PDFs. The EPE PDF has a peak at 0 m and a long low tail in the negative direction, which probably resulted from the negative EPE values due to the multipath-only signals.
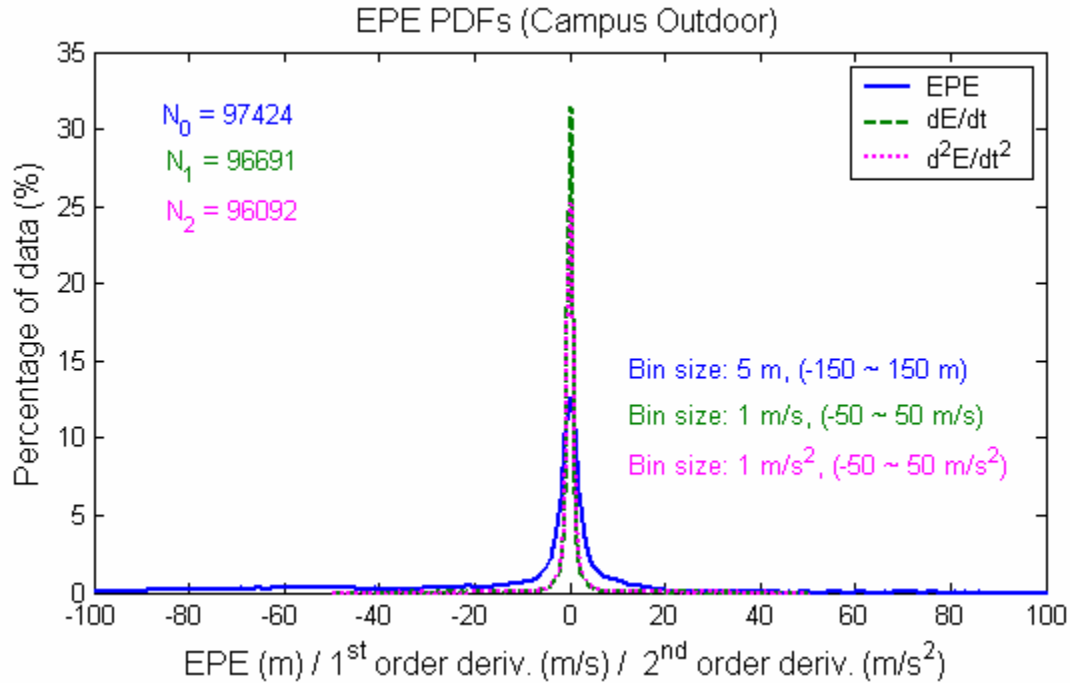
Figure 7.9: PDFs of EPE and associated 1st & 2nd order derivatives — campus outdoor test

7.5 Simulation Results

7.5.1 Simulation Setup

A 40-minute period was chosen for the simulation.   The six satellites chosen are shown in Figure 7.10.   The circles indicate the starting points of the satellite trajectories.   The LMM method was used to create the multipath signals.

PRN 22 was behind the building to the west and set as a multipath-only signal with a 20 m original delay.   Its multipath power levels were set -10 to -15 dB lower than the LOS signal.   PRN 21 was attenuated by trees.   Therefore, a power attenuation of -10 dB to -3 dB was set for its LOS signal.   Its multipath power level was set to about -10 dB lower than the LOS signal.   The multipath signals of PRN

6 and PRN 18 were set to about -10 dB lower than their LOS signals.   PRN 17 and PRN 23 were at higher elevations than the other satellites and, therefore, had less multipath interference.   Their multipath power levels were set to about -20 dB lower than their LOS signals.   The parameter of maximum near echo delay was set to 600 ns, corresponding to a 180 m maximum path delay.
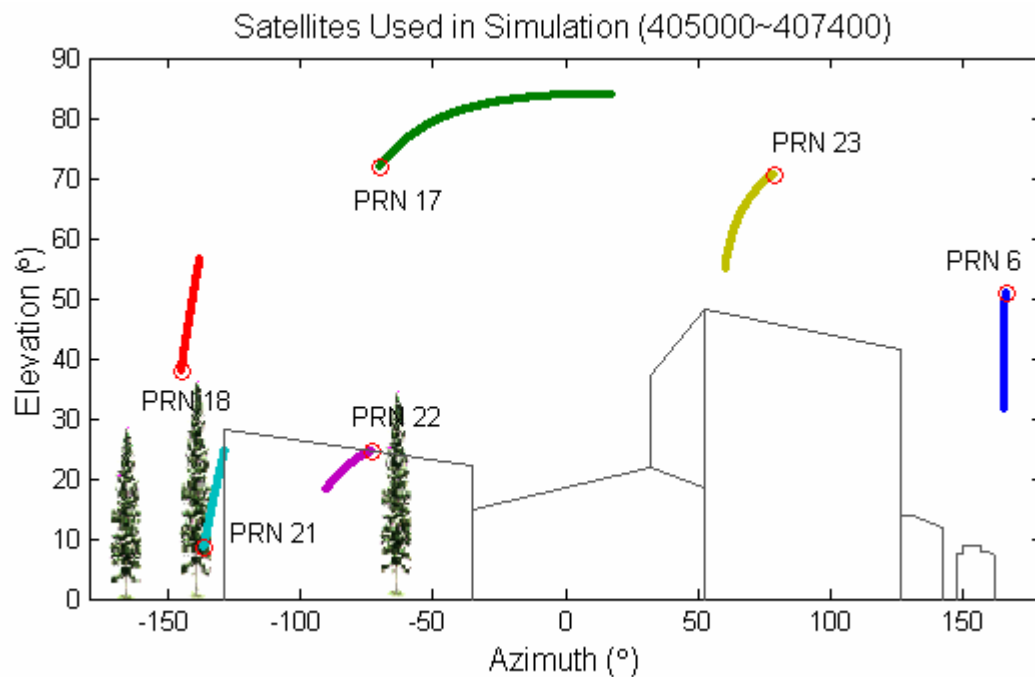
Figure 7.10: Satellites chosen for simulation — campus outdoor test

7.5.2 Satellite Availability

The satellite availability and the associated PDF are shown in Figure 7.11 and Figure 7.12.   At least five satellites could be tracked during both the simulation and field test.   The simulation results displayed very similar performance.
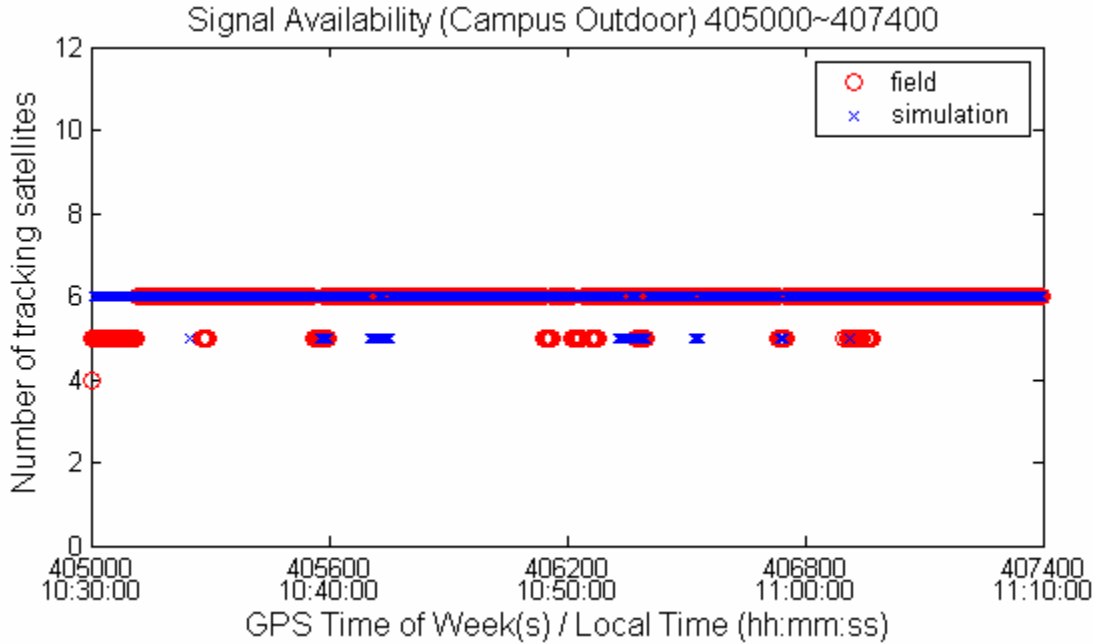
Figure 7.11: Field and simulator satellite availability — campus outdoor test
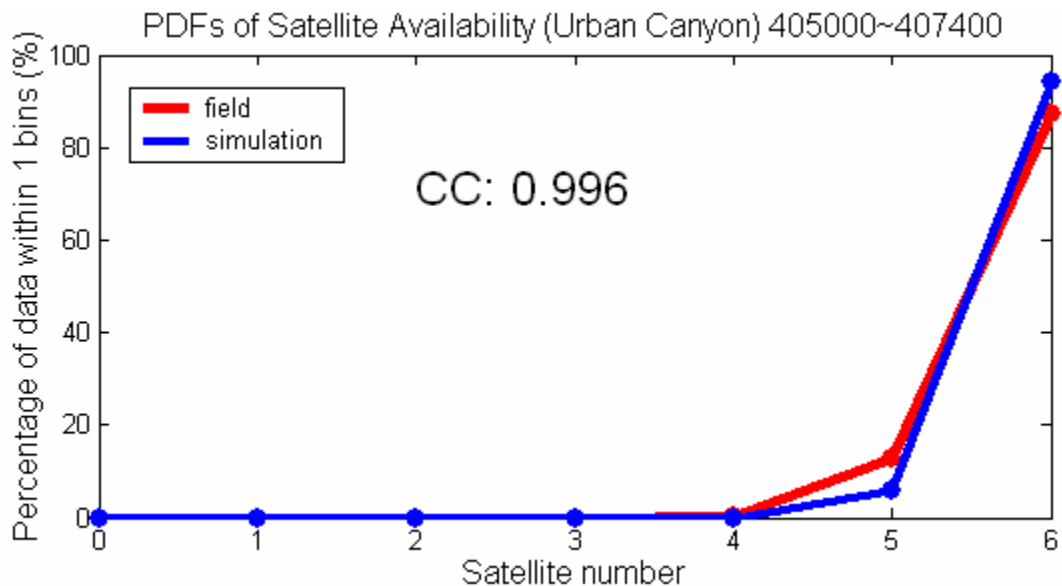
Figure 7.12: Field and simulator PDFs of satellite availability — campus outdoor test

7.5.3 Fading and EPEs

The fading measurements obtained during the simulation and the field test are shown in Figure 7.13.   The fading of PRN 6 exhibits a sinusoidal trend with two clear frequency components.   This implies that two stable multipath signals were present during the test.   PRN 17 does not show obvious signs of attenuation due to its high elevation, and small fluctuations can be observed.   PRN 18, which was rising during the test, was susceptible to signal attenuation due to the presence of trees (see Figure 7.10).   It was characterized by relatively large fading and fluctuations during the first ten minutes, which then declined to a mean level of around 0 dB afterwards.   PRN 21 and PRN22 experienced approximately 10 dB attenuation with fluctuation amplitudes from 10 to 20 dB, which is larger than those observed on the other satellites.   The larger fluctuation implies the existence of strong multipath signals.   PRN 23 exhibits stable fading for the first 20 minutes, and then fluctuates subsequently.   Its fluctuation amplitudes are smaller than those of PRN 6, which indicates that its multipath signals were weaker than those of PRN 6.   The simulated data displayed a very similar trend to the field measurements.

The EPEs for both simulation and field tests are shown in Figure 7.14.   They follow a similar trend to the fading measurements shown in Figure 7.13.   The EPEs of PRN 22 fluctuated about a negative level during the entire period, which coincides with the mulitpath-only assumption.   This negative level was taken as the basic delay of multipath for PRN 22.

Figure 7.15 shows the PDFs of the fading and the EPE PSDs. PRN 6, PRN 18 and PRN 22 display smaller correlation coefficients than do the other satellites. Figure 7.14 shows that the EPEs of PRN 6 and PRN 18 contain very clear sinusoidal components characterized by relatively high frequencies. Hence, peaks appear at those frequencies in their PSD curves. A detailed look at the EPEs of PRN 6 and PRN 18 reveals the possibility that the variation frequency in the field data is slower than in the simulated data for PRN 6, while it is the opposite in the case of PRN 18. It is also clear that the EPEs of PRN 22 fluctuate faster in the field test than in the simulation. Therefore, the PSD correlation coefficients of these three satellites are low.
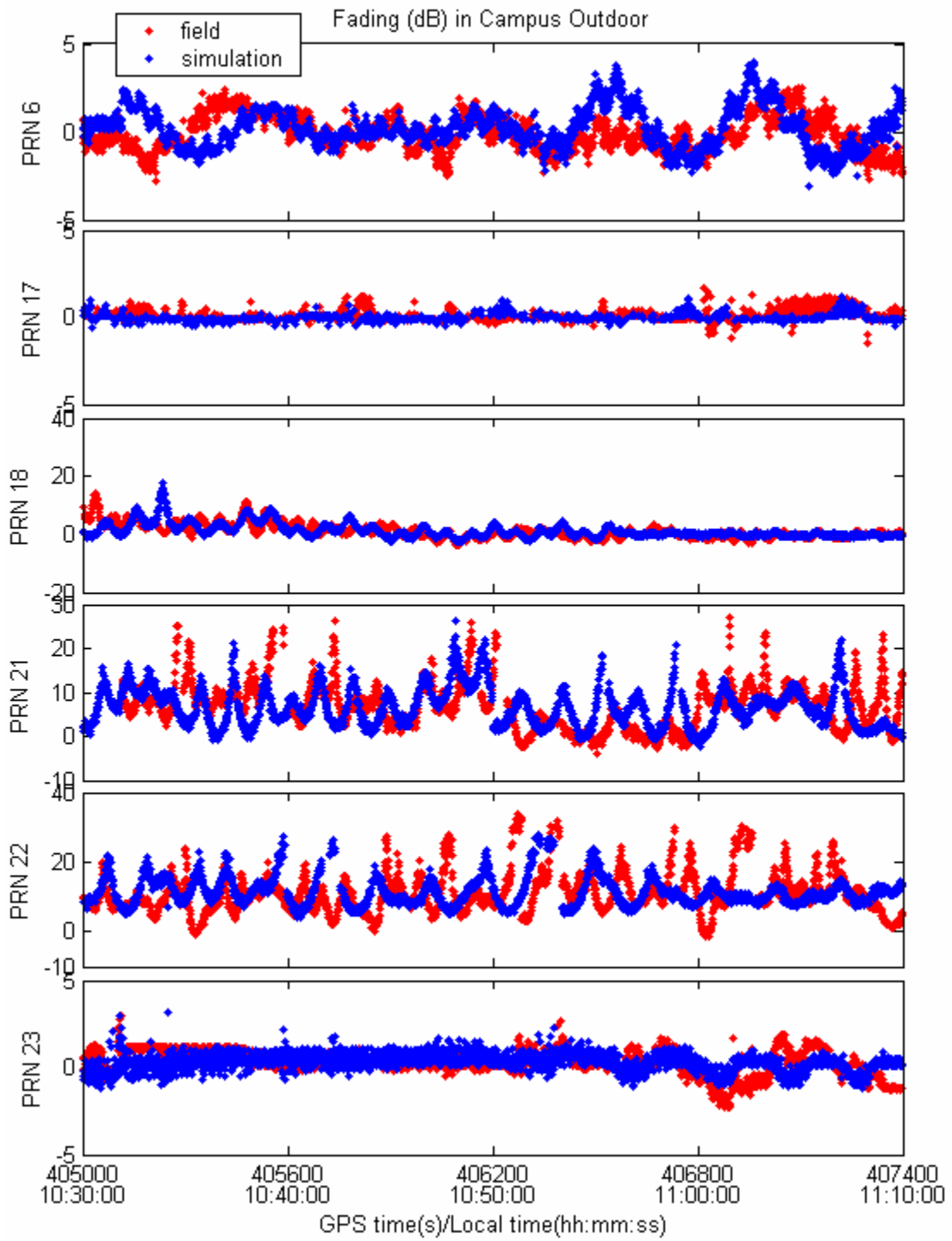
Figure 7.13: Field and simulator fading measurements — campus outdoor test
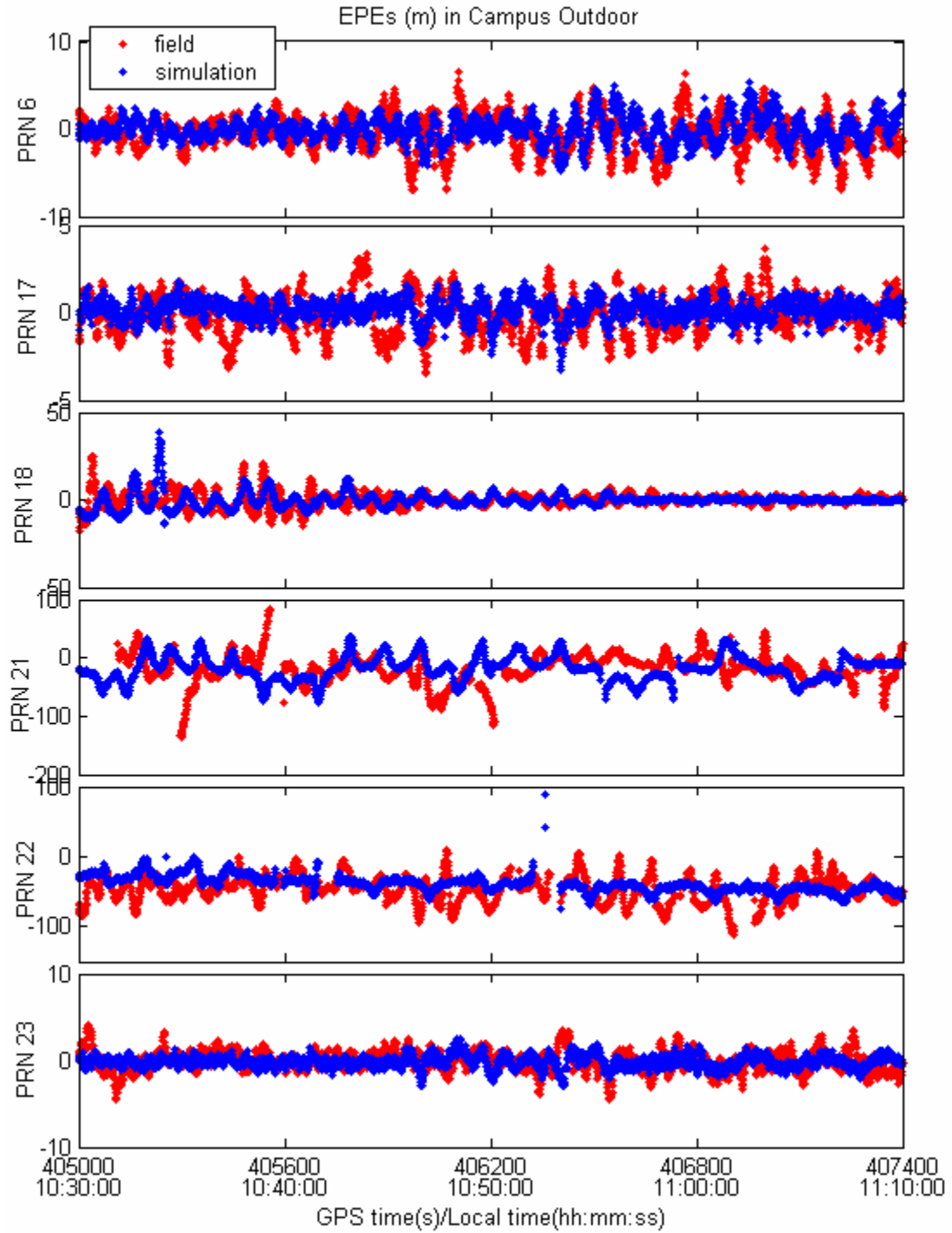
Figure 7.14: Field and simulator EPE measurements — campus outdoor test
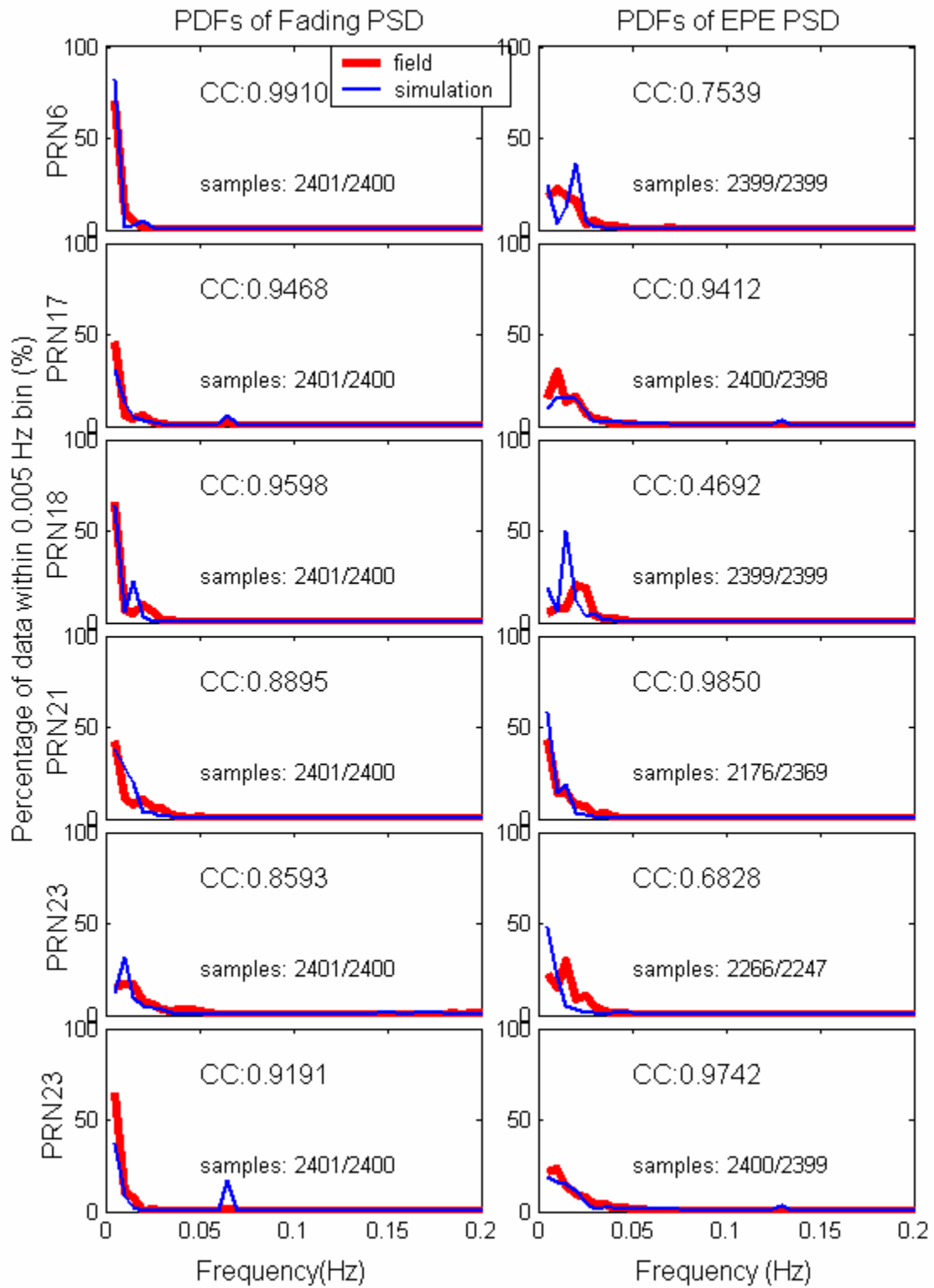
Figure 7.15: Field and simulator PDFs of fading and EPE PSDs — campus outdoor test

Figure 7.16 shows the fading and its first and second order derivative PDFs for both the field test and simulation. The level of correlation between the field and simulation results is high. A high correlation may also be found for EPE, as shown in Figure 7.17.
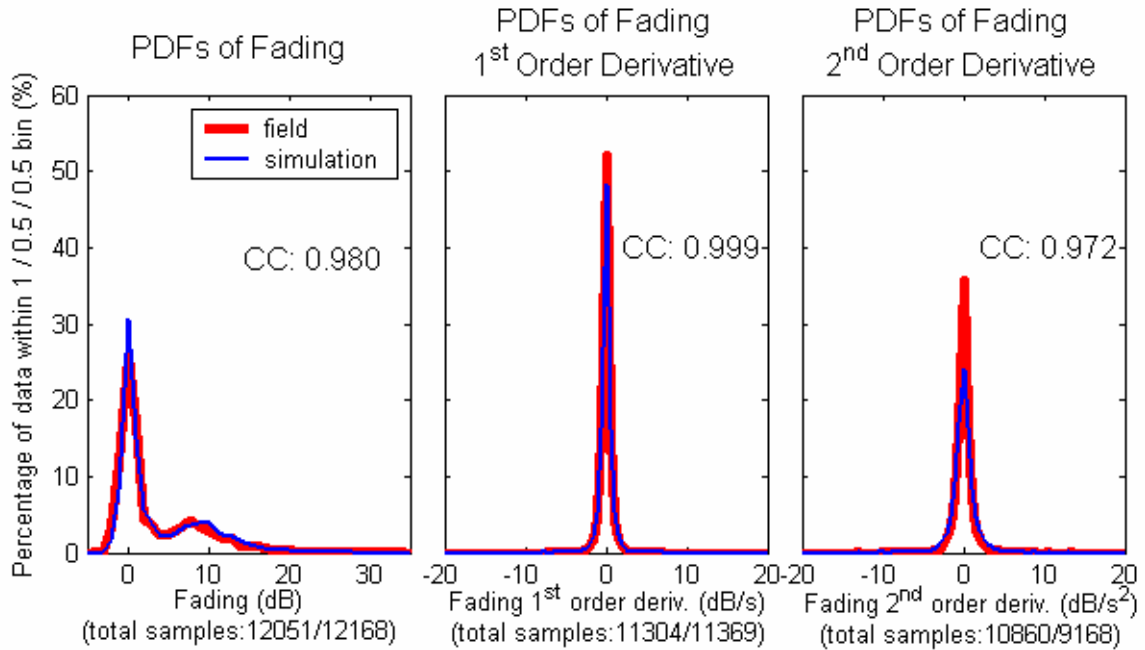
Figure 7.16: PDFs of fading and associated 1st & 2nd order derivatives in field test and simulation — campus outdoor test
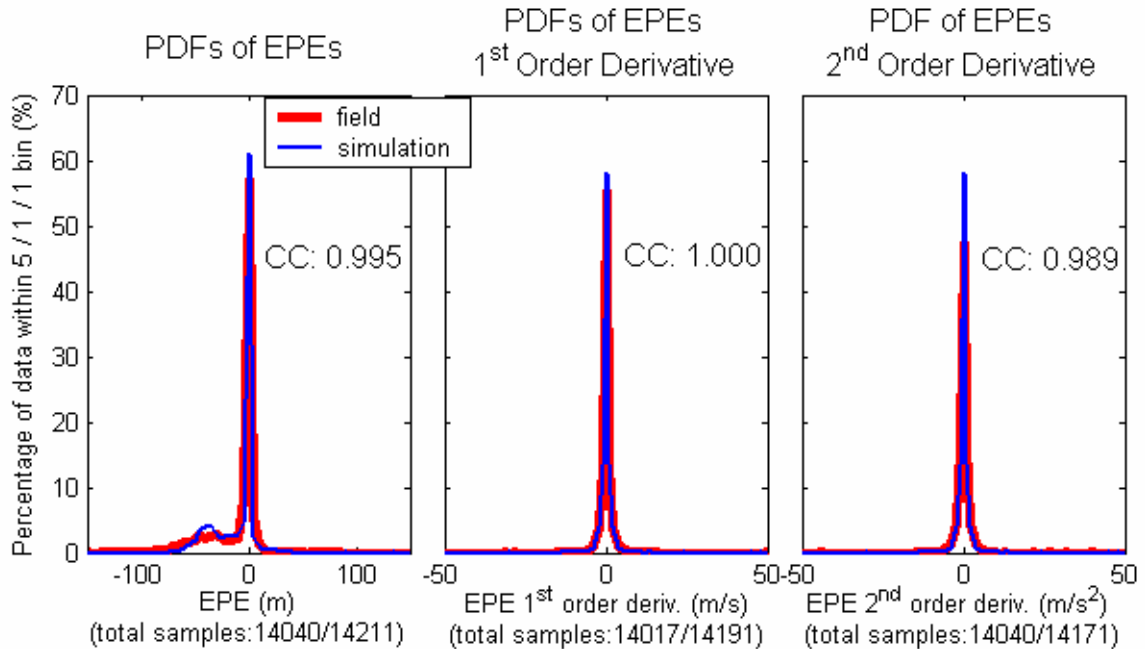
Figure 7.17: PDFs of EPE and associated 1st & 2nd order derivatives in field test and simulation— campus outdoor test

7.5.4 Positioning Accuracy and HDOP

The horizontal position errors for both the field test and simulation are shown in Figure 7.18. The field test position errors are again more dispersed than those of the simulation. The PDFs of horizontal position error, shown in Figure 7.19, indicate that the simulated data has fewer errors in the range of 35 to 60 m than the field data. In this instance, the correlation coefficient is 0.928. If the parameter of MNED in the simulator was increased, larger errors might be produced in the simulation. Figure 7.20 and Figure 7.21 show the HDOP and its PDF. The high correlation coefficient, 0.997, indicates a good match between field and simulated HDOP.
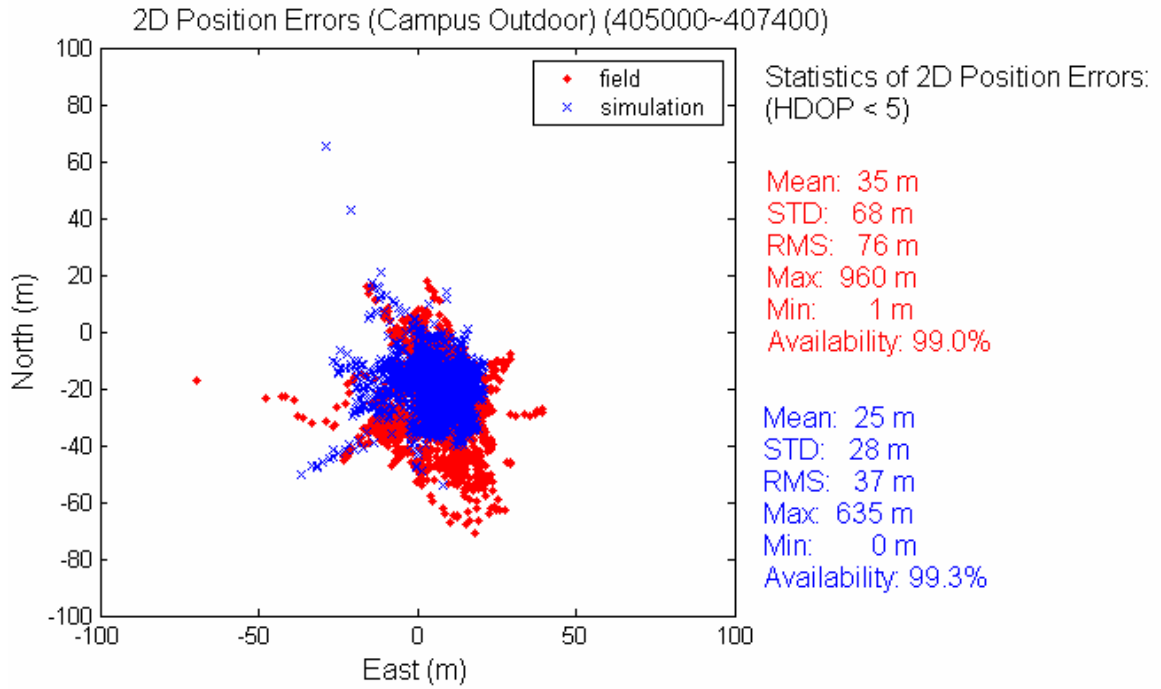
Figure 7.18: Field and simulator horizontal position errors — campus outdoor test
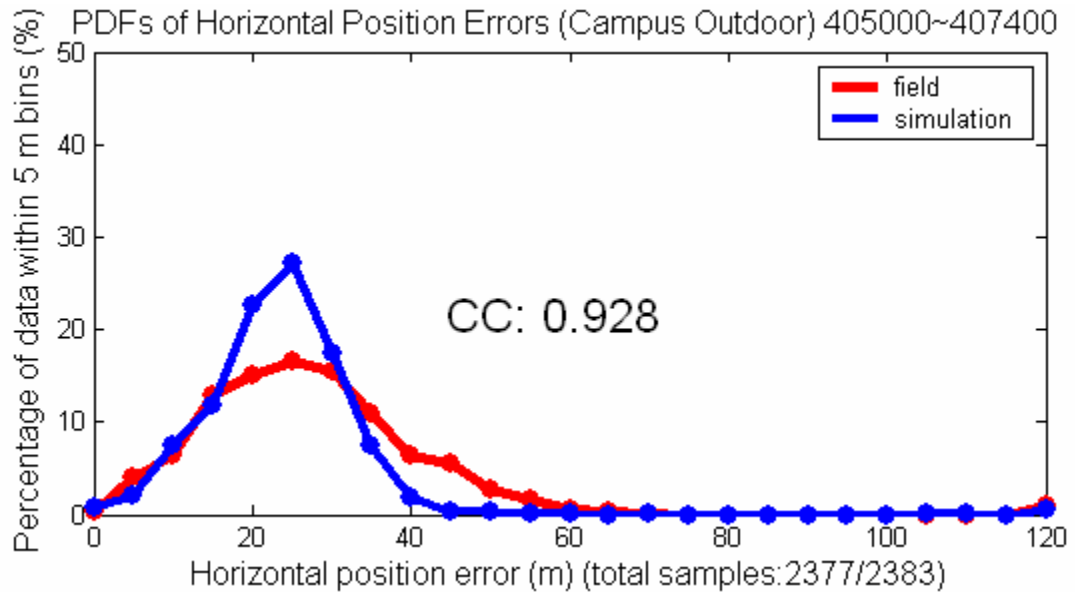
Figure 7.19: Field and simulator PDFs of horizontal position errors — campus outdoor test
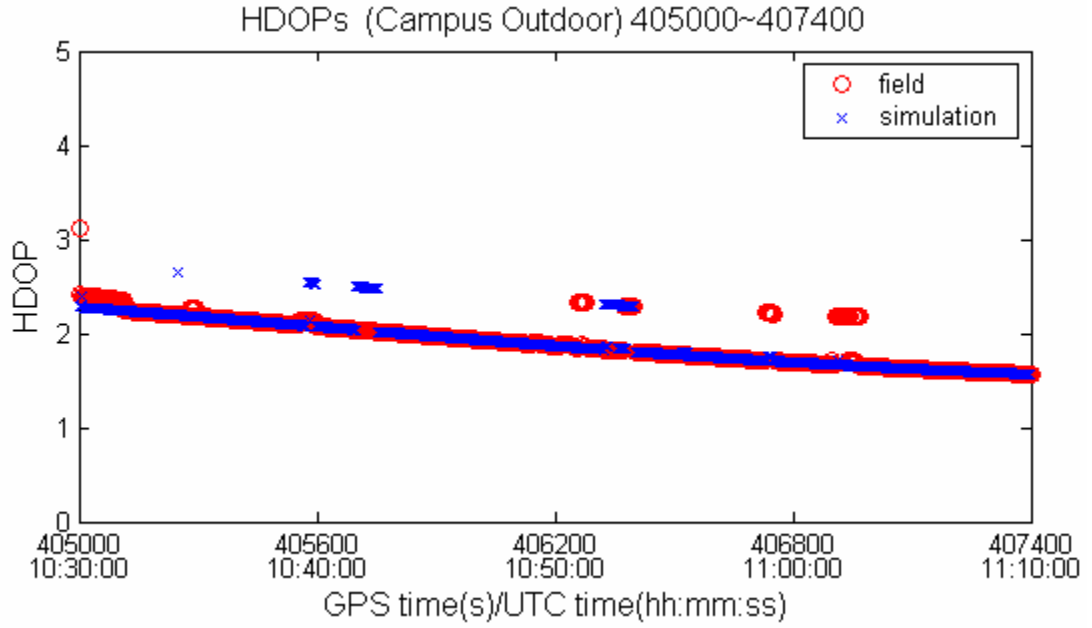
Figure 7.20: Field and simulator HDOPs — campus outdoor test
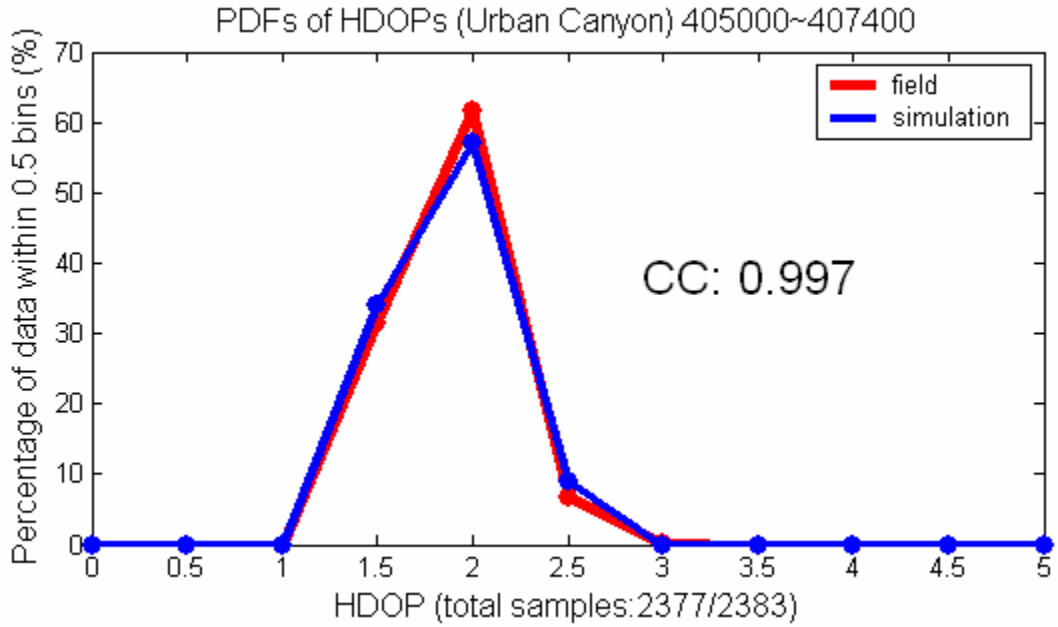
Figure 7.21: Field and simulator PDFs of HDOPs — campus outdoor test

Table 7.1 gives the overall correlation coefficients for both the field test and simulation data. Only three of the EPE PSD correlation coefficients are smaller than 0.85. The relatively strong match between field and simulated data suggests that the environment analysed could be reproduced in simulation.

Table 7.1: Campus outdoor field test and simulation correlation coefficients

Items		Correlation Coefficients	
		Fading	**EPE**
(.) (bin size: 1 dB, 5 m)		0.980	0.995
d(.)/dt (bin size: 0.5 dB, 1 m)		0.999	1.000
$d^2(.)/dt^2$ (bin size: 0.5 dB, 1 m)		0.972	0.989
Power Spectral Density (bin size: 0.005 Hz)	PRN 6	0.9910	0.7539
	PRN 17	0.9468	0.9412
	PRN 18	0.9598	0.4692
	PRN 21	0.8895	0.9850
	PRN 22	0.8593	0.6828
	PRN 23	0.9191	0.9742
	Average	**0.9276**	**0.8011**
Satellite Availability (bin size: 1)		0.996	
Position Error (bin size: 1 m)		0.928	
HDOP (bin size: 0.2)		0.997	

Chapter 8

Conclusions and Recommendations

8.1 Multipath Effects

The characteristics of indoor multipath errors on code and C/N_0 were extensively studied in this research on the basis of both theoretical and empirical analyses. The code and C/N_0 errors are functions of the amplitude ratio of multipath to LOS, multipath phase and multipath delay. Moreover, the multipath code error is also a function of the correlator spacing width. Multipath signal strength and delay are the key factors affecting the multipath errors analyzed herein. The statistics of multipath error are strongly correlated to multipath strength and multipath delay. The following is a summary of the characteristics of multipath errors in the empirical results observed using an HSGPS receiver:

a) Both the mean and standard deviation of the code errors increase with the lengthening of multipath delay;

b) If the multipath signal is stronger than the direct signal, the code error mean increases significantly and is approximately equal to the magnitude of the multipath delay;

c) The C/N_0 error mean is close to zero when the direct signal is stronger than multipath;

d) The standard deviation of the code error and the standard deviation of C/N_0 error both increase when the multipath strength approaches the strength of the direct signal;

e) Increasing the multipath delay causes small changes (< 6 dB) in both the mean and standard deviation of the C/N_0 error;

f) For the case when the multipath signal is stronger than the LOS signal, the C/N_0 error mean increases as the multipath strength increases, given that the multipath delay is constant.

These statistical characteristics proved to be very useful in estimating and adjusting the signal parameters in the simulations.

8.2 Estimation of Simulation Parameters

Signal fading and EPE are two important measures used to represent the C/N_0 and code error in this research. Pierce-point analysis characterizes the statistics of the fading and EPE measurements in relation to their distributions in space and, together with the statistical characteristics previously summarized, assists in estimating the signal parameters for the simulation. General guidelines for estimating the original simulated parameters are summarized as follows.

a) **LOS attenuation**: The fade mean is taken as the original estimate of the attenuation of the LOS signals if the LOS signal is stronger than the multipath signal;

b) **Multipath strength**: The original estimate of the multipath signal strength is 15 dB lower than the strength of the LOS;

c) **Multipath delay**: The largest distance between the antenna and the surrounding objects is taken as the original estimate of the MNED. If a satellite's EPEs fluctuate about an obvious negative level, the signal channels for the corresponding satellite are set to multipath-only and the original delay value is set to the negative mean level.

Applying the original parameters to the simulator, an original simulated result can be obtained. Based on the differences between the field and simulated results in statistics and time series, the simulated signal parameters are adjusted according to the multipath error characteristics until a satisfactory result is achieved. Guidelines for adjusting the simulated parameters are summarized as follows:

a) **LOS attenuation**: Adjust the LOS signal strength by the difference between the mean fading levels of the field and simulated results;

b) **Multipath strength**: Adjust the multipath signal strength according to the fluctuating amplitude of the fading and EPE measurements. Assuming that the LOS signal is stronger than the multipath signal, the larger the amplitudes, the stronger the multipath signals;

c) **Multipath delay**: Adjust the MNED by the fluctuating frequency of the fading and EPE measurements. The higher the frequency, the larger the MNED. For a multipath-only signal, the original delay is adjusted by an

amount equal to the difference between the mean EPE levels of the field and simulated results.

8.3 Signal Characterization in Test Environments

Both the urban canyon-like and indoor environments were tested.   For the former environment, the unattenuated LOS signal existed at high elevation angles.   It was found that the material of the building surfaces affected the power of the multipath signal.   Multipath signals reflected by a glass or a metallic surface are stronger than those reflected by a rough or coarse stone-textured surface.   In the case of indoor environments, all of the LOS signals were attenuated but to different extents, depending on the materials of the buildings.   It was found that the dimensions of the indoor space influenced the length of multipath delay; that is, the larger the space, the longer the delay observed in the tests conducted herein.

8.4 Simulation Validation

Statistical analysis of field and simulator results is a means of assessing the level of compatibility between the respective data sets.   The PDF indicates the statistical characteristics of the signals, while correlation coefficients quantify the statistical similarity between the field results and the simulation results.   Among the simulations of the garage, the High Bay and the campus outdoor environments, values of the correlation coefficients smaller than 0.9 only exist in the items of the PSD distributions.   All the other coefficients are larger than 0.9 and the average values of the PSD distribution coefficients are larger than 0.8.   For the case of the

Olympic Oval, although the complex environment and the limited number of samples resulted in relatively poor correlations between the field and simulated results, two thirds of the correlation coefficients in this case were still larger than 0.9. In general, the high degree of statistical similarity between the simulated results and the field results demonstrates the validity of the simulation for controlled GPS signal degraded environments.

8.5 Recommendations

8.5.1 Enhancement of the Simulator System

Although the LMM and UserActions methods provided by SimGEN v4.21 are both capable of implementing simulations for GPS signal degraded environments, some improvements are recommended to achieve a more effective and convenient simulation.

a) Available channel number: Due to the limited number of channels available in the University of Calgary Spirent GSS6560 simulator, only three multipath signals (in addition to a LOS signal) could be simulated for each satellite in this research. In some cases, the limited number of multipath signals could not replicate very well the nonperiodicity characteristic observed in the field results. A greater number of channels may allow the simulator to more closely simulate the irregularities seen in field results. Simulations with more channels assigned to each satellite are recommended to assess the extent of the improvement.

b) LOS attenuation: LMM model does not provide a function to set the level of LOS attenuation due to penetration loss. Therefore, a parameter controlling penetration loss as a function of elevation and azimuth in space can enhance the operation for LOS signal power level.

c) Multipath strength: Although SimGEN provides a method of setting the multipath signal strength in relation to a given LOS signal, this is irrespective of azimuth. A variation in multipath signal strength according to elevation and azimuth is more typical of certain environments.

d) Multipath delay: In order to implement a more controllable multipath delay for a particular environment, the parameter of maximum near echo is not always sufficient. Rather, a multipath delay parameter related to elevation and azimuth in the space would help to enhance the simulated scenario for a particular environment.

8.5.2 Additional Multipath Models

The multilpath delay model employed in this research depends upon the reflection on a vertical plane. In reality however, there are multipath signals due to other types of reflections and diffractions. Therefore, more multipath models can be further investigated, ground reflection and secondary reflection, for example. Ground reflection requires an antenna gain pattern with negative elevation angles, which were neglected in this research. Secondary reflection needs one more reflector and has more complicated geometries among the satellite, antenna and reflectors. A more complex modelling strategy could be designed, should future

simulator capabilities permit and requirements warrant such an approach.

8.5.3 Additional Field Tests

Although urban canyon and indoor environments are typical GPS degraded signal environments and typical of real life conditions, testing in additional environments, e.g. forested environments, and simulation of these tests is recommended to further assess the effectiveness of the method proposed herein.   The performance of GPS degraded signals in dynamic environments is another important condition calling for simulation.   The latest version of SimGEN has been augmented with a function to support dynamic modelling.   The difficulty of dynamic testing is the determination of the user's true positions with time stamps in the field.   Without knowledge of the user's true position, the EPEs cannot be assessed.   Nevertheless, for trajectories of short duration, this can be done with a high grade inertial navigation system.

REFERENCES

3GPPTM, *Requirements for support of A-GPS*, (FDD) (Release 6), R4-031156, 2003.

Aguirre, S., L. H. Loew and Yeh Lo (1994). *Radio Propagation into Buildings at 912, 1920, and 5990 MHz Using Microcells*. Proceedings of 3rd IEEE ICUPC, Oct 1994, pp. 129-134.

Boccia, L., G. Amendola, and G. D. Massa (2003). *Design A High-Precision Antenna for GPS*. Microwaves & RF, January 2003.
http://www.mwrf.com/Articles/ArticleID/5490/5490.html

Boulton, P., A. Read, G. MacGougan, R. Klukas, M. E. Cannon, G. Lachapelle (2002a), *Proposed Models and Methodologies for Verification Testing of AGPS-Equipped Cellular Mobile Phones in the Laboratory*. Proceedings of ION GPS 2002, Portland, OR, 24-27 September 2002, pp. 200-212

Boulton, P. (2002b). *GSS6560 Multi-Channel GPS/SBAS Simulator Product Specification*. Issue 1.00, 21 May 2002.

Braasch, M. S. (1996), *Multipath Effects, Global Positioning System: Theory and Applications*. Vol. I, ed. B.W. Parkinson and J.J. Spilker Jr., American Institute of Aeronautics and Astronautics, Inc., Washington DC. pp. 547-566

Cannon, M. E., G. Lachapelle, G. MacGougan, P. Boulton, and A. Read (2003). *Mobile Telephony:Testing a High Sensitivity GPS Receiver in Weak Signal Environments*. GPS World, Mar 1, 2003.
http://www.gpsworld.com/gpsworld/article/articleDetail.jsp?id=49421

Cannon, M. E. (2005). *Satellite Positioning*. ENGO 561 Course Notes, Department of Geomatics Engineering, University of Calgary.

Carver, C. (2005). *Myths and Realities of Anywhere GPS High Sensitivity versus Assisted Techniques*. GPS World, Sep 1, 2005.
http://www.gpsworld.com/gpsworld/article/articleDetail.jsp?id=180145

Diament, P. (2002), *Optical Fibers and Lightwave Propagation,* ed. J. D. Gibson, *The Communications Handbook*, second edtion, CRC Press / IEEE Press, Boca Raton FL.

FCC, 2000. *Guidelines for Testing and Verifying the Accuracy of Wireless E911 Location Systems*, Federal Communications Commision, USA, OET BULLETIN No. 71.
www.fcc.gov/Bureaus/Engineering_Technology/Documents/bulletins/ oet71/ oet71.doc

Garin, L. J., M. Chansarkar, S. Miocinovic, C. Norman, and D. Hilgenberg (1999). *Wireless Assisted GPS-SiRF Architecture and Field Test Results*, Proceedings of ION GPS 1999, Nashville, TN, September 14-17, 1999, pp. 489– 497.

Hay, C. (2004). *Urban Canyon SimGEN Scenario for Automotive Applications*. 2004 Spirent Users Conference, Washington, DC, April 1, 2004.

Hoffman-Wellenhof, B., H. Lichtenegger, and J. Collins (2001), *GPS Theory and Practice*, Springer-Verlag Wein, New York NY.

ICD-GPS-200C (2000), *GPS Interface Control Document*, NAVSTAR GPS Space Segment / Navigation User Interfaces, IRN-200C-004, 12, Apr, 2000

Jahn, A. (2001). *Propagation Considerations and Fading Countermeasures for Mobile Multimedia Services*. International Journal of Satellite Communications, Vol 19, May 2001, pp 223-250.

Johnson G. and T. Zaugg (2001). *Measuring Interchannel Bias in GPS Receivers*. ION 57th Annual Meeting/CIGTF 20th Biennial Guidance, Test Symposium, 11-13 June 2001, Albuquerque, NM, pp. 447-480.

Karunanayake, M. D., M. E. Cannon, and G. Lachapelle (2004), *Evaluation of Assisted GPS (AGPS) in Weak Signal Environments Using a Hardware Simulator*, Proceedings of ION GPS 2004, Long Beach, CA, September 13-16, pp. 2416-2426

Karunanayake, M. D., M. E. Cannon, G. Lachapelle, and G. Cox (2005a), *Effects of Kinematics and Interference on Assisted GPS*. Proceedings of NTM 2005, San Diego, 24-26 January, The Institute of Navigation, pp. 1071-1081

Karunanauake, M. D. (2005b), *Hardware Simulator Characterization of Assisted GPS,* MS.c. Thesis, published as Report No. 20231, Department of Geomatics Engineering, The University of Calgary.
http://www.geomatics.ucalgary.ca/links/ GradTheses.html

Klukas, R., G. Lachapelle, C. Ma, and G. Jee (2003). *GPS Signal Fading Model For Urban Centers*. IEE Proceedings – Microwaves, Antennas and Propagation, Vol.150, Issue 4, 8 August 2003, pp. 245-252.

Klukas, R., O. Julien, L. Dong, M. E. Cannon, and G. Lachapelle (2004). *Effects of Building Materials of UHF Ranging Signals*. GPS Solutions (2004) 8:1-8

Kraus, J.D., K.R. Carver (1973), *Electromagnetics,* Second Edition, McGraw-Hill Book Company.

Lachapelle, G., (2003a). *Advanced GPS Theory and Application*. ENGO 625 Course Notes, Department of Geomatics Engineering, University of Calgary.

Lachapelle, G., M. E. Cannon, R. Klukas, S. Singh, R. Watson, P. Boulton, A. Read, and K. Jones (2003b), *Hardware Simulator Models and Methodologies for Controlled Indoor Performance Assessment of High Sensitivity A-GPS Receivers*, Proceedings of ION GNSS 2003, Graz, Austria, April 22-25, 2003.

Lachapelle, G., H. Kuusniemi, D. T. H. Dao, G. MacGougan, and M. E.Cannon (2003c). *HSGPS Signal Analysis and Performance under Various Indoor Conditions*, Proceedings of ION GPS/GNSS 2003, Portland, OR, September 9-12, 2003, pp. 1171-1184.

Lachapelle, G., M. E. Cannon, R. Klukas, S. Singh, R. Watson, P. Boulton, A. Read, and K. Jones (2004), *Hardware Simulator Models and Methodologies for Indoor Performance Assessment of High Sensitivity Receivers*. Canadian Aeronautics and Space Journal, 50, 3, 151-168.

Landron, O., M. J. Feuerstein, and T. S. Rappaport (1996). *A Comparison of Theoretical and Empirical Reflection Coefficients for Typical Exterior Wall Surfaces in a Mobile Radio Environment*. Antennas and Propagation, IEEE Transactions on, Volume: 44, Issue: 3, Mar 1996, pp. 341-351.

Leva J. L., M. U. de Haag, and K. V. Dyke (1996). *Performance of Standalone GPS, Understanding GPS Signal Characteristics*. ed. E.D. Kaplan, Artech House, Inc., 685 Canton Street, Norwood, MA 0206.

Ma, C., G. Jee, G. MacGougan, G. Lachapelle, S. Bloebaum, G. Cox, L. Garin, and J. Shewfelt (2001). *GPS Signal Degradation Modeling*, ION GPS 2001, Session C2, Salt Lake City, UT, September 11-14, 2001, pp. 882-893

MacGougan, G. D., G. Lachapelle, R. Klukas, K. Siu, L. Garin, J. Shewfelt, and G. Cox (2002). *Degraded GPS Signal Measurements with A Stand-alone High Sensitivity Receiver*, Proceedings of ION NTM 2002, San Diego, 28-30 January 2002, pp. 191-204

MacGougan, G. D. (2003). *High Sensitivity GPS Performance Analysis in Degraded Signal Environments*. Ms.c. thesis, published as Report No. 20176, Department of Geomatics Engineering, University of Calgary.
http://www.geomatics.ucalgary.ca/links/ GradTheses.html

Misra, P. and P, Enge (2001), *Global Positioning System Signal*, Measurements, and Performance, Ganga-Jamuna Press, 2001.

Moeglein, M. and Krasner, N. (1998). *An Introduction to SnapTrack Server-Aided GPS Technolog*y. Proceedings of the ION GPS 1998, Nashville, TN, September 15-18, 1998, pp. 333–342.

Parkinson, B.W. (1996), *GPS Error Analysis, Global Positioning System: Theory and Applications*, Vol. I, ed. Parkinson, B.W. and Spilker, J.J. Jr., American Institute of Aeronautics and Astronautics, Inc., Washington DC.

Parsons, J. D. (2000). *The Mobil Radio Propagation channel*, Second Edition, John Wiley & Sons, Ltd.

Peterson, B., Bruckner, D., and Heye, S. (1997). *Measuring GPS Signals Indoors.* Proceedings of the ION GPS1997, Kansas City, Missouri, September 16-19, 1997, pp. 615–624.

Petovello, M.G., M. E. Cannon, and G. Lachapelle, *C^3NAVG^2™ Operating Manual, PLAN Group*, Department of Geomatics Engineering, University of Calgary.

Pérez-Fontán, F., B. Sanmartin, A. Steingass, A. Lehner, J. Selva, E. Kubista, and B. Arbesser-Rastburg (2004). *Measurements and Modeling of the Satellite-to-Indoor Channel for Galileo*. Proceedings of ION NTM 2004, San Diego, Ca, 26-28 Jan 2004, pp.190-202

Rappaport, T. S. (1996). *Wireless Communication Principles and practice.* Prentice Hall PTR, Upper Saddle River, New Jersey 07458.

Raquet, J. F. (2004). *GPS Receiver Design*. Engo 699.91 Course Notes, Department of Geomatics Engineering, University of Calgary.

Ray, J. K. (2000). *Mitigation of GPS Code and Carrier Phase Multipath Effects Using a Multi-Antenna System*. PhD. Thesis, published as Report No. 20136, Department of Geomatics Engineering, University of Calgary. http://www.geomatics.ucalgary.ca/links/ GradTheses.html

Ray, J. K. (2003). *Advanced GPS Receiver Technology*. ENGO 699.73 Course Notes, Department of Geomatics Engineering, University of Calgary, Spring, 2003

Sadiku, M. N. O. (2001). *Elements of Electromagnetics*. Third Edition, New York, Oxford University Press.

Salkhi, A. and J. Shewfelt (2001). *SiRF Application Note Integrating Patch Antennas with SiRF GPS Receivers*. Document Number APNT0022, Revision 1.0.

Singh, S., M. E. Cannon, R. Klukas, and G. Cox (2005). *Field Test Assessment of Assisted GPS and High Sensitivity GPS Receivers under Weak/ Degraded Signal Conditions*. Proceedings of ION GNSS 2005, Long Beach, CA13-16, September 2005.

Schoenbeck, R. J. (1998). *Electronic Communications Modulation and Transmission*. Merrill Publishing Company, A Bell & Howell Information Company, Columbus, Ohio 43216

Schwengler, T. and M. Gilbert (2000). *Propagation Models at 5.8 GHz – Path Loss & Building Penetration.* RAWCON Conference, Denver, CO, September 2000.

Spilker, J.J. Jr. (1996). *GPS Signal Structure and Theoretical Performance, Global Positioning System: Theory and Applications*. Vol. I, ed. Parkinson, B.W. and Spilker, J.J. Jr., American Institute of Aeronautics and Astronautics, Inc., Washington DC.

Stavrou, S. and S.R. Saunders (2003), *Factors Influencing Outdoor to Indoor Radio Wave Propagation*, 12th International Conference on Antennas and Propagation (ICAP 2003), Volume 2, 31 March-3 April 2003 pp. 581 - 585.

Steingass, A. and A. Lehner (2003). *Land Mobile Satellite Navigation – Characteristics of the Multipath Channel. Proceedings of ION GPS/GNSS 2003*, Portland, OR, September 9-12, 2003, pp.1016-1022

van Dierendonck, A. J. P. Fenton, and T. Ford (1992). *Theory and Performance of Narrow Correlator Spacing in a GPS receiver*. NAVIGATION: Journal of The Institute of Navigation, 39(3), pp. 265–283.

van Nee, R., (1993) *A Spread Spectrum Code and Carrier Synchronization Errors Caused by Multipath and Interference,* IEEE Trans. on Aerospace and Electronic Systems, Vol. 29, No. 4, October 1993, pp. 1359-1365.

Ward, P. (1996), Satellite Signal Acquisition and Tracking, Understanding GPS Principles and Applications, E.D. Kaplan, Artech House, Boston, pp. 119-208.

Watson, J. R. A. (2005). *High-Sensitivity GPS L1 Signal Analysis for Indoor Channel Modelling*. MS.c.,Thesis, published as Report No. 20215, Department of Geomatics Engineering, The University of Calgary.
http://www.geomatics.ucalgary.ca/links/ GradTheses.html

Williams, R. H. (2003), *Probability, Statistics, and Random process for Engineering*, THOMSON BROOKS/COLE, p116.